



Icosahedral Ag-In-Yb surfaces: clean surfaces,  
atomic motion and adsorbate structures

Thesis submitted in accordance with the requirements of the University of Liverpool for  
the degree of Doctor in Philosophy by

**Dominic William Burnie**

September 2022



# Abstract

The research described in this thesis involves investigations of clean quasicrystal surfaces and related overlayer structures. This work aims to build on the catalogue of information already acquired in this field by re-investigating and re-evaluating some previously studied structures and exploring some new quasicrystalline structures. The high-symmetry surfaces of the icosahedral (*i*)-Ag-In-Yb quasicrystal underpin all investigations discussed here, with scanning tunnelling microscopy (STM) and low-energy electron diffraction (LEED) being the primary experimental techniques.

In terms of clean surface investigations, new insights into the 2f-Ag-In-Yb surface structure are provided by the realisation of a bias-dependency of STM contrast on the surface. Features at positive bias are assigned to Yb contribution whereas negative bias observations are attributed to a subset of Ag/In sites in the surface model. In an investigation of the clean 5f-Ag-In-Yb surface, ordered motion of atoms is revealed. Movement is observed to occur at 5-fold symmetric locations, matching the substrate symmetry. Proposed driving mechanisms include simple surface diffusion or phason-assisted motion. This opens up a range of interesting avenues for future exploration, where such motion is not a common feature among other quasicrystal surfaces.

In a re-assessment of data taken prior to this work, which involved metal adsorption experiments on the 5f-Ag-In-Yb surface, a similar ordered motion of adsorbate species is also found to be apparent. Pb adsorption data is analysed in depth, with adatoms observed to move across their previously reported quasicrystalline adsorption sites in the first- and second-layers. The same is found to be true in a new adsorption investigation involving Ag deposition on this surface. At low to intermediate coverages, Ag adatoms diffuse across the quasicrystalline first-layer adsorption sites determined in previous density functional theory (DFT) calculations. Nucleation at cluster centre (CC) locations on the substrate surface is also apparent, with pentagonal arrangements of Ag features observed. This is exceeded by disordered 3D growth at high coverages.

With regards to molecular overlayers, deposition of C<sub>60</sub> on the 2f-Ag-In-Yb surface reveals an element of preferential adsorption at Ag/In-based sites. Disorder in the overlayer structure is attributed to the high atomic density at the substrate surface in combination with the large relative size of the C<sub>60</sub> molecules. Disorder becomes more apparent as the coverage is increased.



# Acknowledgements

When beginning my undergraduate Physics degree at the University of Liverpool in 2013, I certainly did not expect I would be embarking on a PhD four years later. It has been a challenging and, at times, seemingly insurmountable task. However, I am pleased to say that it has also been an extremely rewarding and enjoyable one. For the opportunity, I would like to thank Dr. Hem Raj Sharma and Prof. Ronan McGrath for inviting me into their group to undertake this work. I thank you not only for your expertise and guidance, but also for the welcoming atmosphere you provided outside of work at our group lunches and dinners.

For help and advice with the experimental side of this work, and for providing some important life lessons, I would like to thank Dr. Sam Haq. The data in this thesis would not have been acquired without your knowledge of experimental surface science systems and beyond. Likewise, a special thanks goes to Dr. Sam Coates, whose continual help with lab work and analysis (even after moving to the other side of the world) encouraged me to stick at it. I will not forget our wacky STM sessions.

Alongside this, I would like to thank Dr. Nozawa, whose theoretical work and collaboration provided inspiration for the experiments described in the second part of Chapter 6. I extend these thanks to those who provided data for the analysis discussed in the first part of Chapter 6 - Dr. Hem Raj Sharma, Dr. Sanger Hars and Dr. Peter Nugent. Thanks also to the ECMetAC who provided ample opportunity and funding for me to travel and share my work with other scientists in the field. These thanks also go to the EPSRC for funding my travel and attendance at conferences, as well as for funding my research as a whole.

Finally, these thanks would not be complete without acknowledging those closest to me - those who have ultimately motivated me to complete this work. To all friends at the SSRC, past and present, thank you for making each day both silly and enjoyable. The same goes to the rest of my friendship group (you know who you are), although I'm sure I would have had some more productive Monday mornings if it weren't for you! To my brothers, Alex and Joe, who provide me with a consistent source of inspiration and competition. To my Mam, Dad and Grandparents for encouraging the three of us to aim high and raising us to be who we are - you did all right. And lastly, to Harri for putting up with me for these past 7 years. I could not have done this without you.



# Contents

<b>Abstract</b>	<b>i</b>
<b>Acknowledgements</b>	<b>iii</b>
<b>Contents</b>	<b>vii</b>
<b>List of abbreviations</b>	<b>viii</b>
<b>1 Introduction</b>	<b>1</b>
<b>2 Quasicrystals</b>	<b>3</b>
2.1 Periodic crystallography . . . . .	4
2.2 Aperiodicity: Basic concepts . . . . .	6
2.2.1 Fibonacci sequence . . . . .	7
2.2.2 Aperiodicity in 2D . . . . .	8
2.2.3 Icosahedral symmetry . . . . .	10
2.3 Higher-dimensional crystallography . . . . .	11
2.3.1 Section and strip-projection methods in 1D . . . . .	12
2.3.2 Diffraction from a 1D Fibonacci chain . . . . .	13
2.3.3 Generating aperiodic structures in 2D and 3D . . . . .	15
2.4 Phasons . . . . .	16
2.5 Approximants . . . . .	19
2.6 Cluster model . . . . .	20
2.7 Stabilisation mechanisms . . . . .	23
2.8 <i>i</i> -Ag-In-Yb . . . . .	24
<b>3 Surface studies of quasicrystals: clean surfaces and adsorption</b>	<b>27</b>
3.1 Surface energetics . . . . .	28
3.2 High-symmetry surfaces of <i>i</i> -Ag-In-Yb . . . . .	29
3.3 Adsorption energetics . . . . .	31
3.4 Quasicrystalline epitaxy . . . . .	33

3.4.1	Rotational epitaxy . . . . .	34
3.4.2	Aperiodically modulated multilayer structures . . . . .	35
3.4.3	Pseudomorphic growth . . . . .	36
3.4.4	Aperiodic growth on periodic substrates . . . . .	43
<b>4</b>	<b>Experimental methods</b>	<b>45</b>
4.1	Ultra-high vacuum (UHV) . . . . .	45
4.1.1	Achieving UHV . . . . .	46
4.2	Sample preparation . . . . .	51
4.2.1	Growth methods . . . . .	51
4.2.2	Surface preparation . . . . .	52
4.2.3	Material deposition . . . . .	55
4.3	Surface analysis techniques . . . . .	55
4.3.1	Low-energy electron diffraction (LEED) . . . . .	55
4.3.2	Scanning tunnelling microscopy (STM) . . . . .	59
<b>5</b>	<b>Bias-dependency and atomic motion on the clean surfaces of <i>i</i>-Ag-In-Yb</b>	<b>64</b>
5.1	Introduction . . . . .	64
5.1.1	2f-Ag-In-Yb clean surface structure . . . . .	64
5.1.2	Atomic movement at the surface . . . . .	67
5.2	Experimental details . . . . .	69
5.3	Results . . . . .	70
5.3.1	2f-Ag-In-Yb bias-dependency . . . . .	70
5.3.2	5f-Ag-In-Yb atomic motion . . . . .	78
5.4	Summary . . . . .	94
<b>6</b>	<b>Metal adsorbate motion and Ag growth on the fivefold surface of <i>i</i>-Ag-In-Yb</b>	<b>96</b>
6.1	Introduction . . . . .	96
6.2	Experimental details . . . . .	102
6.3	Results . . . . .	102
6.3.1	Metal adsorbate motion . . . . .	102
6.3.2	Ag Growth . . . . .	107
6.4	Summary . . . . .	127
<b>7</b>	<b>C<sub>60</sub> adsorption on the twofold surface of <i>i</i>-Ag-In-Yb</b>	<b>129</b>
7.1	Introduction . . . . .	129
7.2	Experimental details . . . . .	133
7.3	Results . . . . .	133
7.3.1	C <sub>60</sub> growth on the twofold <i>i</i> -Ag-In-Yb surface . . . . .	133
7.4	Summary . . . . .	140

<b>8 Summary and outlook</b>	<b>143</b>
<b>List of Figures</b>	<b>160</b>
<b>List of Tables</b>	<b>160</b>
<b>References</b>	<b>161</b>
<b>Appendices</b>	<b>174</b>
<b>A List of publications</b>	<b>175</b>
A.1 Project publications . . . . .	175
A.2 Future publications . . . . .	175
<b>B List of presentations</b>	<b>176</b>
B.1 Oral . . . . .	176
B.2 Poster . . . . .	176

# List of abbreviations

<b>QC</b>	Quasicrystal
$\tau$	The golden ratio ( $= \frac{(1+\sqrt{5})}{2} = 1.618\dots$ )
<b>STM</b>	Scanning tunnelling microscopy
<b>LEED</b>	Low-energy electron diffraction
<i>i</i>	Icosahedral
<i>d</i>	Decagonal
<b>UHV</b>	Ultra-high vacuum
<b>PT</b>	Penrose tiling
<b>L and S</b>	Long and short segments, the ratio of whose lengths is equal to the golden ratio
<i>nD</i>	Higher-dimensional
<b>OD</b>	Occupation domain
<b>FFT</b>	Fast Fourier transform
<b>C<sub>60</sub></b>	Carbon-60
<b>Pn</b>	Pentacene
<b>DW</b>	Debye-Waller
<b>DFT</b>	Density functional theory
<b>TEM</b>	Transmission electron microscopy
<b>HRTEM</b>	High resolution transmission electron microscopy
<b>ADF-STEM</b>	Annular dark-field scanning transmission electron microscopy
<b>HAS</b>	Helium atom scattering
<b>MEIS</b>	Medium energy ion scattering
<b>XPS</b>	X-ray photoelectron microscopy
<b>RTH</b>	Rhombic triacontahedron
<b>TSK</b>	Terrace-Step-Kink
<b>CC</b>	Cluster centre
<b>ML</b>	Monolayer
<b>DS</b>	Dark star
<b>LDOS</b>	Local density of states
<b>FWHM</b>	Full width at half maximum
<b>PES</b>	Potential energy landscape

**RHS**      Right-hand side  
**LHS**      Left-hand side



# Chapter 1

## Introduction

Understanding surface phenomena is an essential step in the study of any material, where characteristics can vary significantly in comparison to the bulk. The surface of a material is where interfacial reactions take place and where crystal growth occurs. This makes it a key factor in many important technological processes such as catalysis and thin film growth. “Modern surface science” (i.e. the investigation of surfaces with well-defined structure and composition) was established in the 1960s with advances in vacuum technology, surface analytical techniques and high-speed digital computers [1]. Since then, it has undergone continuous progression, with one key milestone being the invention of STM by Binnig and Rohrer in 1986 [2]. This allowed for structural features at the surface of a material to be imaged at the atomic scale. Nowadays, surface science is more important than ever, with advancements in the nanotechnology industry demanding larger and larger surface to bulk matter ratios.

The surfaces of intermetallic alloys have attracted much interest over the years. This is owed to their often complex structures. The first structural solution to an intermetallic alloy was provided by Pauling in 1955 for  $\text{NaCd}_2$ , revealing a large unit cell containing 1152 atoms [3]. Today, many such intermetallic compounds exhibiting “giant” unit cells exist. They fall under the category of complex metallic alloys (CMAs), which are typically defined as an intermetallic compounds displaying a large unit cell, well-defined atomic clusters and inherent disorder in the ideal structure. The surfaces of CMAs have gained increasing attention due to the mechanical and chemical properties they exhibit, which are likely to give rise to many useful applications [4].

Quasicrystals (QCs) are often considered as the ultimate case of CMAs, displaying an

infinite unit cell. They exhibit long-range order whilst lacking periodicity. Their unusual structures provide an attractive stand point to study how the arrangement of atoms in a material affects its properties. The propagation of quasicrystalline order into the surfaces of these materials supplies an accessible route to realise this. As mentioned, the surface of a material is also where most interactions take place and where crystal growth occurs. In this sense, QC surfaces provide an intriguing landscape for both homoepitaxial and heteroepitaxial investigations, where such investigations have produced and continue to produce novel results. Therefore, further investigations of clean QC surfaces and overlayer structures are vital to advance our understanding of these materials and has the potential to provide new, interesting and unexpected results.

In this thesis, investigations of the clean surfaces of the *i*-Ag-In-Yb QC are discussed. As are studies involving deposition and adsorption of different materials on these surfaces. The structure will be as follows. Chapter 2 will provide a general introduction to quasicrystals. It will start with some basic crystallography and will then progress to considering the mathematical concepts associated with aperiodicity, finishing up with some examples of physical QCs. In Chapter 3, the clean surfaces of QCs and associated overlayer structures will be discussed in terms of both basic surface physics and the complex growth modes associated with QC thin film investigations. Pertinent examples will be briefly reviewed. After this, an overview of the experimental methods used to attain data for this thesis will be introduced. In particular, ultra-high vacuum (UHV) methods, sample preparation, LEED and STM will be detailed.

The results chapters are then split according to three main themes:

- Clean surfaces: In Chapter 5, a bias-dependency of STM contrast on the clean 2f-Ag-In-Yb surface will be presented. Also presented is the motion of atoms on the clean 5f-Ag-In-Yb surface, as observed by STM.
- Metal adsorption: In Chapter 6, STM data from previous metal adsorption investigations on the 5f-Ag-In-Yb surface will be revisited to investigate adsorbate motion. The results from an Ag adsorption investigation will also be presented.
- Molecular adsorption: In Chapter 7, an STM investigation of C<sub>60</sub> adsorption on the 2f-Ag-In-Yb surface will be discussed.

Finally, in Chapter 8, a summary and outlook for this work will be given alongside some proposed ideas for future avenues of exploration.

## Chapter 2

# Quasicrystals

Prior to the discovery of QCs, conventional crystallographic structures were defined by their periodicity. All known crystals were modelled as a periodic lattice, with an atom or basis of atoms residing at each lattice point. In this interpretation, crystals exhibit translational symmetry as well as a limited selection of rotational symmetries (1-, 2-, 3-, 4- and 6-fold) - a property often used to classify crystallographic structures. QCs, however, display long-range aperiodic order with no translational symmetry. They exhibit discrete diffraction patterns which often indicate rotational symmetries incompatible with conventional periodic systems (e.g. 5-fold, 10-fold, 12-fold).

The discovery of QCs by Dan Shechtman in 1982 led to a major transition from the conventional views of crystallography. When investigating a rapidly cooled Al-Mn alloy, Shechtman observed a diffraction pattern which appeared to display icosahedral symmetry with a 5-fold rotational symmetry axis [5]. This suggested a structure with long-range aperiodic order. The findings were initially dismissed by many in the scientific community, who proposed that twinned crystal arrangements were the cause of these unusual results [6]. However, subsequent investigations confirmed Shechtman's observations, explaining the structure in terms of 'a random packing of non-overlapping parallel icosahedra' [5]. In 2011, he was awarded a Nobel prize in chemistry for his work.

Nowadays, a range of systems exhibiting traditionally forbidden rotational symmetries have been uncovered. Examples include liquid crystals [7], colloids [8] and polymers [9]. However, intermetallic QCs remain the most common, where a wealth of stable binary [10, 11], ternary [12, 13] and quaternary systems have been observed [14, 15]. They display unexpected properties considering their constituent elements, giving rise to various

potential applications. While the brittle nature of bulk QCs can be a limiting factor in some cases, their high-hardness and low-friction/adhesion properties can be exploited in surface coatings. An example of this is in the QC-coated frying pan (Cybernox<sup>TM</sup>). Similarly, QC precipitation-strengthened steel (Sandvik Nanoflex<sup>TM</sup>) is an attractive material for surgical equipment. Other prospective applications include hydrogen storage, use as a catalyst in the steam reforming of methanol and use as a thermoelectric material [16].

Another major area of research is devoted to the investigation of epitaxial QC thin films. Elemental and molecular thin films have been observed to grow pseudomorphically on a range of QC substrate surfaces [17]. Examples of QC thin films grown on periodic substrates have also been reported [18]. The simplicity of these systems can provide an ideal route for the study of aperiodic order, whilst minimising the effects of chemical complexity. They can also provide insights into the formation of QCs and their stability, often resulting in novel discoveries [19, 20]. Epitaxial QC investigation will be discussed further in Chapter 3.

Although limited so far in terms of large-scale technological use, it is expected that investigations furthering our understanding of QCs will allow us to exploit and fine-tune their properties to reach the desired outcomes. Bearing in mind the applications and ideas discussed above, the study of surface phenomena in particular is expected to provide details on some important unanswered questions. In this lies the motivation for this work. To support this, a general overview of the background will be given in this chapter. Firstly, some aspects of conventional crystallography will be discussed. The mathematical concepts behind long-range aperiodic order will then be introduced and related to the physical structures exhibiting such properties - QCs.

## 2.1 Periodic crystallography

The fundamental concepts of periodic crystallography are vital for understanding the structure of both crystalline and QC substances, as will become apparent as this chapter progresses. A brief overview of some of the notions most relevant to this work will be given here. [21] has been used as a reference throughout this section.

Basic crystallography states that crystalline substances consist of an identical atom or group of atoms, known as the basis, residing at each vertex point on an infinite periodic lattice. The result is a set of repeating identical environments related by the lattice vector ( $\mathbf{R}$ ):

$$\mathbf{R} = n_1\mathbf{a}_1 + n_2\mathbf{a}_2 + n_3\mathbf{a}_3 \quad (2.1)$$

where  $n_1$ ,  $n_2$  and  $n_3$  are arbitrary integers and  $\mathbf{a}_1$ ,  $\mathbf{a}_2$  and  $\mathbf{a}_3$  are lattice vectors in 3D. The parallelepiped formed from the lattice vectors is known as the unit cell, with the smallest unit cell (containing just one lattice point) termed the primitive unit cell.

There are 14 lattices compatible with periodicity, known as the Bravais lattices. These are usually grouped into systems defined by the type of unit cell they exhibit (triclinic, monoclinic, orthorhombic, tetragonal, cubic, trigonal and hexagonal). The finite number of compatible lattices is a result of the crystallographic restriction theorem [22]. This can be illustrated simply by considering the corresponding 5 allowed Bravais lattices in 2D (oblique, rectangular, centred rectangular, square and hexagonal). As can be seen from Figure 2.1, the Bravais lattices can fill all space, mapping onto themselves under an appropriate rotation around an appropriate rotation axis. If a set of points defined by pentagonal symmetry are considered however, the same is not true. Gaps arise in building a pentagonal lattice and rotating around an arbitrary rotation axis does not map the lattice onto itself. The same is true for any other building block exhibiting an integer rotational symmetry that is not one of the permitted values defined by periodic crystallography.

The addition of a basis at each lattice point results in additional symmetry components which must be considered when describing the overall crystal structure. In total, there are 230 different symmetrical arrangements possible for a periodic crystal in 3D, termed the space groups. These are defined using a combination of the translational symmetry of the Bravais lattice and the other symmetry operations (rotation, inversion, screw plane and glide plane) exhibited by the structure.

Positions within a structure can be specified in terms of the axes formed by the three lattice vectors of the unit cell. Take, for instance, the body-centred cubic (bcc) system (Figure 2.2(a)). The conventional unit cell contains two lattice points - an eighth at each corner of the cube and one at the centre. The coordinates of the central lattice point are given by  $\frac{1}{2}\frac{1}{2}\frac{1}{2}$ , as can be seen in Figure 2.2(a). Similarly, these axes can be used to index crystal planes within a structure, useful for defining surfaces. With reference to Figure 2.2(b), the orientation of a plane is specified as follows: first the intercepts of the plane with each axis are found; then, the reciprocal of each intercept is taken; finally, these values are converted into the 3 smallest integers displaying the same ratio. The resultant values ( $hkl$ ) are known as the Miller indices. In the case of Figure 2.2(b), this would be the (263)

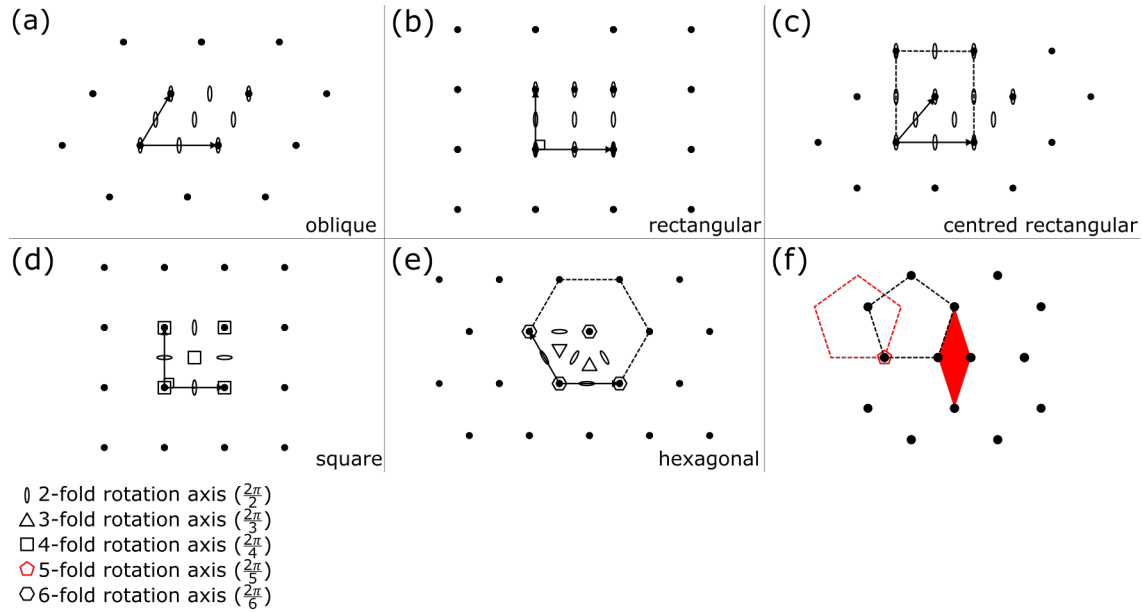


Figure 2.1: (a-f) The five 2D Bravais lattices (oblique, rectangular, centred rectangular, square and hexagonal, respectively), with lattice vectors marked by arrows and axes of rotational symmetry indicated according to the key in each (the number in brackets specifies the angle of rotation). (f) A simple demonstration of the incompatibility of a periodic pentagonal lattice in terms of rotational symmetry and the ability to fill all space.

plane.

## 2.2 Aperiodicity: Basic concepts

Despite the discussion in section 2.1, structures exhibiting long-range order whilst also displaying conventionally ‘forbidden’ rotational symmetries do exist. These structures have long-range, aperiodic order. Here, some illustrative examples of aperiodicity will be looked at, starting from 1D and working up to 3D. This will provide a good basis before moving onto some of the more complex mathematical concepts related to aperiodicity in the next section.

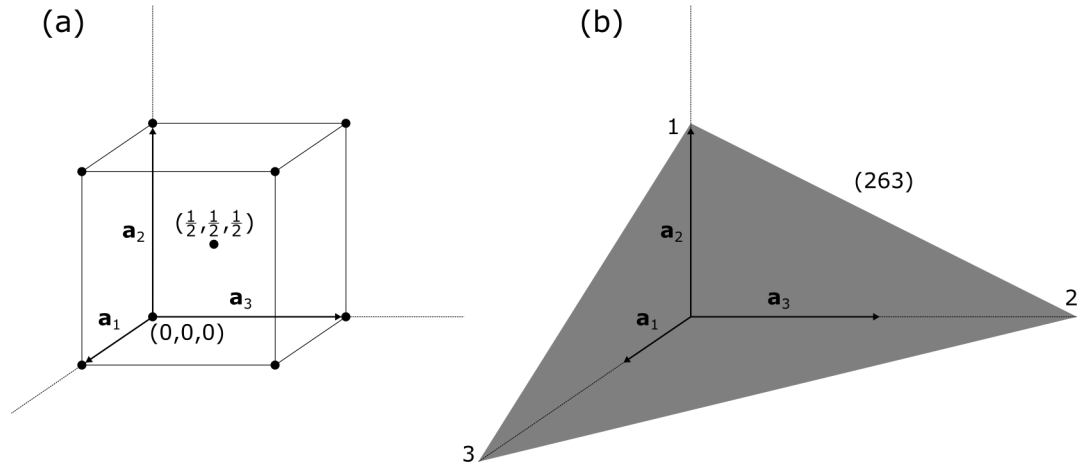


Figure 2.2: (a) Specification of (a) the coordinate system and (b) crystal planes in a cubic unit cell.

### 2.2.1 Fibonacci sequence

The Fibonacci sequence is a simple example of quasiperiodicity in 1D. It is a useful tool in the analysis of many QC structures and will be used throughout this thesis. The most relevant concepts will be introduced here.

A sequence of Fibonacci numbers is formed by taking each successive number as the sum of the two preceding numbers i.e.  $F_n = F_{n-1} + F_{n-2}$ . The initial conditions,  $F_0$  and  $F_1$ , can vary. Similarly, a 1D Fibonacci chain can be created by inflating sequences of long ( $L$ ) and short ( $S$ ) segments. To create successive generations of the chain, the substitution rules  $S \rightarrow L$  and  $L \rightarrow LS$  are used. These constructions are summarised in Table 2.1. It can be seen that the number of  $S$  segments at each generation ( $\#S$  column in the table) is equivalent to a numbered Fibonacci sequence with initial conditions  $F_0 = 1/F_1 = 0$ . The same is true for the number of  $L$  segments ( $\#L$  column in the table) and the combined total of both  $S$  and  $L$  segments ( $\#\text{Tot}$  column in the table), where these numbered Fibonacci sequences have initial conditions  $F_0 = 0/F_1 = 1$  and  $F_1 = 1/F_1 = 1$ , respectively.

An important aspect of the Fibonacci sequence is its relation to the golden ratio ( $\tau = \frac{1+\sqrt{5}}{2} = 1.618\dots$ ). As  $n$  increases, the ratio between two consecutive numbers in the sequence tends towards  $\tau$ . If the ratio of the size of  $L$  and  $S$  segments is constrained to  $\tau$ , it can be ensured that there is no translational symmetry in the Fibonacci chain, thus providing a 1D example of a quasiperiodic structure. In fact, these concepts are interlinked

<b>Fibonacci sequence</b>	<b>#S</b>	<b>#L</b>	<b>#Tot</b>
<i>S</i>	1	0	1
<i>L</i>	0	1	1
<i>LS</i>	1	1	2
<i>LSL</i>	1	2	3
<i>LSLLS</i>	2	3	5
<i>LSLLSLSL</i>	3	5	8
<i>LSLLSLSLLSLLS</i>	5	8	13
<i>LSLLSLSLLSLLSLSLLSLSL</i>	8	13	21
...	...	...	...

Table 2.1: The Fibonacci chain and corresponding Fibonacci numbers generated using *L* and *S* segments.

with the study of icosahedral QCs (iQCs). The vertex coordinates of an icosahedron are defined by  $(0, \pm 1, \pm \tau)$  and its two cyclic permutations (i.e. they are related by some factor or multiple of  $\tau$ ) [23]. As such, observations of structural features exhibiting  $\tau$ -scaling relationships or Fibonacci sequence arrangements are often used as an indication of quasiperiodicity in iQCs. Icosahedral symmetry will be discussed further in Section 2.2.3. QCs of different symmetries can display features related by different scaling ratios. For example, the hallmarks of octagonal and dodecagonal structures are the silver and platinum ratios, respectively [24].

## 2.2.2 Aperiodicity in 2D

It will now be seen that it is possible to generate theoretical structures in 2D which display long-range aperiodic order and classically forbidden rotational symmetries. This can be achieved using multiple building blocks or proto-tiles to create a quasiperiodic ‘tiling’ which fills all space. Aperiodic tilings exhibiting a range of rotational symmetries have been discovered. The 5-fold symmetric Penrose tilings (PTs) will be the focus here [25,26], as they are most relevant for this work.

There are three PTs in total, named the P1, P2 and P3 tilings. An example of the P1 tiling in shown is Figure 2.3(a), with its 6 proto-tiles colour coded differently and shown in Figure 2.3(c). As with the Fibonacci chain, self-similarity is a principal feature, where substitution can be used to inflate/deflate the tiling. This is shown schematically in Figure 2.3(b), where one proto-tile is decomposed into multiple smaller proto-tiles in a hierarchical

pentagonal structure.  $\tau$ -scaling is again evident, where the ratio between the size of the large and small pentagons is equal to  $\tau^2$ . The tiling can also be constructed using matching rules for each proto-tile, such that only specific combinations are permitted. The matching rules for the P1 proto-tiles are displayed in Figure 2.3(c). Tile edges can be placed adjacent assuming they have equal integers and opposite parities. Another important method used to generate the PTs, as well as other aperiodic structures, involves the use of higher-dimensional ( $nD$ ) space (e.g. 5D) [27]. This will be discussed further in Section 2.3.

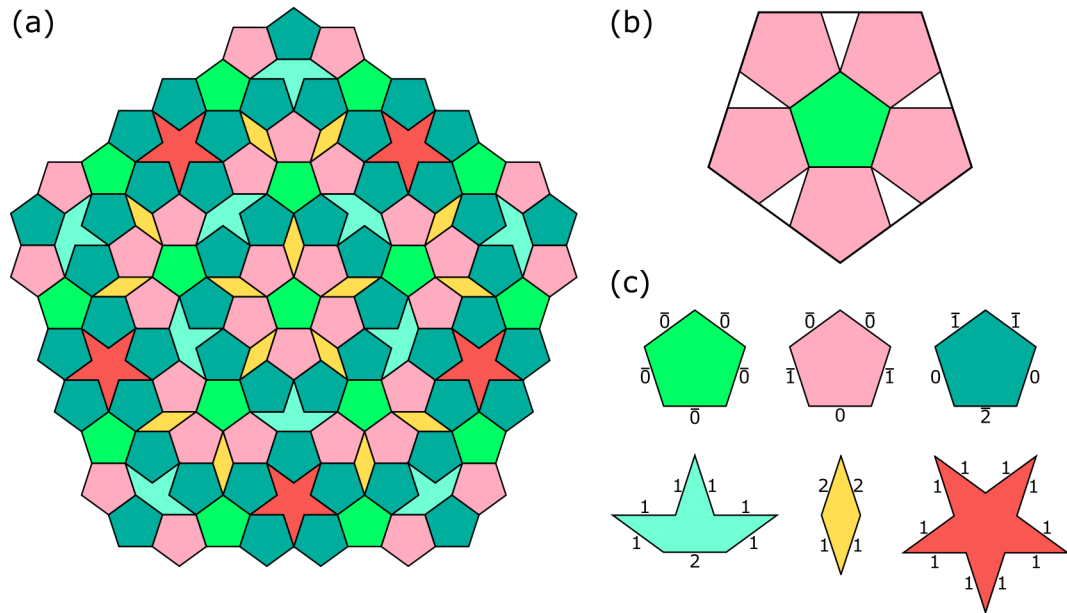


Figure 2.3: (a) A patch of the P1 PT. (b) Inflation/deflation of the tiling using substitution. (c) The proto-tiles and their corresponding matching rules. Tiles are colours coded according to these matching rules in all figures.

In terms of practical use, aperiodic tilings can help explain the structure of 2D planes in many QCs. Comparisons between the observed electron diffraction patterns along different orientations in Shechtman's initial discovery and calculated diffraction patterns from a set of 2D PTs with different symmetries show remarkable similarities [28], as can be seen in Figure 2.4. Overlaying tilings on real-space data is also a common technique used to classify surface features [18, 19, 29].

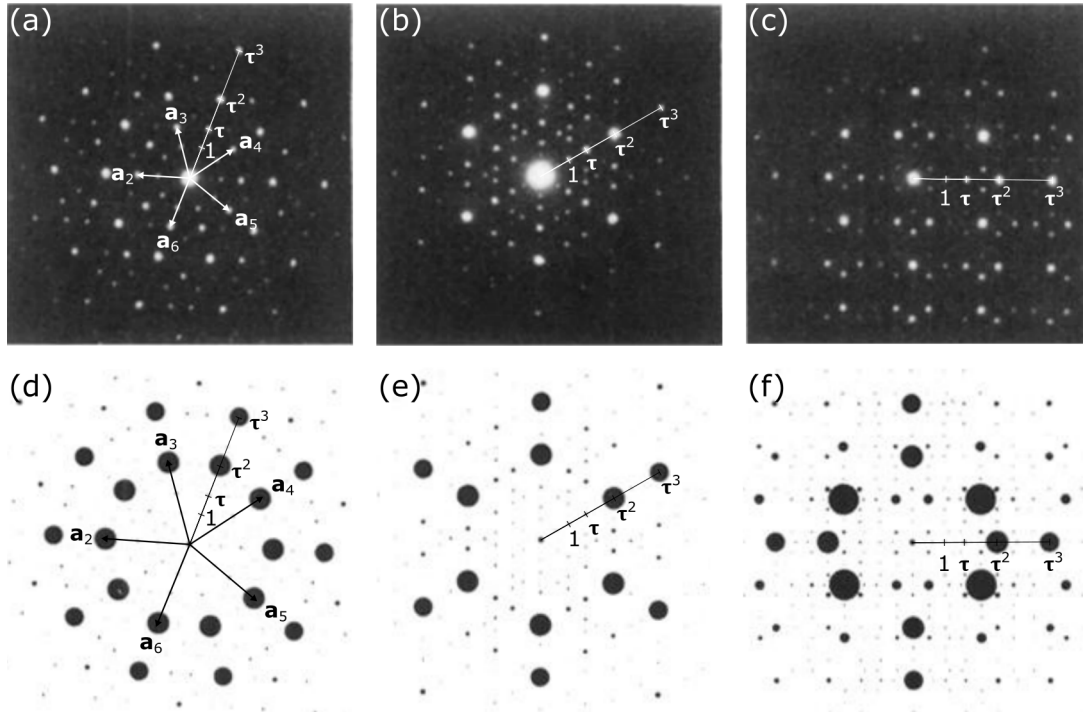


Figure 2.4: (a-c) Observed and (e-f) calculated diffraction patterns from the 5-fold, 3-fold and 2-fold orientations of the *i*-Al-Mn phase from left to right, respectively. The 5-fold patterns have been indexed using the icosahedral reciprocal basis vectors (see Figure 2.5), where vector  $\mathbf{a}_1$  is perpendicular to the page. Reproduced from [5] and [28].

### 2.2.3 Icosahedral symmetry

To extend the discussion of aperiodicity into 3D, the concept of icosahedral symmetry must first be introduced. It is particularly relevant to this thesis, as all results chapters focus on investigations of an iQC. An icosahedron is one of the five platonic solids, composed of twenty equilateral triangular faces with five meeting at each vertex. It contains six 5-fold, ten 3-fold and fifteen 2-fold rotational symmetry axes. As with the example of a pentagonal building block in 2D (Figure 2.1(f)), gaps arise in building a 3D structure from identical polyhedra with icosahedral symmetry. Icosahedra are incompatible with a periodic lattice. However, with multiple polyhedra, structures can be formed which display icosahedral symmetry and long-range aperiodic order in 3D. The most relevant example is the 3D analogue to the PT, known as the 3D PT or Ammann tiling [30]. In its simplest form, this consists of two building blocks: prolate and acute rhombohedra with relative

frequencies of  $\tau : 1$ , respectively. The concept of  $n$ D mathematics will be used to expand upon this further in the Section 2.3.

For now, the importance of icosahedral symmetry can be highlighted by considering the six reciprocal space basis vectors  $\mathbf{a}_j$  ( $j = 1, \dots, 6$ ) defining an icosahedron. These are shown in Figure 2.5(a) and projected along the 5-fold direction in Figure 2.5(b). Starting at the centre of an icosahedron, they point out towards the corners along each 5-fold axis and are defined by  $\mathbf{a}_1 = a(0, 0, 1)$  and  $\mathbf{a}_j = a(\frac{\sin\theta\cos 2\pi j}{5}, \frac{\sin\theta\sin 2\pi j}{5}, \cos\theta)$  for  $j = 2, \dots, 6$ , where  $\frac{1}{a}$  is the lattice constant of a periodic 6D reciprocal lattice (see Section 2.3 for further discussion on this) and  $\theta$  is the angle between two adjacent 5-fold axes ( $\tan\theta = 2$ ) [31]. The basis vectors can be labelled using the generalised Miller indices  $[100000]$ ,  $[010000]$ ,  $[001000]$ ,  $[000100]$ ,  $[000010]$  and  $[000001]$ , respectively [32]. These basis vectors can be used to index the electron diffraction patterns from  $i$ -Al-Mn in Shechtman's initial discovery. This is shown in Figure 2.4(a), on the diffraction pattern along the 5-fold direction. Note that the pattern appears 10-fold here due to inversion symmetry.

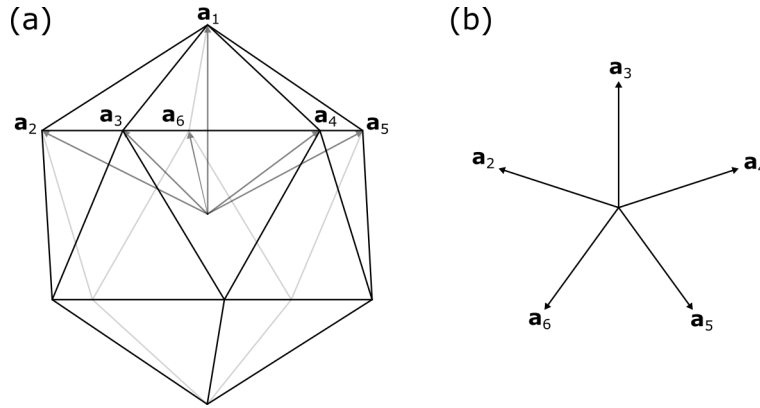


Figure 2.5: (a) The six reciprocal basis vectors of an iQC. (b) Projection of these vectors along a 5-fold direction, where vector  $\mathbf{a}_1$  is perpendicular to the page.

## 2.3 Higher-dimensional crystallography

As touched upon already, the  $n$ D approach is paramount in the current understanding of QCs. Theoretical quasiperiodic structures can be generated from a periodic lattice in a higher dimension. For instance, an icosahedral quasilattice in 3D can be generated from a periodic structure in 6D. This is perhaps not surprising given the indexing of an iQC

diffraction pattern with six reciprocal lattice vectors in Section 2.2. It means many of the well-established methods associated with periodic crystallography can be extended into  $n$ D space, subsequently giving us a better understanding of quasiperiodic structures and related phenomena such as phasons, approximants and atomic clusters (see Sections 2.4, 2.5 and 2.6, respectively).

In this section, a similar layout to the last will be followed. Beginning again in 1D, the Fibonacci sequence will be generated using an  $n$ D approach. It will then be seen how  $n$ D mathematics can be used to calculate the diffraction pattern from such a structure. After this, these ideas will be extended into 2D and 3D space, again using the PT and 3D PT as examples. The concepts introduced here will be of relevance to the analysis presented in Chapter 5.

### 2.3.1 Section and strip-projection methods in 1D

Generation of the Fibonacci sequence using the  $n$ D formalism requires taking a 1D section or projection from a 2D hypercubic (square) lattice. Both the section and strip-projection methods are displayed schematically in Figure 2.6(a) and (b), respectively. A square lattice of lattice constant  $a$  is defined on the orthogonal  $\mathbf{xy}$ -axis. A second set of orthogonal axes ( $\mathbf{V}_{\parallel}$  and  $\mathbf{V}_{\perp}$ ) are also defined, rotated by an angle  $\alpha$  with respect to the  $\mathbf{xy}$ -axis such that  $\cot\alpha = \tau$ .  $\mathbf{V}_{\parallel}$  represents par(allel)-space or physical space and  $\mathbf{V}_{\perp}$  represents perp(pendicular)-space.

In the section method, each point on the square lattice is decorated with a line segment  $A_{\perp}$  of length  $\Delta = a(\cos\alpha + \sin\alpha)$ , with orientation along the  $\mathbf{V}_{\perp}$ -axis. These are termed atomic surfaces or occupation domains (ODs). They are formed via the projection of a unit cell from the square lattice onto the  $\mathbf{V}_{\perp}$ -axis, as shown towards the bottom left of Figure 2.6(a) and (b). At points where atomic surfaces intersect the  $\mathbf{V}_{\parallel}$ -axis, short ( $S = a\sin\alpha$ ) and long ( $L = a\cos\alpha$ ) segments are created, forming a section of the Fibonacci chain. Similarly, in the strip-projection method, a strip of width  $\Delta$  is formed parallel to and centred on the  $\mathbf{V}_{\parallel}$ -axis. Projecting square lattice points lying within this window, along the  $\mathbf{V}_{\perp}$ -axis and onto the  $\mathbf{V}_{\parallel}$ -axis, again results in the formation of a section of the Fibonacci chain (Figure 2.6(b)). In both cases, a 1D quasiperiodic structure has been created in physical space [31, 33].

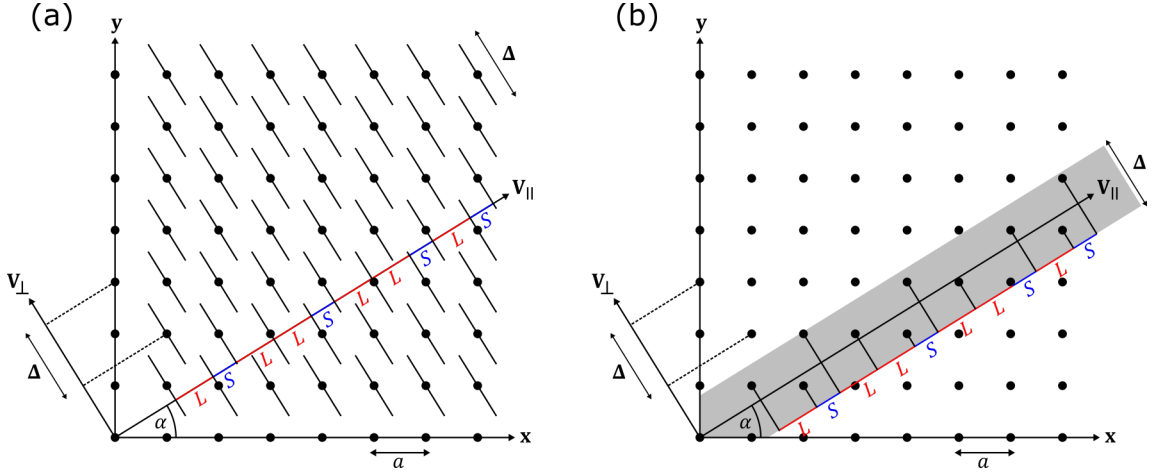


Figure 2.6: Generation of a 1D Fibonacci chain from a 2D hypercubic lattice using (a) the section method and (b) the strip-projection method.

### 2.3.2 Diffraction from a 1D Fibonacci chain

$n$ D structure analysis incorporates reciprocal space information, making comparisons with experimentally observed diffraction data from QCs possible. Sticking with the simple 1D Fibonacci chain example, it will now be seen how the  $n$ D formalism can be used to calculate theoretical diffraction patterns. Features of the section method will be utilised in this example, although the same results can be achieved with the strip-projection method. Only the most relevant aspects of the calculation will be presented here, where the reader is referred to [31, 34, 35] for a full derivation.

In general, this calculation involves taking the Fourier transform of points from the 2D square lattice which contribute to production of the Fibonacci chain. The density distribution of these points is given by a convolution of the overall density of points in the lattice ( $\rho$ ) with the ‘acceptance window’ formed by the ODs which decorate each point ( $A_{\perp}$ ). The Fourier transform of this is then given by the product of the Fourier transforms of each:

$$F'(\mathbf{Q}) = \left[ \frac{1}{a^2} \sum_{hh'} \delta(\mathbf{Q} - \mathbf{Q}^{hh'}) \right] \Delta \frac{\sin(Q_{\perp} \Delta / 2)}{(Q_{\perp} \Delta / 2)} \quad (2.2)$$

where the equation in the square brackets represents the Fourier transform of  $\rho$ , a square lattice in reciprocal space (i.e. on the  $\mathbf{x}^* \mathbf{y}^*$ -axis) with spacing  $\frac{2\pi}{a}$ , and the rest is the

Fourier transform of  $A_{\perp}$ .  $\mathbf{Q}^{hh'}$  are the reciprocal space lattice vectors, with component  $\frac{2\pi}{a}h$  along the  $\mathbf{x}^*$ -axis and  $\frac{2\pi}{a}h'$  along the  $\mathbf{y}^*$ -axis.  $\mathbf{Q}^{hh'}$  can thus be decomposed into the following par-space and perp-space components:

$$Q_{\parallel}^{hh'} = \frac{2\pi}{a} \sqrt{\frac{\tau^2}{\tau^2 + 1}} \left( h + \frac{h'}{\tau} \right) \quad (2.3)$$

and

$$Q_{\perp}^{hh'} = \frac{2\pi}{a} \sqrt{\frac{\tau^2}{\tau^2 + 1}} \left( h' - \frac{h}{\tau} \right) \quad (2.4)$$

Due to the relationship between real space and reciprocal space, a par-space cut through an  $n$ D lattice (i.e. the cut of the  $\mathbf{V}_{\parallel}$ -axis through the square lattice in Figure 2.6) will correspond to a reciprocal space projection onto reciprocal par-space ( $\mathbf{V}_{\parallel}^*$ ). Since a Fourier transform involves a conversion from real space to reciprocal space (and vice versa), the Fourier components of the Fibonacci chain can be determined with a projection of  $F'(\mathbf{Q})$  onto  $\mathbf{V}_{\parallel}^*$ , thus given by:

$$F'(Q_{\parallel}) = \frac{1}{a^2} \sum_{hh'} [\delta(Q_{\parallel} - Q_{\parallel}^{hh'}) \Delta \frac{\sin(Q_{\perp}^{hh'} \Delta/2)}{(Q_{\perp}^{hh'} \Delta/2)}] \quad (2.5)$$

Immediately noticeable from Equation 2.5 is the existence of sharp diffraction peaks, as implied by the  $\delta$  term in the left-hand side (LHS) of the equation. Due to the irrational slope of  $\mathbf{V}_{\parallel}^*$ , the projection will produce a quasiperiodically arranged set of peaks in reciprocal space. Further to this, the pattern is indexable with two integers,  $h$  and  $h'$ , despite the fact the real space structure is a 1D Fibonacci chain. Since for any given  $h$ ,  $h'$  can take any value, this implies a very dense diffraction pattern. However, considering that the intensity is proportional to the squared absolute value of the function in Equation 2.5, it can be seen from the right-hand side (RHS) that this will be maximised for  $Q_{\perp} \rightarrow 0$ . From Equation 2.4, this is achieved when  $\frac{h}{h'} \rightarrow \tau$  i.e. the brightest diffraction peaks will occur when  $(h, h')$  are successive Fibonacci numbers  $((3, 2), (5, 3), (8, 5)$  etc.), existing at  $\tau$ -scaled separations [34, 35].

The features of the calculated Fourier transform in this simple theoretical example are akin to what is observed in experimental diffraction patterns taken from physical QC structures. Taking again the  $i$ -Al-Mn diffraction patterns observed in Shechtman's initial

discovery (Figure 2.4), sharp sets of diffraction peaks at  $\tau$ -scaled distances can be seen. As such, extending these concepts into 2D and 3D is important for the understanding of physical QCs and their long-range aperiodic order.

### 2.3.3 Generating aperiodic structures in 2D and 3D

In the  $n$ D formalism, generating quasiperiodic structures in 2D and 3D requires the use of even higher dimensions. Using this technique has proved extremely useful in predicting the structural properties of planes in 2D QCs (i.e. those with periodic ordering along one axis) as well as the surfaces and overall 3D structure of 3D QCs (iQCs). As mentioned in Section 2.2, the 2D PTs can be produced from a periodic lattice in 5D [27]. As 2D aperiodic structures can also be created via the truncation of aperiodic structures in 3D, and because it is most relevant for this thesis, the generation of a 3D PT from a 6D hypercubic lattice will be discussed in the following.

As with the Fibonacci chain example, projection of the 6D hypercubic unit cell onto 3D perp-space provides the OD, in this case, a set of three nested polyhedra: a triacontahedron, a dodecahedron and an icosahedron from outer to inner shell, respectively. Perp-space components of the 6D lattice lying within the window created by this OD will contribute to the generation of the 3D PT in par-space. The arrangement of neighbouring unit cells in the 6D lattice helps define the structure in par-space. 6D hypercubic unit cells related by the 6D lattice vectors  $(10000)_D$ ,  $(00110\bar{1})_D$  and  $(0010\bar{1}0)_D$  (where the subscript  $D$  denotes the fact these vectors are defined with respect to the 6D crystallographic basis, or  $D$ -basis) share 5D, 3D and 4D faces, respectively. They correspond to specific overlappings in the 3D par-space structure which generate the 3D PT. The overlap regions produced are a rhombic icosahedron, an oblate rhombohedron and a rhombic dodecahedron, respectively [31, 36].

The 6D lattice points can be projected into par-space and perp-space using a projection matrix formed from the six orthonormal basis vectors which describe the 6D hypercubic lattice, defined with respect to  $V$ -space:

$$M = \frac{a}{\sqrt{2+\tau}} \begin{bmatrix} 1 & \tau & \tau & 0 & -1 & 0 \\ \tau & 0 & 0 & 1 & \tau & 1 \\ 0 & 1 & -1 & -\tau & 0 & \tau \\ \tau & -1 & -1 & 0 & -\tau & 0 \\ -1 & 0 & 0 & \tau & -1 & \tau \\ 0 & \tau & -\tau & 1 & 0 & -1 \end{bmatrix} \quad (2.6)$$

where  $a$  is the 6D lattice constant and the dot product of the 6D lattice with:

$$\mathbf{V}_{\parallel} = \begin{bmatrix} M_1 \\ M_2 \\ M_3 \end{bmatrix} \quad (2.7)$$

or:

$$\mathbf{V}_{\perp} = \begin{bmatrix} M_4 \\ M_5 \\ M_6 \end{bmatrix} \quad (2.8)$$

gives the par-space and perp-space components, respectively [37, 38]. This technique will be used in Chapter 5 to generate an aperiodic distribution related to the *i*-Ag-In-Yb QC.

It should be noted here that there are three 6D hypercubic lattices compatible with icosahedral symmetry: primitive (*P*-type), body-centred (*I*-type) and face-centred (*F*-type). Each type produces a different icosahedral quasilattice after projection into par-space following the method outlined above. QCs based on *P*-type and *F*-type lattices have been observed experimentally. The *i*-Ag-In-Yb QC used in thesis is a *P*-type structure [39].

As discussed in Section 2.3.2, the Fourier transform of an OD is a vital component in the understanding of QC diffraction patterns. As diffraction data plays a key role in structure determination, the definition of the shape and positioning of ODs requires careful consideration when modelling physical QCs - different OD geometries can produce different structures in par-space. Modification of the ODs described above is generally required to ensure physically acceptable local atomic environments in the resultant structure. This proceeds by refining the ODs using comparisons between theoretical and experimental diffraction data [40]. This will be discussed further in the context of the *i*-Cd-Yb QC in Section 2.8.

## 2.4 Phasons

The description of QC structures using the  $n$ D approach presents other interesting features resulting from additional degrees of freedom associated with perp-space. In this section, phasons will be introduced. First, a definition will be given and it will be shown how they can be modelled using  $n$ D methods. After this, how phasons have aided the understanding of physical QCs will be discussed. These ideas will come in useful in Chapter 5, where the

movement of features observed by STM will be analysed in relation to phasonic behaviour.

Alongside the phononic behaviour associated with periodic crystals, QCs also display phasonic behaviour. While phonons are characterised by excitations in physical space, and therefore a collective vibrational motion of atoms, phasons can be understood in terms of structural rearrangements or atomic jumps. They can be modelled as excitations in perp-space caused by fluctuations of the ODs which decorate the points of an  $n$ D lattice [41]. This can be illustrated by going back to the example of the generation of a Fibonacci chain from a 2D hypercubic lattice. Consider a simplistic example of an excitation in perp-space as a shift of the  $\mathbf{V}_{\parallel}$ -axis along the direction of the  $\mathbf{V}_{\perp}$ -axis. This, in effect, imitates a fluctuation in the ODs decorating each point of the hypercubic lattice. As can be seen from Figure 2.7(a), the result is the generation of a new Fibonacci chain in which local rearrangement of some tiles has occurred when compared to the original sequence (highlighted by an ellipse). These local rearrangements are termed phason flips and, in real QC structures, correspond to atomic jumps between different positions [40].

Phason disorder can be quenched in as the QC temperature falls from the melting point, where ‘frozen’ structural deviations are termed static phasons. Dynamical phasons, on the other hand, allow for self-diffusion in the QC at lower temperatures [42]. Phason related atomic fluctuations are a key concept in understanding the growth of QCs and their thermodynamic stability. This will be discussed further in Section 2.7.

Experimentally, phason disorder can be inferred from diffraction data. As is well known from the study of phonon modes in periodic crystals, the displacement of atoms from their ‘ideal’ positions results in diffuse scattering. In general, this causes a reduction in the intensity of Bragg peaks in diffraction patterns, defined by the Debye-Waller (DW) factor. For QCs, the DW factor contains both phononic and phasonic contributions. It can be assessed by considering how the experimental diffraction pattern differs in comparison to that modelled from an ‘ideal’ structure, where an ideal structure assumes no disorder (see Section 2.3.2 for the calculation of a diffraction pattern from an ideal 1D Fibonacci chain). Characteristic deviations in the diffraction data (i.e. intensity reduction and peak broadening) will correspond to fluctuations of ODs in par-space or perp-space, caused by diffusive scattering from phonon modes or phason modes, respectively. Analysis of these deviations can reveal important information regarding these phenomena [43].

Direct experimental evidence for phason assisted motion has, in fact, been observed in transmission electron microscopy (TEM) investigations of the decagonal surfaces of two Al-based QCs at high temperatures. Decagonal QCs (dQCs) are 2D QCs, consisting of a

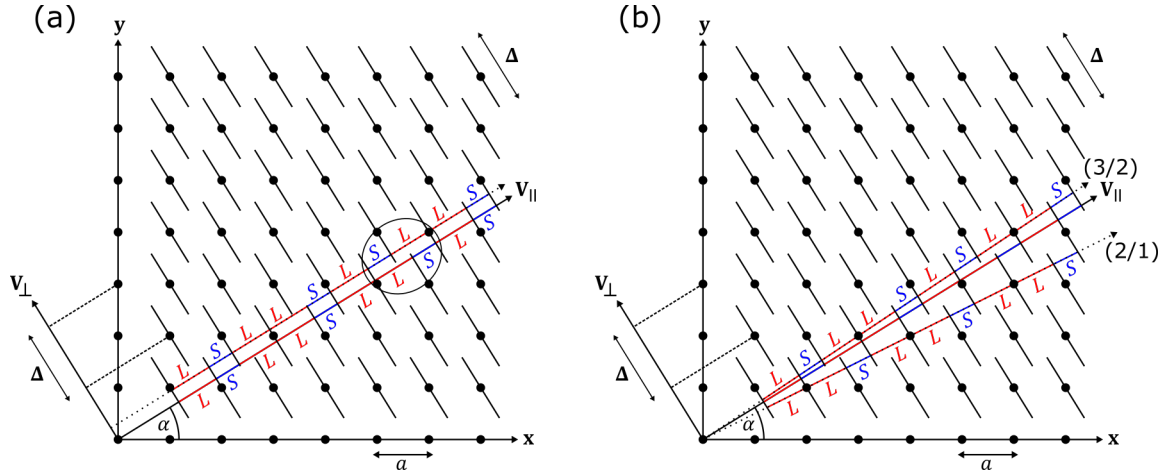


Figure 2.7: Demonstration of (a) a phason flip and (b) (2/1) and (3/2) approximant creation in the 1D Fibonacci chain. Both techniques involve a modification of the generation of a 1D Fibonacci chain from a 2D hypercubic lattice using the section method (Figure 2.6(a)). These modifications are discussed in the text.

periodic stacking of decagonal QC layers. High resolution TEM (HRTEM) investigations of a  $d$ -Al-Cu-Co QC revealed structural rearrangements of atomic clusters as a function of time. This constituted a local redistribution in the Penrose tiling used to map the overall arrangement of the clusters (see Figure 2.8(a-c)). Lifting the rearrangement sites (marked A and B in Figure 2.8) into perp-space, and comparing with an OD which creates an ideal model tiling with the same vertex density as that observed experimentally, shows points closely bordering the OD boundary (Figure 2.8(d)). These observations were thus interpreted as phason assisted jumps resulting from a fluctuating OD boundary. In fact, lifting all vertex positions of the observed tiling into perp-space showed a set of points extending far beyond the boundary of the ‘ideal’ OD, suggesting a large amount of phason disorder [44]. Similarly, annular dark-field scanning TEM (ADF-STEM) studies of a  $d$ -Al-Ni-Co QC showed anomalies in the DW factor at specific local sites in the QC. These sites were also found to reside at the edge of ODs in perp-space, again suggesting a relation to phason jumps caused by fluctuating ODs [45]. As part of the results and analysis in Chapter 5, potential evidence for another direct observation of phason assisted motion in the  $i$ -Ag-In-Yb QC will be presented, studied using STM.

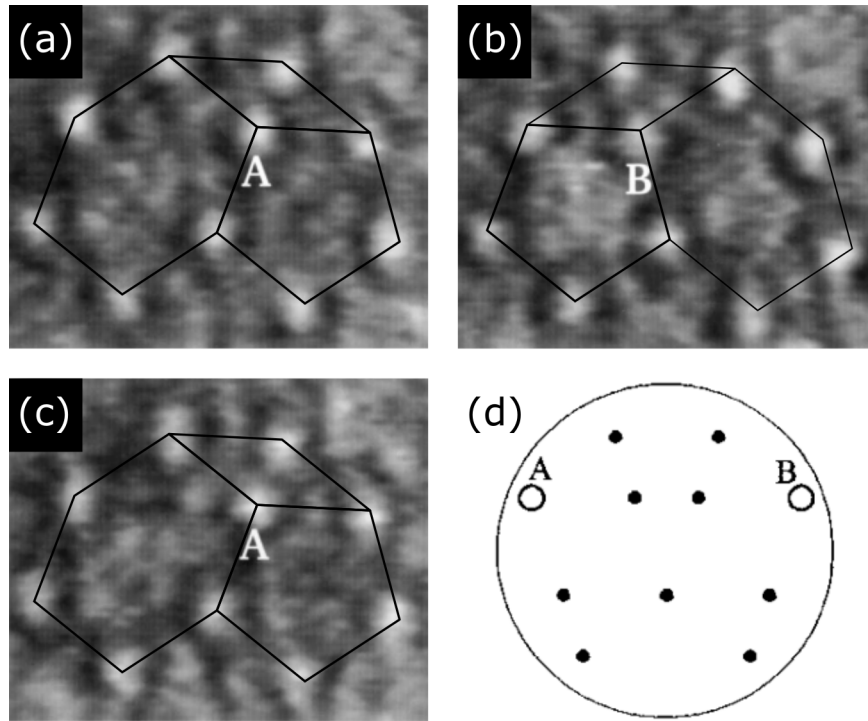


Figure 2.8: (a-c) HRTEM images ( $8 \text{ nm} \times 21 \text{ nm}$ ) from  $d\text{-Al-Cu-Co}$  at  $1123 \text{ K}$  showing structural rearrangements of atomic clusters and the corresponding redistribution of the Penrose tiles as a function of time (0, 8 and 115 s respectively). (d) The positions of the tile vertices marked A and B in (a-c) in perp-space alongside a circular window displaying the size of an OD which generates a Penrose tiling with the same vertex density as that observed experimentally. Reproduced and modified from [44].

## 2.5 Approximants

Another useful approach to understanding QC structures, again closely intertwined with the  $nD$  method introduced in Section 2.3, involves comparison with so-called approximant structures. In this section, a brief introduction to approximants will be given and then it will be seen how the  $nD$  formalism can be used to generate theoretical approximant structures, again using the 1D Fibonacci chain as a simple example.

Approximants are periodic crystalline phases closely related to an associated QC phase. They exhibit similar composition, physical properties and local atomic structures. Although they can display large unit cells, approximant structures can be readily solved using the well-established methods associated with periodic crystallography, subsequently

allowing for the modelling of related QC structures through a process of comparison and refinement [46]. These periodic structures can be produced theoretically using  $nD$  crystallography. Consider again, the generation of a Fibonacci chain from a 2D hypercubic lattice. If the slope of  $\mathbf{V}_{\parallel}$  is chosen to produce a rational value (i.e. by applying a linear phason strain), a periodic structure will result. This is shown in Figure 2.7(b), where angles such that  $\cot\alpha = 2/1$  and  $\cot\alpha = 3/2$  (labelled (2/1) and (3/2), respectively) have been chosen. These are ratios of successive numbers in the Fibonacci sequence (see Table 2.1). The resultant structures created using the section method exhibit repeating periodic sequences with unit cells  $LLS$  and  $LLSLS$ , respectively. The ratio of  $L$  to  $S$  segments in each case matches the corresponding rational ratio which defines the slope angle. If a rational ratio is chosen such that  $\cot\alpha \rightarrow \tau$  more closely (i.e.  $5/3$ ,  $8/5$  etc.), larger unit cells are created in which the structure more closely approximates the aperiodic Fibonacci chain. Approximants are defined in terms of these ratios, where in Figure 2.7(b),  $2/1$  and  $3/2$  rational approximants to the Fibonacci sequence have been generated [47].

This simple example highlights the intimate relationship between approximants and their related QC structures. They bridge the gap between simple periodic structures and long-range aperiodic order. It can be seen how modelling real approximant structures can be accomplished using the  $nD$  method, refining the geometry of the ODs which decorate the 6D hypercubic lattice in order to match experimental data. Approximant ODs can subsequently be used as a basis for the modelling of related QC phases. This procedure has been employed successfully in modelling structures in a range of intermetallic systems, where approximants fall under the more general category of CMAs [40]. CMAs are in fact a broad area of research in their own right, where those which are not directly related to any QC phase also exist. They still are, however, characterised by similar structural features making their study useful in for the general understanding of intermetallic QCs [4].

## 2.6 Cluster model

While the concepts introduced so far have allowed us to produce simple quasilattices using  $nD$  mathematics, explaining the precise positioning of atoms within a QC structure requires further information. The study of approximants and other CMAs has revealed the importance of using well-defined atomic clusters to understand QC structures. In this section, atomic clusters will be defined and their use in describing QC structures will be discussed.

The definition of a cluster can be somewhat arbitrary when regarding the description of atomic structure. On the one hand, clusters can be considered as structural motifs formed from purely geometrical considerations. In this sense, there is no physical or chemical stability associated with the cluster. Consider the face-centred cubic Al structure, for example. The structure around any Al atom can be defined using an infinite set of concentric cluster shells, the first five of which are shown in Figure 2.9(a). However, the clusters in this case have no physical implication and the more appropriate structure description is the cubic close packing model. On the other hand, clusters can be physically or chemically well-defined, existing in some form of stable state where bonding within the cluster is different from that outside [48]. Take buckminsterfullerene ( $C_{60}$ ), for example.  $C_{60}$  consists of sixty C atoms arranged at the vertices of a truncated icosahedral cluster. The result is a structure with 20 hexagonal and 12 pentagonal faces with a C atom at each vertex and bonds along each edge, as shown in Figure 2.9(b). The bonds shared between two hexagonal faces are double bonds, while those between hexagonal and pentagonal faces are single bonds. These bonds ensure energetically stable cluster units which crystallise in a face-centred cubic structure. In this sense,  $C_{60}$  may be considered well-defined in terms of the difference in the intra-cluster and inter-cluster bonding nature.  $C_{60}$  and its use as an adsorbate on QC surfaces will be discussed further in Section 3.4. An investigation of the adsorption of  $C_{60}$  on the 2f-Ag-In-Yb surface will also be presented Chapter 7.

In the case of QCs, cluster-based models are often used to describe the geometric arrangement of atoms in the structure, although their structural stability and relation to the properties of QCs is still debated. In this description, clusters are placed at the vertices of a quasilattice, where the cluster type and quasilattice type depend on the structure being modelled. Cluster overlapping and ‘glue’ atoms at interstitial sites are required for a description of the overall structure. The clusters used to model QC structures are typically derived from associated approximant structures [48].

The Cd-Yb system is a good example, containing a stable iQC and a series of related approximant crystals, all of which have undergone a detailed structural analysis using x-ray diffraction and  $nD$  analysis. Each can be described as a packing of rhombic triacontahedral (RTH) units, or Tsai-type clusters consisting of five concentric atomic shells [49–52]. For this system, the chemical ordering within the Tsai-type clusters is well-defined as a result of the difference in x-ray contrast between Cd and Yb. The outer RTH unit (5<sup>th</sup> shell) is decorated with 92 Cd atoms at the vertices and mid-edges. The atomic subshells from outer to inner consist of: a 30 Cd atom icosidodecahedron (4<sup>th</sup> shell), a 12 Yb atom icosahedron

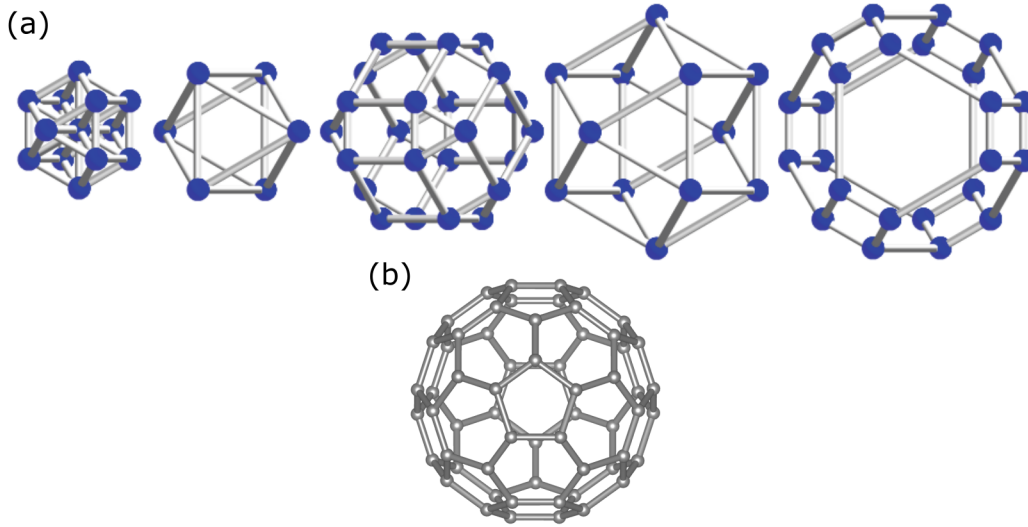


Figure 2.9: (a) The first five of a set of infinite coordination polyhedra that can describe the atomic structure around any Al atom in face-centre Al. Their radii have a ratio from left to right of  $1:\sqrt{2}:\sqrt{3}:\sqrt{4}:\sqrt{5}$ , with the smallest radius being 2.863 Å. Reproduced from [48]. (b) Model atomic structure of a C<sub>60</sub> molecule.

(3<sup>rd</sup> shell), a 20 Cd atom dodecahedron (2<sup>nd</sup> shell) and a 4 Cd atom tetrahedron (1<sup>st</sup> shell) which can exist in different orientations. The dynamic nature of this 1<sup>st</sup> shell means it is disordered and only displays partial occupancy. The cluster shells are shown in Figure 2.10 [52]. The overall cluster unit displays 2-fold, 3-fold and 5-fold rotational symmetry axes. The *i*-Ag-In-Yb QC used throughout this thesis is isostructural to the *i*-Cd-Yb QC. Their bulk structures will be discussed in more depth in Section 2.8.

Similar cluster-based structures have been used to describe other iQC systems, where families of isostructural iQCs can be explained using different cluster types: the Al-Mn-Si, Zn-Mg-Al and Cd-Yb classes exhibit Mackay, Bergman and Tsai-type clusters, respectively [52–54]. 2D clusters are also thought to play an important role in dQCs, where, for example, a single overlapping decagonal cluster unit can be used to explain the structure in the Ni-rich *d*-Al-Ni-Co phase [55]. It must be stressed again here, that whether these clusters are energetically stabilised units or purely geometric visualisations remains an open question. Indeed, STM data from a range of cleaved QC surfaces has indicated nanometer size protrusions, interpreted as evidence for enhanced stability of clusters in some cases. However, it is also true that the assignment of clusters is often arbitrary, where various

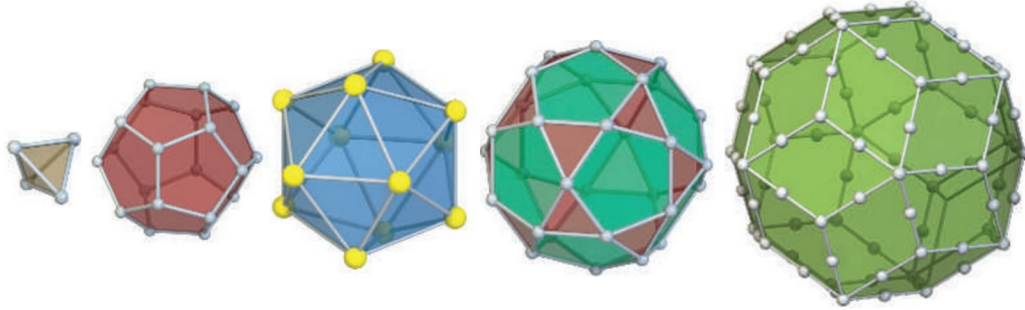


Figure 2.10: The concentric shells of the Tsai-type clusters. From left to right (1<sup>st</sup> shell to 5<sup>th</sup> shell): a disordered 4 Cd atom tetrahedron, a 20 Cd atom dodecahedron ( $r = 0.46$  nm), a 12 Yb atom icosahedron ( $r = 0.56$  nm), a 30 Cd atom icosidodecahedron ( $r = 0.65$  nm) and a 92 Cd atom RTH unit ( $r = 0.78$  nm), where the radii given are those for the Cd-Yb structure. Reproduced and modified from [52].

cluster models can be assigned to the same structure. Regardless of these points, the concept of clusters has played a key role in furthering understanding of QC structures. See [56] and references therein.

## 2.7 Stabilisation mechanisms

Although discovered nearly four decades ago, many questions still remain regarding the growth and stabilisation of QCs. Understanding how and why these structures form is vital to further knowledge and allow for the development any potential applications. In this section, the two principal theories introduced to explain the stabilisation of QCs (energetic and entropic stabilisation) will be discussed. Aspects of these theories have been touched upon already in the previous three sections. Some extra detail will be provided in what follows.

In the case of energetic stabilisation, perfect quasiperiodic order would be the ground state of the QC structure, thermodynamically stable at 0K. This theory predicts local growth rules, mirroring the matching rules used to generate mathematical aperiodic tilings (see Figure 2.3), thus enforcing a perfect quasiperiodic arrangement in the overall structure. In this case, the contribution of phasonic disorder would decrease as the temperature of the QC is reduced, eventually reaching a perfectly quasiperiodic ground state. Indeed, the high structural perfection of some QCs provides supporting evidence for this theory [57]. A good

example is in the Ni-rich *d*-Al-Ni-Co phase, where clusters have been observed to arrange in accordance with near perfect quasiperiodic order under certain conditions [55, 58].

The stability of many iQCs has been assigned to electronic contributions in a Hume-Rothery type mechanism. This involves the formation of a pseudogap at the Fermi energy for a specific electron per atom ratio ( $e/a$ ), thus providing a ground state in the system. In fact, many of the early iQCs were synthesised using the  $e/a$  ratio as a guiding principle (see [59] for a review). The existence of a pseudogap at the Fermi energy has also been observed experimentally in a range of systems (see [60] and references therein).

On the other hand, stabilisation through entropic contributions is also plausible. In this sense, QCs would be high-temperature phases. Considering again the aperiodic tiling picture, so-called ‘random tilings’ can be formed by disregarding matching rules and allowing for a random packing of tiles to fill all space, restricted only by the frequency of constituent tiles. This would imply configurational entropy plays an important role in stabilisation, where the existence of a range of degenerate states is possible. The contribution of phasonic disorder would increase as temperature decreases, eventually resulting in transformation to a low-temperature periodic phase. It is certainly true that the majority of QC phases are stable at high temperature, with related approximant phases existing at lower temperatures. This is, in fact, true for the Ni-rich *d*-Al-Ni-Co phase displaying ideal quasiperiodic order, where a reduction in temperature results in the formation of a QC phase displaying a random tiling structure, alongside some crystalline phases. The formation of the ideal quasiperiodic phase, in this description, could be explained by a compensative increase in chemical entropy resulting from chemical disorder in the system [55, 58].

In reality, the quest to understand the mechanisms behind the stabilisation of QCs continues. It is quite possible that both energetic and entropic factors could contribute towards their stability, with different weighting depending on the system under consideration. Further temperature dependence studies could help resolve this but experimental difficulties are encountered in low temperature investigations. The slow diffusion times associated with such studies can result in equilibration times which extend beyond a human lifetime [56, 57].

## 2.8 *i*-Ag-In-Yb

A broad range of QCs exist with different symmetries and in different systems. The most studied, however, are the intermetallic iQCs and dQCs. Both have been discussed

briefly in previous sections. iQCs exhibit aperiodic order in 3D, while dQCs consist of a periodic stacking of aperiodic 2D layers. A range of phases, both periodic and aperiodic, usually exist within each system. Understanding the structure in either case is of utmost importance to develop understanding of the mechanisms behind the formation and stability of QCs, with an end goal of tunable properties for the development of useful applications. In this section, as it is most relevant for this thesis, the bulk structure of the *i*-Ag-In-Yb QC will be outlined.

As discussed in Section 2.6, *i*-Ag-In-Yb is isostructural to *i*-Cd-Yb, whose structure is unambiguously known. Therefore, to understand the bulk structure of *i*-Ag-In-Yb, it is necessary to give a full description of that for *i*-Cd-Yb first. As mentioned in Section 2.6, the structure of *i*-Cd-Yb and its related approximant crystals can be described as a packing of RTH units (See Figure 2.10 for a description the RTH cluster). X-ray diffraction data for the periodic 1/1 and 2/1 cubic approximants (Yb-Cd<sub>6</sub> and Yb-Cd<sub>5,8</sub>, respectively) reveal a structure in which the RTH units share a face along the 2-fold axis and intersect along the 3-fold axis to form an obtuse rhombohedron. In the 2/1 approximant, an acute rhombohedron is also required to fill the gaps between clusters [49–51]. X-ray diffraction data and *n*D analysis, alongside comparison with the approximant structures, reveals that, in the *i*-Yb-Cd<sub>5,7</sub> QC structure, RTH clusters decorate a subset of vertices in a 3D PT *P*-type icosahedral quasilattice. Their arrangement is such that the linkages between RTH units match with those observed in the approximant structures. The selected vertices can be generated by modification (shrinking the edge-length and truncating the 5-fold vertices) of the triacontahedral OD used to generate the 3D PT (see Section 2.3). The remaining space in between clusters is filled with different combinations of acute and obtuse rhombohedra [52]. The resulting structure displays sets of high-symmetry 2-fold, 3-fold and 5-fold axes.

Similar to the Cd-Yb system, 1/1 and 2/1 approximants also exist in the Ag-In-Yb system, with chemical composition close to the QC structure. Cd is replaced by equal amounts of Ag and In, maintaining a constant  $e/a$  ratio and abiding by Hume-Rothery stabilisation rules. This results in chemical disorder of Ag and In atoms at the well-defined Cd sites, although studies have revealed occupation probabilities for each shell in the Tsai-type clusters in the 1/1 approximant. The 1<sup>st</sup> shell is made up of In, the 2<sup>nd</sup> shell consists of 60% Ag and 40% In, the 4<sup>th</sup> shell contains 20% Ag and 80% In and the 5<sup>th</sup> shell is formed from 78% Ag and 22% In [61, 62]. The distribution will be similar in the *i*-Ag-In-Yb structure. Given this chemical disorder, the Ag and In sites isostructural to the

Cd sites in the *i*-Cd-Yb model will be referred to collectively as Ag/In sites during the remainder of this thesis, unless discussing aspects of the chemical disorder directly.

## Chapter 3

# Surface studies of quasicrystals: clean surfaces and adsorption

Surface investigations are vital for understanding any material. QC surface related phenomena such as catalytic activity, corrosion resistance and high-hardness have already given rise to some potential applications [63–65]. Understanding the clean surfaces of QCs is a key step in extending our knowledge of these phenomena to further these applications. Characterisation of clean surfaces is also paramount to a range of other important technological processes - one being thin film growth. Chapter 5 concerns two such studies of the clean surfaces of QCs. As such, the start of this chapter will give a brief overview of some important surface phenomena before discussing the clean high-symmetry surfaces of the *i*-Ag-In-Yb QC, in particular the 5-fold surface, as it is most relevant for this thesis.

The deposition and adsorption of a material on a substrate surface can provide information on surface structure, chemistry and reactivity. What's more, it can enhance surface properties for a range of applications (e.g. semiconductors, photovoltaics and optical coatings). The surfaces of QCs provide an interesting landscape for adsorption and thin film growth. Such investigations offer the possibility to reveal insights into QC growth and the affects of aperiodic order. Elemental and molecular adsorption studies make up the basis for the results presented in Chapters 6 and 7. Therefore, the second part of this chapter contains a brief review of adsorption studies on QC surfaces. Some basic concepts regarding adsorption processes will first be introduced. After this, an overview of some of the most relevant QC thin film investigations will be given in terms of adsorption mechanisms and resultant structures. For related experimental techniques, the reader is referred to Chapter

4. Oura et al. [1] will be used as the main reference in this chapter when discussing the basics behind surface energetics and adsorption.

### 3.1 Surface energetics

The creation of a surface results in the breaking of interatomic bonds, where the coordination of resultant surface atoms is less than that in the bulk. This leads to surface free energy which must be minimised in order to stabilise the surface. Insights into surface energetics and other surface processes can be drawn from the terrace-step-kink (TSK) model [66,67]. In this model, each atom may be considered as a cube in a simple cubic structure, as in the schematic in Figure 3.1. Atoms sharing faces are bonded with a single bond. The energy of a surface atom can be determined by the number of bonds it has with neighbouring atoms. Consequently, the energy required for an atomic transition is found by considering the number of bonds broken and formed in the atom's initial and final states, respectively. In general, maximising the number of bonds formed will minimise energy. This is a simplified model, correctly predicting the existence of various surface atomic sites and defects which have been observed experimentally. These are shown in Figure 3.1 and described below:

- Adatom: an atom sitting on top of a terrace with a single bond to a terrace atom.
- Step atom: an atom forming part of a step edge between two terraces. It is bonded to three atoms within the terrace it is part of and one atom in the terrace below.
- Step vacancy: a 'missing' atom along a step edge.
- Kink atom: similar a step atom but with bonds to only two adjacent atoms within the terrace it is part of and one atom in the terrace below.
- Step adatom: a lone atom sitting on a step edge (i.e. with a single bond to an atom within the terrace it is part of and a bond to an atom in the terrace below).
- Terrace atom: an atom embedded within a terrace sharing bonds with the five surrounding terrace atoms. Only the surface face is unbound.
- Terrace vacancy: a 'missing' atom within a terrace.

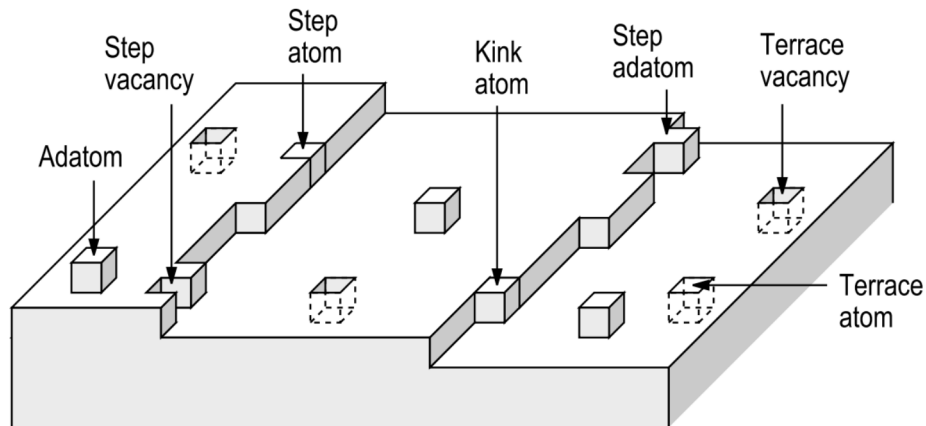


Figure 3.1: A schematic of a step-terrace surface structure in the TSK model. Surface atomic sites and defects are labelled. These are discussed further in the text. Reproduced from [1].

Surface adatoms play a key role in diffusion at the surface of a material, mediating phase formation, cluster nucleation and epitaxial growth. Surface diffusion generally involves adparticles moving across the surface in a random walk type motion, from one low energy adsorption site to the next. Adparticles, in this sense, could be adatoms from the substrate surface in a self-diffusion process, or some foreign element or molecule in so-called heterodiffusion. It can be seen from Figure 3.1 that an adatom could increase its coordination, and thus minimise its energy, by diffusing to a step site. However, its motion can be influenced by interactions with other adparticles, surface atoms and defects in the surface, resulting in a range of different diffusion mechanisms. Orientational and directional anisotropies in the substrate can also play an important role. This is particularly interesting in the case of QCs, where their aperiodic nature results in an unusual potential energy landscape geometrically. These concepts are particularly relevant for Chapter 5 and 6, where investigations involving diffusion on the clean surfaces of QCs and within overlayer structures on these surfaces will be discussed.

### 3.2 High-symmetry surfaces of *i*-Ag-In-Yb

The Ag-In-Yb system is stable under UHV conditions, unlike the Cd-Yb system which suffers due to the high vapour pressure of Cd. It is, therefore, suitable for a range of

surface investigations [68, 69]. Clean high-symmetry surfaces (2-fold, 3-fold and 5-fold) of *i*-Ag-In-Yb have been achieved under UHV using optimised sputter-annealing preparation conditions (the reader is referred to Section 4.2 for further discussion on surface preparation). Under these conditions, LEED and STM reveal long-range quasicrystalline order and x-ray photoelectron spectroscopy (XPS) shows bulk chemical composition is retained. In all high-symmetry surfaces, LEED patterns display discrete diffraction maxima arranged at  $\tau$ -scaled distances with the expected rotational symmetry (Figure 3.2(d-f)). Large-scale STM images indicate a step-terrace morphology with large terraces and specific step heights (Figure 3.2(a-c)) [70–74]. Comparable results are observed by STM on all three surfaces, so the rest of the discussion here will focus on the 5f-Ag-In-Yb surface in particular. Results relating to the 2f-Ag-In-Yb surface will be detailed in more depth in Chapter 5. For further discussion on the 3f-Ag-In-Yb surface, the reader is referred to [73].

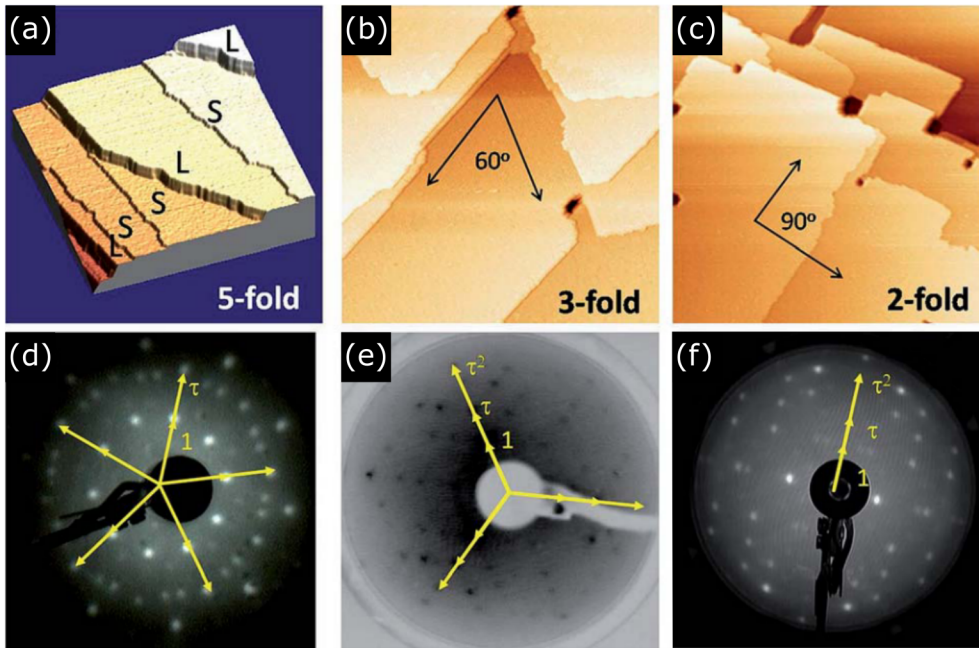


Figure 3.2: (a-c) STM images of the step-terrace morphology ( $250 \text{ nm} \times 250 \text{ nm}$ ,  $300 \text{ nm} \times 300 \text{ nm}$  and  $400 \text{ nm} \times 400 \text{ nm}$ , respectively) and (d-f) corresponding LEED patterns from the 5-fold [71], 3-fold [73] and 2-fold [74] surfaces of *i*-Ag-In-Yb, respectively. Reproduced from [62].

The step-terrace distribution on the 5-fold surface indicates three specific step height

values, the most common being the  $S = 0.28 \pm 0.04$  nm and  $L = 0.85 \pm 0.05$  nm step heights, alongside the less observed  $M = 0.58 \pm 0.03$  nm step height ( $L \sim M + S$ ) which is thought to be less preferred. The sequence of steps (i.e.  $LSLSS$  in Figure 3.2(a)) matches well with planes perpendicular to the 5-fold axis in the *i*-Ag-In-Yb model structure containing a high density of CC sites. The structure of one such bulk plane is shown in Figure 3.3(a), where a Tsai-type cluster, truncated through its centre perpendicular to its 5-fold axis, is shown inset. This is further confirmed by comparison of high-resolution bias-dependent STM data with these model planes. At negative sample bias-voltage (measuring occupied sample states), large protrusions are observed (see Figures 3.3(b,d)), corresponding to 4<sup>th</sup> shell Ag/In sites surrounding CCs in the model. At positive sample bias voltage (measuring unoccupied sample states), these are replaced by ring features (Figure 3.3(e)), corresponding to 3<sup>rd</sup> shell Yb sites in the model. In both cases, these features arrange pentagonally, where a Penrose P1 tiling can be overlaid with vertices residing at the centre of the large protrusions/rings in the STM data and at CC sites in the model structure. These findings are backed up by theoretical calculations, which show that unoccupied states are dominated by Yb-5*d* levels in the 1/1 approximants to the *i*-Cd-Yb and the *i*-Ag-In-Yb QCs [71, 75, 76]. This will be discussed further in Chapter 5.

### 3.3 Adsorption energetics

Adsorption investigations involve the deposition of adparticles on a surface, with the deposited species termed the adsorbate. Here, adsorption will depend on a range of external factors. The flux of impinging adsorbate species is an obvious one. However, it must also be considered that not all impinging particles adsorb at the surface. The number of particles that do adsorb can be defined by the sticking coefficient of the substrate. This varies depending on coverage, temperature and steric contributions from the substrate. The affinity between substrate and adsorbate must also be considered. For instance, in a homoepitaxial process (i.e. one in which substrate and adsorbate species are the same) growth tends to proceed via replication of the bulk structure. However, in a heteroepitaxial process (i.e. when substrate and adsorbate species are different) growth will depend heavily on the commensurability between substrate and adsorbate structures. This will be determined by the strength of the substrate-adsorbate interaction and the lattice mismatch between the two species. In general, adsorption processes can be categorised into two types depending on the substrate-adsorbate interaction. The first is a weak van der

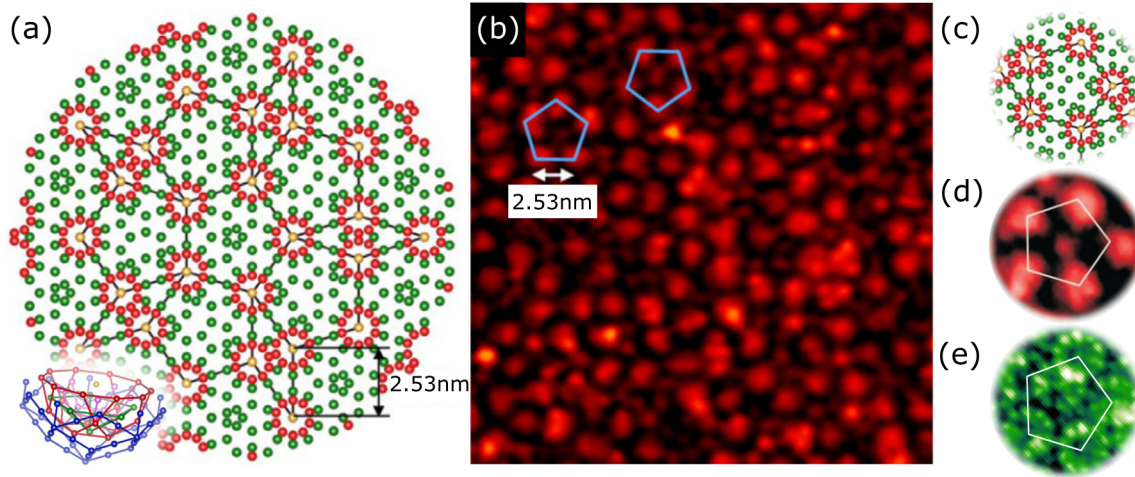


Figure 3.3: (a) 5-fold plane from the *i*-Ag-In-Yb model, where green circles correspond to 3<sup>rd</sup> shell Yb sites, red circles to 4<sup>th</sup> shell Ag/In sites and gold circles to CC positions. Inset is a Tsai-type cluster truncated through its centre perpendicular to its 5-fold axis. (b) STM image of the 5f-Ag-In-Yb surface taken at negative sample bias voltage (30 nm  $\times$  30 nm). (c-e) Comparison of pentagonal features in the model, at negative sample bias voltage and at positive sample bias voltage, respectively. 4<sup>th</sup> shell Ag/In sites are resolved in (d), whilst 3<sup>rd</sup> shell Yb sites are resolved in (e). (a,c) Reproduced and modified from [77], (b) from [78], (d) from [71] and (e) from [72].

Waals interaction, known as physisorption. The second involves the formation of stronger covalent or ionic bonds with substrate atoms, termed chemisorption.

When the coverage of adsorbate species begins to exceed a monolayer (ML), i.e. a single layer of adsorbate, the so-called thin film growth regime begins. There are three thin film growth modes, where each depends on the interplay between substrate-adsorbate and adsorbate-adsorbate interactions in the film. These modes are displayed schematically in Figure 3.4 and described here:

- Layer-by-layer (or Frank-van der Merve) growth is a 2D growth mode, where each layer of adsorbate grows in a successive fashion. In this case, the substrate-adsorbate interaction is stronger than the adsorbate-adsorbate interaction [79, 80].
- Layer plus island (or Stranski-Krastanov) growth proceeds by the growth of a 2D layer, with the subsequent formation of 3D islands. The initial layer can be sub-ML or several MLs thick. Here, substrate-adsorbate interaction is favoured initially,

making way for adsorbate-adsorbate interaction at increased coverages. This is due to an increase in dislocation and strain energy [81].

- Island (or Volmer-Weber) growth involves the nucleation of 3D islands directly on the substrate surface. This occurs when the adsorbate-adsorbate interaction outweighs the substrate-adsorbate interaction [82].

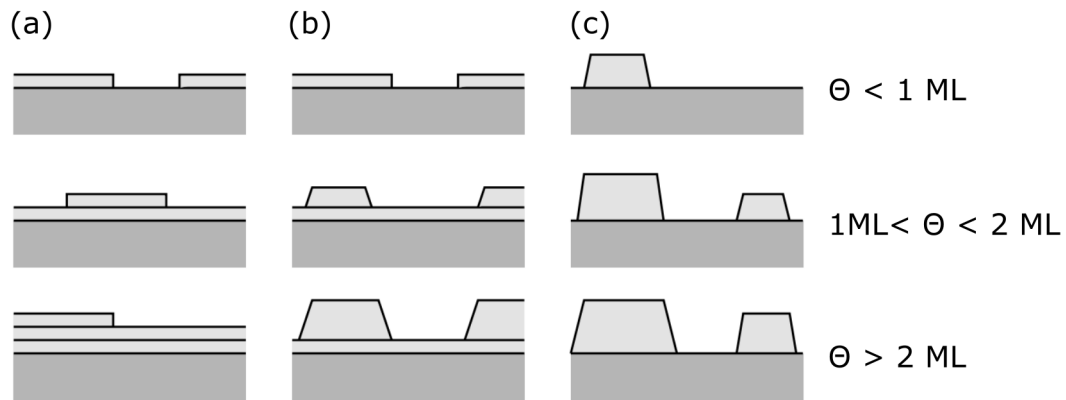


Figure 3.4: The three thin film growth modes, with coverage (displayed to the right) increasing in the downwards direction. (a) Layer-by-layer (Frank-van der Merve), (b) layer plus island (Stranski-Krastanov) and (c) island (Volmer-Weber) growth. Reproduced and modified from [1].

### 3.4 Quasicrystalline epitaxy

As mentioned, QC surfaces provide an especially complex potential energy landscape for adsorption. Local isomorphism ensures a set of similar local environments, while inherent aperiodicity means no sites are completely equivalent. In terms of epitaxial growth, the incommensurability between a QC substrate and an overlayer species which naturally crystallises periodically also requires consideration. A range of systems have been shown to exhibit epitaxial quasiperiodic growth, with varying degrees of substrate-overlayer pseudomorphism. Such investigations have provided insights into the structure and reactivity of many QC substrates. Epitaxial quasicrystalline thin films also present an ideal playground for the investigation of aperiodic order. Single element layers reduce chemical complexity,

allowing for the intrinsic properties of aperiodicity to be studied directly. The interplay between aperiodicity and various physicochemical properties can be investigated in molecular films. Other interesting avenues of exploration include homoepitaxy, which could provide insights into QC growth and structure. In fact, this idea will be investigated somewhat in Chapter 6, where Ag deposition on a 5f-Ag-In-Yb substrate will be discussed.

In the following, the results from a range of QC epitaxy investigations will be presented. This will include selected examples from different substrate-adsorbate systems exhibiting a range of different epitaxial modes and overlayer structures. For a more in-depth review of growth on QC surfaces, the reader is referred to [17, 32, 83], for example. Some of the QC substrates discussed in this section have not been introduced, thus far. Relevant aspects of their structures will be given for a full description of the associated overlayer.

### 3.4.1 Rotational epitaxy

In this epitaxial mode, the substrate has limited impact on the adsorbate structure. Adsorbate layers crystallise with preferential alignment along the high-symmetry directions of the substrate surface. The particular adsorbate allotrope and its orientational relationship with the substrate depends on the lowest energy interfacial configuration.

This mode was first exemplified by Shimoda *et al.* in the growth of Au and Pt on the 10f-Al-Ni-Co and 5f-Al-Pd-Mn surfaces [84–87]. It has also been illustrated effectively in the growth of Ag on the high-symmetry surfaces of *i*-Al-Pd-Mn and related complex substrates [88]. The Ag/*i*-Al-Pd-Mn system will be discussed here as it is most relevant. At coverages above  $\sim 10$  ML, 3D Ag nanocrystals form exhibiting atomically flat, hexagonal top faces. High-resolution STM data from the island tops reveals a hexagonal lattice corresponding to the natural Ag(111) structure (see inset in Figure 3.5(a)). The nanocrystals grow in specific orientations enforced by the substrate structure. On the 5f-Al-Pd-Mn surface, for example, five different domains are apparent, each rotated by  $36^\circ$ . This is consistent with a 5-fold symmetric arrangement and is confirmed by LEED patterns from the Ag film (Figure 3.5(b)), which display a ring of 30 spots each rotated by  $12^\circ$ . These spots correspond to five distinct hexagonal patterns resulting from 5-fold twinning of the five domains of Ag nanocrystals. Indeed, angles between the edges of pairs of hexagonal islands observed by STM are  $12^\circ$  or some multiple, as can be seen in Figure 3.5(a). These results were interpreted in relation to the coincidence of densely packed atomic rows between substrate and adsorbate in this arrangement. The 5f-Al-Pd-Mn surface contains high

atomic density along its five 2-fold axes, which are rotated by  $36^\circ$  with respect to each other. Similar nanocrystalline Ag islands were observed to form on the 2f-Al-Pd-Mn surface and the pseudo 10-fold (p-10f) surface of the  $\zeta'$ -Al-Pd-Mn approximant phase [88, 89]. Other systems exhibiting the 5-fold twinning of nanocrystals include: Al, Fe, Ni, Co and Bi on 5f-Al-Pd-Mn; Al, Ag, Bi and Xe on 10f-Al-Ni-Co; and Sn on 5f-Al-Cu-Fe [17, 32].

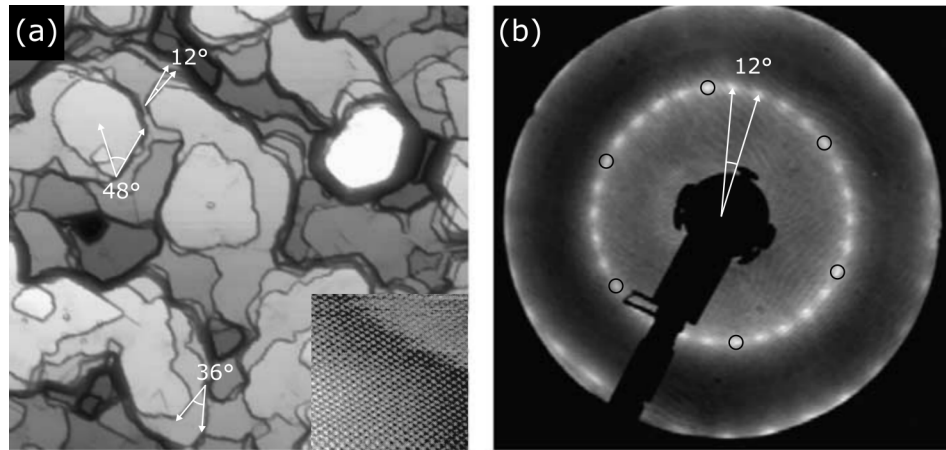


Figure 3.5: (a) STM image ( $150 \text{ nm} \times 150 \text{ nm}$ ) and (b) LEED pattern ( $150 \text{ eV}$ ) from  $\sim 10 \text{ ML}$  of Ag deposited on the 5f-Al-Pd-Mn surface. Angles between island edges and diffraction maxima of  $12^\circ$  or some multiple have been highlighted in (a) and (b), respectively. Inset in (a) is an atomically resolved STM image ( $9.4 \text{ nm} \times 9.4 \text{ nm}$ ) from on top of an Ag island at  $\sim 100 \text{ ML}$  coverage. It indicates hexagonal symmetry. This is due to the formation Ag(111) nanocrystals, rotationally aligned with respect to the substrate. The spots corresponding to one specific hexagonal domain are highlighted by black circles in (b). Reproduced and modified from [89] and [88].

### 3.4.2 Aperiodically modulated multilayer structures

An epitaxial mode in which the substrate imparts slightly more influence on the overlayer is in aperiodically modulated multilayer structures. This is essentially a modification of the rotational epitaxy mode. Adsorbate films again show a crystalline structure aligned along the high-symmetry directions of the substrate. Perpendicular to these directions, however, atomic rows can be seen to arrange in an aperiodic manner. This geometry allows for an enhanced coincidence between the high atomic density features of the substrate and adsorbate.

This mode is uniquely evidenced in the case of Cu deposition on the 5f-Al-Pd-Mn surface [90,91]. Upon initial adsorption, no obvious discernible order is apparent. However, at coverages from  $\sim 5 - 25$  ML, five domains of row structure are observed by STM with alignment along the high-symmetry axes of the substrate surface (see Figure 3.6(a)). The row spacings follow a Fibonacci sequence with  $S = 0.45 \pm 0.02$  nm and  $L = 0.73 \pm 0.03$  nm ( $L/S \sim \tau$ ). This is consistent with spacings between features on the substrate surface. Phason defects are apparent in the Fibonacci arranged rows, assigned to either corresponding defects in the substrate or strain relief in the film. Although atomic resolution within rows was not observed by STM, LEED patterns indicate a periodic structure. This can be seen in Figure 3.6(b), where sets of periodically spaced high-intensity streaks are evident, aligned along the five high-symmetry substrate directions. The periodic spacing between one set of streaks is marked in white. The maxima within streaks, however, are arranged aperiodically perpendicular to the periodic streak direction, as highlighted by a section of the Fibonacci sequence in Figure 3.6(b). This observation confirms the periodic nature along atomic rows. In fact, the periodicity extracted from the LEED pattern matches well with the nearest-neighbour distance in bulk Cu [92]. The suggested structural model comprises of a vicinal surface formed via a  $13.28^\circ$  miscut from the (100) direction in a body-centred tetragonal Cu structure. In this interpretation, a step-terrace structure is formed with separations mirroring the Fibonacci sequence observed in the film (see Figure 3.6(c)). This explains the protruding rows observed by STM as step edges in the vicinal surface plane. This model also explains the delayed development of the film, where multiple layers are required before the step-terrace structure becomes apparent [91].

### 3.4.3 Pseudomorphic growth

Perhaps the maximum degree to which a QC substrate can regulate the overlayer structure is in pseudomorphic growth. In this mode, elements or molecules adsorb at a set or subset of quasilattice sites defined by the substrate. This results in a QC overlayer which is templated by aspects of the underlying substrate structure. Such a growth mode depends heavily on the interplay between substrate and adsorbate and the experimental conditions used. It is the most studied mode in QC epitaxy and, indeed, was the aim of many of the initial adsorption investigations. Some examples of pseudomorphic elemental and molecular overlayers will be presented here.

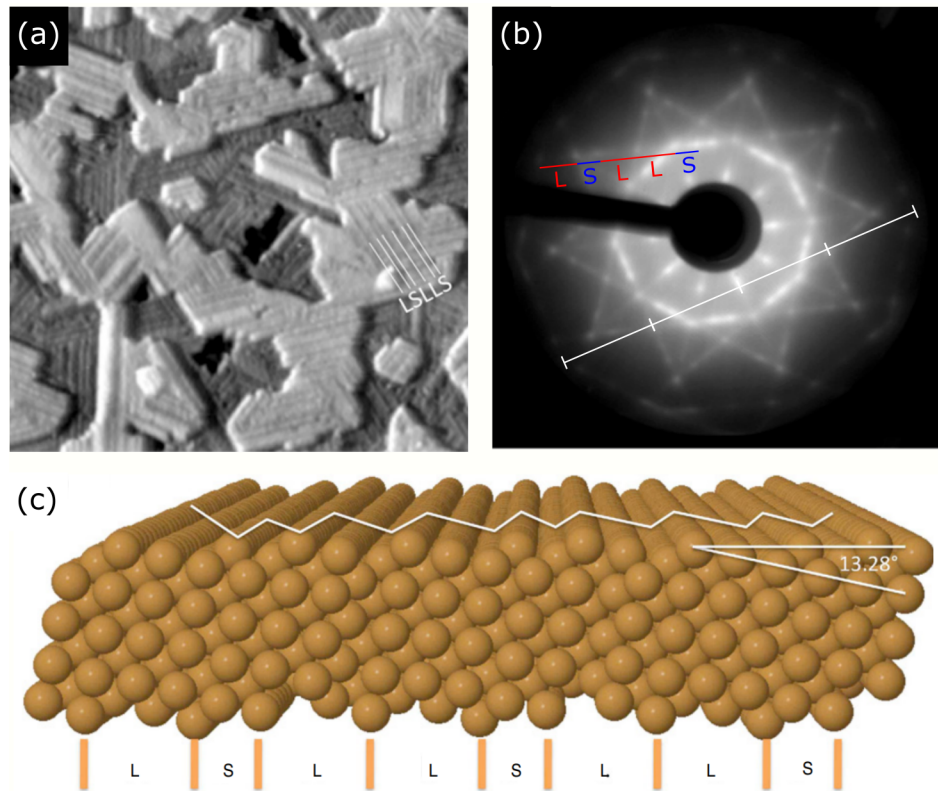


Figure 3.6: (a) STM image ( $70 \text{ nm} \times 70 \text{ nm}$ ) from  $\sim 5 \text{ ML}$  of Cu deposited on the 5f-Al-Pd-Mn surface. Five domains of row structure are evident with orientation along the high-symmetry directions of the substrate. Separations between rows follow a Fibonacci sequence, with one marked in white. (b) LEED pattern ( $177 \text{ eV}$ ) from the Cu film at a substrate temperature of  $85 \text{ K}$ . Periodic separations between high-intensity streaks are marked in white. Aperiodically spaced maxima within streaks are highlighted in red and blue. (c) Structural model comprising of a vicinal surface formed via a  $13.28^\circ$  miscut from the (100) direction in a body-centred tetragonal structure. The step-terrace structure is indicated at the top and  $L$  and  $S$  separations are marked at the bottom. Reproduced and modified from [91].

### Elemental growth

Al adsorbate overlayers are observed to display some degree of pseudomorphic growth on the 5f-Al-Cu-Fe surface after deposition at room temperature. In the low coverage regime, nano-islands composed of six pentagonally arranged Al atoms (with one atom at the centre

of the pentagon) are observed by STM in a ‘starfish’ arrangement (see Figure 3.7(a)). The geometry of these features in comparison to the underlying substrate indicates nucleation at the so-called ‘dark star’ (DS) sites of the substrate surface [93]. These sites consist of a pentagonal arrangement of substrate atoms with a central hollow (see Figure 3.7(b)) [94]. They are related to truncations of the pseudo-Mackay/Bergman clusters which form the bulk structure. Growth proceeds via the trapping of an Al atom in the central vacancy. Subsequently, five further Al atoms nucleate at the bridge sites forming a starfish structure. This growth process is displayed schematically in Figure 3.7(b). It is backed up by the measured central depression at starfish sites in experimental data. Another interesting feature of this adsorbate layer is the location of the five peripheral adatoms, which reside close to bulk atomic sites in the substrate above the truncated surface plane. Further deposition of Al results in a disordered overlayer structure [93].

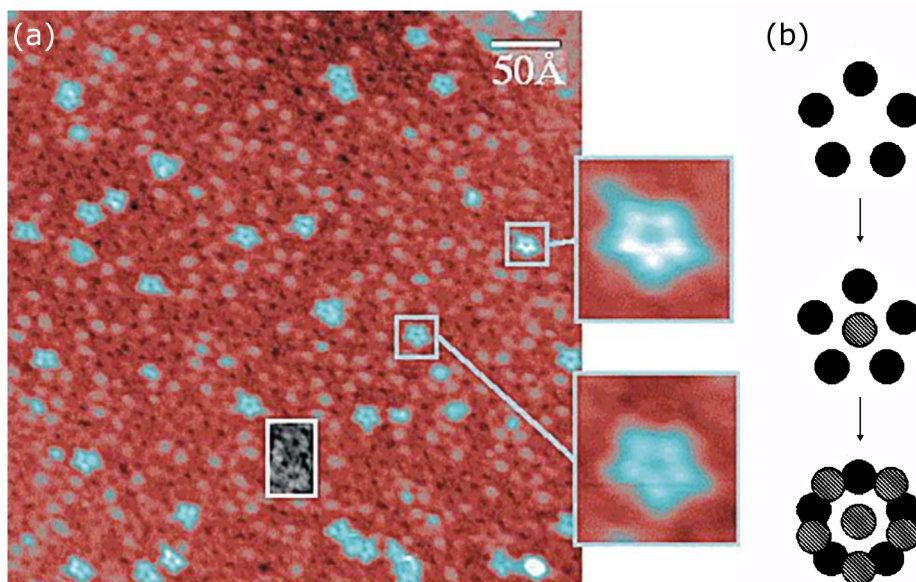


Figure 3.7: (a) STM image ( $45 \text{ nm} \times 45 \text{ nm}$ ) from  $\sim 0.04 \text{ ML}$  of Al deposited on the 5f-Al-Cu-Fe surface. Red contrast corresponds to substrate and blue is deposited Al. Two enlarged ‘starfish’ features are shown to the right. (b) Model of the growth mechanism of Al starfish features. Solid circles represent substrate atoms and hatched circles correspond to deposited Al. Reproduced and modified from [93].

Examples of pseudomorphic growth at ML coverage were first reported for Bi and Sb deposition on the 5f-Al-Pd-Mn and 10f-Al-Ni-Co surfaces. In these systems, adsorbates

were deposited with the substrates held at elevated temperatures, ensuring multilayer desorption and only a single adatom layer. LEED and helium atom scattering (HAS) were used to probe the adsorbate layers, revealing the same symmetries and peak positions when compared to the corresponding clean substrate surfaces [95]. The Bi/5f-Al-Pd-Mn system was further investigated by STM at room temperature. At sub-ML coverages, pentagonally arranged Bi clusters were observed. These were centred on the ‘up’ oriented pentagonal tiles of the Penrose P1 tiling which maps the substrate structure [96]. Similar features were observed in the Pb/5f-Al-Pd-Mn system, where the arrangement of adsorbate atoms was described by a  $\tau$ -inflated Penrose P1 tiling in comparison to that used to model substrate features [97].

Deposition of Pb on the 5f-Ag-In-Yb surface demonstrates pseudomorphic growth of a more complex nature when compared to the sub-ML and ML examples discussed so far [78]. In this system, the adsorbate structure maintains its quasicrystalline nature across multiple layers. The positions of Pb atoms within each layer can be described in terms of vacant atomic planes ‘above’ the surface in the model structure (i.e. atomic sites within RTH clusters above the central surface truncation). See Section 2.8 and 3.2 for an overview of the *i*-Ag-In-Yb structure and its 5-fold surface, respectively. This was confirmed with STM, XPS, LEED and DFT investigations, which indicated the growth of quasicrystalline Pb layers at different heights with different in-plane structures and adsorption energies. A comparison between STM data from each layer and the structure of atomic planes at corresponding heights in the model is shown in Figure 3.8. The Pb-Pb interlayer distances (close to that in bulk Pb) are thought to be an important factor in the stabilisation of this film, where this is maintained via the formation of a Pb underlayer which is not observed by STM. This was the first example of templated 3D QC growth and presents a system in which chemical complexity is reduced, but aperiodicity is maintained [78]. Similar results have been reported for the growth of Bi on 5f-Ag-In-Yb [77] and for Pb on 3f-Ag-In-Yb [98].

### Molecular growth

Templating the growth of molecules in a similar pseudomorphic fashion can produce an array of interesting systems. Molecular overlayers open up the opportunity to study the influence of aperiodicity on systems with a variety of properties. For instance, a templated quasiperiodic overlayer of magnetic molecules would provide an ideal system for the study of frustrated quasicrystalline magnetic systems. Initial attempts at forming pseudomor-

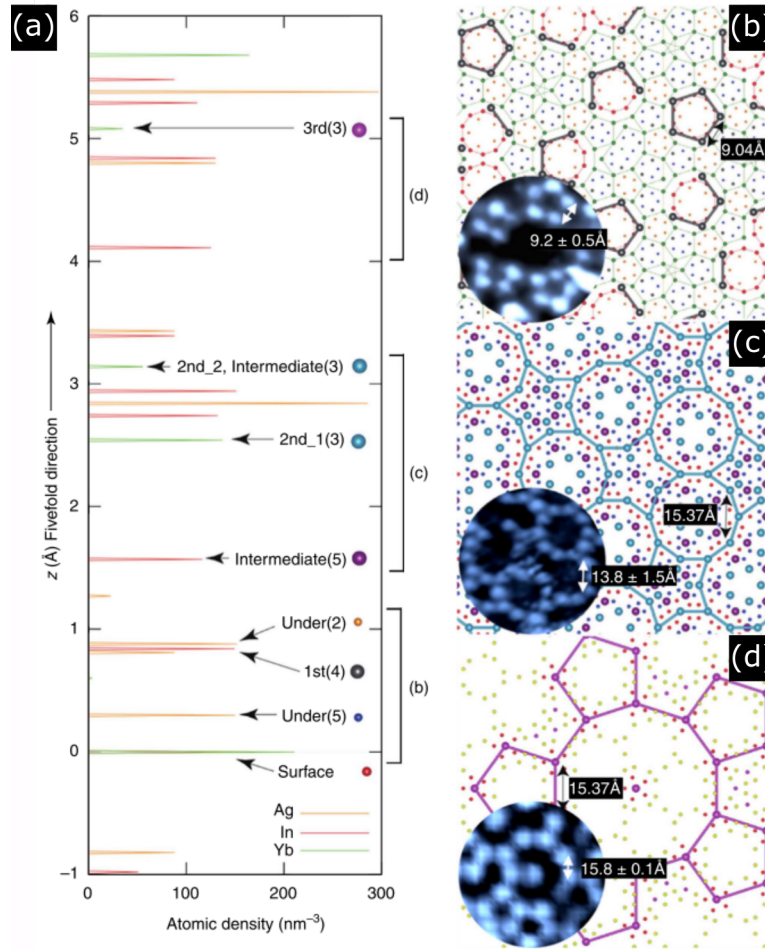


Figure 3.8: (a) Atomic density distribution along the 5-fold direction in the *i*-Ag-In-Yb model. The surface plane and planes which describe Pb layers in the overlayer structure are marked. The corresponding shell in the RTH cluster is given in parentheses. (b-d) Corresponding in-plane atomic structure for the first, second and intermediate, and third layer respectively. STM images of each layer are shown inset. (b) Surface In and Yb sites represented by red and green circles, respectively. In sites corresponding to first layer Pb adsorption positions are shown in grey. (c) Blue and magenta circles correspond to Yb and In sites and second an intermediate Pb adsorption positions, respectively. (d) Purple circles represent Yb sites corresponding to third layer Pb adsorption positions. Reproduced and modified from [78].

phic molecular overlayers were unsuccessful; the adsorption of benzene and ethylene on the 5f-Al-Pd-Mn and 10f-Al-Ni-Co surfaces, respectively, indicated no evidence for ordered adsorption [83]. However, it was found that, much like for templated elemental overlayers, with the selection of the right substrate-adsorbate system and growth conditions, pseudomorphic molecular overlayers could be formed.

Deposition of  $C_{60}$  on the 5f-Al-Pd-Mn surface at room temperature provided the first molecular overlayer exhibiting some degree of pseudomorphicity [99].  $C_{60}$  was chosen as it tends to stay intact upon adsorption and its cage diameter provides a good match to the DS sites on the substrate surface. More generally, symmetry matching between  $C_{60}$  (which contains 2-fold, 3-fold and 5-fold axes) and iQCs is apparent - a property which can enhance preferential adsorption [100]. Indeed, at very low coverages,  $\tau$ -scaling between adsorbed  $C_{60}$  was observed by STM, with the proposed adsorption sites being DS hollows, as in the case of Al adsorption on the same surface [93]. As coverage was increased, the onset of a disordered layer quickly became apparent. This was attributed to a strong substrate-adsorbate interaction, where the film would crystallise in its natural hexagonal close-packed structure if  $C_{60}$ - $C_{60}$  interactions were to dominate [99].

Ordered overlayers of  $C_{60}$  at increased coverages have been achieved via deposition on a heated QC substrate, thus allowing for the diffusion of molecules on the substrate surface. The first example was in the  $C_{60}/5f\text{-Al-Cu-Fe}$  system [101] (with similar results reported in the  $C_{60}/10f\text{-Al-Ni-Co}$ ,  $/10f\text{-Al-Cu-Co}$  and  $/5f\text{-Al-Pd-Mn}$  systems soon after [100]). STM of the structure indicates an array of bright (B) and dark (D) contrast molecules, all of which occupy quasiperiodically arranged sites (see Figure 3.9(a)). This is confirmed by the autocorrelation of extracted molecular positions, which displays 10-fold symmetry (see Figure 3.9(b)). B molecules reside at the vertices of a pentagonal tiling whose edge-length is consistent with adsorption at surface Fe sites. D molecules are described by a  $\tau$ -scaled larger tiling, where locations are consistent with subsurface Fe atoms. This observation of a quasicrystalline adsorption network defined by the least abundant element in the substrate (Fe, in this case) is consistent with a range of other QC adlayer systems. Take, for example, some of the systems that have been discussed already. In the  $C_{60}/5f\text{-Al-Pd-Mn}$  system, the DS adsorption sites reside on top of Mn atoms in the subsurface layer. In the Bi/, Sb/ and Pb/ $5f\text{-Al-Pd-Mn}$  systems, an adsorption network dependent on surface Mn atoms was also apparent. Mn is the minority constituent in  $i\text{-Al-Pd-Mn}$  [101]. Similar observations have been made more recently in the  $C_{60}/2f\text{-Al-Pd-Mn}$  system [19]. This system will be discussed further at the start of Chapter 7. In each of these cases, the

adsorption mechanism and bond formation is still driven by the chemical affinity between the adsorbate and substrate atomic species. However, the density of the least abundant element at the substrate surface seems to influence whether film grows quasiperiodically or not.

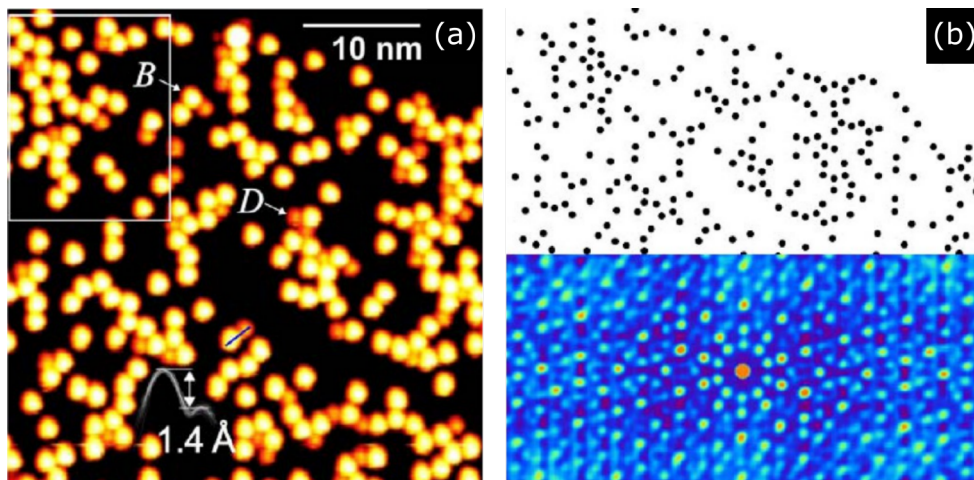


Figure 3.9: (a) STM image ( $50 \text{ nm} \times 50 \text{ nm}$ ) from a quasicrystalline  $\text{C}_{60}$  layer on the 5f-Al-Cu-Fe surface. Bright (B) and dark (D) contrast molecules are indicated. The apparent height difference between a pair of B and D molecules is indicated in the form of a line scan. (b) Extracted positions of B molecules (top) and corresponding autocorrelation pattern (bottom). Reproduced and modified from [101].

Attempts to grow  $\text{C}_{60}$  on the 5f-Ag-In-Yb surface have also been undertaken, but resulted in disordered growth at all coverages and substrate temperatures [72]. This was assigned to the existence of a range of competing adsorption networks, all displaying similar adsorption energies [102]. However, by choosing a suitable molecule to optimise substrate-adsorbate and adsorbate-adsorbate interactions, overlayers displaying long-range quasiperiodic order on this substrate could be achieved. This was demonstrated in the growth of pentacene (Pn) on the 5f-Ag-In-Yb surface at room temperature [101]. Pn is a rod-shaped molecule composed of five linearly fused benzene rings. After deposition, the growth of a quasiperiodic layer was again evidenced by the autocorrelation of extracted molecular positions (see Figure 3.10). The orientation of molecules provides an extra degree of freedom here. Taking this into account when creating the molecular map results in an improved autocorrelation, as evidence in Figure 3.10(b). This indicates molecules are arranged in a quasiperiodic manner both positionally and orientationally. Adsorption sites were de-

terminated at pairs Yb atoms in the substrate model, whose separation fits well with the length of a Pn molecule [101]. Similar results have been reported for Pn adsorption on the other high-symmetry surfaces of *i*-Ag-In-Yb [103,104]. Quasiperiodic layers of corranulene on the 5f-Ag-In-Yb surface, a molecule with structural similarities to C<sub>60</sub> but a different dipole moment, have also been grown. Here, the difference in growth modes was assigned to different symmetry compatibilities between adsorbates and substrate sites [102].

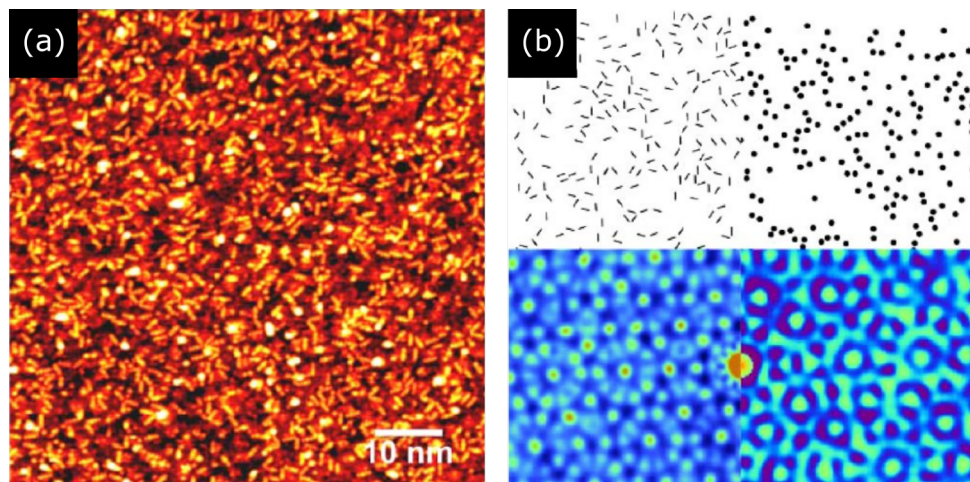


Figure 3.10: (a) STM image ( $75 \text{ nm} \times 75 \text{ nm}$ ) from a quasicrystalline Pn layer on the 5f-Ag-In-Yb surface. (b) Extracted positions of Pn molecules (top) with (left) and without (right) orientation included and corresponding autocorrelation (bottom). Reproduced and modified from [101].

#### 3.4.4 Aperiodic growth on periodic substrates

Aside from epitaxial growth on QC substrates, growth of aperiodic thin films on simple periodic metal substrates has also been reported. In this case, film formation can be driven by adsorbate-adsorbate interactions. Examples include the use of organic linkers to form complex aperiodic molecular coordination networks [105–107] and the self-assembly of quasiperiodic overlayers driven by hydrogen bonding [108]. In other systems, growth is reliant on the interplay between substrate and adsorbate, where frustration at the interface between two naturally periodic materials can induce aperiodicity in the overlayer structure. For example, ultrathin films of BaTiO<sub>3</sub> with 12-fold symmetry have been grown on a Pt(111) substrate. Here, growth was assigned to lattice mismatch between the natural

crystalline states of the substrate and adsorbate [18]. 12-fold symmetry was also evident in the growth of a 2D layer of  $C_{60}$  on a Pt-terminated  $Pt_3Ti(111)$  substrate. An interface-driven formation mechanism was again apparent here [109]. In this system, molecules were observed to adsorb in two different orientations, where the application of a voltage pulse could alter molecular orientation at specific sites. As such, this system presents an aperiodic array of rotational switching elements - a key component in molecular electronic circuits [20].

## Chapter 4

# Experimental methods

In this chapter, the experimental methods used to prepare and characterise QC surfaces and adsorbate structures will be considered. First, the concept of UHV and the technology used to achieve such conditions will be explained. After this, the techniques required for preparing atomically clean QC surfaces and depositing materials will be discussed. Finally, the surface characterisation techniques used in this work will be introduced. Oura et al. [1] has, again, been used as a reference throughout this chapter. Experience in setting up and maintaining experimental hardware has also provided useful insight.

### 4.1 Ultra-high vacuum (UHV)

UHV is broadly defined as a pressure environment below  $\approx 10^{-9}$  mbar. These conditions are required in surface investigations to maintain a clean surface composition long enough for the appropriate experiments to be undertaken. The functionality of many surface sensitive analysis techniques also relies on a vacuum environment. Both of these points can be highlighted by considering the kinetic theory of gases.

The incident flux of gas molecules ( $F$ ) per unit area of a surface may be calculated using the following equation (known as the Hertz-Knudsen formula):

$$F = \frac{P}{\sqrt{2\pi mk_B T}} \quad (4.1)$$

where  $P$  is pressure,  $m$  is molecular mass,  $k_B$  the Boltzmann constant and  $T$  is temperature. By assuming that all molecules impacting on the surface adsorb (i.e. a sticking coefficient

$S = 1$ ), an estimate for the time taken for a complete ML ( $\approx 10^{19}$  atoms per  $m^2$ ) to form can be determined. The time per monolayer values displayed in Table 4.1, where  $O_2$  molecules at room temperature have been taken as an example, indicate that the maintenance of a clean surface for a practical amount of time requires pressures of  $\leq 10^{-8}$  mbar. This is even more significant for many QCs, where oxidation disrupts order at the surface [110,111].

Also shown in Table 4.1 are the mean free paths ( $\lambda$ ) of molecules at different pressures, calculated using the following formula:

$$\lambda = \frac{k_B T}{\sqrt{2} \pi d^2 P} \quad (4.2)$$

where  $d$  is the molecular diameter. The larger mean free paths calculated for the lower pressure regimes specify that a medium to high vacuum minimises gas phase scattering, thus allowing for ion and electron based surface sensitive experimental techniques to proceed without undue interference.

Pressure (mbar)	Time/ML (s)	Mean Free Path (m)
1	$3.7 \times 10^{-5}$	$7.4 \times 10^{-5}$
$1 \times 10^{-3}$	$3.7 \times 10^{-2}$	$7.4 \times 10^{-2}$
$1 \times 10^{-5}$	3.7	7.4
$1 \times 10^{-8}$	$3.7 \times 10^3$	$7.4 \times 10^3$

Table 4.1: Theoretical calculations of the time per ML coverage of a surface and mean free path for different pressures as calculated for  $O_2$  molecules at room temperature.

#### 4.1.1 Achieving UHV

In this section, the main components of a UHV setup will be introduced. A general overview of the process required to reach the UHV regime from atmospheric pressure will then be given. The UHV system used for the majority of data acquisition in this thesis is shown in Figure 4.1, with all major components labelled.

##### UHV chamber

To achieve UHV, a sealed chamber which can maintain these low pressures is required. Such a chamber is composed of materials with low-outgassing properties that can endure

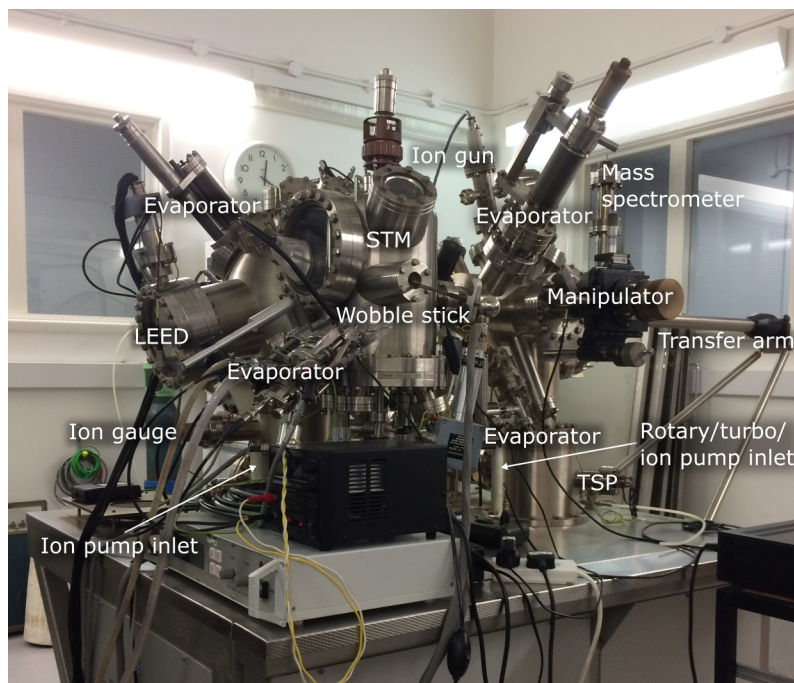


Figure 4.1: The UHV surface analytical system used for acquisition of the majority of data presented in the results sections of this thesis. Major components have been labelled.

the temperatures necessary for bakeout (this procedure will be discussed further later in this section). As such, the main vessel is generally constructed using stainless steel or mu-metal, where components are assembled through connecting flanges with bolts to tighten. The flanges sandwich around a copper gasket, where a knife edge on the flange face cuts into the gasket when the bolts are tightened, forming a secure seal. Other components of the chamber are generally formed from materials including, but not strictly limited to, glass, ceramics, tantalum, tungsten and molybdenum.

## Pumps

A range of pumps functioning in different pressure ranges are required to pump the chamber down. **Rotary vane pumps** are used to obtain a rough vacuum ( $\approx 10^{-3}$  mbar). These are mechanical compression pumps which operate by creating a periodically changing volume at the inlet and outlet to the pump, allowing for the removal of gases from the chamber. This is accomplished using a rotor/stator combination, as highlighted in Figure 4.2(a).

Gas enters at the inlet and is subsequently compressed by the rotating rotor vanes. The gas is then released upon reaching the exhaust.

One of the main pumps used to reach the UHV regime is the **turbomolecular pump**. This is another type of mechanical compression pump which transfers gases from a low pressure region to a high pressure region. The design consists of a set angled rotor/stator pairs which transfer momentum to the gas particles in order to remove them from the chamber and into the region of the roughing pump (conventionally a rotary vane pump). A schematic example is displayed in Figure 4.2(b). The large revolutions per minute of the rotor vanes typically allows for operation between  $\approx 10^{-3}$  to  $10^{-10}$  mbar, meaning a rough vacuum is required before operation.

**Ion pumps** are also implemented to attain UHV pressures. They consist of two titanium cathode plates surrounding an array of tubular anodes held at high voltage, as shown in Figure 4.2(c). Electric discharge causes ionisation of residual gas molecules. The ions are subsequently accelerated towards the cathode through the potential difference where they are captured. By applying a magnetic field normal to the cathode plates, the electrons will follow a helical path resulting in increased ionisation and hence the removal of larger amounts of unwanted gas particles. Titanium cathodes also present a major advantage in that the impinging ions can sputter titanium ions which can in turn capture other gas particles via chemisorption, forming stable titanium compounds with low vapour pressures. It must be noted that ion pumps can only operate at lower pressures, meaning a turbomolecular pump must first be used to create a medium vacuum.

The chemisorption properties of titanium are also employed in the **titanium sublimation pump**. The operation of this pump involves the sublimation of a titanium filament, causing the formation of a thin film of titanium on the inner walls of the vacuum chamber. Any gas particles impinging on the walls of the chamber are then chemisorbed by the titanium atoms forming a stable product and thus reducing the pressure in the chamber.

### Pressure measurement

The most common techniques used for determining pressures in a UHV chamber involve an indirect measurement. For pressure measurements within the rough vacuum range, **Pirani gauges** are usually employed. These are required in a UHV system in order to monitor the backing pressure created by a roughing pump. The Pirani gauge relies on changes in the temperature of a filament within the vacuum region for a corresponding pressure

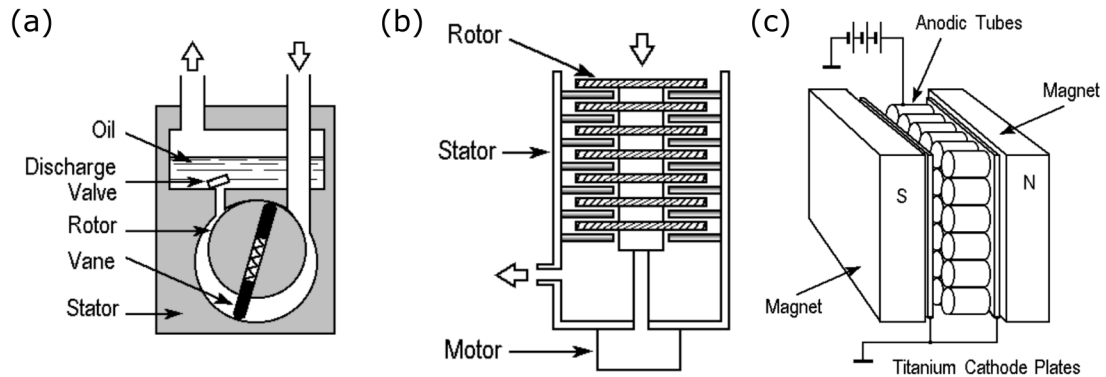


Figure 4.2: Operation of (a) a rotary pump, (b) a turbomolecular pump and (c) an ion pump. Reproduced and modified from [1].

measurement. A schematic example is shown in Figure 4.3(a). At pressures of  $\approx 10^3$  mbar, the variation in a gases thermal convection is strongly dependent on its mean free path. This means that, within this region, the convection of heat away from the filament becomes strongly dependent on the pressure. As such, electrical variations in the filament such as the resistance can be monitored and corresponding pressure measurements obtained.

For pressure measurements within the higher vacuum regions, **ionisation gauges** are usually employed. The most common ionisation gauge consists of a cathode filament, an anode and an ion collector (as shown schematically in Figure 4.3(b)). In this setup, the filament is heated causing the thermal emission of electrons. These electrons are subsequently accelerated towards an anode grid via a potential difference, ionising gas particles along their path. Ions formed outside the anode grid are collected in the ion collector where the current gives a measure of the number density of gas particles and hence the pressure within the system.

Another option for pressure measurement within the higher vacuum regions is by means of a **quadrupole mass spectrometer**, or residual gas analyser. Not only does this technique provide an overall pressure measurement, it also allows for determination of residual gas composition within the chamber. This can be extremely useful for leak checking and general maintenance of UHV conditions. The basic working principle involves filtering ionised gas molecules by their mass-to-charge ratio. Residual gases within the chamber are ionised via electron bombardment from a heated filament. The ions are subsequently accelerated through an electrostatic lens towards four parallel metal rods. The rods are

electrically biased with both DC and RF voltages, with one pair at opposite polarity to the other. The path of an ion through the resulting electric field, and hence whether it will pass the length of the quadrupole, is heavily dependant on its mass-to-charge ratio. As such, sweeping over a range of voltages in essence scans over a range of masses. Ions passing through the filter are detected by an electron multiplier, allowing for a mass spectrum to be obtained [112].

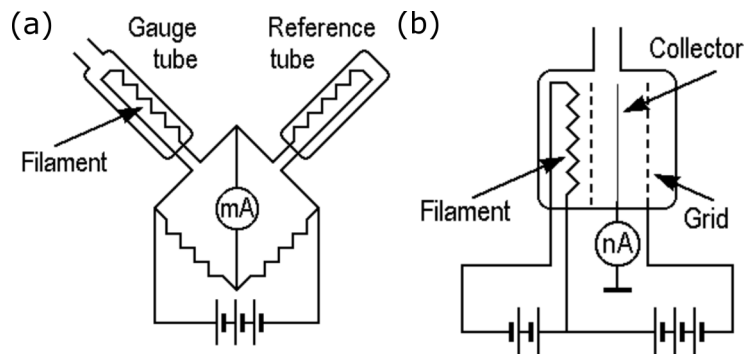


Figure 4.3: Operation of (a) a Pirani gauge and (b) an ion gauge. Reproduced and modified from [1].

### Sample positioning

Once under UHV, samples must be moved throughout the chamber without breaking the vacuum. This is achieved using sample manipulators, wobble sticks and transfer arms. A sample manipulator allows for precise  $xyz$  and rotational positioning within a certain volume of the chamber. This is important for sample preparation, material deposition and subsequent analysis techniques. Wobble sticks employ a hand-operated pincer mechanism for transferral of samples between the manipulator and other analytical stages. Both instruments utilise flexible edge-welded bellows to allow for coarse movement whilst maintaining UHV pressures. Transfer arms employ a magnetic linear drive for longer travel. These are used for transferral of samples in a system containing multiple chambers, or insertion/removal of samples from a load lock chamber.

Load lock chambers usually use a separate pumping system and are linked to the main chamber by means of a gate valve. Gate valves consist of a “flap” which seals against the body of the valve by means of a viton O-ring when closed. This allows for sample insertion

into the load lock and subsequently the main chamber with no major disruption to the overall pressure. Gate valves are also used to isolate the mechanical pumping system. This is required when turning off the mechanical pumping system to reduce vibrations during an STM experiment (discussed further in Section 4.3.2) or to protect the pumps when venting the chamber. A gate valve is also often attached between an evaporator and the main chamber. This allows for evaporation materials to be exchanged without breaking the vacuum.

### Procedure

To begin the process of obtaining UHV, the chamber is evacuated using a rotary vane pump. Once under a rough vacuum, a turbomolecular pump is employed to reach the high-vacuum regime ( $\approx 10^{-7} - 10^{-8}$  mbar). Subsequently, the bakeout process is commenced. This involves heating the whole system to approximately  $120 - 200^\circ\text{C}$  for 12+ hours, accelerating the removal of water molecules adsorbed onto the chamber walls. The system is enclosed in a set of insulating panels or sheets and a simple heating system is used to reach the desired temperature. The temperature and length of the bake is dependent on various factors such as the components attached to the chamber and the desired final pressure. An ionisation gauge is used to monitor the pressure throughout this process. During and after the baking process, instruments connected to the chamber are slowly degassed. This typically involves running the instrument at its usual operating conditions, thus heating and allowing for the removal of adsorbed gas molecules. Once all instruments have been degassed and the chamber has fully cooled, the system should be under UHV.

## 4.2 Sample preparation

This section will describe the process of QC sample preparation, from sample growth down to the preparation of atomically clean surfaces for surface-based experiments. Careful preparation is required both ex-situ and in-situ in the UHV chamber to achieve a surface of the required cleanliness and stoichiometry.

### 4.2.1 Growth methods

Large single-grain QCs can be grown using conventional crystal growth techniques, including the Czochralski, Bridgman, floating zone and self-flux methods [113]. The samples

used in the experimental section of this thesis were grown by Tsai et al. The 5f-Ag-In-Yb sample was grown using the Bridgman method [68,69]. The 2f-Ag-In-Yb sample was grown using the Czochralski method [114]. A brief description of these two methods is now given.

### **Czochralski method**

In the Czochralski method [115], a specified amount of feed materials (dependent on the stoichiometry of the required crystal) are melted in a cylindrical crucible by means of resistance or radio-frequency heating. The tip of a seed crystal is then dipped into the melt and slowly withdrawn, whilst often simultaneously rotating. This results in crystallisation of the melt at the interface and hence the formation of a new section of crystal. Careful control of melt temperature, pulling rate and rotation rate allows for the size of the crystal to be specified. A schematic displaying this setup is shown in Figure 4.4(a) [113].

### **Bridgman method**

The Bridgman method [116] employs a similar technique, where a seed crystal is inserted into a melt of specific composition. In this method however, the melt is slowly cooled from the seed crystal end by means of a temperature gradient. A schematic of this setup is displayed in Figure 4.4(b). The feed materials are placed in a quartz ampoule which is filled with an inert gas (e.g. Ar). Initially, the ampoule is held in the upper (higher temperature) zone, allowing the feed materials to melt. It is then slowly pulled down into the lower zone which is held a lower temperature. The temperature gradient causes crystallisation of the melt from the bottom up [113].

## **4.2.2 Surface preparation**

### **Ex-situ**

Once grown using one of the techniques described above, the sample is cut along the required axis. An accurate cut is assured through the use of Laue diffraction. Subsequently, the surface is polished with progressively finer grades of diamond paste ( $6 - 0.25 \mu\text{m}$ ). This is achieved by hand, with use of a lapping film. Care must be taken to ensure an even polish. Sonicating the sample in a beaker of methanol between cycles ensures no cross-contamination of different grades of paste. Once a mirror-like finish has been obtained, the sample is mounted on a standard sample plate. These are typically made from stainless

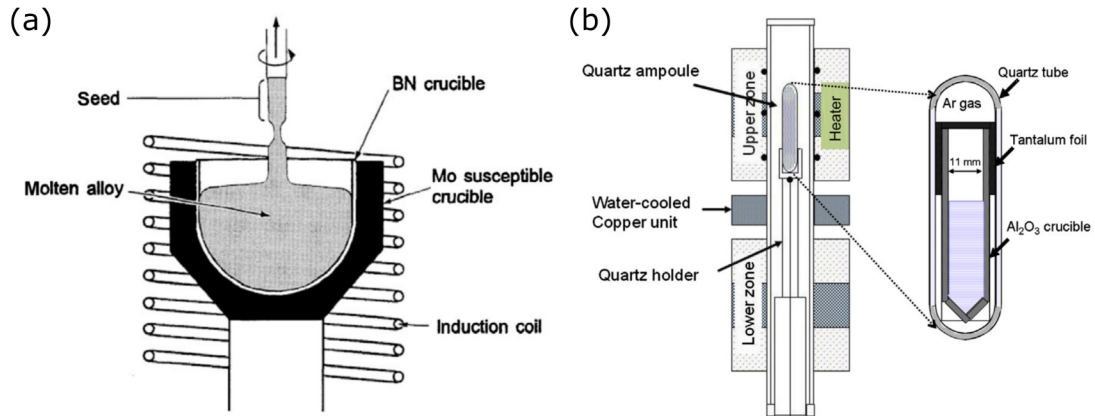


Figure 4.4: Setup used for (a) the Czochralski and (b) the Bridgman crystal growth methods. Reproduced and modified from [113].

steel, tantalum or molybdenum. They are designed to fit tightly in holders throughout the chamber, ensuring no movement but also allowing for smooth transferral. Fixing the sample is accomplished by spot welding tantalum wire straps to the sample plate to hold the sample in place. Again, care must be taken here to ensure that the sample is held tightly and does not move.

### In-situ

When the sample has been polished and mounted as described above, it is inserted into the UHV chamber using the load lock. In-situ preparation of QC surfaces typically involves cycles of sputter-annealing. Bombarding the surface with noble gas ions ( $\text{Ar}^+$  in this case), or sputtering, allows for the removal of surface contaminants. This process is displayed schematically in Figure 4.5(a). Initially, Ar gas is released into the chamber using a leak valve. An ion gun arrangement is then used to direct a beam of  $\text{Ar}^+$  ions towards the sample surface. In the ion gun, electrons are emitted from a heated filament and collected by an anode. Electron bombardment results in the ionisation of Ar gas atoms. The ions are subsequently accelerated (typically to an energy of 0.5-5.0 keV) towards the sample surface using a negatively biased grid [117]. During this process, the sample is grounded to ensure no build up of charge on the surface. Impinging ions eject both contaminant species and sample atoms at the surface. Some ions also embed into the sample surface. This process cleans the surface but also results in deterioration of the surface structure, as can be seen

from the right-hand side of 4.5(a). In the case of QCs, sputtering can result in a crystalline surface layer due to the preferential removal of lighter constituent elements [118–120]. As such, further treatment is required to regain bulk composition at the surface.

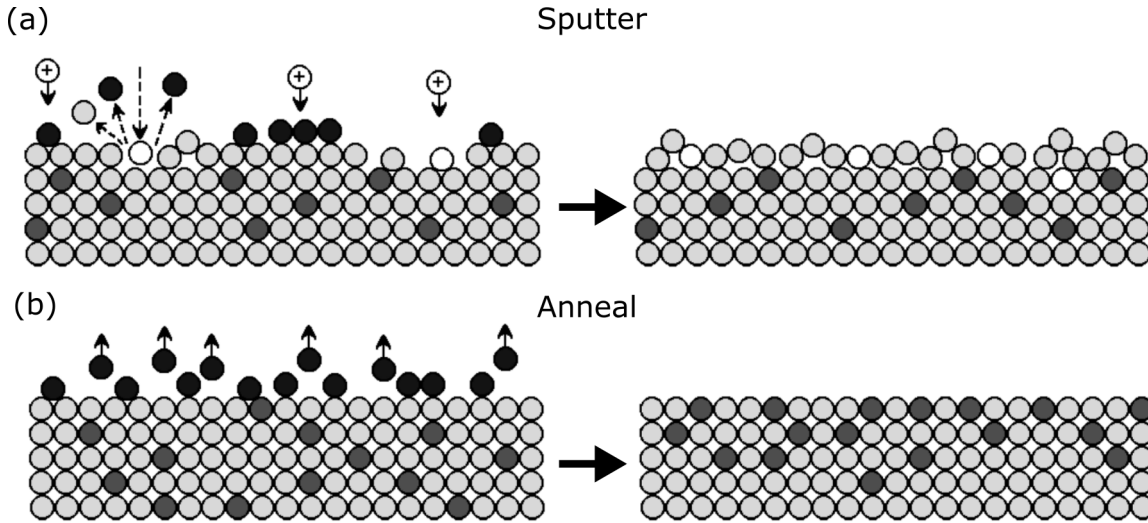


Figure 4.5: (a) Ion sputtering and (b) annealing as surface cleaning techniques. The resulting surface composition after each process is displayed to the right. Atoms of the sample are coloured grey, foreign species within the sample bulk are coloured dark grey, surface contaminants are coloured black and impinging ions are coloured white. Reproduced and modified from [1].

Annealing involves heating the sample to a fraction of its melting temperature. This can be achieved by filament heating (usually a W filament is used) and, if a higher temperature is required, electron bombardment via the application of a potential difference between the plate and filaments. Annealing can help remove adsorbed species at the surface assuming they can be evaporated at a lower temperature than the melting point of the sample. This is important in the earlier stages of cleaning, where annealing allows for the sample to be degassed. It is also important after sputtering to ensure any adsorbed  $\text{Ar}^+$  ions are removed. Heating enhances the diffusion of atoms within a material. This can restore order and stoichiometry at the surface. As can be seen from Figure 4.5(b), sputter-annealing cycles result in a clean, atomically flat surface- an important requirement for subsequent surface studies.

### 4.2.3 Material deposition

Preparation of adsorbate structures on a sample surface proceeds by in-situ evaporation of the required materials. For lower-melting point materials, this can be achieved using a simple thermal source. A typical setup houses the evaporant in a high-melting point tube (e.g. Pyrex), with the open end directed towards the substrate surface. Heat is then applied to the material by passing an electric current through a W filament wound around the cell. Similarly, W, Ta or Mo foils may be used to form tube or boat shaped structures to house the evaporant. Sublimation is again achieved via the application of an electrical current, this time directly to the evaporator cell. In the case of materials which exhibit sufficient vapour pressure below their melting point, sublimation can also be achieved by direct application of an electrical current to a rod of the material.

As with high-temperature annealing, evaporation of a higher-melting point material is achieved using electron bombardment. In this case, the evaporant is housed within a crucible (typically Mo) or held in its rod form. A filament in close proximity emits electrons via thermionic emission. The electrons are subsequently accelerated towards the crucible/rod via a large applied potential difference causing heating.

## 4.3 Surface analysis techniques

A vast range of techniques are available for surface and adsorbate analysis. The techniques used to attain the results presented in this thesis, namely LEED and STM, utilise electrons to analyse structure and order at the surface. LEED was typically used to ensure a well prepared surface prior to a more in-depth structural investigation using STM. An overview of theory behind both will be given in this section.

### 4.3.1 Low-energy electron diffraction (LEED)

Diffraction techniques conventionally utilise elastically scattered particles/waves to probe surface structure. After interaction with a sample, scattered waves interfere with each other, producing an arrangement of maxima and minima which can provide information on sample structure. In the case of LEED, electrons with an energy typically in the range 10-200 eV are used as the probe. At this energy, the de Broglie wavelength of electrons is of similar magnitude to the interatomic spacings within a sample. This is an important condition for atomic diffraction. Further to this, the mean free path of an electron within

this energy range is short, meaning elastically scattered electrons are restrained to the first few layers of the sample (i.e. only the surface is probed).

The spatial arrangement of diffracted beams can provide information on the lattice in a crystal structure. By considering conservation of momentum between incident and scattered waves, the following condition holds true for diffraction from a crystal lattice:

$$\mathbf{k} - \mathbf{k}_0 = \mathbf{G}_{hkl} \quad (4.3)$$

where  $\mathbf{k}_0$  is the incident wavevector and  $\mathbf{k}$  is the scattered wavevector. As elastic scattering is considered here, conservation of energy applies and  $|\mathbf{k}_0| = |\mathbf{k}| (= 2\pi/\lambda)$ .  $\mathbf{G}_{hkl}$  is the reciprocal lattice vector, which corresponds to the momentum transfer. Similar to a real-space lattice (see Equation 2.1), the reciprocal lattice is defined by:

$$\mathbf{G}_{hkl} = h\mathbf{a}_1^* + k\mathbf{a}_2^* + l\mathbf{a}_3^* \quad (4.4)$$

where  $h$ ,  $k$  and  $l$  are the Miller indices and  $\mathbf{a}_1^*$ ,  $\mathbf{a}_2^*$  and  $\mathbf{a}_3^*$  are the reciprocal lattice vectors corresponding to the real-space lattice vectors  $\mathbf{a}_1$ ,  $\mathbf{a}_2$  and  $\mathbf{a}_3$ , respectively. The reciprocal space and real-space lattice vectors are related by:

$$\mathbf{a}_1^* = \frac{2\pi\mathbf{a}_2 \times \mathbf{a}_3}{\mathbf{a}_1 \cdot (\mathbf{a}_2 \times \mathbf{a}_3)} \quad \mathbf{a}_2^* = \frac{2\pi\mathbf{a}_3 \times \mathbf{a}_1}{\mathbf{a}_2 \cdot (\mathbf{a}_3 \times \mathbf{a}_1)} \quad \mathbf{a}_3^* = \frac{2\pi\mathbf{a}_1 \times \mathbf{a}_2}{\mathbf{a}_3 \cdot (\mathbf{a}_1 \times \mathbf{a}_2)} \quad (4.5)$$

In this sense, it can be seen how the distribution of scattered beams, defined by  $\mathbf{k}$ , is directly related to the crystal lattice geometry in real-space. In the case of LEED, diffraction only from a 2D surface layer is considered, where components perpendicular to the surface can be ignored. As such, Equation 4.3 becomes:

$$\mathbf{k}^{\parallel} - \mathbf{k}_0^{\parallel} = \mathbf{G}_{hk} \quad (4.6)$$

where conservation of momentum applies only for the wavevector components parallel to the surface ( $\mathbf{k}^{\parallel}$  and  $\mathbf{k}_0^{\parallel}$ ) and the 2D surface reciprocal lattice vector ( $\mathbf{G}_{hk}$ ).

The diffraction process can be illustrated graphically using an ‘Ewald construction’ in reciprocal space. The 2D Ewald construction for surface diffraction is displayed in Figure 4.6(a). In this method, each 2D reciprocal lattice point is considered as a rod perpendicular to the surface (vertical lines in Figure 4.6(a)). This is due to the fact the 2D surface lattice displays infinite periodicity along the normal direction (i.e. the lattice vector  $\mathbf{a}_3$  is infinitely large). This means the reciprocal lattice vector ( $\mathbf{a}_3^*$ ) in the normal

direction tends towards zero and is, therefore, infinitely dense in reciprocal space. The  $\mathbf{k}_0^{\parallel}$  vector is then plotted such that it terminates at one of these reciprocal lattice rods. If a circle is drawn, with its origin and radius defined by  $\mathbf{k}_0$ , scattered wavevectors can be determined from the sphere/reciprocal lattice rod intersections, as shown in Figure 4.6(a). Aside from the relationship between incident and scattered wavevectors and the surface reciprocal lattice points, this construction demonstrates that a larger Ewald sphere (i.e. larger incident beam energy) will result in more intersections and therefore more scattered beams.

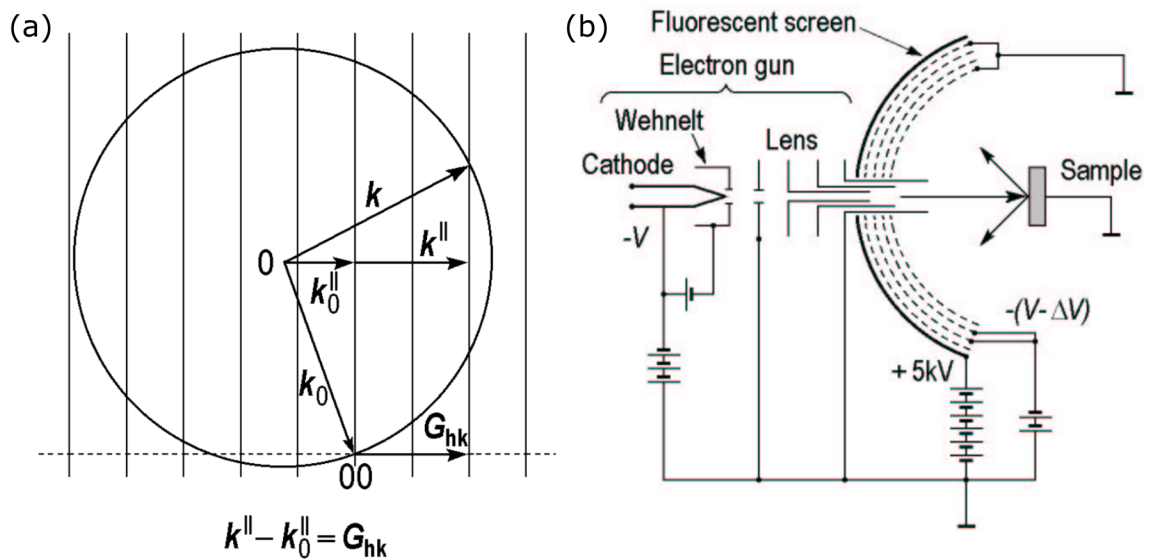


Figure 4.6: (a) Projected 2D Ewald construction for diffraction from a 2D surface lattice. (b) Schematic of a standard LEED experimental setup. Reproduced and modified from [1].

Experimentally, LEED is performed using a setup like that portrayed schematically in Figure 4.6(b). An electron gun (consisting of a cathode filament, a focussing Wehnelt cylinder and an electrostatic lens) accelerates a beam of electrons towards a sample surface via a potential difference. The layout of the apparatus is such that electrons backscattered from the sample are radially incident on a hemispherical fluorescent screen, preceded by a concentric set of hemispherical grids. The first grid is grounded such that there is no field between the sample and the grid. This ensures the path of the electrons in this region remains unaffected. The second and third grids suppress inelastically backscattered electrons using a negative potential difference. The voltage of these grids can be varied

to ensure good contrast between diffraction maxima and background. The final grid is grounded, forming a ‘shield’ from the fluorescent screen, which is held at a high voltage ( $\sim 5\text{kV}$ ) to reaccelerate electrons towards the screen and cause fluorescence. The overall result is that only elastically scattered electrons pass through to the screen to form the diffraction pattern.

By comparison of the LEED setup and the Ewald construction, both shown in Figure 4.6, it can be seen that the diffraction pattern observed on the fluorescent screen, analogous to the Ewald sphere here, essentially provides a view of  $\mathbf{G}_{hk}$  (the surface reciprocal lattice). Each spot corresponds to an intersection of the Ewald sphere with a surface reciprocal lattice rod. For an electron beam of normal incidence, the (0,0) ‘specular’ diffraction peak will reside at the centre of the LEED pattern. Increasing the incident electron beam energy, and thus increasing the size of the Ewald sphere, will cause the outer spots to enclose around the specular, with additional spots appearing at the edges of the fluorescent screen.

Aside from the reciprocal lattice information that can be gained from the geometrical arrangement of diffraction spots, information is routinely drawn from spot sharpness in a LEED pattern. A well-prepared surface (clean and well-ordered) will display sharp diffraction maxima with little background. However, peak broadening and increased background will be observed when a surface contains structural defects and contamination. No spots will be apparent if a surface is disordered. As such, LEED is often used to monitor the surface preparation process (i.e. in between sputter-annealing cycles and during/after material deposition). A more in-depth analysis of spot profiles can reveal information on structural imperfections at the surface, where deviations from an ‘ideal’ structure will result in characteristic alterations in peak shape and intensity. Further to this, analysis of spot intensity as a function of incident electron beam energy can provide information on the arrangement of atoms within the surface lattice in a technique known as LEED I–V. This is a complex process involving comparison between theoretical calculations and experimental data. Iterative improvements are applied to the theoretical model until an adequate agreement with experimental data is met. This agreement is measured quantitatively using the reliability factor (R-factor) where a lower value indicates a better match.

Despite their aperiodicity, LEED patterns from QC surfaces still display sets of well-defined diffraction peaks. It has been demonstrated theoretically in Section 2.3.2, that diffraction from an aperiodic structure results in an infinitely dense diffraction pattern, with only certain peaks, arranged aperiodically in reciprocal space, displaying an appreciable intensity. This is evidenced in LEED patterns from QC surfaces, as can be seen, for

example, in those taken from the high-symmetry surfaces of the *i*-Ag-In-Yb QC (Figure 3.2). Sharp diffraction peaks are visible, arranged at  $\tau$ -scaled separations. High-symmetry axes and therefore the rotational symmetry of the surface can also be inferred from the arrangement of spots around the centre.

### 4.3.2 Scanning tunnelling microscopy (STM)

STM was invented by Gerd Binnig and Heinrich Rohrer, who were awarded the Nobel Prize in Physics in 1986 for development of this experimental technique [2]. It involves investigation of the joint electronic density of states of a conductive sample surface and sharp tip in close proximity. This can provide information on structural features and topography at the surface.

The basic principle of STM lies in the quantum tunnelling effect. If a tip is placed close enough to a sample surface ( $\sim 5\text{-}10 \text{ \AA}$ ), the wavefunctions of surface atoms and the tip atom closest to the surface will overlap. Applying a bias voltage between the tip and sample then allows for electrons to quantum mechanically tunnel across the gap. The bias voltages reported in this thesis are stated with respect to the sample. A negative sample voltage will cause electrons to tunnel from sample to tip, thus probing filled electronic states at the sample surface. With a positive sample voltage, the opposite is true and empty sample surface states are probed. This process is displayed schematically in Figure 4.7(a) for a positive sample voltage. The resultant tunnelling current is given by:

$$j = \frac{D(V)V}{d} \times \exp(-A\phi_B^{1/2}d) \quad (4.7)$$

where  $D(V)$  represents the electron state densities of tip and sample,  $V$  is the bias voltage,  $d$  is the effective tunnelling gap,  $A$  is a constant and  $\phi_B$  is the effective barrier height. Immediately noticeable from Equation 4.7 is the exponential dependence of tunnelling current,  $j$ , on  $d$ . This means a small change in tip-sample separation, in the form of a protruding surface adatom, for example, will result in a large change in tunnelling current, thus providing a high vertical resolution. The lateral resolution is determined by tip shape, where a singular atom at the end of the tip will provide maximum resolution. As such, raster scanning an atomically sharp tip across the surface of a sample can provide a view of the surface topography. It must be born in mind, however, that increases in local density of states, (LDOS) and hence tunnelling current, do not necessarily correspond to topological features.

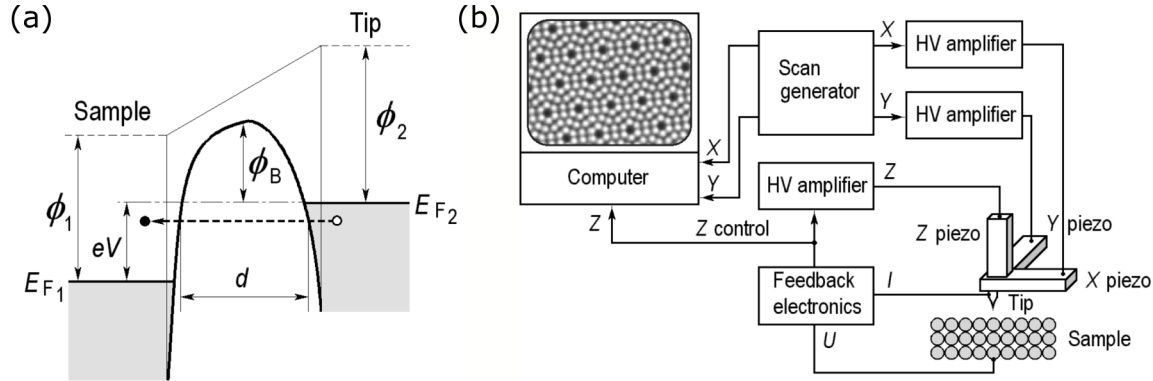


Figure 4.7: (a) Energy diagram showing the quantum mechanical tunnelling of electrons from an STM tip to a sample surface held a positive bias.  $E_{F1}$  and  $E_{F2}$  are the Fermi levels of the surface and tip, respectively.  $\phi_1$  and  $\phi_2$  are the work functions of the surface and tip, respectively.  $\phi_B$  is the effective barrier height,  $d$  is effective tunnelling gap and  $V$  is the bias voltage. (b) Schematic of an STM setup. Reproduced and modified from [1].

The main components of an STM setup are displayed schematically in Figure 4.7(b). A tip, made from tungsten in the setup used for data collection in this thesis, is prepared ex-situ via an electrochemical etching process. Sputter and annealing, voltage pulses and controlled tip-surface “crashes” are also applied for further tip preparation in-situ. The tip is mounted on a scanning stage, which is suspended using a combination of soft springs and magnets during STM operation to ensure isolation from mechanical vibrations. The stage consists of a set of piezoelectric ceramics, where application of electric signals across the ceramics allows for fine control of the tip’s motion in the  $x$ ,  $y$  and  $z$  directions. A coarse positioning system can also be utilised for initial tip approach, or retraction when sample transferral is required. A complex system of feedback electronics monitors the tunnelling current and controls the tip-sample separation. Acquired data is converted to an image on a computer system, where the tip position and various scanning parameters (i.e. bias voltage, tunnelling current, scan size etc.) can also be controlled.

There are two main modes of STM operation, namely constant current and constant height mode. In the former, the tunnelling current is held at a constant set-point while scanning, where the feedback electronics alters the signal across  $z$ -piezo to maintain a constant tip-sample separation. An image is then formed by considering the tip’s  $z$  position as a function of its  $x$  and  $y$  position. In the latter, the tip’s  $z$  position is held constant, with an image formed from the measured tunnelling current as a function of the tip’s  $x$

and  $y$  position. Constant current mode was used to acquire data in this thesis.

Although not used during data collection for this thesis, the scanning tunnelling spectroscopy (STS) technique can utilise the STM setup to gain further information on chemistry at the surface. As can be seen from Equation 4.7 and Figure 4.7(a), the tunnelling current is directly related to the electron state densities in an energy window determined by the bias voltage. This concept is used in STS to obtain LDOS information as a function of energy. By positioning an STM tip at a specific sample surface location, the tunnelling current at that location can be measured as a function of bias voltage, or energy. The resulting spectrum is known as an  $I$ - $V$  curve. The slope of the  $I$ - $V$  curve at each voltage, termed the  $dI/dV$  curve, corresponds closely to the electron density of states at the location of the tip (i.e. the LDOS). From this data, it can be possible to distinguish between surface atoms of a different chemical nature where they will exhibit different signatures in their LDOS.

### Analysis techniques

Aside from the structural information that can be inferred by eye, image processing techniques are routinely used for a more thorough analysis of STM data. Two software packages were used for such analysis in this thesis, namely WSxM and Gwyddion [121, 122]. An outline of some of the main tools and techniques will be given here.

STM is an extremely sensitive technique, meaning artefacts often appear in data which do not correspond to real surface features. As such, the first step in processing an STM image usually involves correction for any distortion. Plane levelling is used to rectify slopes in the data, which arise due to the tip-sample inclination. Different levelling procedures are applied depending on the data (i.e. whether the area is atomically flat or contains features at a range of different heights). Scan line defects are also a common artefact. They arise from the line by line acquisition of data during a raster scan across the surface. Corrupted lines can be corrected in a ‘scar removal’ process. Finally, drift correction is applied to data to rectify distortion effects appearing from thermal expansion in the scanner. In this thesis, a manual drift correction process was often employed by considering expected symmetries on the surface.

After image correction, direct measurement of surface features can be undertaken. Line profiles are one of the most common tools for this, allowing for separations and apparent height measurements to be taken. Similarly, height histograms are useful for measuring step

heights and adsorbate layer heights, for example. Two other processing techniques used regularly for STM data analysis are the fast Fourier transform (FFT) and autocorrelation function. Both allow for an assessment of inherent order within data that may not be easily discernible by eye. An FFT decomposes the image signal into its harmonic components (i.e. sums of sine and cosine functions with different amplitudes and frequencies). These are then represented in the Fourier domain, where each point corresponds to a certain frequency contained within the real-space image. In this sense, repeating features in the data will correspond to points of high-intensity in the Fourier domain, much like a LEED pattern. As such, common separations and rotational symmetry at the surface can be inferred from an FFT. Filtering high-intensity FFT spots and applying an inverse FFT means these features can be viewed back in the real-space domain. Such a process can also be useful for filtering out unwanted noise in the data. Care must be taken here, however, to ensure that real surface information is not lost. The autocorrelation function of an STM image can also provide details on repeating features and order within the data. In this processing technique, the image is shifted some distance in the  $x$  and  $y$  directions with respect to the image origin. The difference between the shifted and original images is then computed and presented in real-space. As such, any repetitive patterns in the data will also be apparent in the autocorrelation image.

Throughout this work, both FFTs and autocorrelations have been used to assess the long-range order apparent in STM data from QC surfaces and adsorbate layers. As discussed already, a well-established indicator of quasicrystalline order is in the existence of  $\tau$ -scaled features. This hallmark is maintained in the FFTs and autocorrelations of STM data from QC surfaces, where  $\tau$ -scaled separations between high-intensity spots is observed. However, care must be taken to ensure  $\tau$ -scaling is not imitated by the twinning of multiple periodic phases, forming high-intensity features with separations close to some  $\tau$ -scaled value.

One final analysis technique which requires discussion is the process of taking multiple STM scans from the same area of the surface in order to assess surface diffusion and bias-dependency. The main idea here, is to overlay scans from exactly the same area of the surface directly on top of each other. Changes between scans can then be monitored by flicking between frames in a ‘spot the difference’ type procedure. One of the main issues here is drift, which means successive STM scans are never on exactly on the same area of the surface. Automatic in-software drift correction can be performed, with further manual corrections applied after, if required. When assessing surface diffusion, another key

consideration is the tip condition and scanning parameters (i.e. bias voltage, tunnelling current and scan speed), which should be held constant between successive scans to ensure any observed ‘movement’ between frames is not related to a change in tip shape or, for example, bias-dependency. When assessing bias-dependency, the same rules are applied, with the bias voltage being altered between scans.

## Chapter 5

# Bias-dependency and atomic motion on the clean surfaces of *i*-Ag-In-Yb

In this chapter, two sets of results will be presented. Firstly, a previously unobserved bias-dependency of STM contrast will be explored on the clean 2-fold surface of the *i*-Ag-In-Yb QC. Some of the results and analysis presented in this section are featured in reference [123], a publication of work undertaken during this thesis. Secondly, the motion of atomic species at room temperature on the clean 5-fold surface of the *i*-Ag-In-Yb QC will be investigated by STM.

### 5.1 Introduction

#### 5.1.1 2f-Ag-In-Yb clean surface structure

The *i*-Ag-In-Yb QC and its 5-fold surface were discussed in Section 2.8 and 3.2, respectively. It was shown how high-resolution STM data indicates that the 5-fold surface is terminated at high-density CC planes in the *i*-Ag-In-Yb model (see Figure 3.3). Bias-dependency in the data was attributed to the probing of 3<sup>rd</sup> shell Yb sites and 4<sup>th</sup> Ag/In sites at positive and negative bias-voltages, respectively [71]. On the 3-fold surface, a termination through bulk planes intersecting CCs has again been evidenced by STM. Yb atoms were resolved at both bias polarities, but Ag/In sites were resolved at neither. A degree of bias-dependency

was observed, however, where resolution of Yb atoms was enhanced at positive bias [73].

The 2f-Ag-In-Yb surface exhibits the highest atomic density of all three high-symmetry surface planes in the *i*-Ag-In-Yb system. It contains all three high-symmetry axes of the bulk icosahedral symmetry (2-fold, 3-fold and 5-fold) within its surface - a feature which will be used to characterise aspects of the surface in the results section. In the first STM investigation of this surface, a bulk truncation through CC sites was apparent [74], as with the 3-fold and 5-fold surfaces. A step-terrace structure was observed (see Figure 3.2(c)), with two basic step heights of  $S = 0.27 \pm 0.03$  nm and  $L = \tau S = 0.45 \pm 0.04$  nm. These are consistent with separations between high-density CC planes perpendicular to the 2-fold direction in the *i*-Ag-In-Yb model. In high-resolution STM images taken at positive bias, a zigzag row-structure was observed parallel to one of the 2-fold surface axes, as can be seen in Figure 5.1(a). This is highlighted in detail in Figure 5.1(b), where rows are marked in red and zigzag features in blue. These observations were attributed to contribution from 5<sup>th</sup> shell Ag/In sites in the model (red in Figure 5.1(c)), where the model separation between rows (1.57 nm) and the inner angle of zigzag features ( $116^\circ$ ) matched well with experimental observations. Brighter elongated ‘linking’ features were also observed in between rows at  $\tau$ -scaled distances, marked in pink in Figure 5.1(b). These were assigned to 1<sup>st</sup>, 2<sup>nd</sup> and 4<sup>th</sup> Ag/In sites in close proximity to CCs, where their inhomogeneous distribution was thought to be a result of the partial occupancy of 1<sup>st</sup> shell positions (see Section 2.6). Bias-dependency was not discussed in this report [74].

More recently, higher resolution STM data from the 2f-Ag-In-Yb surface was achieved at lower positive bias [124]. In this work, alignment along both 2-fold axes was evident, with rows of individual bright protrusions observed on a ‘bed’ of darker contrast features, as can be seen in Figure 5.2(a). The bright protrusions were compared to 4<sup>th</sup> shell Ag/In sites, where vertical and horizontal row separations matched up well with 4<sup>th</sup> shell features (see Figure 5.2(b)). Note that the horizontal rows in Figure 5.2(a) are placed at an average of the two experimentally observed row separations ( $2.06 \pm 0.07$  nm and  $2.4 \pm 0.1$  nm). The bright protrusions were assigned to contribution from In atoms, in particular. This was backed up by the occupancy of In in the 4<sup>th</sup> shell in the *i*-Ag-In-Yb QC model, which is upwards of 80%, matching well with the ‘coverage’ of bright protrusions in STM data. Darker contrast features were accredited to Yb contribution. The enhanced resolution observed here, in comparison to the previous report, was attributed to STM tip condition. Bias-dependency was not studied [124].

So, a common feature of all high-symmetry surfaces is the existence of a stable step-

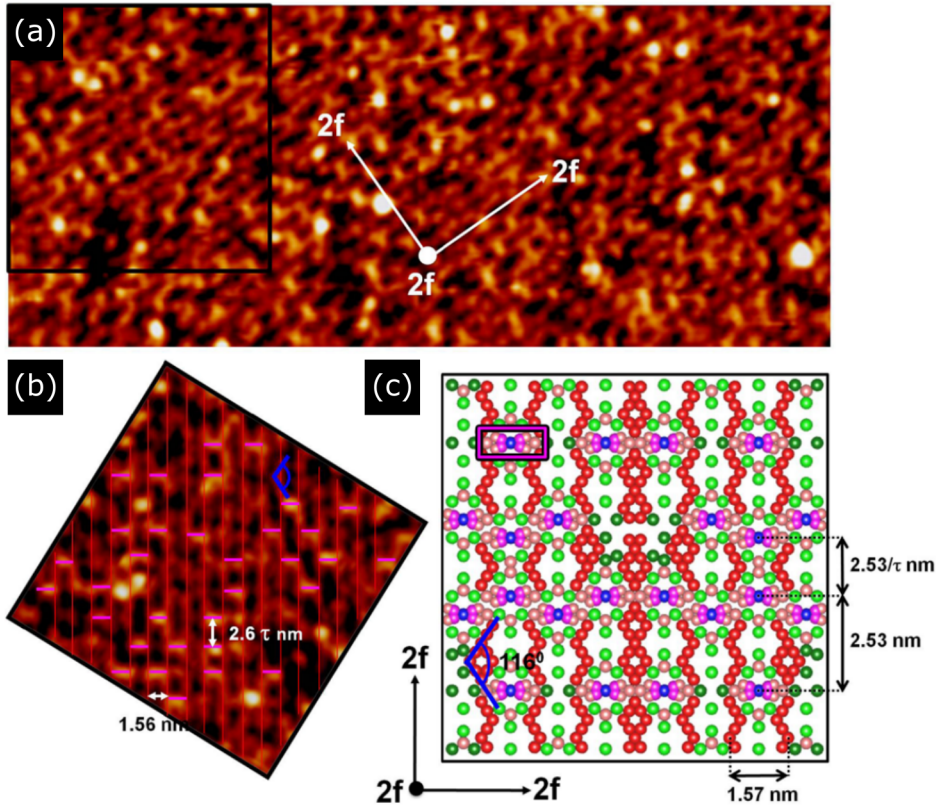


Figure 5.1: (a) STM image ( $75 \text{ nm} \times 35 \text{ nm}$ ,  $V_b = +1.1 \text{ V}$ ) from the clean 2f-Ag-In-Yb surface displaying a zigzag row structure. (b) The section of the image marked by a square in (a), rotated and enlarged. Rows are highlighted in red, their zigzag nature in blue and  $\tau$ -scaled ‘linking’ protrusions in pink. (c) Model  $i$ -Ag-In-Yb plane ( $10 \text{ nm} \times 10 \text{ nm}$ ) intersecting CCs. Clusters centres are blue, 1<sup>st</sup> shell Ag/In atoms are pink, 2<sup>nd</sup> and 4<sup>th</sup> shell Ag/In atoms are light pink, 3<sup>rd</sup> shell Yb atoms are light green, 5<sup>th</sup> shell Ag/In atoms are red and glue Yb atoms are dark green. This model plane describes the features observed by STM, which are again marked on the image with the same colour coding as in (b). Reproduced and modified from [74].

terrace structure with large terraces. The structure of terraces in all cases can be related to bulk planes intersecting CCs in the  $i$ -Ag-In-Yb model. In the case of the 2-fold surface, these planes exhibit the highest atomic density in comparison to other atomic planes along the 2-fold direction. In the 3-fold and 5-fold surfaces, the CC planes have moderate atomic density in comparison to other atomic planes along their respective directions. However, in all cases, a high relative density of In and Yb in the surface plane is evident, suggesting

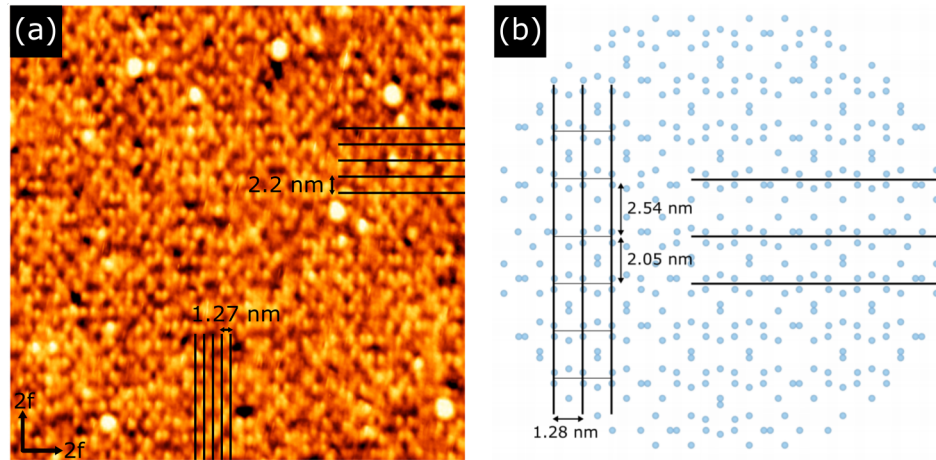


Figure 5.2: (a) High resolution STM image ( $65 \text{ nm} \times 65 \text{ nm}$ ,  $V_b = +0.8 \text{ V}$ ) from the clean 2f-Ag-In-Yb surface. Row structures and corresponding separations along both 2-fold axes are marked. The separation between horizontal rows is placed at an average of the two observed row separations ( $2.06 \pm 0.07 \text{ nm}$  and  $2.4 \pm 0.1 \text{ nm}$ ). (b) 4<sup>th</sup> shell of the model *i*-Ag-In-Yb plane used to describe the 2f-Ag-In-Yb surface. Row structures are again marked, formed by 4<sup>th</sup> shell dimers. Reproduced and modified from [124].

In/Yb rich terminations aid in the minimisation of surface free energy, thus enhancing stability (see discussion in reference [62]). It should be noted, however, that this is more pronounced in the 3-fold and 5-fold surfaces, where there is a larger relative proportion of In and Yb surface atoms when compared to the 2-fold surface [62].

In this chapter, new STM data from the clean 2f-Ag-In-Yb surface will be presented, shedding more light on the atomic structure of the surface. In this data, bias-dependency is studied. Features at both positive and negative bias polarities can be explained in terms of atomic planes intersecting the centre of Tsai-type clusters which make up bulk structure, where different bias voltages probe different atomic species at the surface. At positive bias voltage, contribution from Yb atoms is enhanced, while at negative bias voltage, there is an increase in contribution from Ag/In atoms. The newly observed bias-dependency is attributed STM tip condition and the larger range of bias voltages explored.

### 5.1.2 Atomic movement at the surface

Also presented here is STM data indicating the motion of atomic species embedded in the 5f-Ag-In-Yb surface at room temperature. The motion of adatoms deposited on a surface

is relatively well-studied, where STM has often been used to investigate such processes in simple periodic systems (see [125–127], for example, for reviews). Adatom movement on QC surfaces has also been observed [93, 128–130]. Direct observation of the diffusion of atoms embedded at sites within a surface layer is more rare, however. One example is in the vacancy diffusion observed on the  $\text{Ge}(111)c(2\times 8)$  surface at room temperature [131]. In this system, a single vacancy or pair of vacancies were created artificially via atomic manipulation with an STM tip. Movement of vacancies was then observed in successive STM scans, as can be seen in Figure 5.3(a-d). This diffusion mechanism typically takes place on surfaces in which the majority of atomic sites are occupied (i.e. those with a low vacancy concentration). A surface atom ‘jumps’ into a vacant site, thus creating a vacancy at its original location. A neighbouring atom then fills this new vacancy, creating another vacancy for the next neighbouring atom to fill and so on [1]. Similar observations have been made on the 5f-Al-Pd-Mn surface, where the filling of interstitial hollow sites was observed after scanning repeatedly on the same area of the surface [93]. As with the artificial creation of an atomic vacancy on the  $\text{Ge}(111)c(2\times 8)$  surface, the movement here was supposed to be a result the STM tip picking up a surface atom during scanning and depositing it within the interstitial hollow site.

In the majority of systems, where only ‘natural’ vacancies exist, such diffusion processes are generally considered too quick for direct observation using a technique such as STM, unless a tracer particle is used. Take, for example, the vacancy-assisted heterodiffusion of In atoms embedded in a  $\text{Cu}(001)$  surface [132]. In this system, In atoms were observed to ‘jump’ over distances larger than one lattice spacing between successive STM scans (as shown in Figure 5.3(e-g)). They play the role of a tracer particle here, where their movement between successive STM scans was assigned to multiple interactions with rapidly diffusing vacancies in the substrate surface (diffusing adatoms were ruled out as the mediator in this system). Simultaneous jumping of neighbouring In atoms was also observed, explained by the increased interaction probability between a diffusing vacancy and multiple In atoms in close vicinity. The vacancies themselves were not detected here due to their low concentration and high mobility.

In this chapter, it will be seen how successive scans taken from the same area of the 5f-Ag-In-Yb surface, with the same tip conditions, indicate the movement of surface atoms. This motion is observed at negative bias, suggesting a relation to Ag/In surface atoms. The movement also appears to occur at well-ordered sites. The possibility of both ‘simple’ surface diffusion and phason-assisted motion, like that discussed for two Al-based dQCs in

Section 2.4, will be examined.

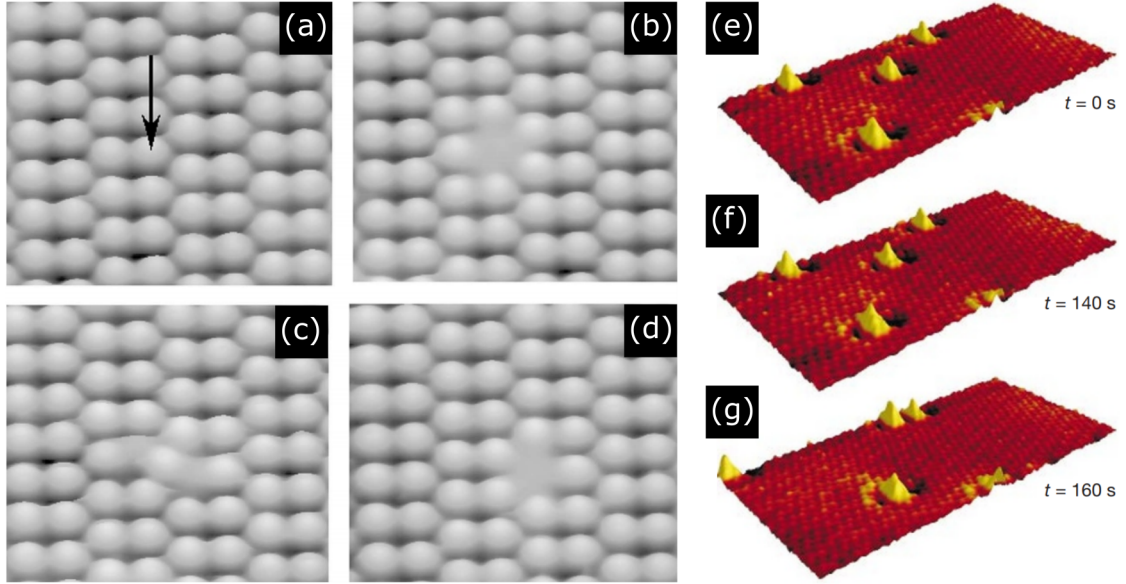


Figure 5.3: (a-d) Successive STM scans ( $5 \text{ nm} \times 5.5 \text{ nm}$ ) showing the diffusion of a single atomic vacancy on the  $\text{Ge}(111)c(2 \times 8)$  surface at room temperature. The time between scans varies from 37-67 s. The arrow in (a) shows where an atomic vacancy was created via atomic manipulation with the STM tip. Reproduced and modified from [131]. (e-g) Successive STM scans ( $14 \text{ nm} \times 7 \text{ nm}$ ) showing the diffusion on In atoms (bright protrusions) embedded in a  $\text{Cu}(001)$  surface layer at room temperature. The time between scans is indicated. Reproduced and modified from [132].

## 5.2 Experimental details

The *i*-Ag-In-Yb QC samples were grown using the Bridgman method. Cuts perpendicular to the 2-fold and 5-fold rotational axes were made to study the 2-fold and 5-fold surfaces, respectively [114]. Ex-situ preparation involved polishing the surface with successively finer grades of diamond paste ( $6\text{-}0.25 \mu\text{m}$ ), before washing with methanol in an ultrasonic bath. Upon insertion into the UHV chamber, surfaces were cleaned with repeated sputter-annealing cycles. Each sputter used  $\text{Ar}^+$  ions at 2-3 keV for 30 minutes, before annealing at  $425 \text{ }^\circ\text{C}$  for 2 hours. The temperature of the sample during annealing was measured with an infra-red optical pyrometer with emissivity set to 0.35. This is a well-established method

for the preparation of clean well-ordered surfaces in the *i*-Ag-In-Yb system [71, 73, 74]. Local ordering and cleanliness were monitored using STM (Omicron VT-STM) for both samples, as well as LEED (Omicron SPECTALEED) for the 5-fold surface. The samples were held at room temperature during all data acquisition.

## 5.3 Results

### 5.3.1 2f-Ag-In-Yb bias-dependency

After preparing the 2f-Ag-In-Yb surface using the procedure described in Section 5.2, a step-terrace morphology was evidenced by STM. Lengths within some terraces can reach up to micrometers in size. Measured step heights were consistent with those reported previously [74]. STM was performed at a range of bias voltages (from +2.5 V to -2.5 V). As outlined in Section 4.3.2, multiple scans were taken on the same area of the surface, changing the bias voltage between scans to assess bias-dependency. A representative image from the same area of the surface at each bias polarity will be discussed here.

Figure 5.4(a) shows an STM image taken at high positive bias (+2.5 V). The high-symmetry axes of the surface are the same as those marked by arrows in Figure 5.4(e), where these were determined using the FFT (shown in Figure 5.4(c)). Although not shown by the arrows in the figure, these axes are mirrored along the 2-fold directions. This will be the same for all subsequent figures in this thesis where high-symmetry axes arrows are displayed. Resolution in the STM data here, is similar to that observed previously at higher positive bias (see Figure 5.1(a)) [74]. A row-structure along one 2-fold axis (vertical direction in Figure 5.4(a)) is again apparent. The average separation between rows, as determined from the autocorrelation pattern (not shown here), is  $R_H = 1.32 \pm 0.04$  nm. This separation is slightly lower than that reported by Cui et al. [74] (see Figure 5.1(b)), but consistent with that observed by Coates [124] (see Figure 5.2(a)). Similar to the brighter ‘linkages’ observed previously, a range of large, bright protrusions are evident in Figure 5.4(a). They exhibit a more uniform nature than the elongated features displayed in Figure 5.1(a) and (b) [74]. Alignment of these protrusions along the horizontal 2-fold axis results in a row-like arrangement along this direction. The average vertical separation, again determined using the autocorrelation pattern, is  $R_V = 2.16 \pm 0.04$  nm. This is consistent with that reported previously (see Figure 5.2(a)) [124]. Alignment of these features along the 5-fold axes is also apparent. This combination of 2-fold and 5-fold alignment often

results in the formation of diamond features, with edges oriented along the 5-fold axes. One has been highlighted in Figure 5.4(a) and enlarged inset. The average small and large diagonals of these diamond features are  $2.56 \pm 0.03$  nm and  $4.13 \pm 0.04$  nm, respectively, where the ratio of these two values is  $\sim \tau$ . They are approximately double the measured row separations  $R_H$  and  $R_V$ , respectively. Incomplete diamonds (i.e. those with missing vertex protrusions) are also common.

As the voltage is decreased to +0.8 V (the same voltage used to produce Figure 5.2(a)), similar resolution to that obtained in the previous report is again obtained (not shown here) [124]. As the voltage is further decreased into negative bias, slight differences are observed. Figure 5.4(b) shows an STM image taken at -0.8 V. The high-symmetry axes are oriented along the same direction as in Figure 5.4(a). Alignment along the horizontal 2-fold axis is less prominent. However, a more pronounced alignment of bright protrusions along the 5-fold axes is evident. Diamond features are still observed, where a diamond residing on the same area of the surface, exhibiting the same dimensions as in Figure 5.4(a), has been highlighted in Figure 5.4(b) and enlarged inset. Protrusions again reside at the vertices. However, their size decreases and new protrusions of comparable size and contrast appear along the diamond edges. This contributes to the more pronounced alignment of features along the 5-fold direction. Note here that decreasing the bias voltage further has no effect, with STM resolution remaining mostly unchanged.

The FFTs of Figure 5.4(a) and (b) are shown in Figure 5.4(c) and (d), respectively. The high-symmetry axes are marked at the bottom of Figure 5.4(c) and are the same for Figure 5.4(d). A set of  $\tau$ -scaled concentric rectangles, with aspect ratio also equal to  $\tau$ , have been overlaid on both FFTs. The sides of the largest rectangle in Figure 5.4(d) are cropped out. The majority of diffraction maxima reside at the vertices or edges of these rectangles. In fact, all spots can be indexed using the four reciprocal basis vectors marked in white in Figure 5.4(c) and (d), confirming the quasicrystalline 2-fold symmetry of the surface. Different coloured circles highlight spots oriented along different directions. Those aligned along the high-symmetry axes of the surface are colour coded the same as the arrows indicating these directions in Figure 5.4(c).

Some features of the FFTs, which will be useful for later discussion, will now be picked out. In both FFTs, blue-circled spots arranged along the 2-fold axes are observed. The separations between first order spots are the same in both FFTs and are consistent with the row separations observed in the real-space data ( $R_H = 1.33 \pm 0.03$  nm and  $R_V = 2.16 \pm 0.06$  nm for the +2.5 V FFT and  $R_H = 1.33 \pm 0.03$  nm and  $R_V = 2.14 \pm 0.09$  nm for the

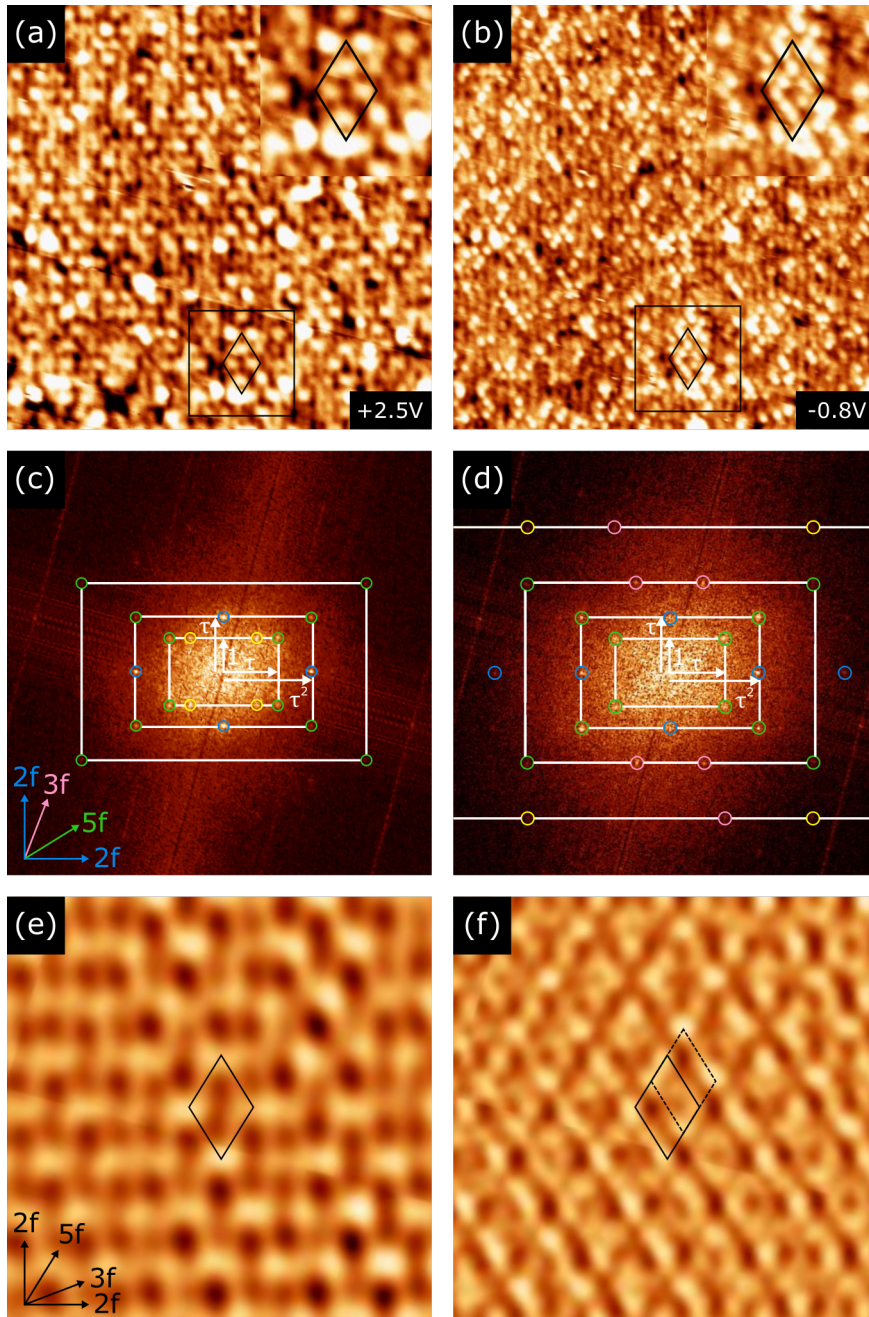


Figure 5.4: (a) and (b) STM images ( $50 \text{ nm} \times 50 \text{ nm}$ ,  $I_t = 0.186 \text{ nA}$ ) from the same area of the 2f-Ag-In-Yb surface taken at  $V_b = +2.5 \text{ V}$  and  $-0.8 \text{ V}$ , respectively. Magnified views ( $12 \text{ nm} \times 12 \text{ nm}$ ) of the sections marked by a black square in (a) and (b) are shown inset. (c) and (d) FFTs of (a) and (b), respectively. High-symmetry axes are marked at the bottom of (c) and are oriented the same for (d). Spots are marked by different coloured circles depending on their orientation. Spots oriented along high-symmetry axes are colour coded the same as the arrows in (c). The basis vectors marked in white can be used to index all spots. (e) and (f) A zoomed in section ( $17 \text{ nm} \times 17 \text{ nm}$ ) of the inverse of the filtered FFTs from all maxima in (c) and (d), respectively. The high-symmetry axes marked by arrows at the bottom of (e) and are oriented the same for (a), (b) and (f). Diamond features referred to in the text have been marked in (a), (b), (e) and (f).

-0.8 V FFT). At -0.8 V, the spots arranged along the vertical 2-fold direction in the FFT (corresponding to the horizontal 2-fold direction in Figure 5.4(b)) appear comparatively dim compared to those arranged horizontally and to those observed at +2.5 V, as can be seen in Figure 5.4(d). This is consistent with the less prominent alignment of features along the horizontal 2-fold direction in Figure 5.4(b) when compared to in Figure 5.4(a). Also noticeable, is the existence of weak second order spots arranged along the horizontal 2-fold axis in Figure 5.4(d). These spots reside at double the separation of the first order spots (half the separation in real-space,  $R_{H2} = 0.662 \pm 0.006$  nm). This is consistent with the appearance of small bright protrusions along the diamond edges at -0.8 V. They contribute to the alignment of features along the vertical 2-fold axis in real-space at half the separation of those aligned along this direction at +2.5 V.

Sets of  $\tau$ -scaled spots arranged along the 5-fold axes are also evident in both FFTs, as marked by green circles. They exhibit the same separations at both bias voltages. At -0.8 V, these spots appear to have increased intensity, which is consistent with the enhanced alignment observed along this direction in the corresponding real-space image. Sets of spots arranged along the 3-fold axes also appear in the -0.8 V FFT, as marked by pink circles. These were observed previously and will be discussed in more depth later [124]. Finally, yellow-circled spots arranged at  $45^\circ$  from the horizontal are observed in both FFTs. They exist at a smaller separation in the +2.5 V FFT when compared to the -0.8 V FFT. They will again be discussed later.

Zoomed in sections of the inverse of the filtered FFTs, taking into account all spots in Figure 5.4(c) and (d), are displayed in Figure 5.4(e) and (f), respectively. Diamond features exhibiting the same dimensions as those in Figure 5.4(a) and (b) display an enhanced nature in both. This confirms the observation of these motifs as a common feature throughout the STM data. One has been highlighted by a solid black diamond tile in Figure 5.4(e). The vertices of this tile are centred on large protrusions. The same tile has been superimposed on Figure 5.4(f). Vertices again reside on bright protrusions. However, in the -0.8 V inverse FFT, extra diamond features are visible. One is highlighted by a dashed black tile in Figure 5.4(f). This tile has the same size as the solid black tile, but is shifted along the 5-fold direction such that its vertices lie on protrusions residing on the edges of the solid black tile. Similar instances of this motif are observed throughout the -0.8 V inverse FFT.

Now, a possible explanation for the features observed by STM at each bias will be given by comparing with the *i*-Ag-In-Yb model. The model *i*-Ag-In-Yb plane used to describe the 2f-Ag-In-Yb surface is displayed in Figure 5.5(a). The high-symmetry directions are

marked and are the same for Figure 5.5(b-e). Different coloured circles correspond to different shells in the model Tsai-type cluster (blue: 1<sup>st</sup> shell Ag/In, purple: 2<sup>nd</sup> shell Ag/In, light green: 3<sup>rd</sup> shell Yb, light pink: 4<sup>th</sup> shell Ag/In, dark pink: 5<sup>th</sup> shell Ag/In and dark green: glue Yb). Diamond motifs, similar to those observed experimentally, can be seen throughout the model plane. A set of diamond tiles, displaying the same geometry and dimensions as those in Figure 5.4(f), have been superimposed on Figure 5.5(a). The vertices of the solid black tile reside at specific sites consisting of a square of four 3<sup>rd</sup> shell Yb atoms surrounding a 4<sup>th</sup> shell Ag/In dimer. The vertices of the dashed black tile reside at areas dominated by 1<sup>st</sup>, 2<sup>nd</sup> and 4<sup>th</sup> shell Ag/In sites.

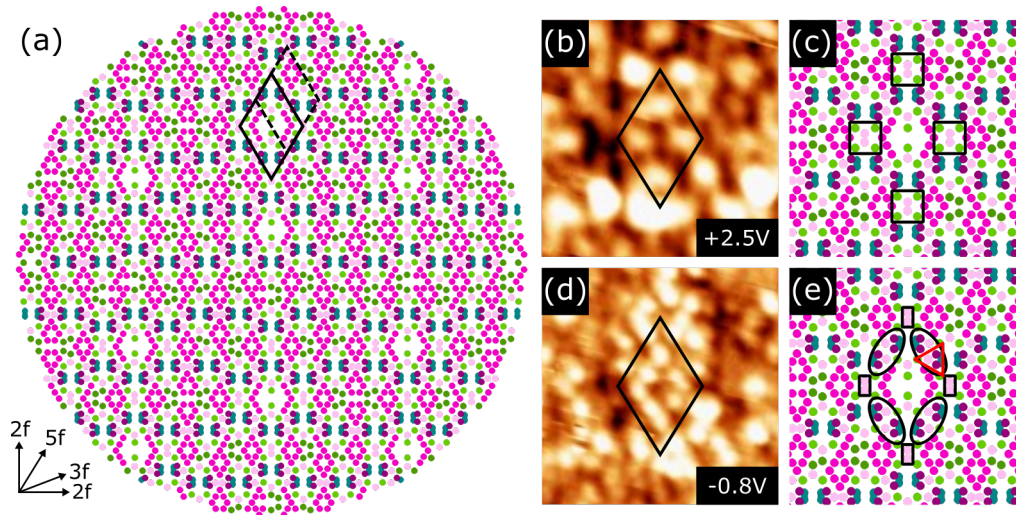


Figure 5.5: (a) Model *i*-Ag-In-Yb plane describing the 2f-Ag-In-Yb surface structure (20 nm  $\times$  20 nm). Different coloured circles represent different shells in the Tsai-type cluster (blue: 1<sup>st</sup> shell Ag/In, purple: 2<sup>nd</sup> shell Ag/In, light green: 3<sup>rd</sup> shell Yb, light pink: 4<sup>th</sup> shell Ag/In, dark pink: 5<sup>th</sup> shell Ag/In and dark green: glue Yb). Diamond tiles describing the arrangement of bright protrusions in STM data have been marked. The high-symmetry axes are marked at the bottom and are oriented the same for all figures. (b) and (d) Diamond features observed at +2.5 V and -0.8 V, respectively (12 nm  $\times$  12 nm, same as inset in Figure 5.4(a) and (b), respectively). (c) and (e) Model features corresponding to those in (b) and (e), respectively (7 nm  $\times$  7 nm).

In Figure 5.5(b-e), the two diamond motifs observed by STM on exactly the same area of the surface at each bias polarity (inset in Figure 5.4(a) and (b)) are compared directly to a diamond feature in the atomic model. The bright contrast areas forming diamond motifs in the STM images in Figure 5.5(b) and (d) are marked on the model

planes in Figure 5.5(c) and (e), respectively. Given this comparison, it is suggested that, at high positive bias, Yb contribution dominates STM contrast. This results in the large protrusions observed by STM, which correspond to contribution from four Yb atoms (i.e. the Yb rich sites at the vertices of solid black tile in Figure 5.5(a), marked by a square in Figure 5.5(c)). At negative bias, contribution from Ag/In sites is enhanced. In particular, correspondence of STM features with 2<sup>nd</sup> and 4<sup>th</sup> shell model sites is apparent. The close spacing of these sites along the 5-fold direction results in the extra diamond motifs (i.e. the dashed black tiles) observed by STM. Note here, however, elongated protrusions along the diamond edges in Figure 5.5(d) are not observed, as would be expected if all the 2<sup>nd</sup> and 4<sup>th</sup> shell Ag/In atoms marked within ovals in Figure 5.5(e) were resolved equally. It is suggested, then, that only a subset of these atoms are resolved. Indeed, the ‘mid-edge’ protrusion towards the top-right of the diamond in Figure 5.5(d) seems to reside closer to the right hand side vertex protrusion rather than the top vertex of the diamond. This perhaps suggests correspondence with the 2<sup>nd</sup> and 4<sup>th</sup> shell sites marked by a red triangle in Figure 5.5(e). The same can not be said for the other mid-edge protrusions, however, which indicate correspondence with a different combination of 2<sup>nd</sup> and 4<sup>th</sup> shell sites within the oval. This inhomogeneity in the STM data will be discussed in more depth later. Note here, as in Section 2.6, that the 1<sup>st</sup> shell exhibits a dynamic nature, changing orientation within the bulk Tsai-type cluster [49, 133]. As such, it is often excluded from surface models. It is suggested that contribution to STM contrast from 1<sup>st</sup> shell Ag/In sites at -0.8 V is unlikely here, although observation of a time-averaged position can not be ruled out.

This assignment of STM features is further backed up by considering the FFTs discussed earlier (Figure 5.4(c) and (d)). Figure 5.6(a) and (b) show the same model plane as in Figure 5.5(a) considering only Yb sites and 2<sup>nd</sup> and 4<sup>th</sup> shell Ag/In sites, respectively. The four Yb atom squares, believed to contribute to the large bright protrusions observed at +2.5 V, have been marked in Figure 5.6(a). First of all, the existence of a smaller separation between vertical rows of high atomic density is apparent for the 2<sup>nd</sup> and 4<sup>th</sup> shell Ag/In model plane when compared to the Yb plane. The corresponding row separations have been marked on both Figure 5.6(a) and (b), where that for the Ag/In plane is approximately half that for the Yb plane. This is in accordance with the appearance of second order spots at double the separation along the horizontal 2-fold axis in the -0.8 V FFT. Indeed, the model row separations marked are consistent with those calculated from the FFTs. Also clearly noticeable is a more pronounced alignment of 2<sup>nd</sup> and 4<sup>th</sup> shell Ag/In sites along

the 5-fold axes when compared to Yb sites, as marked in Figure 5.6(b). This explains the increased intensity of spots arranged along the 5-fold direction in the -0.8 V FFT. Spots aligned along the 3-fold axes, which are visible in the -0.8 V FFT but not the +2.5 V FFT, can also be explained by a more pronounced alignment of 2<sup>nd</sup> and 4<sup>th</sup> shell model features along this direction. Examples have been highlighted in Figure 5.6(b). Finally, considering features aligned at an angle 45°, it can be seen that very small separations are observed for 2<sup>nd</sup> shell Ag/In sites, shown inset in Figure 5.6(b). For Yb sites, much larger separations are apparent, as marked on Figure 5.6(a). This is perhaps the reason for the smaller separation between yellow-circled spots in the +2.5 V FFT, thus corresponding to a larger separation in real-space. One FFT feature that can not be explained by consideration of the model planes in Figure 5.6 is the weakening of spots arranged along the vertical 2-fold direction in the -0.8 V FFT. Alignment of 2<sup>nd</sup> and 4<sup>th</sup> shell Ag/In sites appears prominent along both 2-fold axes in Figure 5.6(b). A possible reason for this will be discussed later.

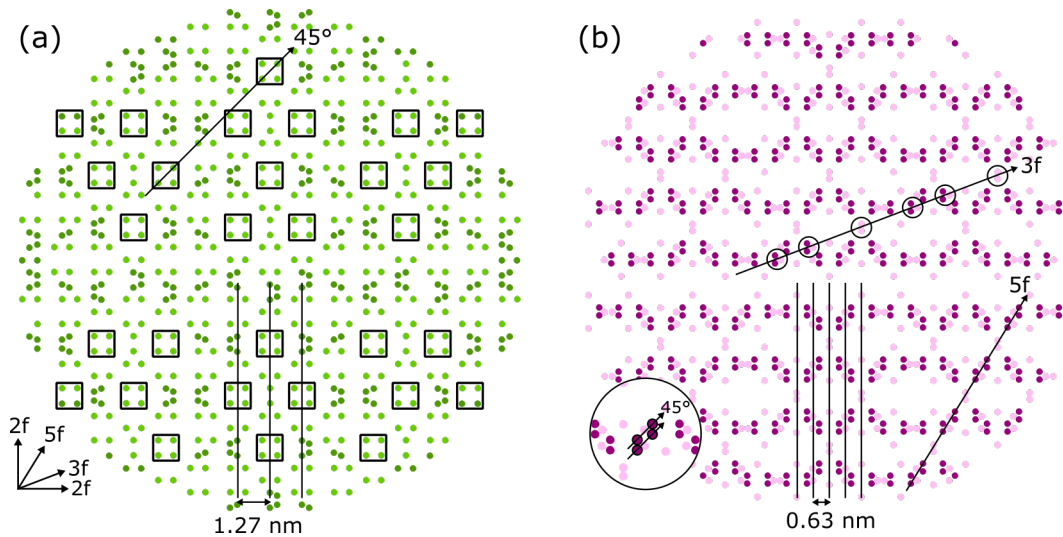


Figure 5.6: (a) and (b) Model 2f-Ag-In-Yb planes ( $20 \text{ nm} \times 20 \text{ nm}$ ) considering only Yb sites and 2<sup>nd</sup> and 4<sup>th</sup> shell Ag/In sites, respectively. Colour coding is the same as in Figure 5.5. Four Yb atom squares corresponding to the large bright protrusions observed by STM have been marked in (a). Rows of high atomic density have been marked in both (a) and (b), with the corresponding row separations given. Alignment of model features along different directions have been marked in both (a) and (b).

Given this observation of bias-dependency and the suggested assignment of model features at each bias, similarities to the 5-fold surface are clear; Yb atoms are resolved at

higher positive bias voltage, while at negative bias voltage, Ag/In atoms are resolved [71]. For the 5-fold surface, this was explained with regards to electronic structure calculations, as mentioned in Section 3.2. Theoretical calculations for the 1/1 approximants to the *i*-Cd-Yb and the *i*-Ag-In-Yb QCs indicate that unoccupied states above the Fermi level are dominated by Yb. Closer to the Fermi level, contribution from Yb states decreases, becoming comparable to that from Ag/In states. Just below the Fermi level, contribution from Ag/In states is enhanced. This supports the suggestion that the large bright protrusions observed by STM at positive bias correspond to Yb contribution, while at negative bias, contribution from Ag/In sites is observed [75, 76].

We now discuss a potential reason for the non-uniform nature of features observed by STM. Comparing the STM data in Figure 5.4(a) and (b) and the related model planes in Figure 5.6(a) and (b), respectively, it is clear that not all features of the model planes are resolved by STM. This is particularly true in the -0.8 V STM image, where small bright protrusions seem to be distributed relatively inhomogeneously in comparison to the model plane considering 2<sup>nd</sup> and 4<sup>th</sup> shell Ag/In sites. This can be explained by considering the chemical disorder of Ag and In atoms in the *i*-Ag-In-Yb model. As discussed in Section 2.8, it is known that the 2<sup>nd</sup> shell contains approximately 60% Ag and 40% In and the 4<sup>th</sup> shell consists of 20% Ag and 80% In [61]. However, the exact atomic sites which Ag and In occupy within each shell is not known. It is plausible that their arrangement could induce the observed inhomogeneity in STM data. This could be further amplified by a bias-dependency associated with Ag and In atoms say, for example, if only In atoms were resolved, as is suggested in reference [124] for low positive bias data. Such a bias-dependency associated with Ag and In would also explain why 5<sup>th</sup> shell features were not observed in this data, where an occupancy of 78% Ag and 22% In is expected for the 5<sup>th</sup> shell. Indeed, previous theoretical calculations for a 1/1 approximant to the *i*-Ag-In-Ca QC, again isostructural to the *i*-Ag-In-Yb QC, showed that In sites dominate STM resolution at negative bias. Ag sites do not contribute and, in fact, Ag surface atoms intrude into the bulk [134]. It should be noted, however, that features of the STM images simulated in this report do not match up directly with the experimental observations here. In fact, it is In atoms from the 5<sup>th</sup> shell which produce the bright contrast in these calculations.

Another contributor to the complexity of this STM data is the high atomic density of the 2-fold surface plane. It contains atoms from all shells of the Tsai-type model clusters, unlike the 3-fold and 5-fold surfaces which only contain Yb and 4<sup>th</sup> shell atoms. For the

2-fold surface, specific features observed at high positive bias and negative bias have been assigned to Yb and 2<sup>nd</sup> and 4<sup>th</sup> shell Ag/In model sites in particular here. Contribution from atoms of other shells at both bias polarities, however, is still feasible. This makes the assignment of all features observed by STM a complex task, where the combination of a large number of atoms of different species and local geometries can result in irregular variations in the LDOS. This is, perhaps, the reason for the less pronounced alignment of features along the horizontal 2-fold direction and the corresponding weakening of FFT spots along the vertical 2-fold direction at -0.8 V (see Figure 5.4(b) and (d), respectively).

Finally, it is noted that the data presented here indicates similarities and differences in comparison to previous reports. The differences are assigned to the condition of the STM tip and the larger range of tunnelling parameters explored here.

### 5.3.2 5f-Ag-In-Yb atomic motion

As with the 2f-Ag-In-Yb surface, preparing the 5f-Ag-In-Yb surface using the procedure described in Section 5.2 resulted in a clean, well-ordered surface, consistent with previous reports [71,72]. Figure 5.7(a) and (b) show a LEED pattern from the surface after sputter-annealing cycles. Discrete diffraction maxima are evident.  $\tau$ -scaled distances between spots are observed, as marked in Figure 5.7(a). The projected 5-fold reciprocal basis vectors of an icosahedron (see Section 2.2.3) have been overlaid on the pattern in Figure 5.7(b). This confirms the quasicrystalline 5-fold symmetry and long-range order of the surface.

To assess atomic motion, multiple STM scans were taken from the same area of the surface, maintaining the same scanning parameters between each, as outlined in Section 4.3.2. Bias voltages ranging from +2.5 V to -2.5 V were investigated. However, attaining multiple scans at positive bias proved difficult, where tip changes would often occur. A set of seven scans taken at  $V_b = -0.8$  V,  $I_t = 0.08$  nA and scan speed =  $617$  nm s<sup>-1</sup> (corresponding to  $\sim 130$  seconds between each scan) will be presented here. As already discussed, 4<sup>th</sup> shell Ag/In atoms are resolved at this bias voltage on the 5f-Ag-In-Yb surface. It is noted again here that the 5f-Ag-In-Yb surface is terminated at high density CC planes consisting of 3<sup>rd</sup> shell Yb, 4<sup>th</sup> shell Ag/In and glue Yb atoms.

Firstly, the reader is referred to Supporting Figure 5.1 for a video in which each consecutive frame is one of the seven successive STM scans taken from exactly the same area of the surface. The scan number is shown at the top-left of the video. The area of each scan is  $46$  nm  $\times$   $46$  nm. Large protrusions arranged in a pentagonal fashion are observed,

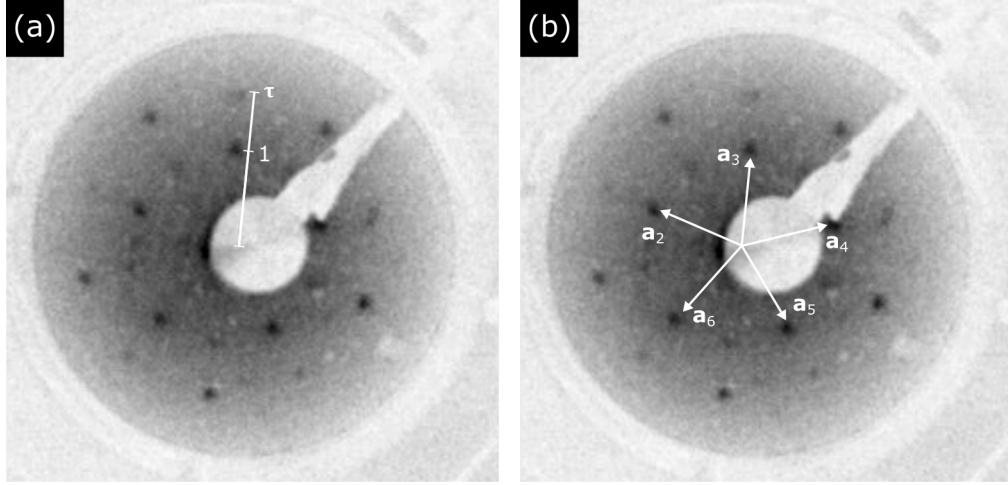


Figure 5.7: LEED pattern (15 eV) from the 5f-Ag-In-Yb surface.  $\tau$ -scaled separations between spots have been marked on (a). The projected 5-fold icosahedral reciprocal basis vectors have been marked on (b).

where one such arrangement has been marked by a pentagon. The average edge-length of these pentagonal features is  $2.53 \pm 0.05$  nm. These large protrusions remain unaltered and ‘stationary’ between successive scans. From previous reports, it is known that they correspond to rings of ten 4<sup>th</sup> shell Ag/In atoms surrounding CC sites (see Section 3.2, Figure 3.3) [71,72]. Laterally smaller protrusions can also be seen, however, appearing and disappearing at points closely surrounding the larger protrusions as the video progresses. Their average diameter, estimated from the full width at half maxima (FWHM) of height profiles ( $= 1.03 \pm 0.03$  nm), is  $\sim 32\%$  smaller than that of the large protrusions. This suggests they are composed of one atom, or small number of atoms less than the ten making up the large, stationary protrusions. Unless, of course, their apparent size is related to some variation in the LDOS. As these images are taken at negative bias, it is proposed these smaller, dynamic protrusions are Ag/In atoms. Their average apparent height is just  $0.22 \pm 0.06$  Å above that of the large, stationary protrusions, where the apparent root mean square roughness of the surface is  $0.188 \pm 0.005$  Å. This indicates that the moving species most likely consist of atoms embedded in the surface layer, as opposed to adatoms above the surface, where a larger height difference would be expected if the latter were true. This is, again, assuming the apparent height differences measured by STM correspond to physical surface topography, rather than some electronic effect. Such small protrusions have

been reported previously for this surface, where their arrangements observed by STM at negative bias voltage were assigned to concentrations in the LDOS at specific sites caused by the unknown distribution of Ag and In in the ring of 4<sup>th</sup> shell Ag/In atoms. Movement was not studied in this report [72]. One other thing to note here, is that a reasonably large amount of motion is apparent between each scan. This would suggest that the diffusing species exhibit a relatively high mobility, regardless of any potential tip induced effects.

Figure 5.8(a-e) show the first five individual scans from the area marked by a black square in Supporting Figure 5.1. The first five have been chosen as the dynamic nature of the smaller protrusions is most apparent in these scans. Areas where movement is observed between successive scans have been marked by different types of circles. Solid white circles highlight protrusions which disappear in the subsequent frame, while dashed white circles indicate the corresponding empty site in the subsequent frame. Dashed black circles show empty sites which are filled in the subsequent frame and solid black circles highlight the corresponding filled site in this subsequent frame. Semi-circles indicate areas where movement observations are made at the same site between successive frames. Take, for instance, the empty site marked by a dashed black circle at the left hand side of Figure 5.8(a). A protrusion appears at this site in Figure 5.8(b) and then disappears/reappears multiple times in consecutive frames up to Figure 5.8(e).

The disappearance and subsequent appearance of protrusions at closely spaced sites in consecutive frames perhaps indicates the existence of small-scale ‘jumps’ of the same group of atoms from one site to the next. See, for example, the sites marked by an arrow in Figure 5.8(d) and (e). Given the time elapsed between subsequent STM scans, however, it is likely that multiple such jumps occur between each successive scan resulting in the observation of larger scale ‘jumps’. This would explain the somewhat random appearance of some protrusions, for which a corresponding disappearance in the same local area in the previous scan is not apparent. Regardless of this, a subset of closely-spaced sites in which surface atoms diffuse are evident. In fact, measuring common smaller spaced separations between sites where movement is observed reveals the existence of  $\tau$ -scaled distances between sites. The largest separation ( $2.48 \pm 0.09$  nm) is consistent with the edge-length of the pentagonal arrangements of the large, stationary protrusions.  $\tau$ -deflated ( $1.57 \pm 0.04$  nm) and  $\tau^2$ -deflated ( $0.96 \pm 0.05$  nm) separations are also common. Further to this, these separations appear most often along the high-symmetry directions of the surface, with the most common orientations being  $72 \pm 2^\circ$  and  $35 \pm 1^\circ$  from the horizontal (high-symmetry axes occur at multiples of  $36^\circ$ ). This indicates a set of ordered sites

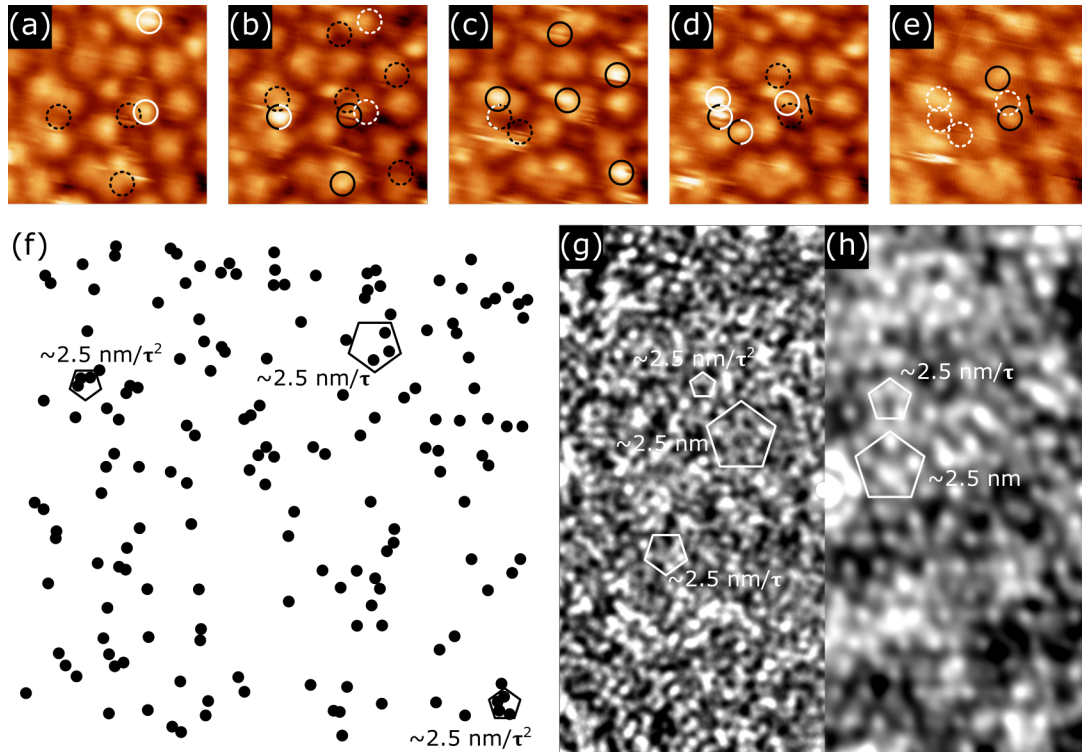


Figure 5.8: (a-e) Successive STM scans ( $12 \text{ nm} \times 12 \text{ nm}$ ,  $V_b = -0.8 \text{ V}$ ,  $I_t = 0.08 \text{ nA}$ ) taken from the same area of the  $5f$ -Ag-In-Yb surface (marked by a square in Supporting Figure 5.1). The time between scans is  $\sim 130 \text{ s}$ . Different circles mark areas where movement is observed: solid white circles indicate a protrusion which disappears in the subsequent frame, dashed white circles show the empty site in this subsequent frame, dashed black circles highlight empty sites which are filled in the subsequent frame and solid black circles mark the filled site. Semi-circles indicate areas where a protrusion appears/disappears at the same site between multiple consecutive frames. (f) A map ( $46 \text{ nm} \times 46 \text{ nm}$ ) of all sites where movement is observed between the seven successive scans in Supporting Figure 5.1. (g) Autocorrelation ( $23 \text{ nm} \times 46 \text{ nm}$ ) of the map in (f). (h) Autocorrelation ( $23 \text{ nm} \times 46 \text{ nm}$ ) of the STM image in the first frame of Supporting Figure 5.1.  $\sim 2.5 \text{ nm}$  edge-length pentagons,  $\tau$ -deflated versions and  $\tau^2$ -deflated versions have been marked in (f-h).

reflecting the surface symmetry.

This is backed up by considering the map composed of all sites where movement is observed across the seven successive STM scans in Supporting Figure 5.1, which is shown in Figure 5.8(f). Each spot here represents a position where a protrusion was observed to appear or disappear between consecutive scans. Marked on Figure 5.8(f) are pentag-

onally arranged features exhibiting  $\tau$ -scaled edge-lengths consistent with the separations discussed above. Taking an autocorrelation of the movement map emphasises these features, where  $\tau$ -scaled pentagonal motifs are again evident, as shown in Figure 5.8(g). For comparison, an autocorrelation of the STM image in the first frame of Supporting Figure 5.1 is displayed in Figure 5.8(h).  $\tau$ -scaled pentagonal features with the same edge-lengths have been marked. The smallest pentagon is not observed in Figure 5.8(h). All of these observations suggest that movement is observed at a subset of sites with quasicrystalline order and 5-fold symmetry, consistent with the overall surface structure. Some potential reasons for the observed movement will be considered below.

### **‘Simple’ surface diffusion**

Firstly, we will discuss the potential for a ‘simple’ surface diffusion mechanism. It is reiterated here, that the low apparent height of the small protrusions which appear/disappear between successive STM scans suggests they are composed of atoms embedded within the surface layer. As such, the movement observed is different from the typical diffusion of adatoms deposited on simple periodic surfaces and on other QC surfaces, where larger heights for moving species are evident [93, 125–130]. Another interesting aspect of this movement in comparison to previous surface diffusion studies is the lack of step edge decoration or aggregation of these moving species into clusters or islands. As discussed in Section 3.1, such processes typically occur at the surface in order to maximise bonds and thus minimise the overall energy of the system, as predicted by the TSK model [66, 67]. Moreover, such processes generally take place on rapid time-scales as a sample cools from its annealing temperature. Once the sample reaches room temperature and an STM investigation is began, only the end result (i.e. decorated step edges, islands etc.) would be observed. This rules out the possibility of one of these processes being under way on the 5f-Ag-In-Yb surface during the study.

Instead, the movement of atoms across a set of seemingly equipotential sites is observed by STM. One possible explanation for this is a particle-assisted diffusion mechanism, like the vacancy-mediated diffusion discussed in the introduction to this chapter for the Ge(111) $c(2\times 8)$  surface and for In atoms embedded in a Cu(001) surface [131, 132]. The low concentration of vacancies and their relatively slow diffusion rate in the Ge(111) $c(2\times 8)$  system seems counter to observations on the 5f-Ag-In-Yb surface, however, where a relatively large amount protrusions appear/disappear between successive scans. This would

suggest either a higher concentration of vacancies or a faster diffusion rate, or both. The heterodiffusion of In atoms embedded in a Cu(001) surface bears more similarities to the 5f-Ag-In-Yb data. As discussed, larger scale separations between movement sites are observed between successive STM scans on the 5f-Ag-In-Yb surface. These most likely result from multiple smaller ‘jumps’ of dynamic species during the time elapsed between scans. This is akin to the observations in the In/Cu(001) system. Simultaneous movement of closely spaced protrusions is also evident. See, for example, Figure 5.8(d-e), where the disappearance of three closely spaced protrusions occurs. This might suggest the observed motion arises due to the interaction of a low concentration of rapidly diffusing surface vacancies or adatoms (not resolved by STM) with other atoms embedded in the surface layer (resolved as small, bright protrusions by STM).

Another plausible explanation for this movement is the diffusion of adatoms across a subset of equipotential interstitial sites, like that discussed for the 5f-Al-Pd-Mn surface in the introduction to this chapter [93]. Indeed, previous metal adsorption investigations on this surface indicate adsorption of a first layer of atoms at the interstices between the inner 4<sup>th</sup> shell Ag/In and outer 3<sup>rd</sup> shell Yb decagonal rings which surround CCs in the model atomic structure. This adsorption regime was discussed in Section 3.4 for Pb deposition on 5f-Ag-In-Yb (see Figure 3.8(b)) [78]. Similar results have been reported for the Bi/5f-Ag-In-Yb system [77]. Although no adsorbate movement was reported in these systems, a re-analysis of the datasets will be presented in Chapter 6 indicating adsorbate movement in both. Similar results will also be presented for other metal adsorbate layers on this surface. It should be noted here, that comparatively large apparent heights were evident for the adsorbate species in these studies, matching with unoccupied atomic sites above the truncated surface plane. The apparent heights observed by STM for the dynamic protrusions in this investigation are too small to indicate any correspondence with vacant atomic sites above the surface. Furthermore, the in-plane structures of the closest unoccupied planes above the surface do not match well with the distribution of movement sites observed in this study. Still, a similar set of interstices could provide a set of low energy ‘adsorption sites’ for diffusing surface adatoms to embed themselves into.

One important question considering the ‘simple’ surface diffusion mechanisms discussed so far is: where do these dynamic atomic species come from? One possible explanation is the segregation of bulk atomic material at the surface. Indeed, the chemical composition at the surfaces of many ternary QCs can differ from the expected bulk composition after sputter-annealing preparation cycles [135]. Sputtering can preferentially remove lighter el-

elements or those with lower surface free energy. Similarly, annealing can cause segregation and desorption of elements with lower surface free energy and weaker bonding. Medium energy ion scattering (MEIS) studies from the 5f-Ag-In-Yb surface, taken after employing the same sputter-annealing preparation conditions in this work, indicated a slightly off ideal surface composition. The concentration of Yb was higher than expected. The concentration of Ag and In could not be accurately determined due to their similar masses [136]. This could indicate the existence of segregation at this surface after the sputter-annealing preparation cycles

In these ‘simple’ surface diffusion cases, whether adatom/vacancy-assisted or involving movement across a set of interstices, a subset of movement sites reflecting the surface ordering and symmetry would be apparent. Indeed, this is observed on the 5f-Ag-In-Yb surface, as was discussed at the start of this section and shown in Figure 5.8(f-h). The sites where movement is observed also reside in close proximity to the large, stationary protrusions. Given these considerations, the movement observed by STM will now be compared directly to the model 5f-Ag-In-Yb surface structure. As discussed, the large, stationary protrusions reside at model CC sites, where each CC is surrounded by an inner decagon of 4<sup>th</sup> shell Ag/In atoms and an outer decagon of 3<sup>rd</sup> shell Yb atoms. Two models for the experimentally observed motion will be considered: 1. movement at 4<sup>th</sup> shell Ag/In sites in a vacancy-assisted diffusion mechanism and 2. movement at the interstices between 4<sup>th</sup> shell Ag/In and 3<sup>rd</sup> shell Yb decagonal rings (i.e. the adsorption sites observed Pb and Bi deposition on the 5f-Ag-In-Yb surface [77, 78]).

Figure 5.9(a) shows a zoomed in area of Figure 5.8(c), magnifying the pentagonal arrangement of large protrusions which is visible towards the centre. A 2.5 nm edge-length pentagon, with vertices residing at large protrusions, has been overlaid. The locations of all areas where a small protrusion appears or disappears across the seven successive STM scans in Supporting Figure 5.1 have been marked and numbered. Sites 1, 5 and 6 are filled in this image, while the others are empty (they are filled in previous or subsequent scans). The separations between closely spaced sites are shown in Table 5.1, where the site numbers are used to define the separation (i.e. 1→2 corresponds to the separation between site 1 and 2). The smallest angle to the horizontal between the two sites is also given in Table 5.1. It is noted here, that the large apparent errors for some of these measurements arise due to the relatively large size and close proximity of the protrusions which appear/disappear between successive STM scans.

In Figure 5.9(b), a section of the model 5f-Ag-In-Yb plane corresponding to the area

of the surface in the STM image in Figure 5.9(a) is shown, where the scale is the same between both. A pentagon of the same size as in Figure 5.9(a) has been overlaid where, as already discussed, vertices consist of 4<sup>th</sup> shell Ag/In and 3<sup>rd</sup> shell Yb decagonal rings surrounding CC sites. A set of model 4<sup>th</sup> shell Ag/In atomic sites have been marked in Figure 5.9(b) which display a similar geometry to the movement sites in Figure 5.9(a). They are numbered the same as in Figure 5.9(a). The corresponding model separations and angles are given in Table 5.1. This is model 1, where movement at these sites would suggest an adatom/vacancy-assisted diffusion mechanism in which atoms jump into vacant sites, therefore leaving vacancies at their original locations for other atoms to fill. Figure 5.9(c) shows the same model plane, where a set of interstitial sites with similar geometry to the movement sites in Figure 5.9(a) are shown. The corresponding distances and angles between closely spaced sites are again given in Table 5.1. This is model 2, where movement at these sites would suggest diffusion across a set of equipotential interstices.

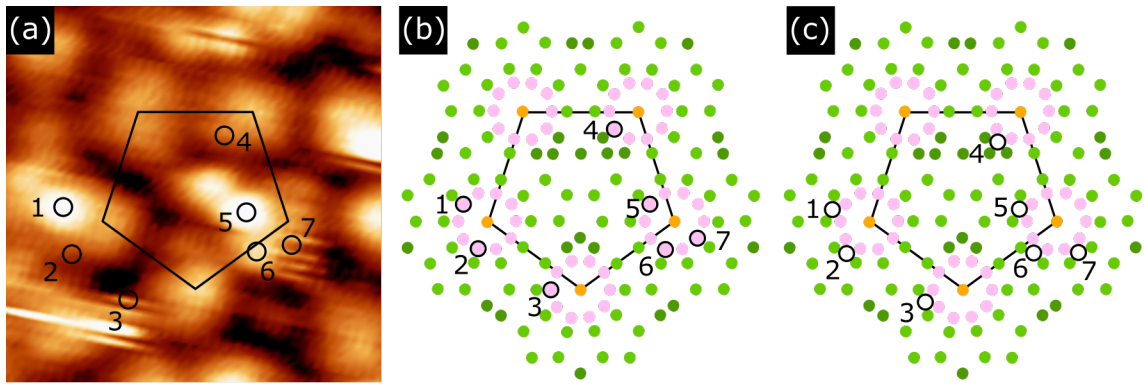


Figure 5.9: (a) STM image ( $8 \text{ nm} \times 8 \text{ nm}$ ,  $V_b = -0.8 \text{ V}$ ,  $I_t = 0.08 \text{ nA}$ ) taken from the 5f-Ag-In-Yb surface (magnified section of Figure 5.8(c)). Sites where movement is observed across the seven successive scans in Supporting Figure 5.1 are marked and numbered. Sites 1, 5 and 6 are filled in this image. (b) and (c) A section of atomic sites from the 5f-Ag-In-Yb surface model corresponding to the area of the surface in (a) (gold: CCs, light green: 3<sup>rd</sup> shell Yb, light pink: 4<sup>th</sup> shell Ag/In and dark green: glue Yb). The scale is the same as in (a). Atomic sites and interstitial sites with geometry similar to the movement sites marked in (a) have been marked in (b) and (c), respectively, and numbered accordingly. Small-scale separations and angles between sites are summarised in Table 5.1. 2.5 nm edge-length pentagons have been overlaid on all figures.

Comparing Figure 5.9(b) and (c), it can be seen that both models provide a very similar set of sites, with only a small shift between the sites in each. Comparing the experimental

No.	Separation (nm)			Angle (degrees)		
	STM	Model 1	Model 2	STM	Model 1	Model 2
1→2	$1.1 \pm 0.3$	1.0	1.0	$80 \pm 9$	72	72
2→3	$1.8 \pm 0.3$	1.8	2.1	$32 \pm 6$	28	30
4→5	$1.8 \pm 0.2$	1.8	1.6	$71 \pm 6$	65	72
5→6	$1.0 \pm 0.2$	1.0	1.0	$75 \pm 8$	72	72
6→7	$0.8 \pm 0.2$	0.8	1.0	$11 \pm 11$	18	0

Table 5.1: Distances and angles between numbered sites in Figure 5.9(a), (b) and (c). Angles are measured as the smallest angle from the horizontal direction.

and model measurements displayed in Table 5.1, it can be seen that both models provide a set of sites with dimensions consistent with STM observations. The atomic sites in the model 1 (Figure 5.9(b)) perhaps provide a better match, but uncertainties in the separations measured by STM make this speculative. The angles between movement sites in both models are again consistent with STM observations, where some model values seem to provide a slightly better match. For instance, model 2 (Figure 5.9(c)) provides an angle closer to that measured by STM for the 4→5 separation. Model 1 provides an angle closer to the STM value for the 6→7 separation. Uncertainties in the angles measured from the STM data again preclude a more in depth comparison. So, both theoretical models seem to provide a reasonable match to the experimental STM data. The close proximity of movement sites between each model, alongside the uncertainties inherent in the STM data, makes determining the likelihood of each model difficult.

### Phason-assisted motion

Another possible reason for the movement observed by STM on the 5f-Ag-In-Yb surface is a phason-assisted mechanism. For an overview of phasons, the reader is referred to Section 2.4. Here, it is noted that the phason flips intrinsic to QC structures are equivalent to a switch between two states separated by a small energy barrier (i.e. one which thermal excitations can overcome). These flips can percolate throughout a QC structure, resulting in macroscopic diffusion. The corresponding local atomic rearrangements and jumps associated with this phason disorder would occur at sites reflecting the symmetry of a QC structure, as is observed on the 5f-Ag-In-Yb surface. They would also take place independently of any conventional surface diffusion mechanism [137]. However, direct observations of such structural rearrangements are limited. So far, two examples have been reported in

TEM investigations of the *d*-Al-Cu-Co and the *d*-Al-Ni-Co systems at high temperatures, as discussed in Section 2.4 [44, 45]. Similar to these reports, *n*D analysis will be utilised here in order to assess the possibility of phason-assisted motion of atoms on the 5f-Ag-In-Yb surface. The Matlab programming software was used for this analysis and related calculations in this section. Code was developed in collaboration with Dr. Sam Coates.

The seven successive STM scans in Supporting Figure 5.1 are again used in the following analysis. The first step in this analysis involves ‘indexing’ the area of the surface imaged in these scans with respect to 6D space. As the large, stationary protrusions reside at model CC sites, it follows that they can be mapped by a CC plane arranged along the 5-fold direction in the *i*-Ag-In-Yb model. Such a mapping has been performed already on a small scale for the pentagonal arrangement of large protrusions in Figure 5.9. As discussed in Section 2.8, the *i*-Ag-In-Yb model structure was formed utilising *n*D analysis. Assuming the information for the projection from 6D space (see Section 2.3) which generates this model structure is known, mapping experimental CCs like this constitutes an indexing of the surface in 6D space; the coordinates of each model CC site in physical space will correspond to some specific coordinates in 6D space.

To perform the indexing for the area of the 5f-Ag-In-Yb surface scanned in this study, the positions of a set of large, stationary protrusions were extracted from the STM data in Supporting Figure 5.1. In Figure 5.10(a), the STM image in the first frame of Supporting Figure 5.1 is displayed, where a set of these positions have been marked by black crosses. The positions were then extracted and compared to a large set of 5f-Ag-In-Yb model CC planes. Model planes were generated via projection from a 6D hypercubic lattice (as outlined in Section 2.3) using an OD which generates only CC sites.  $55^6$  6D lattice points were used, corresponding to  $\sim 71\,000$  points in 3D par-space after projection of the points lying within the OD in perp-space. This provided a set of model CC positions large enough for comparison with the STM data. The comparison of experimentally extracted CC positions with model CCs was an iterative process, separately taking into account each individual model CC plane along the 5-fold direction and shifting it with respect to experimental map in order to find the best fit and therefore the model plane with the best match to the experimental data. In this process, two points were considered as ‘matching’ if they fell within 0.76 nm of each other (50% of the average FWHM of the large, stationary protrusions). In Figure 5.10(b), the model CC plane with the best fit to experimental data is shown. It exhibits a 77% match to the experimental data, given the conditions outlined above. It is a moderate density plane consisting of 2.5 nm edge-

length and  $\tau$ -deflated pentagonal arrangements ( $\sim 1.6$  nm edge-length), where examples of both have been marked on the figure. In Figure 5.10(c), the section of this model plane which matches well with the experimental data has been overlaid on the STM image from Figure 5.10(a). The experimentally extracted CC positions have again been marked by black crosses, showing where correspondence with the model sites occurs. As can be seen from Figure 5.10(c), the model CC plane does appear to have a higher density of the  $\tau$ -deflated CC separations in comparison to the experimentally extracted CC sites, which predominantly exhibit the 2.5 nm edge-length. However, although this  $\tau$ -deflated CC separation is a common feature in model planes, it is often not resolved by STM [72]. Further to this, taking a reverse FFT and autocorrelation from the STM image in Figure 5.10(a)/(c) reveals that this  $\tau$ -deflated edge-length is, in fact, a common feature in the experimental data, as can be seen inset bottom left and right, respectively, in Figure 5.10(c). This has been shown already in Figure 5.8(h) for the autocorrelation.

With the area of the surface imaged by STM adequately indexed in 6D space, the next step involves comparison of the movement observed across successive STM scans with a set of phason-related positions. As discussed in Section 2.4, phasons can be thought of as excitations in perp-space and thus can be modelled by fluctuations in the ODs which decorate each point in the  $n$ D lattice. Here, a projection of the 6D lattice points through an enlarged OD was employed to create a phason-related distribution corresponding to the model CC sites. The phason-related plane associated with the model CC plane exhibiting the best match to the experimental CC distribution, was then extracted. Figure 5.10(d) shows the phason-related model distribution generated using an OD enlarged to  $\times 1.6$  that used to create the model CC sites. Red circles indicate the new phason-related positions, with the original CC sites shown again as gold circles.  $\tau$ -scaled pentagonal arrangements are again marked. The smallest pentagon ( $\sim 1.0$  nm edge-length) is  $\tau^2$ -deflated in comparison to the 2.5 nm edge-length pentagons most commonly observed by STM and  $\tau$ -deflated compared to the smallest arrangement in the associated model CC distribution in Figure 5.10(b). In fact, the phason-related sites correspond directly to a  $\tau$ -deflated version of the corresponding model CC distribution. A patch of the Penrose P1 tiling, used to describe the 5f-Ag-In-Yb surface structure, has been overlaid the phason-related distribution in Figure 5.10(d) and enlarged inset. Dashed tiles indicate where a possible tiling rearrangement could occur, taking into account phason-related model sites. As discussed in Section 2.4, structural rearrangements like this correspond to the phason flips characteristic of QC structures.

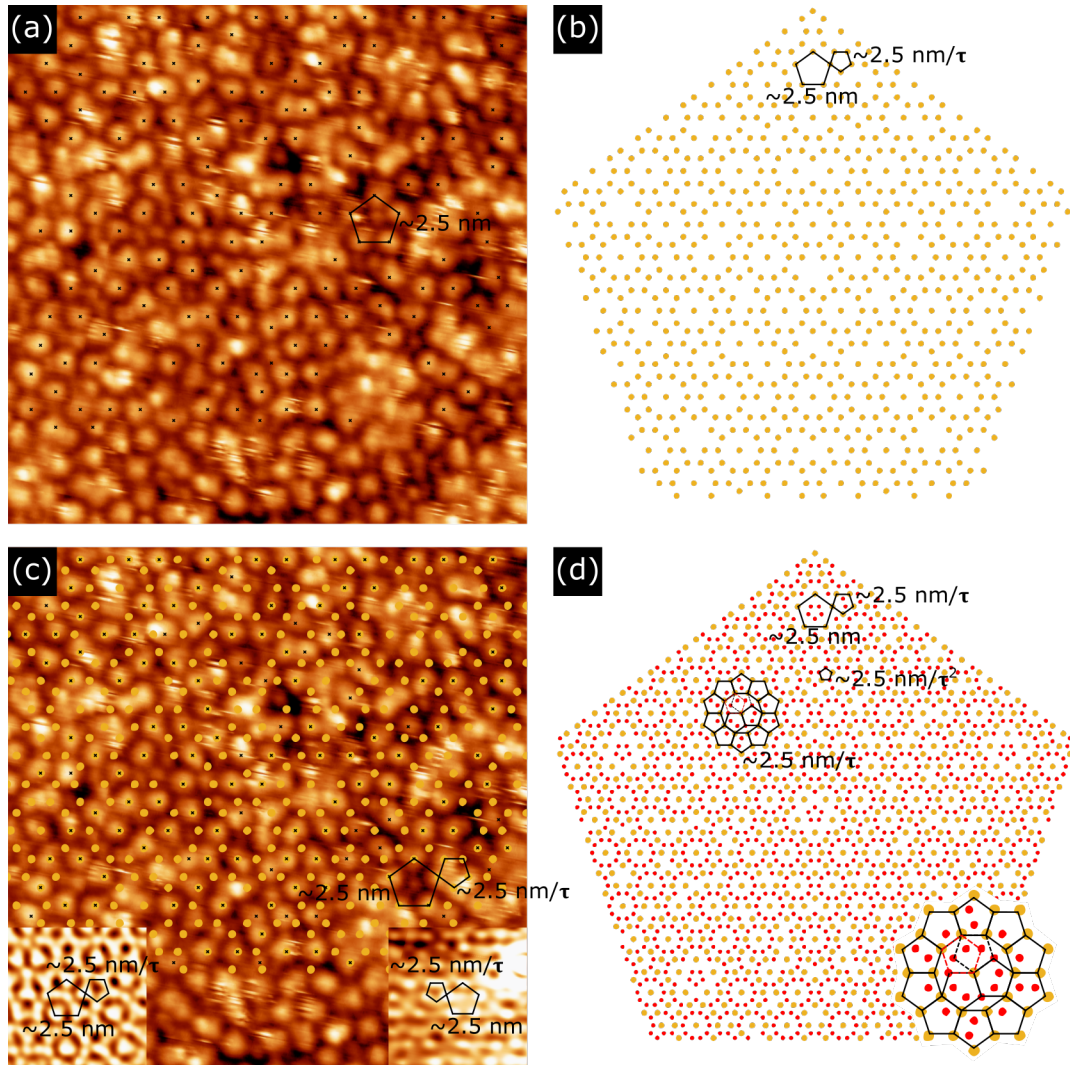


Figure 5.10: STM image ( $46 \text{ nm} \times 46 \text{ nm}$ ,  $V_b = -0.8 \text{ V}$ ,  $I_t = 0.08 \text{ nA}$ ) taken from the 5f-Ag-In-Yb surface (same as frame 1 in Supporting Figure 5.1). A set of large, stationary protrusions corresponding to an experimental CC distribution have been marked by black crosses. (b) The model 5-fold *i*-Ag-In-Yb CC plane ( $60 \text{ nm} \times 60 \text{ nm}$ ) with the best match to the experimentally extracted CC distribution from (a). (c) Same as (a) with a section of the matching model plane in (b) overlaid. Inset bottom left and right are the reverse FFT and autocorrelation of the STM image, respectively. (d) Model phason-related CC distribution ( $60 \text{ nm} \times 60 \text{ nm}$ ) associated with the CC distribution in (b). Additional phason-related sites are shown as red circles. A patch of the Penrose P1 tiling has been overlaid and enlarged inset. Dashed tiles indicate a possible tile flip considering phason-related positions.  $2.5 \text{ nm}$  edge-length pentagons,  $\tau$ -deflated versions and  $\tau^2$ -deflated versions are overlaid on all figures.

Before comparison of the phason-related model distribution with the movement observed by STM, it is noted that CC sites do not directly correspond to atomic positions. In fact, no atoms reside at the CCs. Similar groups of atoms do, however, occupy sites in close proximity to CCs, as already discussed. This leads to the large protrusions observed by STM at CC sites corresponding to 4<sup>th</sup> shell Ag/In atoms. It is reasonable to assume that the phason-related sites will display similar attributes. Therefore, if the movement of an atom or small group of atoms at the surface is phason-assisted, it would take place at locations in close proximity to the points of the phason-related distribution, even though the sites themselves are not directly occupied. It follows that the sites where movement is observed by STM can be directly compared to the phason-related model CC distribution to assess any connection with phasonic behaviour. Any correspondence between the experimental and theoretical sites would infer a phason-assisted motion.

To compare the movement observed by STM with the phason-related model plane in Figure 5.10(d), the movement map in Figure 5.8(f) was overlaid at the correct point on the plane. This is shown for an enlarged section of the model plane in Figure 5.11(a), where black circles correspond to movement map positions. As can be seen from the figure, many experimental movement sites coincide quite nicely with model sites. The overall match between the two distributions is 62%, where two points were considered as matching if they lay within 0.52 nm of each other (50% of the FWHM of the small protrusions which appear/disappear between successive STM scans). This is a reasonable match, suggesting plausibility for a phason-assisted motion mechanism. This is especially true considering the distortion effects associated with STM which could reduce the overall match. Figure 5.11(b) shows the perp-space profile of the matching experimental movement map and phason-related model plane positions. The circular window corresponds to the size of the original OD used to generate only model CC sites. ~50% of matching points reside outside of the original OD suggesting a reasonable amount of phason-related movement.

As in Figure 5.9, the movement observed by STM is now compared to phason-related model sites on a local scale. In Figure 5.12(a), Figure 5.9(a), which shows the movement observed by STM on a local scale, has been reproduced. In Figure 5.12(b), a section of the phason-related model plane coinciding with the area of the surface in the STM image in Figure 5.12(a) is shown. Model sites with a similar geometry to the movement sites observed by STM have again been marked and numbered, as in Figure 5.12(a). Two potential model positions have been highlighted for movement site 3. The separations and angles between sites are compared in Table 5.2. Good correspondence between theoretical

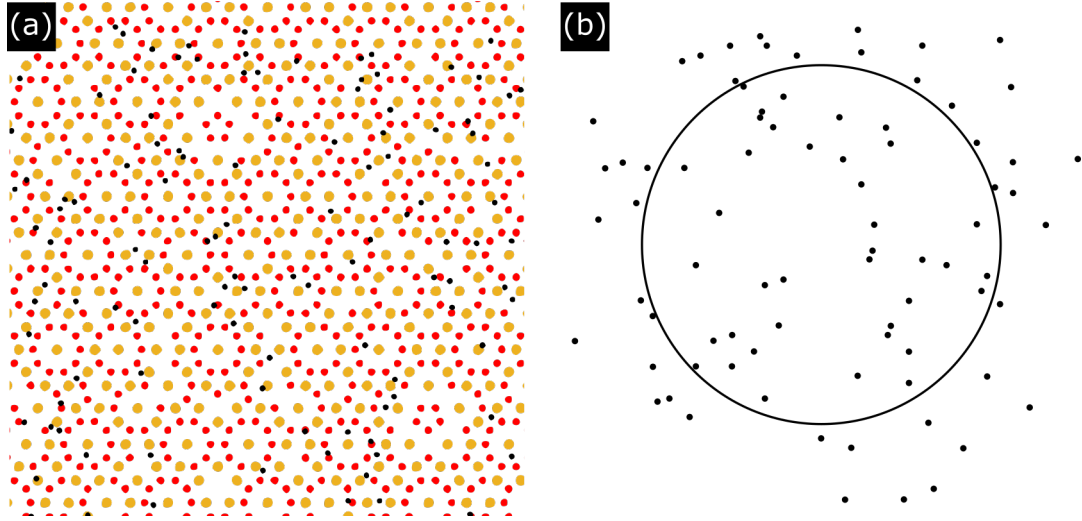


Figure 5.11: Enlarged version ( $35 \text{ nm} \times 35 \text{ nm}$ ) of the model phason-related plane in Figure 5.10(d). Experimental movement positions (black circles) are overlaid. (b) Per-space profile of the matching experimental movement sites and phason-related model sites. The large circle indicates the size of the original OD used to generate CC model sites only.

and experimental data is again observed. This is with the exception of site 3, where either the 2 $\rightarrow$ 3 site separation or angle is inconsistent, depending on which model site is chosen for movement site 3. Despite earlier discussion, the fact that atoms are not expected to reside exactly at the phason-related model sites could, perhaps, explain the inconsistency here.

No.	Separation (nm)		Angle (degrees)	
	STM	Phason	STM	Phason
1 $\rightarrow$ 2	$1.1 \pm 0.3$	1.0	$80 \pm 9$	72
2 $\rightarrow$ 3	$1.8 \pm 0.3$	1.8/2.5	$32 \pm 6$	18/36
4 $\rightarrow$ 5	$1.8 \pm 0.2$	1.6	$71 \pm 6$	72
5 $\rightarrow$ 6	$1.0 \pm 0.2$	1.0	$75 \pm 8$	72
6 $\rightarrow$ 7	$0.8 \pm 0.2$	1.0	$11 \pm 11$	0

Table 5.2: Distances and angles between numbered sites in Figure 5.12(a) and (b). Angles are measured as the smallest angle from the horizontal.

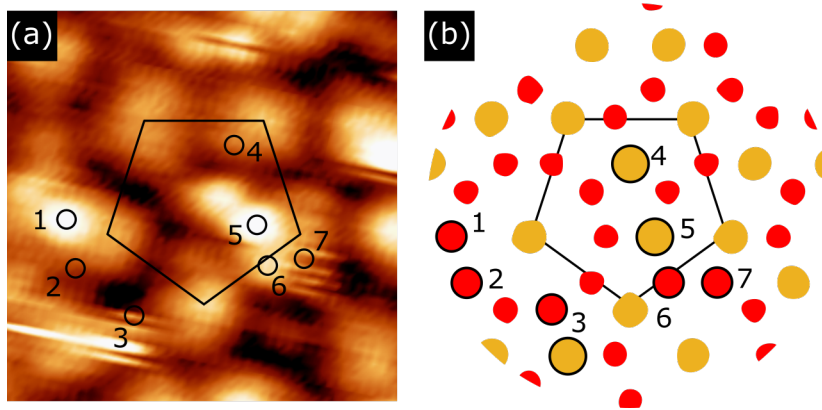


Figure 5.12: STM image ( $8 \text{ nm} \times 8 \text{ nm}$ ,  $V_b = -0.8 \text{ V}$ ,  $I_t = 0.08 \text{ nA}$ ) taken from the 5f-Ag-In-Yb surface (same as Figure 5.9(a)). (b) A section of the phason-related model CC distribution (gold: original CC sites and red: phason-related sites). The scale is the same as in (a). A set of sites with geometry similar to (a) have been marked in (b) and numbered accordingly. Two potential model sites are marked for 3. Small-scale separations and angles between sites are summarised in Table 5.2. A 2.5 nm edge-length pentagon has been overlaid in both figures.

### Comparison

A brief discussion and comparison of the three models proposed here to explain the movement observed by STM on the 5f-Ag-In-Yb surface at room temperature will now be given. From the analysis of movement sites on a local scale (see Figure 5.9 and 5.12 and Table 5.1 and 5.2, respectively), the vacancy model (model 1) seems to provide the best match with experimental data, while the phason-related model matches least closely. However, all models provide a reasonable match overall. In fact, each model consists of a very similar set of sites, displaying a  $\tau$ -deflated geometry in comparison to the 2.5 nm edge-length arrangements of large protrusions/CCs at the surface. Certainly, this is expected for the ‘simple’ surface diffusion models given the small length scales between individual atomic sites and interstices at the surface and the self-similarity inherent in QCs. Similarly, the additional positions gained in the phasonic expansion would, in fact, be expected to reside at a grid of quasicrystalline interstitial sites at the surface. This makes it hard to distinguish between each model and therefore determine their likelihood. One other thing to consider is that, despite the good match achieved via this direct comparison with model sites, the centres of the small protrusions observed to appear/disappear by STM do not

necessarily correspond to a singular atom at one of the proposed sites. They could actually represent an averaging of the LDOS across a small group of atoms at a set of closely spaced sites, much like the large, stationary protrusions corresponding to rings of 4<sup>th</sup> shell Ag/In atoms. Indeed, this is what would be expected in the phason-related model, where small groups atoms would reside in a similar arrangement around each phason-related site.

Regardless of the specific mechanism, a possible reason for the movement could be the low Debye temperature ( $\Theta_D$ ) of the *i*-Ag-In-Yb QC. The mean square displacement of atoms under thermal motion above 100 K ( $\langle(\Delta \vec{r})^2\rangle$ ) is related to the  $\Theta_D$  by the following approximate proportionality (assuming constant mass) [138]:

$$\langle(\Delta \vec{r})^2\rangle \propto \frac{T}{\Theta_D^2} \quad (5.1)$$

where  $T$  is the temperature of the material. From this, it can be seen that decreasing  $\Theta_D$  will increase  $\langle(\Delta \vec{r})^2\rangle$ . As such, lower temperatures will be required for the thermal motion of atoms in a material exhibiting a low Debye temperature. Although there is no value for  $\Theta_D$  for *i*-Ag-In-Yb in the literature, it is reasonable to assume it is similar to the closely-related *i*-Cd-Yb QC, in which  $\Theta_D = 140$  K [139,140]. Comparing this to the value for the *d*-Al-Ni-Co QC,  $\Theta_D = 549$  K [138], it can be seen that larger temperatures would be required to induce a similar amount of thermal motion in *d*-Al-Ni-Co as for *i*-Ag-In-Yb at room temperature. This increased diffusivity could result in segregation on the 5f-Ag-In-Yb surface at room temperature, thus explaining the nature of the moving species if a simple diffusion mechanism was apparent. Alternatively, this increased diffusivity could also explain the potential observation of phason-assisted motion at room temperature, where previous direct observations in dQCs required the use of higher temperatures.

Finally, although not presented here, further analysis has indicated similar atomic motion on the 2f-Ag-In-Yb surface and on the surfaces of related 1/1 approximant structures (Ag-In-Yb, Ag-In-Gd and Ag-In-Tb) by STM. This suggests this is inherent to this system. Although movement at positive bias, hence probing Yb atoms, was not investigated here, data from the 2f-Ag-In-Yb surface indicates increased motion at negative bias. This would suggest a relation to Ag/In atoms, in particular.

## 5.4 Summary

In this chapter, a previously unobserved bias-dependency of STM contrast on the 2f-Ag-In-Yb surface was assessed. Features resolved at high positive bias voltage were assigned to contribution from Yb atoms. Negative bias data indicated contribution from Ag/In atoms, in particular, those of the 2<sup>nd</sup> and 4<sup>th</sup> shells of the Tsai-type building blocks which make up the structure. This is similar to the bias-dependency observed on the 5f-Ag-In-Yb surface and is consistent with previous theoretical density of states calculations for related 1/1 approximant structures [71, 75, 76]. Inhomogeneity in the STM data was assigned to chemical disorder at the Ag/In sites. It was suggested that the structural distribution of Ag and In in the 2<sup>nd</sup> and 4<sup>th</sup> shells (which is unknown) contributed to the observed inhomogeneity. This was perhaps amplified by a bias-dependency associated with the two elements. Further work in the form of DFT calculations would be useful to confirm these experimental observations.

Also presented in this chapter, was STM data indicating the motion of atoms at room temperature on the clean 5f-Ag-In-Yb surface. The data here was taken at negative bias voltage, suggesting moving species were composed of Ag/In atoms. Movement was observed at a set of well-ordered sites reflecting the quasicrystalline 5-fold symmetry of the surface. Three different mechanisms were proposed for explanation of the observed motion. The first two involved ‘simple’ surface diffusion of atoms across vacant atomic sites or interstitial sites at the surface. The third was a phason-assisted mechanism. All proposed mechanisms seem to provide a good fit with experimental data making it hard to rule in favour of any.

Successive scans with enhanced resolution, like the atomic resolution observable at positive bias (see Figure 3.2(e) in Chapter 2), could detail the observed motion more intricately. Larger datasets (i.e. more scans on the same area) would also be useful in order to get a better statistical picture of the observed motion and the locations where movement is observed. This would mean the specific locations of movement could be determined with more accuracy, helping to rule in favour of one of the three proposed mechanisms. As mentioned, however, tip changes often occur when scanning at positive bias, making the attainment of multiple scans with these conditions difficult. Also, compensating for tip changes and STM distortion effects such as drift becomes more difficult as scan numbers become larger. Variable temperature STM studies could be useful in this sense, where low temperature experiments would decrease thermal motion at the surface, reducing the chance of any tip-surface interaction. Low temperature investigations could also provide

further information regarding smaller-scale atomic jumps, where less movement would be apparent between each successive scan. Not only this, if the movement is indeed phason induced, variable temperature studies could advance our understanding of the growth of QCs and the role of energetic and entropic stabilisation (see Section 2.7). Finally, gaining a better understanding of the chemical composition at the surface, specifically the make-up of the species which diffuse, would be useful to provide further insight into the movement. STS investigations at lower temperatures could help identify these species. Assessing surface composition as a function of temperature using XPS could complement this and help to reveal information on any surface segregation. Accompanying DFT calculations would provide further evidence to supplement each of these areas of exploration.

## Chapter 6

# Metal adsorbate motion and Ag growth on the fivefold surface of *i*-Ag-In-Yb

In this chapter, metal adsorption on the 5f-Ag-In-Yb surface will be investigated. First, some STM datasets from previous studies will be re-analysed to assess adsorbate movement on this surface at room temperature. After this, results from a new adsorption investigation involving Ag deposition on the 5f-Ag-In-Yb surface will be presented. STM data will be used to analyse the structure of the Ag overlayer and to assess any adsorbate motion from the low to high coverage regimes.

### 6.1 Introduction

For an introduction to the *i*-Ag-In-Yb QC and its 5-fold surface, the reader is referred to Section 2.8 and 3.2, respectively and to the second set of results presented in Chapter 5 (Section 5.3.2). An overview of a range of relevant metal adsorption investigations on QC surfaces has also been given in Chapter 3. It was shown that pseudomorphic overlayers of different metal adsorbates have been grown on a range of QC surfaces. Such studies have revealed information on the structure and reactivity at the surfaces of these QCs. The reduced chemical complexity associated with single-element overlayer structures also gives rise to systems which are ideal for the study of aperiodic order.

As discussed in Section 3.4, the 5f-Ag-In-Yb surface was the first substrate for which

3D growth of a quasicrystalline single element metal overlayer was reported [78]. Both Pb and Bi have been observed to follow this growth mode on the 5-fold surface, where adsorbate atoms occupy vacant sites above the surface plane across multiple layers [77]. Pseudomorphic quasicrystalline overlayers of Sb and In have also been reported [141,142]. Other metal adsorption investigations on this surface include Cu deposition [143]. In this system, order was less apparent, where Cu adatoms were observed by STM to cluster together upon deposition. FFTs still, however, revealed quasicrystalline ordering of clusters at intermediate coverages. Increasing the coverage of Cu enlarged the size and spread in sizes of clusters both laterally and vertically, eventually resulting in a disordered overlayer structure. At the start of this chapter, datasets from the Pb/5f-Ag-In-Yb system will be briefly revisited in order to evaluate adsorbate movement. It will be seen that adsorbate atoms diffuse across their previously determined adsorption sites. Comparisons with the motion observed in the underlying clean substrate will be given.

Movement of adsorbate atoms like this has been observed previously by STM for the early stages of Pb growth on the 5f-Al-Pd-Mn surface [130]. In this system, successive scans from the same area of the surface revealed movement of Pb adatoms across specific truncated CC sites. This movement was ascribed to the high mobility of Pb adatoms on the surface, as well as induced motion from the STM tip. Upon further deposition of Pb, pentagonally arranged adsorbate structures were resolved, akin to the ‘starfish’ arrangements observed for Al growth on 5f-Al-Cu-Fe [93] (see Section 3.4). At these slightly higher coverages, the mobility of Pb adatoms is reduced, suggesting adsorbate-adsorbate interaction is key in stabilising the nucleation of Pb ‘starfish’ clusters. Upon further Pb deposition, these clusters coalesce into a quasicrystalline ML. However, once the ML forms, a dramatic decrease in sticking coefficient becomes apparent and either no further Pb is adsorbed or large 3D Pb clusters form which are not observed experimentally [144].

Also presented here, is new data from an investigation of Ag adsorption on the 5f-Ag-In-Yb surface. Ag deposition has been attempted previously on a range of QC substrates. As discussed in Section 3.4, high coverages of Ag deposited on the 5f-Al-Pd-Mn surface, the 2f-Al-Pd-Mn surface, the p-10f surface of the  $\xi'$ -Al-Pd-Mn approximant phase and the 10f-Al-Ni-Co surface results in the formation of nanocrystalline Ag islands in a rotational epitaxial growth mode [145]. In Figure 6.1(a-c) and (d-f), the low and intermediate coverage regimes for the Ag/5f-Al-Pd-Mn and the Ag/p-10f- $\xi'$ -Al-Pd-Mn systems are presented, respectively. In the low-coverage regime in both systems (Figure 6.1(a) and (d)), small Ag islands are apparent at monatomic height ( $\sim 0.2$  nm). This is deduced from the inset height

histograms, where smaller peaks (corresponding to Ag islands) exist at  $\sim 0.2$  nm above the larger substrate peaks which are visible at lower height (a result of the intrinsic substrate surface corrugation). By consideration of island density as a function of deposition flux and of island size at different coverages, a heterogeneous mechanism for nucleation of these islands was suggested. Diffusing Ag adatoms become trapped at specific sites on the substrate surface, thereby nucleating Ag island growth.

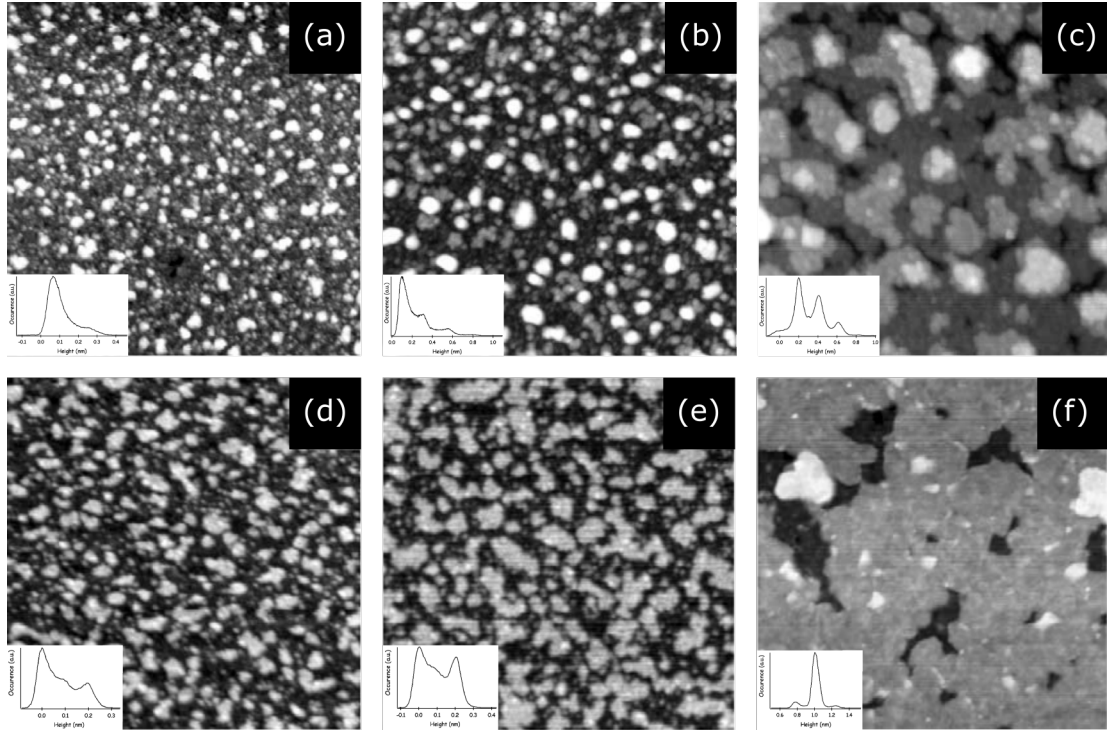


Figure 6.1: (a-c) STM images ( $10 \text{ nm} \times 10 \text{ nm}$ ) of Ag deposited on the 5f-Al-Pd-Mn surface at 0.2, 0.5 and 1.7 ML, respectively. (d-e) STM images ( $10 \text{ nm} \times 10 \text{ nm}$ ) of Ag deposited on the p-10f surface of the  $\xi'$ -Al-Pd-Mn approximant phase at 0.2, 0.4 and 5 ML, respectively. The height histograms for each image are shown inset. Reproduced and modified from [145].

As the Ag coverage is increased, slightly different growth modes become apparent on both surfaces. On the 5f-Al-Pd-Mn surface, 3D growth perpendicular to the surface is observed. This can be seen in the progression of height histograms at increasing coverage (Figure 6.1(a-c)). Extra Ag peaks appear at multiples of the  $\sim 0.2$  nm monatomic height at a coverage of 0.5 ML (Figure 6.1(b)), although only a slight increase in lateral island

size is observed. At a coverage of 1.7 ML (Figure 6.1(c)), wetting of the substrate occurs as the 3D islands spread laterally across the surface and coalesce, forming flat-topped islands. The structure on top of these islands (not shown here) is disordered. On the p-10f surface of the  $\xi'$ -Al-Pd-Mn approximant, however, a layer-by-layer growth mode is observed, where each layer is almost complete before the formation of the subsequent layer begins. This can be seen in Figure 6.1(d-e), where islands of monatomic height spread across the surface. Peaks again appear in the height histograms at multiples of the  $\sim 0.2$  nm monatomic height as coverage is increased, but their development is slower, with each peak overtaking the last when corresponding layer is complete. At 5 ML coverage and above, flat-topped islands begin to form (see Figure 6.1(f)), where a disordered top surface is again apparent (not shown here) [145].

The differences in growth mode were assigned to the surface free energies associated with each substrate in comparison to Ag. For instance, given the 3D growth observed on the 5f-Al-Pd-Mn surface, it is reasonable to assume that the surface energy of the substrate is less than that of the Ag adsorbate. The opposite is then true for the p-10f surface of the  $\xi'$ -Al-Pd-Mn approximant, where layered growth is observed. Contribution from the interfacial energy is assumed to be small here [145].

Aside from the attractive aspects of single-element QC overlayers discussed so far, Ag deposition on the 5f-Ag-In-Yb surface is of particular interest due to the homoepitaxial nature of the interaction. In this sense, it bears parallels to the In/5f-Ag-In-Yb study. An interesting aspect of the In/5f-Ag-In-Yb system is the adsorption sites of In, which are described in terms of vacant Ag/In sites above the surface plane only. This is opposed to the adsorption sites for Pb and Bi, which include vacant Yb positions. Homoepitaxial investigations like this have the potential to provide insights into growth mechanisms and could illuminate structural aspects of the QC, such as its cluster-based nature (see Section 2.6) or the chemical ordering at Ag/In sites. Theoretical calculations have been undertaken for the low coverage regime in the Ag/5f-Ag-In-Yb system [146]. In these calculations, the substrate structure was modelled assuming a top layer consisting of In and Yb only, with no Ag. This is consistent with observations from the cubic approximant structure. In Figure 6.2(a) and (b), the calculated potential energy landscapes (PES) for first and second layers of Ag adsorption are shown, respectively. The colour scheme is shown on the right hand side of both figures, where blue corresponds to a more negative adsorption energy and thus a more stable adsorption site. The opposite is true for red contrast areas.  $z$  denotes the height of the Ag adsorbate atom above the surface layer. As can be seen in Figure

6.2(a), a range of stable first-layer adsorption sites are available at  $z = 1.2 \text{ \AA}$  marked A, B1 and B2. Sites A and B2 correspond to interstitial sites between the inner and outer rings of In and Yb decagons, respectively. As discussed in Section 3.4 and in Chapter 5, Pb and Bi have been observed to reside at these sites in the early stages of adsorption. The first-layer of Pb adsorbs in a pentagonal arrangement at A sites (i.e. at the vertices of the black pentagon in Figure 6.2(b)), while the first-layer of Bi adsorbs at B2 sites in a similar arrangement, rotated by  $36^\circ$  (i.e. at the vertices of the red pentagon in Figure 6.2(b)). In both cases, the distribution of these sites and the measured height of adsorbates above the substrate were matched to vacant model planes above the 5f-Ag-In-Yb surface truncation (a 4<sup>th</sup> shell plane for Pb and two closely-spaced 5<sup>th</sup> shell planes for Bi) [77, 78]. These vacant model ‘adsorption’ planes are shown overlaid on the model 5f-Ag-In-Yb surface plane in Figure 6.2(c). First-layer Pb and Bi adsorption sites are coloured blue and grey, respectively. Red and black dashed pentagons have been overlaid at one set of sites to show the arrangements of A and B2 sites. The atomic density distribution of the *i*-Ag-In-Yb QC along the 5-fold direction is also shown in Figure 6.2(d), where the corresponding vacant model planes have been marked with arrows and colour coded accordingly. It is noted here that the adsorption sites for Pb and Bi were predicted theoretically to be more stable than those for Ag [146].

B1 sites, in fact, exhibit the most stable adsorption site at the lower height of  $z = 0.3 \text{ \AA}$  above the surface (PES not shown here). However, given considerations of the adsorption energies as a function of height, it was determined that, at room temperature, first-layer adsorption at B2 sites is expected for Ag at a height of  $z = 1.4 \text{ \AA}$  from the surface. The result is a pentagonal arrangement of adsorbed Ag with edge-length  $0.97 \text{ nm}$  (i.e. residing at the vertices of the red pentagon in Figure 6.2(a-c)). This is the same as for first-layer Bi adsorption. In fact, the theoretically predicted stable first-layer adsorption height for Ag is close to the height above the surface of the vacant *i*-Ag-In-Yb model planes describing the arrangement of Bi in the deposited first-layer. They reside at  $1.3 \text{ \AA}$  and  $1.6 \text{ \AA}$  above the surface, as can be seen in Figure 6.2(d). The most stable second-layer site is site A (i.e. at the vertices of the black pentagon in Figure 6.2(a-c)), as can be seen in Figure 6.2(b). This is the same arrangement as for first-layer Pb adsorption. It was noted in this study, however, that experimental observation of the second-layer may be difficult using STM due to the fact it displays a stable adsorption height in between the surface and the first-layer. Although a value for the theoretically predicted stable second-layer adsorption height was not given, the vacant model plane describing first-layer Pb adsorption resides

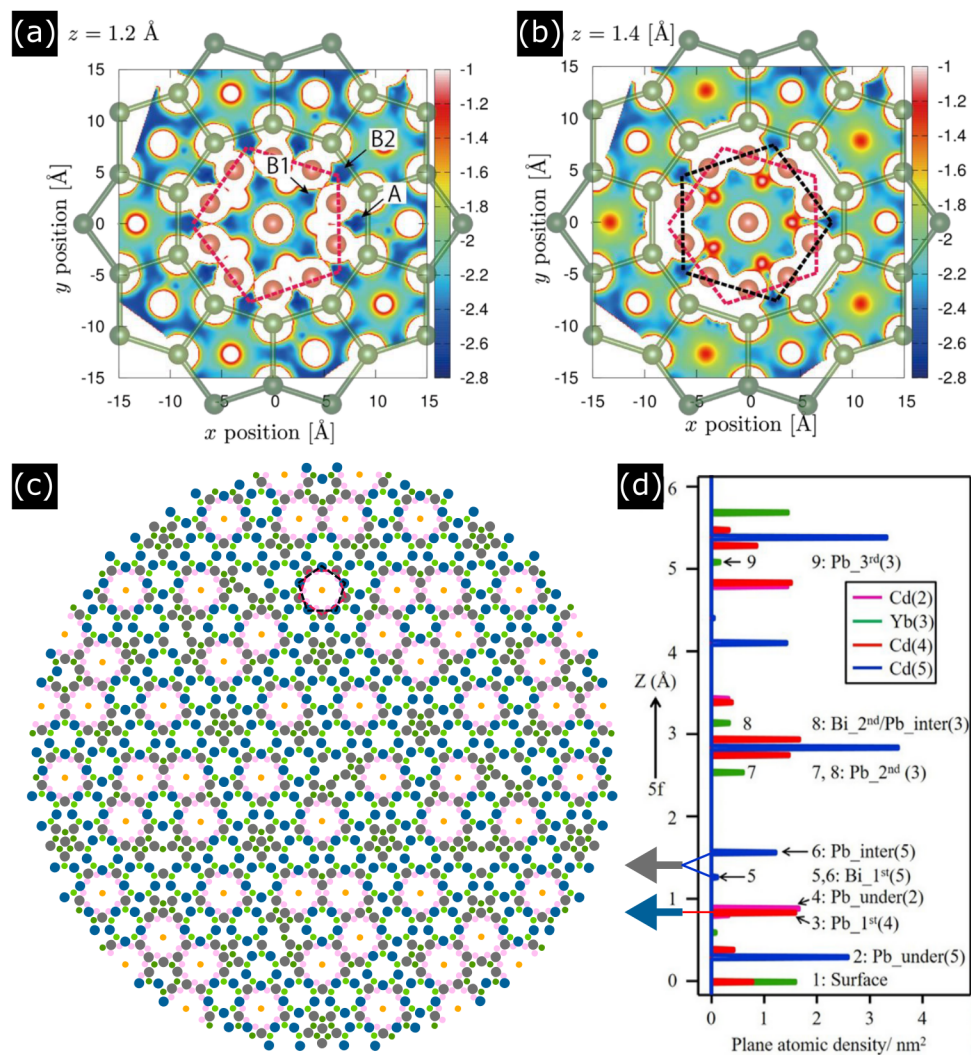


Figure 6.2: (a) and (b) Calculated adsorption energies for first-layer and second-layer Ag adsorption at heights  $z = 1.2 \text{ \AA}$  and  $1.4 \text{ \AA}$ , respectively. The calculated adsorption energies (in eV) and corresponding colour-coding are shown on the right hand side of both figures, where a more negative energy relates to a more stable adsorption site. Red and black pentagons have been overlaid corresponding to the expected first- and second-layer adsorption sites. Substrate Yb and In atoms are shown in green and red, respectively. Reproduced and modified from [146]. (c) A section of atomic sites from the 5f-Ag-In-Yb surface model with sites from the vacant model planes representing first-layer Bi/theoretical first-layer Ag and first-layer Pb/theoretical second-layer Ag adsorption overlaid (gold: CCs, light green: 3<sup>rd</sup> shell Yb, light pink: 4<sup>th</sup> shell Ag/In, dark green: glue Yb, grey: first-layer Bi/theoretical first-layer Ag and blue: first-layer Pb/theoretical second-layer Ag). (d) Atomic density distribution of the *i*-Ag-In-Yb QC along the 5-fold direction. Arrows indicate the vacant model planes corresponding to first-layer Bi/theoretical first-layer Ag and first-layer Pb/theoretical second-layer Ag adsorption. Reproduced and modified from [77].

at 0.86 Å above the surface truncation. The possibility of simultaneous adsorption of Ag in other layers could also inhibit second-layer observation [146].

In the second part of this chapter, Ag adsorption on the 5f-Ag-In-Yb surface will be investigated by STM in order to complement these theoretical calculations. It will be seen that experimental observations replicate theory somewhat, but a more disordered overlayer becomes apparent at intermediate coverages. The growth mode is different to that reported for Pb, Bi, In and Sb, but mirrors that reported for Cu. Similarities with Ag adsorption on the 5f-Al-Pd-Mn surface and the p-10f surface of the  $\xi'$ -Al-Pd-Mn approximant are also apparent.

## 6.2 Experimental details

The results presented at the start of this chapter (Section 6.3.1) relate to a previous STM investigation of Pb deposition on the 5f-Ag-In-Yb surface, reported by Sharma et al. [78]. The corresponding experimental methods can be found within this reference.

For the experiments described in the second part of this chapter (Section 6.3.2), the 5f-Ag-In-Yb sample was prepared as described in Section 5.2. Ag was evaporated from an Mo crucible mounted within a water cooled Omicron EFM 3 single-cell evaporator. The flux was held at a constant rate during deposition. An ion flux (directly proportional to the flux of evaporated atoms) of 490 nA was used for the data presented in this section. This corresponds to a deposition rate of  $\sim 0.025$  ML per minute. Limited datasets at higher ( $\sim 5\times$ ) and lower ( $\sim 4\times$ ) deposition rates were also attempted. Deposition was undertaken with the substrate held at room temperature. Heating the substrate to a range of different temperatures after deposition was also attempted.

## 6.3 Results

### 6.3.1 Metal adsorbate motion

As outlined in Section 4.3.2 and discussed in Chapter 5, assessment of motion on the surface by STM requires multiple successive scans taken from the same area of the surface with the same scanning parameters. Two sets of scans were selected from the Pb/5f-Ag-In-Yb data. The first was a set of four scans taken from the first-layer of Pb deposited on the surface (coverage  $\sim 0.3$  ML), with scanning parameters  $V_b = -0.9$  V,  $I_t = 0.5$  nA and scan

speed =  $488 \text{ nm s}^{-1}$  (corresponding to  $\sim 110$  seconds between each scan). The second was a set of three scans taken from the Pb second-layer (coverage  $\sim 0.85 \text{ ML}$ ) with scanning parameters  $V_b = -0.9 \text{ V}$ ,  $I_t = 0.5 \text{ nA}$  and scan speed =  $732 \text{ nm s}^{-1}$  (corresponding again to  $\sim 110$  seconds between each scan). The two sets of scans are displayed in video format in Supporting Figure 6.1 and 6.2, respectively. The scan number is shown at the top-left of the video. The area of each scan is  $26 \text{ nm} \times 26 \text{ nm}$  in both figures. Bright protrusions correspond to Pb atoms adsorbed on the surface.

Before analysis of the adsorbate motion, a recap of the first-layer and second-layer adsorption sites of Pb, as determined by Sharma et al. [78], will be given. Figure 6.3(a) and (b) show the third and first scan from Supporting Figure 6.1 and 6.2, indicating the first and second layers of Pb adsorption, respectively. Highlighted by circles in Figure 6.3(a) are the characteristic pentagonal arrangements of Pb adatoms associated with the first-layer (average edge-length =  $0.92 \pm 0.05 \text{ nm}$  and average apparent Pb height above substrate =  $\sim 0.11 \pm 0.01 \text{ nm}$ ). Not all pentagon vertices are occupied by a Pb adatom at this coverage in these motifs. The corresponding model adsorption sites are marked in grey on a section of 5f-Ag-In-Yb model in Figure 6.3(c). As discussed already, these sites reside at alternate interstices between inner 4<sup>th</sup> shell Ag/In and outer 3<sup>rd</sup> shell Yb decagons surrounding CCs, forming a pentagon of edge-length  $0.97 \text{ nm}$ .

Highlighted by circles in Figure 6.3(b), are a selection of the decagonal arrangements of Pb adatoms associated with the second-layer (average apparent height of Pb above substrate =  $\sim 0.31 \pm 0.01 \text{ nm}$ ). Most arrangements are again incomplete at this coverage. Pentagonal features form initially during the early stages of second layer adsorption, developing into decagons as coverage is increased. The initial second-layer pentagons are rotated by  $36^\circ$  with respect to those in the first-layer and inflated by a factor of  $\tau$  (i.e. average edge-length =  $1.4 \pm 0.2 \text{ nm}$ ). The model second-layer adsorption sites are marked on Figure 6.3(c) in blue (pentagon edge-length =  $1.57 \text{ nm}$ ). These sites reside at the centres of the Yb pentagons which surround CCs. Pb also adsorbs in a quasiperiodic third-layer and a range of underlayers and intermediate layers. These layers are not discussed here.

Referring the reader again to Supporting Figure 6.1 and 6.2, movement of adsorbed Pb is clearly observed. In fact, considering the motifs discussed above for the previously determined first- and second-layer adsorption sites, diffusion across these sites is apparent. This can be seen by considering the same first-layer pentagonal arrangements and second-layer decagonal arrangements, again marked by circles in Supporting Figure 6.1 and 6.2, respectively. Within these arrangements, the intermittent occupation of Pb adatoms at

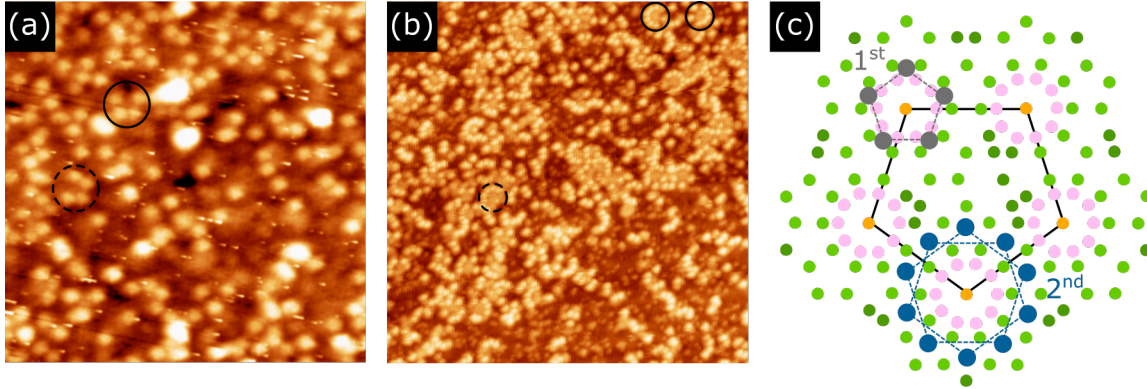


Figure 6.3: (a) and (b) STM images ( $26 \text{ nm} \times 26 \text{ nm}$ ,  $V_b = -0.9 \text{ V}$ ,  $I_t = 0.5 \text{ nA}$ ) taken from the first-layer and second-layer of Pb deposited on the 5f-Ag-In-Yb surface. Examples of first-layer pentagonal arrangements and second-layer decagonal arrangements have been marked in (a) and (b), respectively. (c) A section of atomic sites from the 5f-Ag-In-Yb surface model (gold: CCs, light green: 3<sup>rd</sup> shell Yb, light pink: 4<sup>th</sup> shell Ag/In and dark green: glue Yb). A 2.5 nm edge-length pentagon has been overlaid on the pentagonal arrangement of CCs. The model first-layer and second-layer adsorption sites determined by Sharma et al. [78] are shown in grey and blue, respectively. A 0.97 nm edge-length pentagon has been overlaid on first-layer sites, with  $\tau$ -inflated pentagons (rotated by  $36^\circ$  with respect to each other) overlaid on the second-layer sites.

the expected adsorption sites is evident, where bright protrusions are observed to appear/disappear across successive STM scans as the videos progress. To back this up, the motifs marked by dashed black circles in Supporting Figure 6.1 and 6.2 (same as those in Figure 6.3(a) and (b), respectively) have been enlarged and each individual scan is shown in Figure 6.4(a-d) and (i-k), respectively. Below each of these figures, a section of the 5f-Ag-In-Yb surface model with the previously determined first-layer (grey in Figure 6.4(e-h)) and second-layer (blue in Figure 6.4(l-n)) model adsorption sites overlaid are shown. Sites marked by filled circles in Figure 6.4(e-h) and (l-n) represent sites which are occupied by a Pb adatom in the corresponding STM images in Figure 6.4(a-d) and (i-k), respectively. Empty circles denote unoccupied sites. The geometry and dimensions of the sites where movement is observed in successive STM scans match directly with the previously determined first-layer and second-layer model adsorption sites, where the experimental and model pentagon edge-lengths are the same as those quoted above.

Given the adsorption regime determined by Sharma et al. [78] (discussed above), no

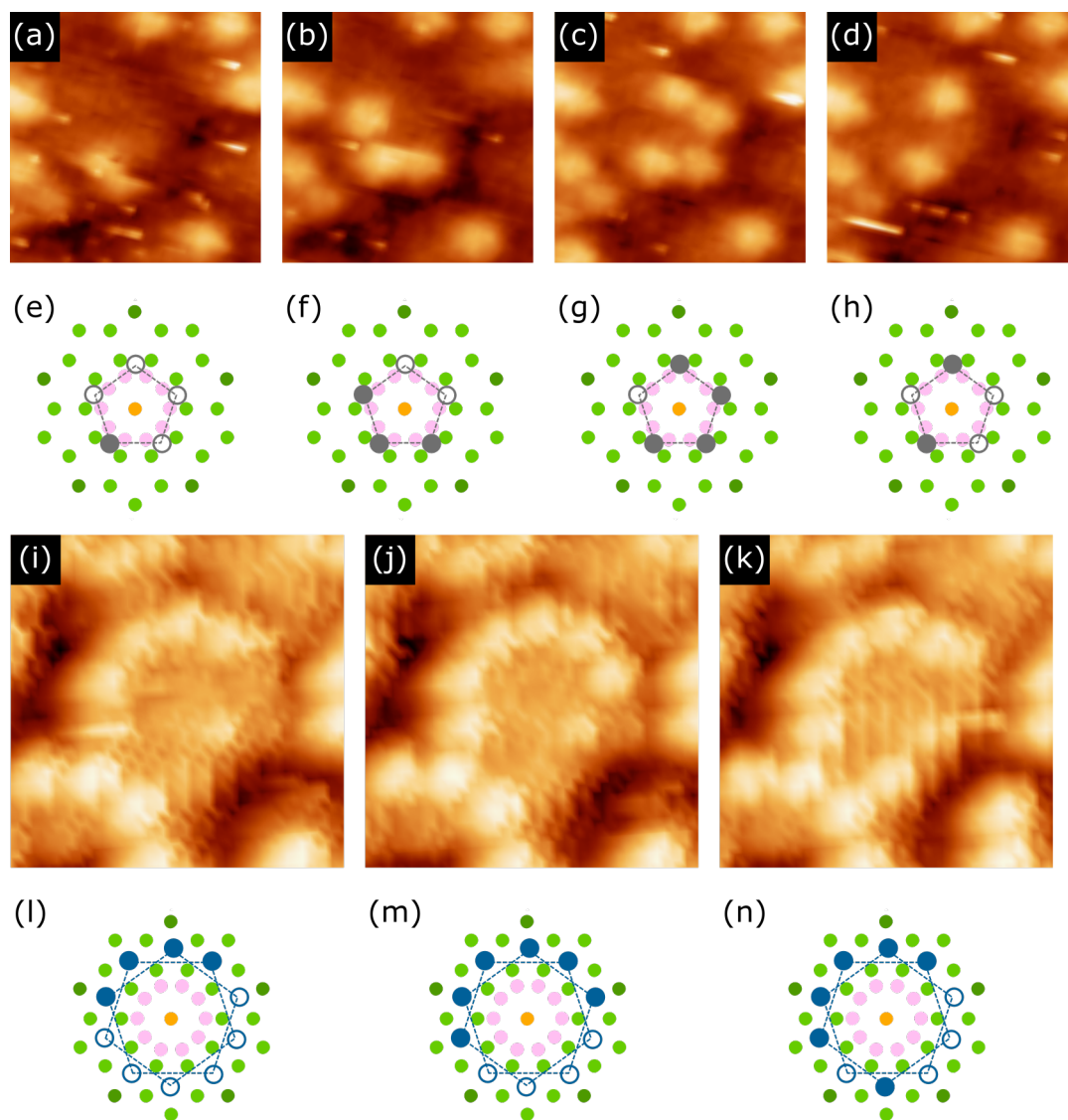


Figure 6.4: (a-d) and (i-k) Successive STM scans ( $5 \text{ nm} \times 5 \text{ nm}$ ,  $V_b = -0.9 \text{ V}$ ,  $I_t = 0.5 \text{ nA}$ ) taken from the same area of the first- and second-layer of Pb deposited on the 5f-Ag-In-Yb surface, respectively. The corresponding motifs are marked by a dashed circle in Supporting Figure 6.1/Figure 6.3(a) and Supporting Figure 6.2/Figure 6.3(b), respectively. (e-h) and (l-m) Sections of the atomic sites from the 5f-Ag-In-Yb surface model (gold: CCs, light green: 3<sup>rd</sup> shell Yb, light pink: 4<sup>th</sup> shell Ag/In and dark green: glue Yb). The scale is the same as in (a-d) and (i-k). Occupied adsorption sites in (a-d) and (i-k) are shown by filled grey circles in (e-h) and blue circles in (l-m), respectively. Empty circles represent unoccupied sites.

further analysis is required to state that the movement of Pb adatoms occurs at a set of ordered quasicrystalline sites with 5-fold symmetry. This is perhaps not surprising, given the similar observations of movement of atoms on the clean 5f-Ag-In-Yb surface, as presented in Chapter 5. It is clear that the substrate plays a vital role in the structure of the adsorbate overlayer, hence the pseudomorphicity apparent across multiple layers. It would be expected, then, that the varying potential energy landscape created by the moving atoms on the clean surface would have some effect on the overlayer structure. Indeed, the sites proposed for the movement observed on the clean surface in Chapter 5 reside either at exactly the same interstices as the expected adsorption sites for Pb in the first-layer, or in very close proximity to these sites (see Figure 5.9 and 5.12). Therefore, changes in local adsorption energies would be expected as a result of the clean surface movement, thus stimulating the movement of Pb adatoms in the first-layer. A similar phenomenon would then be apparent for the second-layer, where the clean surface movement and the first-layer adsorbate movement would affect the lowest energy adsorption configuration in the second-layer. Indeed, although only Pb movement on the 5f-Ag-In-Yb surface has been analysed in depth here, comparable adsorbate movement is observed in the first-layers of the Bi/, In/ and Sb/5f-Ag-In-Yb systems. This can be seen Supporting Figure 6.3, 6.4 and 6.5, respectively, where the intermittent formation of  $\sim 1$  nm edge-length pentagonal adsorbate features is evident, as marked by black circles. This backs up the notion that the substrate plays a vital role in the observed adsorbate motion, where different adsorbate species produce the same results. It is noted here, that some of these datasets are insufficient for a thorough analysis, where only a small number of successive scans on the same area of the surface with the same scanning parameters are available.

As discussed in the introduction to this chapter, similar movement has been reported in STM investigations of Pb deposited on the 5f-Al-Pd-Mn surface at low coverages [130]. However, in this system, motion was significantly reduced upon increased Pb deposition, with growth above ML coverage not observed. This was explained in terms of stabilisation of the Pb overlayer via a strong adsorbate-adsorbate interaction. As only a single adsorbate layer was achievable in this system, this stabilisation would be through an intralayer interaction (i.e. a lateral interaction between Pb adatoms). In the Pb/5f-Ag-In-Yb system, multiple QC layers form in a 3D growth mode. Movement is also still apparent across multiple layers. Limited data at higher coverage than that shown in Supporting Figure 6.2 show that movement still occurs in the second to third layer regime (not shown here). Adlayer-adlayer or interlayer interactions were previously reported to be a key factor in the

stabilisation of the Pb overlayer in this system [78]. This could explain the movement of Pb across multiple layers on the 5f-Ag-In-Yb surface, where intralayer interactions between Pb are not as restrictive as in the Pb/5f-Al-Pd-Mn system and Pb adatoms can diffuse laterally across a subset of low energy adsorption sites in each layer.

### 6.3.2 Ag Growth

After preparation of the 5f-Ag-In-Yb surface, as described in Section 5.2, a clean, well-ordered surface was observed by LEED and STM. Ag was subsequently deposited at a range of coverages using the methods outlined in Section 6.2. The overlayer structures were investigated by STM. The results will be presented here, starting with low coverage data and working through to the high coverage regime. Data taken after depositing Ag and then heating the substrate to different temperatures provided no noticeable difference in Ag growth, aside from desorption at  $\sim 463$  K. As such the room temperature data will be the focus here.

#### Low-coverage

Figure 6.5(a) and (c) show STM images taken after dosing Ag on the 5f-Ag-In-Yb surface for two minutes. Both images are from the same area of the surface, with Figure 6.5(a) taken at negative bias voltage and Figure 6.5(c) at positive bias voltage. Substrate features are still clearly observed at this coverage. In Figure 6.5(b) and (d), the STM images in Figure 6.5(a) and (b), respectively, have been merged with their inverse filtered FFTs taken considering only substrate contribution (not shown here) in order to accentuate substrate features. Patches of a 2.5 nm edge-length Penrose P1 Tiling have then been overlaid on the same area in both images to indicate the arrangement of substrate features observed by STM. As discussed in Section 3.2 and Chapter 5, at negative bias voltage, tiling vertices reside at the centre of large protrusions representing 4<sup>th</sup> shell Ag/In atoms surrounding CCs. At positive bias, they are located at the centre of ring features which correspond to 3<sup>rd</sup> shell Yb surface atoms surrounding CCs. Note that a relatively low positive bias voltage ( $V_b = 0.4$  V) was used to acquire the STM image in Figure 6.5(c). This most likely means some contribution from Ag/In atoms is still apparent and would explain why the ring features are not overly pronounced. Alongside the substrate features, brighter protrusions are visible in the STM images in Figure 6.5(a-d). Some examples have been highlighted in red, blue and green. These brighter features correspond

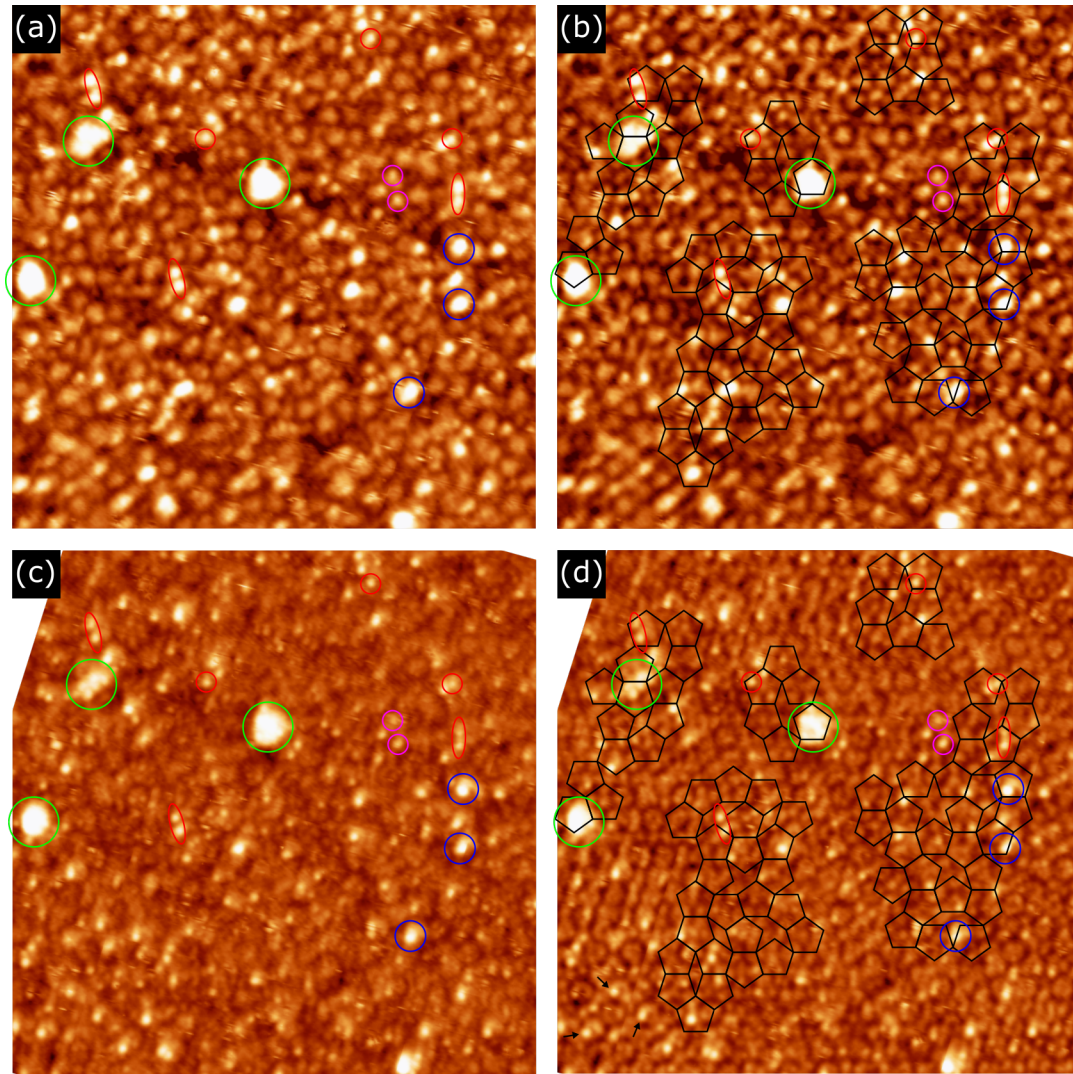


Figure 6.5: (a) and (c) STM images ( $60 \text{ nm} \times 60 \text{ nm}$ ) of  $\sim 0.05 \text{ ML}$  of Ag deposited on the 5f-Ag-In-Yb surface ( $V_b = -0.8 \text{ V}$ ,  $I_t = 0.1 \text{ nA}$  and  $V_b = 0.4 \text{ V}$ ,  $I_t = 0.1 \text{ nA}$ , respectively). (b) and (d) The same STM images as in (a) and (c), respectively, where substrate features have been enhanced by merging the image with its inverse filtered FFT taken considering only substrate contribution. Patches of a  $2.5 \text{ nm}$  edge-length Penrose P1 tiling have been overlaid with vertices residing at large protrusions corresponding to  $4^{\text{th}}$  Ag/In atoms surrounding CCs in (b) and ring features corresponding to  $3^{\text{rd}}$  Yb atoms surrounding CCs in (d). The features marked in different colours in all figures are discussed in the text.

to deposited Ag. By considering the area of the image covered by these Ag features in comparison to the area covered by the substrate, the coverage is estimated to be  $\sim 0.05$  ML.

Now, some aspects of the Ag overlayer at this coverage will be discussed. Firstly, it is noted that no ordering is apparent in the FFT or autocorrelation taken considering only Ag contribution. The small protrusions marked by red circles in Figure 6.5(a-d) correspond to the smallest Ag adsorbate features observed at this coverage. They are very similar to the small substrate protrusions observed at negative bias on the clean surface (discussed in chapter 5), where examples of these substrate protrusions have been marked by pink circles in Figure 6.5(a-d). The small Ag adsorbate protrusions display a slightly increased FWHM in comparison to the small substrate protrusions at negative bias ( $1.26 \pm 0.04$  nm and  $1.03 \pm 0.03$  nm, respectively). This difference is less pronounced at positive bias, where the small Ag adsorbate protrusions are slightly reduced in lateral size when compared to those at negative bias. The two can be distinguished more clearly, however, by the larger apparent height for the small Ag adsorbate protrusions, which is measured to be  $0.125 \pm 0.006$  nm. This is  $\sim \times 3.5$  larger than that for the small substrate protrusions when measured with respect to the same point. It is also consistent with that of other metal adsorbates on this surface at low coverage [77, 78]. It is therefore suggested that the small red-circled protrusions observed here correspond to isolated Ag adatoms. It can be seen that the majority of these small Ag adsorbate protrusions reside in close proximity to the vertices of the patches of Penrose P1 Tiling overlaid on Figure 6.5(b) and (d) (i.e. they surround CC sites). In fact, these protrusions reside on top of the rings observed at positive bias. This can be seen for the protrusions marked by black arrows towards the bottom left of Figure 6.5(d). ‘Pairs’ of small Ag protrusions also seem to be a common feature, where some have been highlighted by red ovals in Figure 6.5(a-d). The average separation between protrusions in these pairs is  $1.6 \pm 0.1$  nm. This is  $\tau$ -deflated in comparison to edge-length of the of the Penrose P1 tiling which describes the arrangement of substrate features. They are oriented most commonly along the high-symmetry directions of the substrate, at intervals of  $\sim 36^\circ$ . Some reside at smaller intervals of  $\sim 18^\circ$ .

Also visible in Figure 6.5(a-d) are some larger Ag adsorbate features, marked by blue and green circles. The blue-circled protrusions are similar to the small red-circled Ag protrusions in that they display a relatively homogeneous nature. Their average FWHM, however, is  $1.62 \pm 0.07$  nm when measured from the negative bias data, which is larger than that measured for the red-circled protrusions. Their average apparent height is 0.175

$\pm 0.004$  nm, which is also larger than the red-circled protrusions (both were measured with respect to the same substrate feature). This would suggest that these intermediate size Ag adsorbate protrusions result either from an Ag adatom adsorbed at a different site in comparison to the red-circled protrusions or from a small cluster of more than one Ag adatom. Both would result in a change in the local density of states and thus the measured FWHM and apparent height. As can be seen in Figure 6.5(b) and (d), blue-circled protrusions again reside close to the vertices of the overlaid Penrose P1 tiling. This would suggest a similar adsorption site and thus point towards the latter of the two suggested explanations being true.

The larger Ag features marked by green circles in Figure 6.5(a-d) have an average FWHM of  $2.6 \pm 0.3$  nm. The increased error here results from the irregular nature of the protrusions around their perimeter. Their average apparent height is consistent with the blue-circled protrusions at  $0.17 \pm 0.01$  nm. From Figure 6.5(b) and (d), it can again be seen that these larger protrusions surround the vertices of the overlaid Penrose P1 tiling. These observations would again suggest the existence of small Ag clusters on the surface, which nucleate laterally from CC sites. In fact, the inner structure of green-circled cluster at the top-left of Figure 6.5(c) and (d) has been resolved at positive bias and appears to be formed from a cluster of five intermediate size Ag protrusions.

The majority of features discussed so far back up the theoretical predictions for Ag adsorption on this surface [146]. First of all, the measured apparent heights of Ag adsorbate features are close to the theoretically predicted stable first-layer adsorption height (= 0.14 nm) and the heights of the vacant model planes above the surface truncation which mirror the arrangement of adatoms in the theoretically predicted first-layer (see Figure 6.2(d)). A section of the 5f-Ag-In-Yb surface model and the theoretically predicted first- and second-layer adsorption sites surrounding CCs (marked by grey and blue circles, respectively) is shown in Figure 6.6(f-j). Note that both the filled and empty grey and blue circles correspond to theoretically predicted adsorption sites. They are marked this way for later discussion. As can be seen in Figure 6.6(f-j), proximity of predicted Ag adsorption sites to CCs is clearly predicted. This matches experimental observations, where, as already discussed, Ag adsorbate features of all sizes reside close to the vertices of the overlaid Penrose P1 tiling in the STM images in Figure 6.5(b) and (d). Further to this, the  $1.6 \pm 0.1$  nm ‘pair’ separation observed by STM is a common feature in the theoretical adsorption sites as the diagonal of the 0.97 nm edge-length pentagonal arrangements of Ag adsorption sites. Examples have been marked by black arrows in Figure 6.6(f). The separation

between these model sites is  $\sim 1.6$  nm (i.e.  $\tau$  inflated in comparison to the edge-length of the pentagon of predicted adsorption sites). The orientation of same-layer model pairs (i.e. first-layer to first-layer or second-layer to second-layer) occur at intervals of  $36^\circ$ . Smaller  $18^\circ$  intervals are also apparent if separations between first- and second-layer pairs are considered. It is noted here, however, that some model second-layer adsorption sites around the CCs are replaced by first-layer sites if adsorption is considered in terms of the vacant model planes above the surface truncation (see the introduction to this chapter and Figure 6.2(c) and (d)). This will be discussed in more depth later.

Before further comparison of experimental observations with the model and theoretically predicted adsorption sites, it is noted that, as with other metal adsorbate studies on this surface (see Section 6.3.1), motion of deposited Ag is apparent. This can be seen in Supporting Figure 6.6, where the four subsequent STM scans taken after that shown in Figure 6.5(a) are displayed in video format. Each were taken from exactly the same area of the surface with the same scanning parameters;  $V_b = -0.8$  V,  $I_t = 0.1$  nA and scan speed =  $579$  nm  $s^{-1}$  (corresponding to  $\sim 150$  seconds between each scan). The scan number is shown at the top-left of the video. Some Ag adsorbate features have been highlighted, where the same colour coding as in Figure 6.5(a-d) has been used (i.e. red circles correspond to single Ag adatoms, blue circles to intermediate size Ag adsorbate protrusions and green circles to larger Ag adsorbate clusters). Ag adsorbate features have again been distinguished from substrate features by their larger apparent height.

As can be seen from the red-circled areas, isolated Ag adatoms are mobile on the surface. The intermediate and larger Ag adsorbate clusters (marked in blue and green) remain mostly stationary, although the addition or loss of individual adatoms to/from these clusters is sometimes observed between successive STM scans. To assess the motion, the locations of a set of isolated Ag adatoms in the vicinity of a pentagonal arrangement of large substrate protrusions will be compared directly to the substrate surface model and the theoretically predicted adsorption sites. In Figure 6.6(a-e), each individual scan from the area marked by a black square in Supporting Figure 6.6 is shown. A pentagon has been overlaid on each figure with vertices residing at a pentagonal arrangement of large substrate protrusions corresponding to 4<sup>th</sup> Ag/In atoms surrounding CCs. Also overlaid are a set of numbered circles. Solid circles represent positions occupied by an Ag adatom in that image, whereas dashed circles represent sites filled by an Ag adatom in previous or subsequent scans. Measured separations and angles between closely-spaced numbered sites are given in Table 6.1. The large apparent errors for some of these measurements arise

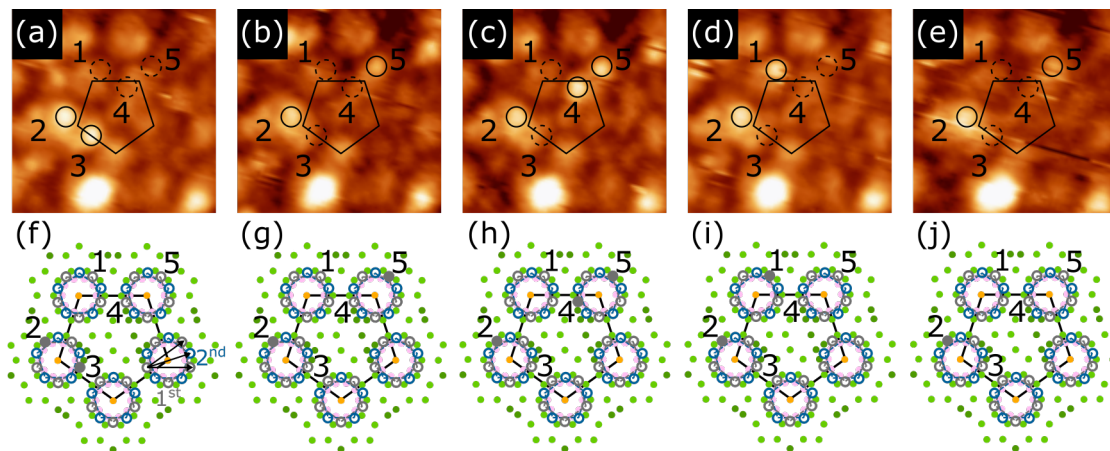


Figure 6.6: (a-e) Successive STM scans ( $10 \text{ nm} \times 10 \text{ nm}$ ,  $V_b = -0.8 \text{ V}$ ,  $I_t = 0.1 \text{ nA}$ ) taken from the same area of  $\sim 0.05 \text{ ML}$  of Ag deposited on the 5f-Ag-In-Yb surface (same as area marked by black square in Supporting Figure 6.6). Solid circles mark sites occupied by an Ag adatom. Dashed circles mark sites occupied by an Ag adatom in a previous or subsequent scan. (f-j) Sections of atomic sites from the 5f-Ag-In-Yb surface model corresponding to the area of the surface in (a-e), respectively (gold: CCs, light green: 3<sup>rd</sup> shell Yb, light pink: 4<sup>th</sup> shell Ag/In and dark green: glue Yb). Theoretically predicted first- and second-layer Ag adsorption sites [146] are shown in grey and blue, respectively. A set of first-layer sites with geometry similar to sites in (a-e) are marked and numbered accordingly. Filled grey circles represent positions which are occupied in the corresponding STM image and empty grey circles represent those which are not. 2.5 nm edge-length pentagons have been overlaid on all figures.

due to the relatively large size and close proximity of the Ag adsorbate protrusions. The model sites in Figure 6.6(f-j) correspond to the area of the surface in the STM images in Figure 6.6(a-e), respectively. A set of model first-layer adsorption sites displaying a similar geometry to those observed experimentally have been numbered accordingly in Figure 6.6(f-j). Filled grey circles represent positions which are occupied in the corresponding STM image. The model separations and angles are again given in Table 6.1. As can be seen, there is a good match between experimental measurements and model predictions. It is evident then, that Ag adatoms diffuse across the theoretically predicted first-layer adsorption sites at this low coverage.

Referring the reader back to Supporting Figure 6.6, it can be seen that, in the area marked by a half red/half blue circle, a small Ag adsorbate protrusion makes way for an intermediate size Ag adsorbate protrusion in the third scan. This intermediate size Ag

No.	Separation (nm)		Angle (degrees)	
	STM	Model	STM	Model
1→2	$3.0 \pm 0.3$	3.0	$53 \pm 4$	54
2→3	$1.7 \pm 0.3$	1.6	$35 \pm 7$	36
3→4	$3.1 \pm 0.2$	3.0	$53 \pm 3$	54
4→5	$1.7 \pm 0.2$	1.6	$40 \pm 5$	36

Table 6.1: Distances and angles between numbered sites in Figure 6.6(a-j). Angles are measured as the smallest angle from the horizontal.

adsorbate feature then stays stable in the subsequent scans. For clarity, zoomed areas of each individual scan displaying this feature are shown in Figure 6.7(a-e). As an aid to the eye, a black line of the same size has been overlaid on the same area in each image. It can be seen that the size of the Ag adsorbate protrusion increases in Figure 6.7(c) and remains at this larger size in Figure 6.7(d) and (e). This would suggest that deposited Ag adatoms diffuse across the surface at the theoretically predicted first-layer adsorption sites before becoming trapped at a specific site. Here, they act as a seed for nucleation and further Ag growth. This is similar the clustered growth of Ag on the 5f-Al-Pd-Mn and the p-10f- $\xi'$ -Al-Pd-Mn surfaces at low coverage [145], as well as the the ‘starfish’ nucleation observed in the Al/5f-Al-Cu-Fe [93] and Pb/5f-Al-Pd-Mn [130] systems (discussed in the introduction to this chapter). As it is difficult to resolve the inner structure of the intermediate and larger clusters in this data, it is hard to say whether they correspond to continued growth across the theoretically predicted first-layer sites, growth at theoretically predicted second-layer sites or growth at other sites. As mentioned in the introduction to this chapter, second-layer Ag features were predicted to be difficult to detect by STM due to their lower adsorption height in comparison to the first-layer and due to the possibility of simultaneous adsorptions of Ag in other layers. This might explain why it is hard to resolve the inner structure.

### Intermediate coverage

Figure 6.8(a) and (c) show STM images taken after depositing Ag on the surface for eight minutes. The scans were taken from a similar but shifted area of the surface, where yellow pentagons mark features residing at the same location on the surface in both figures. Figure 6.8(a) was taken at -0.8 V and Figure 6.8(c) at 1.5 V. Ag adsorbate features are clearly visible here, with the coverage estimated as  $\sim 0.3$  ML. In Figure 6.8(c), some ring features

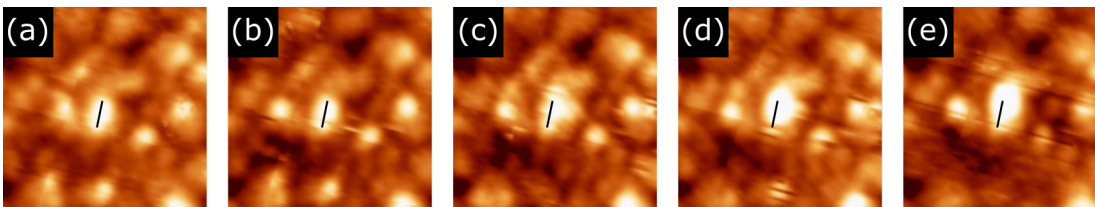


Figure 6.7: (a-e) Successive STM scans ( $10 \text{ nm} \times 10 \text{ nm}$ ,  $V_b = -0.8 \text{ V}$ ,  $I_t = 0.1 \text{ nA}$ ) taken from the same area of  $\sim 0.05 \text{ ML}$  of Ag deposited on the 5f-Ag-In-Yb surface. Same area as motif marked by a half red/half blue circle in Supporting Figure 6.6. In the third scan (c), the size of the central protrusion increases. It stays at this larger size in (d) and (e). A black line has been overlaid on the same area in each figure to highlight this size increase.

corresponding to 3<sup>rd</sup> shell substrate atoms are resolved in between Ag adsorbate features. Taking the inverse filtered FFT with Ag contribution removed and merging it with the original STM image enhances these substrate features, as is shown in Figure 6.8(d). This suggests a relatively large amount of bare substrate is still visible in between Ag features. It is less easy to distinguish the large substrate protrusions expected at negative bias in Figure 6.8(a). However, merging the STM image in Figure 6.8(a) with the inverse filtered FFT taken with Ag contribution removed shows the expected substrate features and ordering are still apparent, as can be seen in 6.8(b). As in Figure 6.5(b) and (d), patches of a 2.5 nm edge-length Penrose P1 tiling have been overlaid in Figure 6.8(b) and (d) to indicate the arrangement of substrate features, specifically CC sites and the surrounding substrate surface atoms.

In this low to intermediate coverage regime, small, intermediate and large Ag adsorbate features are again visible (examples have been marked in red, blue and green, respectively, in Figure 6.8(a-d)). As can be seen in Figure 6.8(b) and (d), these features again appear to surround CC sites (i.e. the vertices of the overlaid Penrose P1 tiling). However, no ordering is apparent in the FFT or autocorrelation taken from Ag adsorbate only contribution. The average FWHM and apparent height of the small Ag adsorbate features are  $1.29 \pm 0.08 \text{ nm}$  and  $0.150 \pm 0.005 \text{ nm}$ , respectively, when measured from the negative bias data. These are close to those observed at  $\sim 0.05 \text{ ML}$  ( $1.26 \pm 0.04 \text{ nm}$  and  $0.125 \pm 0.006 \text{ nm}$ , respectively), with a marginally increased apparent height. The intermediate size Ag adsorbate protrusions have a FWHM and apparent height of  $1.9 \pm 0.1 \text{ nm}$  and  $0.20 \pm 0.02 \text{ nm}$ , respectively. These are again close to those at  $\sim 0.05 \text{ ML}$  ( $1.62 \pm 0.07 \text{ nm}$  and  $0.175 \pm 0.004 \text{ nm}$ , respectively), but with an increased FWHM. ‘Pairs’ of Ag adsorbate protrusions

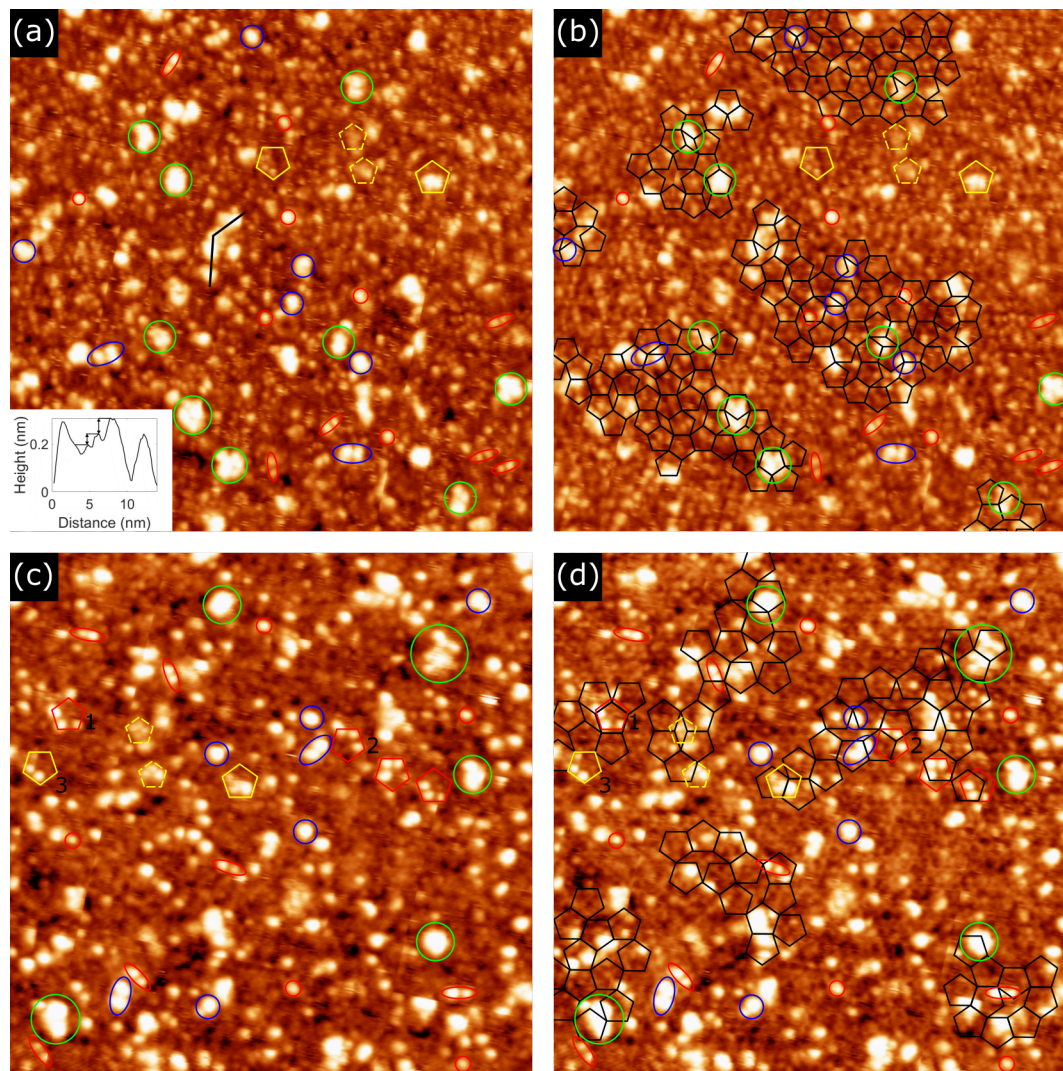


Figure 6.8: (a) and (c) STM images of  $\sim 0.3$  ML of Ag deposited on the 5f-Ag-In-Yb surface ( $81 \text{ nm} \times 81 \text{ nm}$ ,  $V_b = -0.8 \text{ V}$ ,  $I_t = 0.1 \text{ nA}$  and  $60 \text{ nm} \times 60 \text{ nm}$ ,  $V_b = 1.5 \text{ V}$ ,  $I_t = 0.1 \text{ nA}$ , respectively). Inset in (a) is the height profile taken along the black line in the figure. (b) and (d) Same STM images as in (a) and (c), respectively, where substrate features have been enhanced by merging the image with its inverse filtered FFT taken considering only substrate contribution. Patches of a 2.5 nm edge-length Penrose P1 tiling have been overlaid with vertices describing the arrangement of substrate features. The features marked in different colours in all figures are discussed in the text.

with average separation ( $= 1.7 \pm 0.2$  nm) and orientations consistent with those observed at  $\sim 0.05$  ML coverage are again apparent, as highlighted by ovals in Figure 6.8(a-d). At this coverage, however, pairs formed from both small Ag adsorbate protrusions and intermediate size Ag adsorbate protrusions are visible, highlighted by red and blue ovals, respectively.

Ag adsorbate features appear more well-defined in the positive bias data. This can be seen by comparing the areas marked by yellow pentagons in Figure 6.8(a-d). As mentioned, these areas reside at the same location on the substrate surface. In the positive bias data (Figure 6.8(c) and (d)), part-formed pentagons with Ag adsorbate protrusions at the vertex positions are observed, marked by solid yellow pentagons. They are oriented the same as the pentagonal arrangements of CCs in the substrate surface and their average edge-length is  $1.52 \pm 0.05$  nm.  $\tau$ -deflated pentagonal arrangements (edge-length =  $1.04 \pm 0.09$  nm) are also visible in this data, marked by dashed yellow pentagons. Their orientation again matches that of the substrate pentagons. In the negative bias data (Figure 6.8(a) and (b)), however, these features are less discernible, where only in the far-left solid yellow pentagon are protrusions at the vertices resolved. The reason for this difference could be due to some electronic coupling effect between the Ag overlayer and the substrate. Other examples of the larger part-formed pentagonal arrangements have been marked by solid red pentagons in Figure 6.8(c) and (d), suggesting these are a common feature throughout the positive bias data. This is presumably a development of the ‘pair’ features, which display the same separation as the larger pentagon edge-length and are aligned along the same directions. It is noted that vertex protrusions in the larger Ag adsorbate pentagon motifs do not always exhibit the same apparent height and FWHM.

In terms of larger Ag adsorbate clusters, their number density is clearly increased in comparison to the  $\sim 0.05$  ML data. Their irregular nature at this coverage makes FWHM measurements difficult. The inner structure of the larger clusters, when resolved, again shows clumps of intermediate sized Ag protrusions. This can be seen, for instance, in the large green-circled cluster towards the top-right of Figure 6.8(c) and (d). However, no order is apparent. Coalescence of some closely-spaced clusters into much larger, elongated clusters is observed. This can be seen for the cluster overlaid with a black line in Figure 6.8(a). Looking at the same feature in Figure 6.8(b), it can be seen that the cluster is spread across the vertices and edges of the overlaid Penrose P1 tiling. These larger clusters display a rather lumpy nature, where this can be seen from the inset height profile, which was taken along the black line overlaid on the cluster in Figure 6.8(a). Three closely-spaced

heights are clearly distinguishable here, where each has been marked on the linescan. These heights appear at multiples of  $0.032 \pm 0.001$  nm. This suggests growth of Ag adsorbate clusters in a 3D manner. Figure 6.9(b) shows the height histogram taken from the whole image in Figure 6.8(a). The height histogram taken from clean surface data is shown in Figure 6.9(a) for comparison. The large peak in both Figure 6.9(a) and (b) corresponds to substrate contribution. This is expected given the amount of bare substrate still visible at this coverage. Note that the shift in  $z$ -value for the substrate peak in Figure 6.9(b) is due to the fact the definition of  $z = 0$  is dependent on the individual scan, meaning the two are not directly comparable. In the height histogram taken from the Ag-dosed surface (Figure 6.9(b)), a large tail at higher  $z$  values is clearly visible. However, there are no well-defined peaks associated with deposited Ag contribution. This, alongside the height profile inset in Figure 6.8(a), suggests that Ag is adsorbed at a range of closely-spaced heights in proximity to the substrate surface at this coverage.

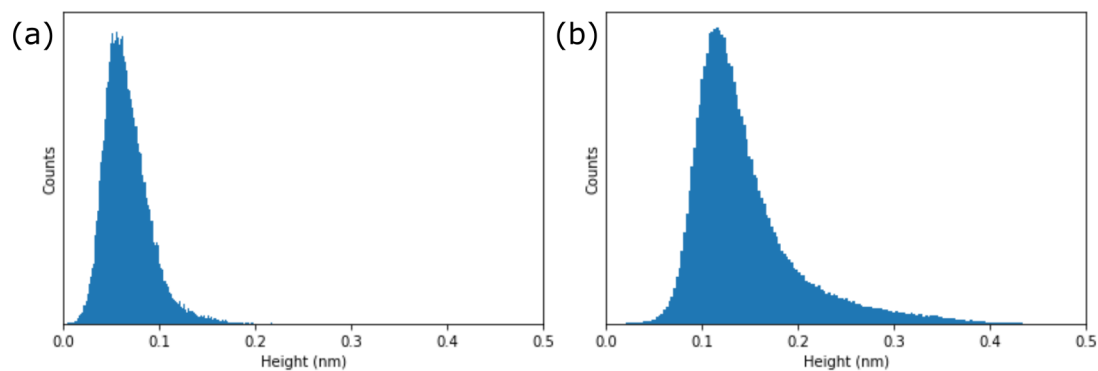


Figure 6.9: (a) and (b) Height histograms taken from an STM image of the clean 5f-Ag-In-Yb surface and of  $\sim 0.3$  ML of Ag deposited on the surface (Figure 6.8(a)), respectively.

Finally, it is noted that movement of deposited Ag is still observed at this coverage. A large amount of successive scans are not available for in depth analysis but, as at lower coverage, smaller Ag protrusions can be seen to appear/disappear across small numbers of successive scans taken using the same scanning parameters (not shown here). Larger clusters remain mostly stationary.

Now, the features observed by STM at this intermediate coverage will be related to the surface model structure and theoretical predictions. Due to the fact the small Ag adsorbate features display a similar FWHM and apparent height as at  $\sim 0.05$  ML, it is suggested they

correspond to continued growth of individual Ag adatoms at the theoretically predicted first-layer sites. This is backed up by the observation of part-formed pentagonal arrangements of adsorbed Ag (i.e. those marked by dashed yellow pentagons in Figure 6.8(c) and (d)) displaying an edge-length consistent with that predicted theoretically ( $1.04 \pm 0.09$  nm and  $0.97$  nm, respectively). The area of the image in Figure 6.8(d) which contains two of these features has been reproduced and enlarged in Figure 6.10(a). As can be seen, the part-formed Ag adsorbate pentagons exhibit an ‘upwards’ orientation. They also reside along the edges of the overlaid Penrose P1 tiling. In Figure 6.10(e), a section of model atomic sites at the surface and the theoretically predicted first-layer and second-layer Ag adsorption sites are displayed. Note that the model adsorption sites shown here (grey and blue circles) are the same as those shown in Figure 6.2(c) and correspond to the sites of the two vacant model planes above the surface truncation which match the theoretically predicted adsorption sites. This means extra adsorption sites are included, as opposed to just the pentagonal arrangements of first- and second-layer adsorption sites surrounding CCs (i.e. those marked by grey and blue dashed pentagons on the top vertex of the large pentagon numbered 0 in Figure 6.10(e)). As can be seen from the model plane, the pentagonal arrangements of theoretically predicted first-layer adsorption sites surrounding CCs exhibit a ‘downwards’ orientation. However, similar arrangements in between CCs (i.e. along the edges of the large pentagonal arrangement of CCs) display an ‘upwards’ orientation. One example has been marked by a dashed grey pentagon on the RHS of pentagonal feature 0. Adsorption at the top three vertices of one of these motifs (i.e. at the sites marked by filled grey circles in this dashed grey pentagon) could explain the smaller part-formed pentagonal arrangements observed experimentally.

The continuation of first-layer growth is further confirmed by consideration of the larger part-formed pentagonal arrangements of adsorbed Ag (i.e. those marked by solid yellow and red pentagons in Figure 6.8(c) and (d)). In Figure 6.10(b-d), three part-formed pentagonal arrangements of small Ag adsorbate protrusions displaying the average  $1.52 \pm 0.05$  nm edge-length have been enlarged. The large numbers inside each pentagon (1, 2 and 3) correspond to the same numbered features in Figure 6.8(b) and (d). A pentagon has been overlaid on each figure to show the arrangement of substrate CCs. The smaller numbers mark a set of small Ag adsorbate protrusions. Note that the numbers 3 and 4 in Figure 6.10(c) mark the ends of a slightly elongated, crescent-like feature. This will be discussed in more depth later. In the model in Figure 6.10(e), three large pentagonal arrangements of CCs have also been marked with the large numbers matching those in Figure 6.10(b-d).

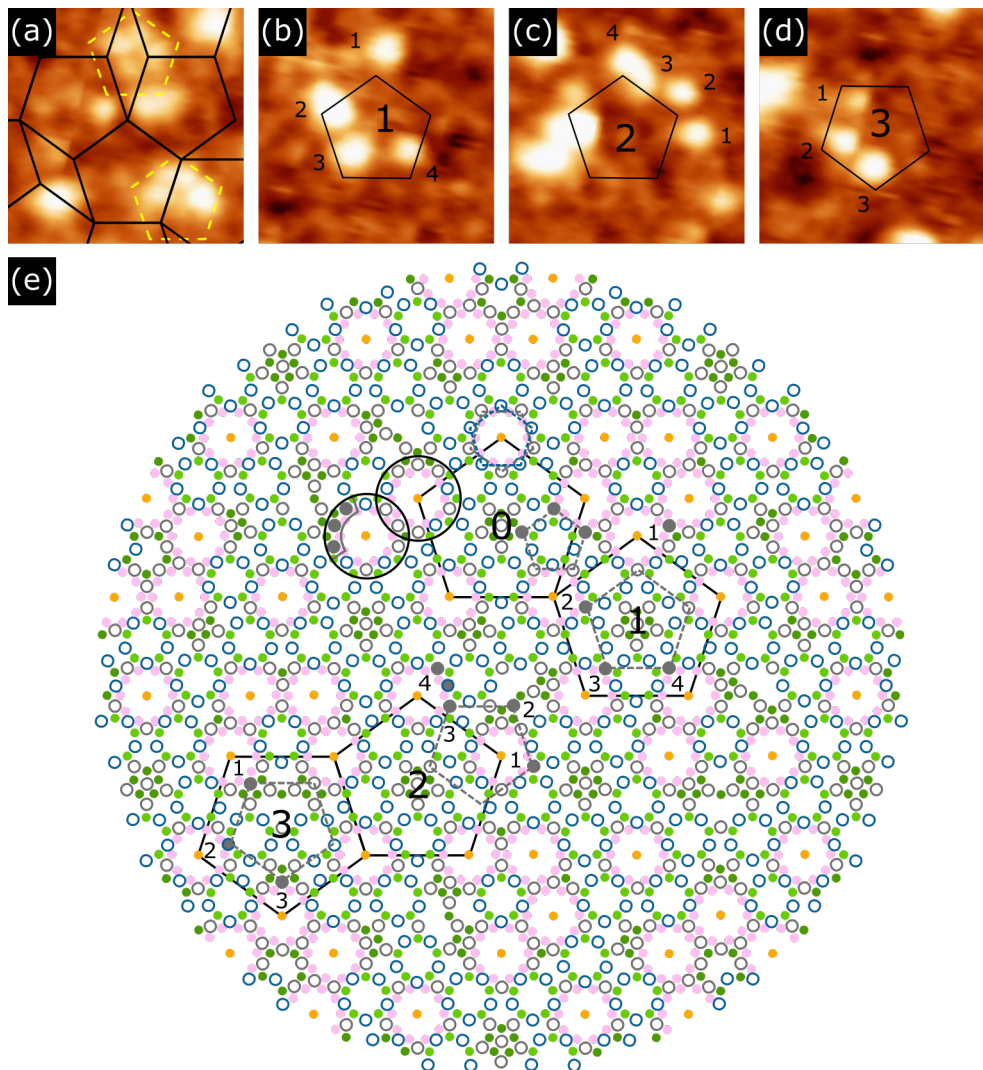


Figure 6.10: (a-d) Sections of the STM scan of  $\sim 0.3$  ML of Ag deposited on the 5f-Ag-In-Yb surface in Figure 6.8(d) ( $9 \text{ nm} \times 9 \text{ nm}$ ,  $V_b = 1.5 \text{ V}$ ,  $I_t = 0.1 \text{ nA}$ ). The dashed yellow pentagons in (a) and the numbered pentagons in (b-c) are the same as the features marked this way in Figure 6.8(c) and (d). Sets of small Ag protrusions have been numbered in (a-d). (e) A section of atomic sites from the 5f-Ag-In-Yb surface model (gold: CCs, light green: 3<sup>rd</sup> shell Yb, light pink: 4<sup>th</sup> shell Ag/In and dark green: glue Yb). Theoretically predicted first- and second-layer Ag adsorption sites [146] are shown in grey and blue, respectively. Features have been marked on the model which correspond to features observed in the STM data. These are discussed in the text. 2.5 nm edge-length pentagons have been overlaid in black on all figures.

A set of model adsorption sites displaying a similar geometry to the arrangement of the small Ag adsorbate protrusions observed experimentally have been marked by filled grey circles and numbered according to the corresponding protrusions in Figure 6.10(b-c). The experimental and model separations and angles between the numbered Ag adsorption sites are shown in Table 6.2. The large apparent errors for some measurements results from the relatively large size and close proximity of the Ag adsorbate protrusions. As can be seen, a good match between theory and experiment is again achieved. The slightly different apparent heights and FWHMs for some of the Ag adsorbate protrusions at the vertices of these larger pentagon arrangements might suggest adsorption of more than one Ag adatom at other sites in close proximity to those marked by filled grey circles in Figure 6.10(e). For example, the larger comparative size of the Ag adsorbate protrusion at the bottom vertex of pentagonal feature 3 in Figure 6.10(d) could result from adsorption at one or more of the four first-layer adsorption sites surrounding site 3 in Figure 6.10(e), as well as at site 3 itself. A similar separation would still be observed by STM if this was the case.

It is noted that some of the filled model adsorption sites marked in Figure 6.10(e) reside at second-layer positions (i.e. blue circles). However, the arrangement first- and second-layer adsorption sites predicted by the two vacant model planes above the surface truncation can vary around CC sites. This can be seen in the decagonal arrangements of model adsorption sites marked by black circles in Figure 6.10(e). Instead of the rotated pentagonal arrangements of five first-layer and five second-layer adsorption sites (like those marked at the top vertex of pentagon 0 in Figure 6.10(e)), arrangements of seven first-layer sites and three second-layer sites are apparent. Different combinations of first- and second-layer sites are evident at other CC locations. Further to this, the model surface plane and vacant plane adsorption sites shown in Figure 6.10(e) represent just one of many potential atomic planes which are similar, but slightly differently arranged. This means that, although some of the features observed experimentally do not directly match with the model first-layer adsorption sites presented in Figure 6.10(e), they could still correspond to first-layer adsorption.

These considerations also help explain the crescent-like feature observed around the top vertex of pentagon 2 in Figure 6.10(c). The differing arrangements of model first- and second-layer adsorption sites surrounding CCs in Figure 6.10(e) results in crescent-like features of multiple closely-spaced first-layer adsorption sites, where one has been marked with filled grey circles within one of the black-circled areas as an example. Such crescent features were observed by STM for first-layer Bi adsorption on the 5f-Ag-In-Yb surface

and they were related to these model sites [77]. The crescent-like feature of adsorbed Ag observed around the top vertex of pentagon 2 could therefore result from adsorption at sites 3 and 4, as well as at the site marked by a filled grey circle in between 3 and 4.

No.	Separation (nm)		Angle (degrees)	
	STM	Model	STM	Model
Feature 1				
1→2	2.9 ± 0.4	2.9	45 ± 6	45
2→3	1.8 ± 0.4	1.6	63 ± 10	72
3→4	1.9 ± 0.4	1.6	2 ± 8	0
Feature 2				
1→2	1.8 ± 0.4	1.6	69 ± 8	72
2→3	1.5 ± 0.3	1.6	5 ± 8	0
3→4	0.9 ± 0.3	1.0	70 ± 15	72
Feature 3				
1→2	1.6 ± 0.3	1.6	74 ± 8	72
2→3	1.6 ± 0.4	1.6	39 ± 9	36

Table 6.2: Distances and angles between numbered sites in Figure 6.10(b-e). Angles are measured as the smallest angle from the horizontal.

The two areas marked by black circles in Figure 6.10(e), as well as other similarly arranged features in the model, also provide a plausible explanation for the ‘pairs’ of intermediate size Ag adsorbate protrusions observed by STM. The model separation between the CCs residing at the centre of these circles is 1.6 nm. It follows that continued growth and nucleation of Ag at the model adsorption sites surrounding these CCs would result in the observation of two larger protrusions separated by this distance along an orientation displaying correspondence with the substrate surface. In fact, an example of an Ag pair consisting of intermediate size protrusions with location, separation and orientation similar to the black circled areas in Figure 6.10(e) is visible on the LHS vertex of pentagonal feature 2 in Figure 6.10(c). The non-circular nature of these protrusions would perhaps suggest adsorption at a subset of the theoretically predicted adsorption sites in the decagonal arrangements surrounding CCs in the model. However, as with the lower coverage data, it is difficult to ascertain the specific adsorption sites within these arrangements due to the fact no inner structure is resolved. Regardless, the slight increase in the measured average FWHM of the intermediate size Ag adsorbate protrusions at this coverage would suggest continued growth at or near these locations.

The coalescence of intermediate size Ag adsorbate features into larger clusters which

spread from the vertices across the edges of the overlaid Penrose tiling in Figure 6.8(b) and (d) again backs up the idea of nucleation and growth of Ag from CCs. In limited datasets taken from separate experiments using different flux values for Ag deposition, the number density of Ag islands appears to be comparable when similar coverages are apparent, despite the differences in deposition flux. This points towards a heterogeneous growth of clusters at specific sites on the substrate surface [145]. However, the comparative datasets are not sufficient enough to confirm this. It is again difficult to draw any major conclusions in terms of specific adsorption sites in the larger clusters due to their irregular nature and the lack of resolution within clusters. However, the range of heights within larger clusters suggests adsorption beyond the theoretically predicted first- and second-layer adsorption sites. As alluded to by Nozawa [146], a range of competing adsorption sites are predicted for Ag deposition on this surface. The simultaneous adsorption of Ag across multiple different layers may explain the differing adsorption heights, as well as the difficulty in obtaining high-resolution within the larger Ag adsorbate clusters by STM. Indeed, in the Pb/ and Bi/5f-Ag-In-Yb systems, the growth of underlayers and intermediate layers was predicted to be crucial for the development and stability of the overall overlayer structure [77, 78]. Some of these layers were not directly observed by STM. It is noted, however, that the growth mode for Ag seems to be different from the Pb and Bi cases.

### High-coverage

In Figure 6.11(a), an STM image taken after depositing Ag on the surface for 20 minutes is displayed. The estimated coverage here is  $\sim 0.8$  ML. Continued growth and coalescence of Ag adsorbate clusters is clearly apparent at this coverage. Small isolated Ag adsorbate features are still observed alongside the larger coalesced clusters. These small Ag adsorbate protrusions display a FWHM and height consistent with those observed at lower coverages. Intermediate size Ag adsorbate features are also apparent, where they generally exist as part of a larger cluster and exhibit a range of heights and lateral sizes. Again, no ordering is apparent in the FFT taken considering just Ag overlayer contribution. However, examples of Ag adsorbate ‘pairs’ and  $\tau$ -scaled pentagonal arrangements of Ag adsorbate features are again evident, as at lower coverages. This can be seen in Figure 6.11(b), where the STM image in Figure 6.11(a) has been reproduced. Pairs of Ag adsorbate features formed from small and intermediate sized Ag adsorbate protrusions are marked by red and blue ovals, respectively. Their average separation ( $= 1.57 \pm 0.05$  nm) and the angular intervals

at which they are oriented are consistent with those observed at lower coverages. Dashed black pentagons in Figure 6.11(b) mark pentagonal arrangements of Ag adsorbate features with an average edge-length ( $= 1.67 \pm 0.05$  nm) close to those observed at  $\sim 0.3$  ML coverage. Examples of  $\tau$ -inflated pentagonal motifs (i.e. displaying a similar edge-length to the pentagonal arrangements of CCs on the substrate surface) are also visible, as marked by solid black pentagons in Figure 6.11(b). The measured average edge-length of these features is  $2.4 \pm 0.1$  nm. The FWHMs and heights of protrusions residing at their vertices can again vary. These observations are consistent with those at low and intermediate coverages, suggesting that nucleation and growth at the theoretically predicted adsorption sites surrounding CCs continues alongside the growth and coalescence of larger clusters.

A range of heights are again apparent within the larger coalesced clusters, as can be seen by line scan height profile taken along the black line in Figure 6.11(b), which is shown inset. Five different closely-spaced heights are visible here, where the average separation between heights ( $= 0.034 \pm 0.003$  nm) is consistent with that observed at  $\sim 0.3$  ML coverage. The increased maximum height and number of different heights observed at this coverage suggests the growth of Ag clusters continues to proceed in a 3D fashion. The height histogram taken from the the whole image in Figure 6.11(a) is shown inset in the figure. Substrate contribution is just visible as the large peak towards low  $z$ . A peak at higher  $z$  is also observed, corresponding to Ag contribution. This is a broad peak which merges with the substrate contribution. A rough estimation for the separation between these peaks is  $\sim 0.12$  nm. This is close to the theoretically predicted stable first-layer adsorption height ( $= 0.14$  nm) and the measured height of isolated small Ag adsorbate features at lower coverages. However, the broadness of this peak, the observed tail at higher  $z$ -values and the line scan inset in Figure 6.11(b) suggests that Ag adsorbs at many different heights, thus corresponding to a range of different adsorption layers. As mentioned, this clustered 3D nature of the overlayer hampers STM resolution, making direct comparison with vacant model planes beyond those associated with the first- and second-layer difficult.

Figure 6.11(c) and (d) show STM images after depositing Ag on the surface for 35 minutes and 60 minutes, respectively. The corresponding estimated coverages are  $\sim 1.4$  ML and  $\sim 2.4$  ML, respectively. No ordering is apparent in the FFT from either image. Also, no examples of common structural motifs are observed at either coverage. This suggests a disordered overlayer in both cases. It can be seen from Figure 6.11(c) that all larger clusters have coalesced at  $\sim 1.4$  ML coverage. The result is a rough Ag film. This is backed up by the inset height histogram, where a large, broad peak corresponding to Ag

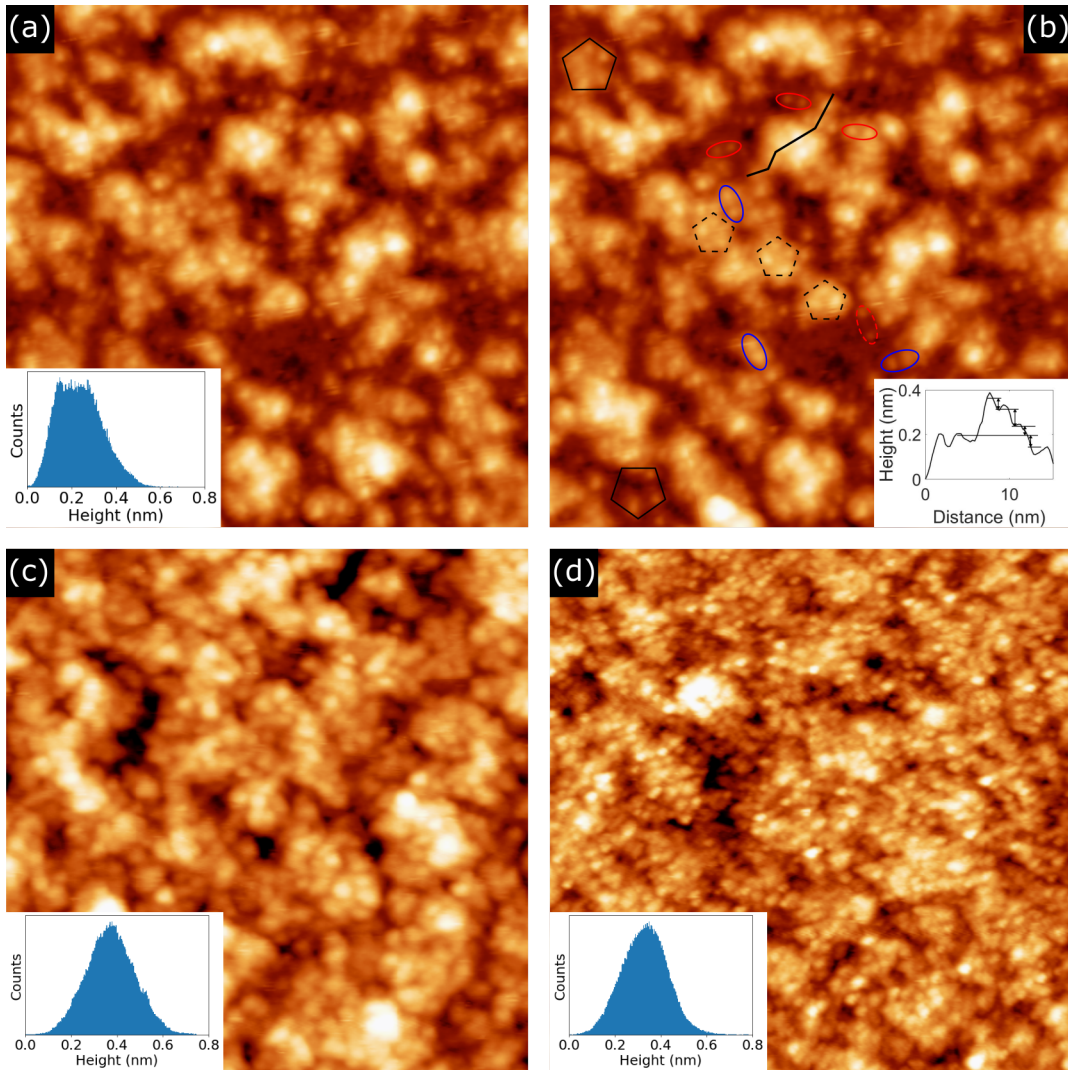


Figure 6.11: (a) STM image of  $\sim 0.8$  ML of Ag deposited on the 5f-Ag-In-Yb surface ( $54 \text{ nm} \times 54 \text{ nm}$ ,  $V_b = 1.8 \text{ V}$ ,  $I_t = 0.1 \text{ nA}$ ). Inset is a height histogram taken from the image. (b) Same as (a), where features discussed in the text have been marked. Inset is a the height profile taken along the black line in the figure. (c) STM image of  $\sim 1.4$  ML of Ag deposited on the 5f-Ag-In-Yb surface ( $64 \text{ nm} \times 64 \text{ nm}$ ,  $V_b = -1.1 \text{ V}$ ,  $I_t = 0.1 \text{ nA}$ ). (d) STM image of  $\sim 2.4$  ML of Ag deposited on the 5f-Ag-In-Yb surface ( $98 \text{ nm} \times 98 \text{ nm}$ ,  $V_b = 1.0 \text{ V}$ ,  $I_t = 0.1 \text{ nA}$ ). Inset in (c) and (d) are height histograms taken from the image.

adsorbate contribution is apparent. The inset height histogram in Figure 6.11(d) shows an asymmetry towards higher  $z$ -values indicating the continuation of clustered 3D growth.

### Further discussion and comparison

Although the growth of Ag on the 5f-Ag-In-Yb surface bears some likeness to previous investigations in similar systems, clear differences are apparent. In terms of Ag adsorption investigations on other QC surfaces, the clustered growth of Ag deposited on the 5f-Al-Pd-Mn and the p-10f- $\zeta'$ -Al-Pd-Mn surfaces at lower coverages seems similar [145]. However, progressive growth of the overlayer at successive monatomic Ag heights is not observed here. Instead, Ag clusters exhibit a range of closely-spaced heights, with the maximum height and spread in heights increasing with coverage. This is confirmed by the progression of height histograms and line scan height profiles at increasing coverages. Differences to most other metal adsorption investigations on the 5f-Ag-In-Yb surface are also apparent. Quasiperiodic growth of Pb and Bi across multiple layers was clearly evidenced in previous reports [77, 78]. Clear quasiperiodic growth at different coverages was also reported in the In/ and Sb/5f-Ag-In-Yb systems [141, 142]. The same cannot be said for Ag growth in which a sparse first-layer forms initially at the theoretically predicted quasiperiodic sites, quickly making way for the concurrent growth of 3D Ag adsorbate clusters, even at lower coverages. This difference can perhaps be explained by the energetic stability of adsorption sites, which were theoretically predicted to be more stable for Pb and Bi in comparison to Ag for first- and second-layer adsorption [146].

Ag growth bears more similarities to Cu growth on the 5f-Ag-In-Yb surface, where a clustered 3D growth regime surrounding CC sites was also observed [143]. Ag and Cu display much higher surface free energies in comparison to Pb, Bi, In and Sb [147], as can be seen in Table 6.3. Surface free energy is positively correlated with the strength of bulk interactions in a material in its natural crystalline form. This explains why Ag and Cu in their natural form also exhibit much higher melting temperatures than Pb, Bi, In and Sb. It is plausible that the clustered growth regime observed for Ag and Cu is a result of the energetic stability of these materials in their bulk form. This might mean adsorbate-adsorbate interactions take precedent over substrate-adsorbate interactions as coverage is increased, thus promoting 3D growth as opposed to growth in a layer-by-layer fashion. The surface free energy value for 5f-Ag-In-Yb is not known. However, estimated values for surface free energies in Al-based QCs are lower than the surface free energies

of their constituent elements [148]. If the same is true for 5f-Ag-In-Yb, this would back up the driving mechanism of Ag growth discussed above. Note that the Yb surface free energy is the lowest of all three constituent elements in the 5f-Ag-In-Yb surface at  $0.482 \text{ J m}^{-2}$ .

However, the observed growth at CC sites and the irregular nature of the Ag adsorbate clusters would suggest the substrate still imparts some influence on the overlayer structure. Also, as the inner structure of these clusters is not resolved, it is difficult to be sure of the nature of the clusters, even if the surface free energy argument would suggest growth of Ag in its bulk form. Another possible contributor to the difference in growth modes is the electron valency of each adsorbate species. Ag and Cu display a lower electron valency in comparison to Pb, Bi, In and Sb, as can be seen in Table 6.3. This could result in a different interaction between adsorbate atoms and substrate surface atoms, thus influencing the growth of the overlayer structure.

Adsorbate	Surface free energy	Electron valence	Deposition rate
Pb	$0.321 \text{ J m}^{-2}$	4	120 nA
Bi	$0.537 \text{ J m}^{-2}$	5	120 nA
In	$0.488 \text{ J m}^{-2}$	3	120 nA
Sb	$0.608 \text{ J m}^{-2}$	5	120 nA
Cu	$1.952 \text{ J m}^{-2}$	1	$\gg$ Pb, Bi, Sb and Ag
Ag	$1.17 \text{ J m}^{-2}$	1	490 nA

Table 6.3: Comparative properties of different metal adsorbates deposited on the 5f-Ag-In-Yb surface.

Another thing to note is that the data presented here for the Ag/5f-Ag-In-Yb system and that reported previously for the Cu/5f-Ag-In-Yb system [143] were taken using higher adsorbate deposition rates in comparison to the Pb, Bi, In and Sb investigations [77,78,142], as can be seen in Table 6.3. As Pb, Bi, In, Sb and Ag were deposited on the surface using the same Omicron EFM 3 evaporator, the deposition rates are directly comparable in terms of ion flux. Cu was deposited from a homebuilt resistive heating evaporator meaning no ion flux reading is available [143]. However, by comparing coverage as a function of dose time, a deposition rate of an order of magnitude larger than that for Pb, Bi, Sb and Ag is apparent. An increased flux decreases the mean free path of adatoms on the surface, thus promoting cluster formation [149]. The same deposition flux used in the Pb, Bi, In and Sb investigations was attempted for Ag here and no obvious difference in growth

mode was observed (i.e. clustered 3D growth was still apparent at comparative coverages). Deposition of Ag at even lower flux values could perhaps promote lateral mobility of Ag adatoms and result in a less-clustered growth mode.

## 6.4 Summary

In this chapter, previous results from metal adsorption investigations on the 5f-Ag-In-Yb surface were re-analysed in order to assess adsorbate motion on the surface. Focussing on the Pb/5f-Ag-In-Yb STM data, it was found that Pb adatoms diffuse across the previously determined adsorption sites [78] in both the first- and second-layers. Movement in limited datasets at higher coverage was also apparent. Although not analysed in depth here, comparable motion was observed in first-layers of Bi, In and Sb adsorbed on the same surface. It is suggested this movement is related to the changing potential energy landscape created by the mobile atoms on the clean 5f-Ag-In-Yb surface, as discussed in Chapter 5. Reduced intralayer interactions may also explain the lateral movement of Pb within each layer.

Also presented in this chapter was the results of an Ag adsorption investigation on the 5f-Ag-In-Yb surface. At low coverages, STM revealed the existence of a range of Ag adsorbate features. Isolated Ag adatoms and Ag clusters of different sizes were observed. Analysis of successive scans from the same area of the surface showed that isolated Ag adatoms were mobile on the surface. Observations suggest they diffuse across the theoretically predicted, pentagonally arranged first-layer adsorption sites, before becoming trapped at some specific site close to a CC. Here, further Ag adatoms nucleate, forming small and large Ag clusters which appear to be more stable. As it is difficult to resolve the inner structure of these clusters, it is hard to determine their specific nature and whether they correspond to growth of the theoretically predicted first- and second-layers of Ag or growth at some other sites. However,  $\tau$ -scaled pentagonal arrangements do appear to be a common feature. Similar observations were made at intermediate coverage. Continued growth of isolated Ag adatoms at the theoretically predicted, pentagonally arranged first-layer adsorption sites was again evident. Ag clusters were observed to grow at CC locations (i.e. at the vertices of the Penrose tiling describing their arrangement), where an increase in their number density was apparent. Larger elongated Ag adsorbate clusters were also visible, formed via the coalescence of smaller clusters spreading from these CC sites. The irregular nature of these larger clusters, both laterally and height wise, suggests adsorption

at a range of sites beyond the theoretically predicted first- and second- layers. This is consistent with the multiplicity of competing stable adsorption sites predicted theoretically for this system. So, although no order was evidenced by FFTs and autocorrelations considering only Ag adsorbate contribution, clustered growth at quasiperiodically arranged pentagonal sites (i.e. CCs) was still apparent at intermediate coverages. Larger scale STM images or LEED patterns from the overlayer would perhaps confirm this. Quasiperiodicity on a smaller scale may also be apparent if the inner structure of the larger Ag adsorbate features was resolved. Finally, at higher coverage, the clustered 3D growth continues, but seems to do so in a disordered fashion. Again, a LEED investigation would be interesting to assess any quasiperiodicity at larger length-scales. Depositing Ag at even higher coverages may also reveal the existence of a rotational epitaxial mode.

Similarities and differences to other adsorption investigations involving Ag deposition on other QC substrates and other metal adsorbates on the same 5f-Ag-In-Yb surface were discussed for the Ag/5f-Ag-In-Yb system. The most similar growth mode appears to be the Cu/5f-Ag-In-Yb system in which growth also proceeds in a clustered 3D fashion [143]. It is proposed that this could be related to the higher surface free energies apparent for Ag and Cu, their lower electron valency or the increased deposition fluxes used.

## Chapter 7

# $C_{60}$ adsorption on the twofold surface of *i*-Ag-In-Yb

In this chapter, the results from an adsorption investigation involving  $C_{60}$  deposition on the 2f-Ag-In-Yb surface will be presented. This was an attempt to create a molecular overlayer with ‘simple’ quasicrystalline symmetry. STM data will be used to assess the structure of the overlayer at a range of different coverages.

### 7.1 Introduction

The *i*-Ag-In-Yb QC has been discussed in depth throughout this thesis (for an overview, the reader is referred to Section 2.8 and 3.2). In the introduction to Chapter 5, a review of previous clean surface investigations on the 2f-Ag-In-Yb surface was given. In the first set of results presented in Chapter 5, the structure of the clean 2f-Ag-In-Yb surface was further explored in terms of a previously unobserved bias-dependency of STM contrast.  $C_{60}$  was introduced in Section 2.6 and an overview of its use as an adsorbate on QC surfaces given in Chapter 3.

In general, QC surfaces with ‘simple’ symmetries (i.e. 2-fold and 3-fold) remain relatively unexplored in terms of adsorption investigations when compared to those with higher orders of symmetry (i.e. 5-fold and 10-fold). An interesting example, however, is the adsorption of  $C_{60}$  on the 2f-Al-Pd-Mn surface at 600 K [19]. As discussed in Chapter 3,  $C_{60}$  has been utilised in a wide range of adsorption investigations on QC surfaces with higher orders of symmetry. In this system,  $C_{60}$  adsorbs selectively on top of Mn atoms in the sub-

strate surface. Given the arrangement of Mn atoms, the result is an overlayer in which the majority of  $C_{60}$  molecules reside at the vertices of a Fibonacci square grid with quasicrystalline 4-fold symmetry. This can be seen in Figure 7.1(a), where a black Fibonacci square grid has been overlaid on an STM image of the  $C_{60}$  overlayer. The remaining molecules which do not reside at the vertices of this tiling are located at the vertices of a  $\tau$ -deflated Fibonacci square grid (overlaid in white in Figure 7.1(a)). They still, however, correspond to Mn sites in the substrate surface. A comparison between STM data and the 2f-Al-Pd-Mn surface model is shown in Figure 7.1(b) and (c). The distribution of  $C_{60}$  molecules in the inset STM images in Figure 7.1(b) and (c) match well with the distribution of Mn atoms shown in the substrate surface model in each figure. Model  $C_{60}$  molecules have been overlaid at model Mn locations with geometry matching observations in the inset STM images. Adsorption of  $C_{60}$  at Mn sites was assigned to chemical affinity between the two, where  $C_{60}$  is an electron acceptor and Mn is electron rich. The geometry of Mn atoms at the substrate surface, and their sparse density in comparison to Al and Pd, further aid in the growth of an overlayer with quasicrystalline order [19].

This investigation highlights the usefulness of  $C_{60}$  as a chemical probe, adsorbing at a specific site and therefore providing information on the complex surface structure. The reader is again referred to Chapter 3 for other pertinent examples. This system was the first experimental realisation of a Fibonacci square grid structure, which had been explored in previous theoretical studies [150–152]. Although QC surfaces with simple symmetries have typically been of lesser interest within the community, it is evident from this study that they can provide a fruitful avenue of investigation.

So far, only two adsorption investigations on the 2f-Ag-In-Yb surface have been reported: Pn and Pb. Pn adsorption resulted in a quasicrystalline overlayer with 2-fold symmetry. This was evidenced by STM investigations of the overlayer, where a quasicrystalline FFT was apparent when considering only Pn contribution (see Figure 7.2(b)). Both the alignment and orientation of Pn molecules were consistent with the high-symmetry directions of the substrate surface (see Figure 7.2(a)). An adsorption network dependent on Yb sites was proposed [103]. A similar dependency was observed for Pn adsorption on the 5-fold surface (as discussed Section 3.4) and, more recently, on the 3-fold surface [101, 104]. On the 3-fold surface (the other surface in this system with ‘simple’ symmetry), FFTs and autocorrelations of the Pn overlayer again displayed quasicrystalline symmetry (see Figure 7.2(d) and (e), respectively). The majority of molecules displayed orientation and alignment along the high-symmetry directions of the substrate surface, with triangular

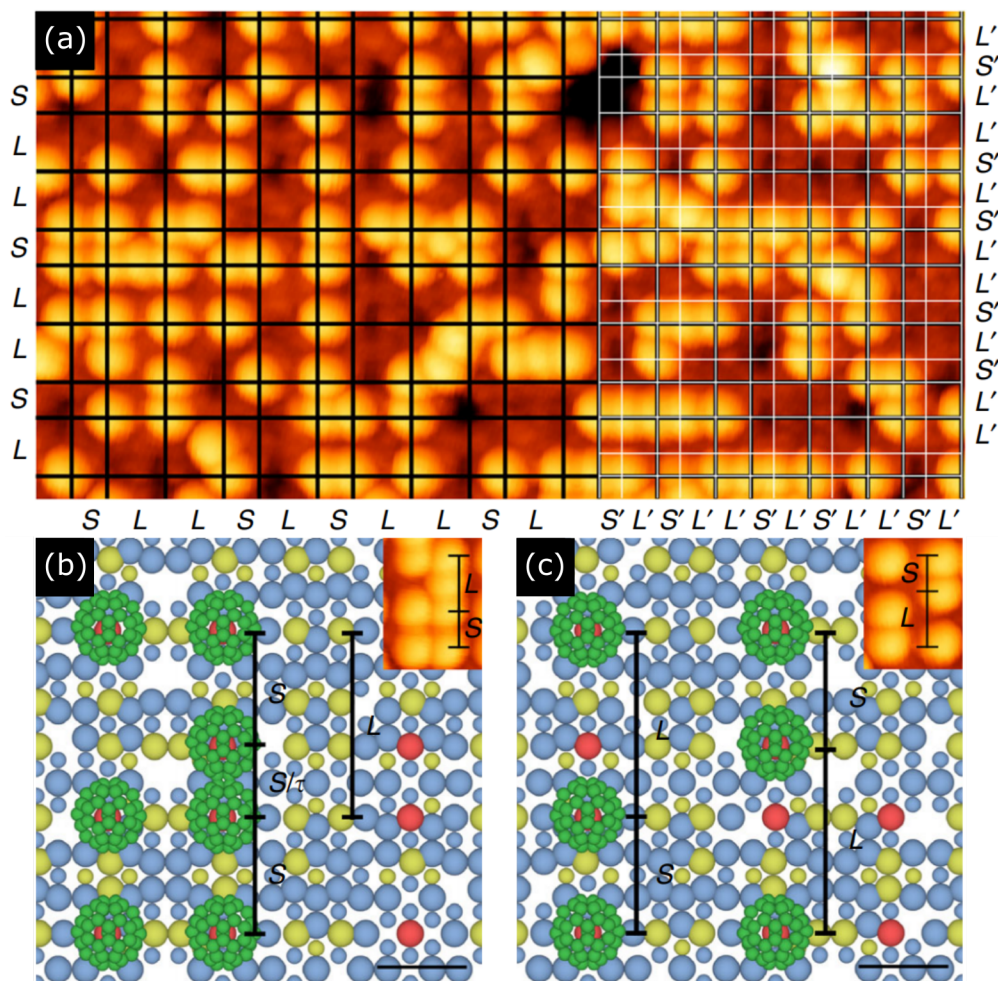


Figure 7.1: (a) STM image of  $C_{60}$  on the 2f-Al-Pd-Mn surface. A black Fibonacci square grid has been overlaid ( $S = 1.26$  nm,  $L = 2.04$  nm) where the majority of  $C_{60}$  molecules reside at the vertices. A white  $\tau$ -deflated Fibonacci square grid ( $S' = S/\tau$ ,  $L' = L/\tau$ ) has also been overlaid explaining the remaining minority of  $C_{60}$  molecules. (b) and (c) Comparison of  $C_{60}$  features observed by STM and the model 2f-Al-Pd-Mn structure.  $S$  and  $L$  and  $\tau$ -deflated distances are marked. Reproduced and modified from [19].

motifs being common, as can be seen in Figure 7.2(c). A review of Pn adsorption on the high-symmetry surfaces of  $i$ -Ag-In-Yb concluded that the preferential adsorption of Pn at Yb sites is a result of both geometric and electronic factors, as in the  $C_{60}/2f$ -Al-Pd-Mn system. Yb-Yb separations at the substrate surface match well with internal distances in

the Pn molecules giving good geometric registry for these sites. Pn is an electron donor and Yb dominates the unoccupied electronic states in the *i*-Ag-In-Yb QC. This points towards a chemical affinity between the two [104].

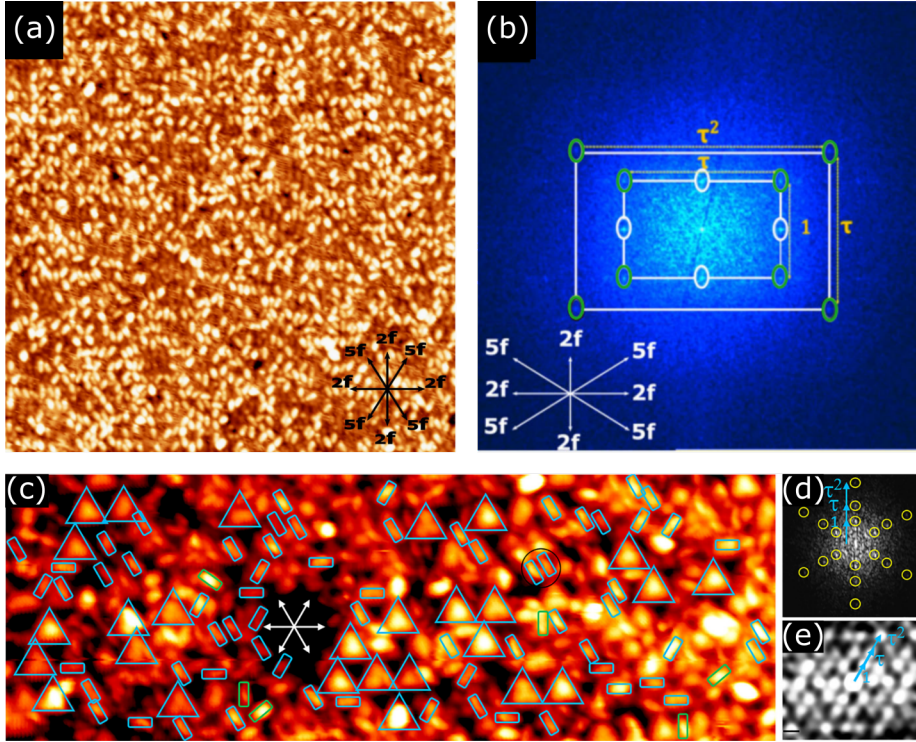


Figure 7.2: (a) STM image of  $\sim 0.37$  ML of Pn deposited on the 2f-Ag-In-Yb surface ( $76 \text{ nm} \times 76 \text{ nm}$ ). The high-symmetry directions of the substrate are shown in black. (b) FFT of (a) taken considering only Pn contribution. Spots aligned along the 2-fold axes are circled white.  $\tau$ -scaled spots aligned along the 5-fold direction are circled green. (c) STM image of  $\sim 0.8$  ML of Pn deposited on the 3f-Ag-In-Yb surface ( $17 \text{ nm} \times 50 \text{ nm}$ ). High-symmetry directions of the substrate are shown in white. Common Pn motifs are marked in blue. (d) and (e) FFT and autocorrelation, respectively, of (c) considering Pn contribution only. (a) and (b) Reproduced and modified from [103]. (c-e) Reproduced and modified from [104].

On the other hand, although not molecular adsorption, no evidence for quasicrystallinity was apparent at any coverage in the Pb/2f-Ag-In-Yb system. Instead, a row-like structure was observed in the first and second layers in a Stranski-Krastanov type growth mode. This is unlike Pb adsorption on the 3-fold and 5-fold surfaces, where a 3D QC

growth mode was evident (see Chapter 3). This difference in growth mode was assigned to the increased atomic density and chemical homogeneity at the 2-fold surface, which contains atoms from all shells of the Tsai-type clusters from which it is formed [153].

The similarities and differences between these adsorption investigations, which utilise the same adsorbate deposited on different surfaces of the same substrate, highlight the complex nature of adsorption on these surfaces. In this chapter, C<sub>60</sub> adsorption on the 2f-Ag-In-Yb surface will be investigated by STM in the hope of creating a quasicrystalline molecular overlayer with simple symmetry. Previous investigations exploring C<sub>60</sub> deposition on the 5f-Ag-In-Yb surface resulted in a disordered overlayer [72]. In the C<sub>60</sub>/2f-Ag-In-Yb system, however, ordering of C<sub>60</sub> molecules is apparent at low to intermediate coverages, with preferential adsorption at some specific substrate surface sites. The large relative size of the C<sub>60</sub> molecules alongside the high-density and proximity of the adsorption sites hinders the growth of a quasicrystalline overlayer.

## 7.2 Experimental details

The 2f-Ag-In-Yb sample was prepared as described in Section 5.2. Powdered C<sub>60</sub> (supplier: Thomas Swan & Co. Ltd. Elicarb, purity: 99%) was evaporated from a Pyrex tube by applying a current to a tungsten filament wrapped tightly around the tube. The data presented here was taken after depositing C<sub>60</sub> with the substrate held at room temperature.

## 7.3 Results

### 7.3.1 C<sub>60</sub> growth on the twofold *i*-Ag-In-Yb surface

#### Low-coverage

Figure 7.3(a) and (c) show STM images taken from the same area of the 2f-Ag-In-Yb surface after depositing C<sub>60</sub> for five minutes. Figure 7.3(a) was taken at positive bias and Figure 7.3(c) was taken at negative bias. In both figures, C<sub>60</sub> molecules are resolved as bright circular features. They are more easy to distinguish from the substrate at negative bias and therefore this data can be used to confirm the location of C<sub>60</sub> molecules in the positive bias data. The coverage of C<sub>60</sub>, estimated by considering the area of the substrate surface covered by these brighter features, is  $\sim 0.05$  ML. The substrate is resolved well in both images, where the features discussed in Chapter 5 for the clean 2f-Ag-In-Yb surface (i.e.

larger protrusions corresponding to Yb contribution at positive bias and smaller features representing 2<sup>nd</sup> and 4<sup>th</sup> shell Ag/In atoms at negative bias) are clearly observed. The substrate features have been emphasized by merging the images in Figure 7.3(a) and (c) with their inverse filtered FTTs taken considering only substrate contribution (not shown here), as can be seen in Figure 7.3(b) and (d), respectively.

As with the clean surface analysis in Chapter 5, the diamond features resolved on the substrate surface at both bias polarities will be used as a basis for further discussion and consideration of C<sub>60</sub> adsorption sites. A selection of these diamond features residing on the exact same area of the surface and in close proximity to locations where C<sub>60</sub> molecules have been adsorbed are marked in Figure 7.3(a-d). In these cases, it is clear that C<sub>60</sub> molecules have adsorbed close to the vertices of the diamond tiles or, given the analysis presented in Chapter 5, at sites dominated by Yb and 4<sup>th</sup> shell Ag/In substrate atoms. These adsorption locations are highlighted on the model of the 2f-Ag-In-Yb surface structure shown in Figure 7.4(a), where black circles represent C<sub>60</sub> adsorption locations. Given the close proximity and chemical inhomogeneity of the substrate atoms in the vicinity of these sites, it is difficult to say whether adsorption occurs at a specific atomic site or within some hollow at the surface. Some possibilities will now be discussed.

From the bias-dependency analysis of the clean 2f-Ag-In-Yb STM data in Chapter 5, it is known that Yb dominates positive bias data and therefore the unoccupied electronic states at the surface. Contribution from Ag/In sites (2<sup>nd</sup> and 4<sup>th</sup> shell sites, in particular) is more apparent at negative bias meaning an increased contribution to the occupied electronic states at the surface for these sites. Unlike for Pn adsorption on this surface, discussed in the introduction to this chapter, C<sub>60</sub> is an electron acceptor rather than an electron donor [154]. Therefore, chemically, adsorption of C<sub>60</sub> at the sites which contribute most to the occupied electronic states at the surface would be likely due to electron transfer. Indeed, a dimer of 4<sup>th</sup> shell Ag/In atoms arranged along the 2-fold direction resides at the centre of the proposed adsorption sites marked by black circles on the surface model in Figure 7.4(a) (i.e. at the diamond vertices). An example is marked by a blue oval on the model. In fact, the model separation between the two atoms in this dimer is 0.28 nm. The average separation of two C atoms at the long diagonals of the hexagonal faces of a C<sub>60</sub> molecule is close to this at 0.29 nm. This distance is marked on the model of a C<sub>60</sub> molecule shown in Figure 7.4(b). This suggests, alongside chemical affinity, a good geometric registry for these sites if C<sub>60</sub> adsorbs with these two C atoms atop of the dimer of 4<sup>th</sup> shell Ag/In substrate atoms.

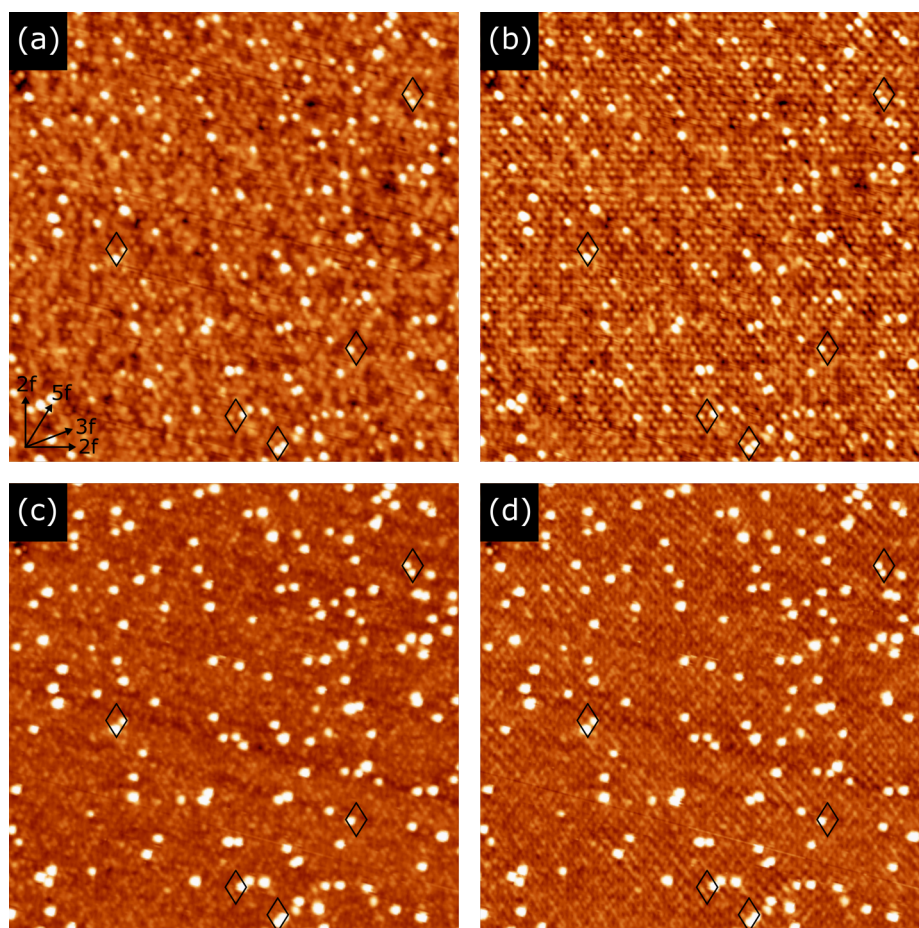


Figure 7.3: (a) and (c) STM images ( $122 \text{ nm} \times 122 \text{ nm}$ ) of  $\sim 0.05 \text{ ML}$  of  $C_{60}$  deposited on the 2f-Ag-In-Yb surface ( $V_b = +2.0 \text{ V}$ ,  $I_t = 0.2 \text{ nA}$  and  $V_b = -1.5 \text{ V}$ ,  $I_t = 0.1 \text{ nA}$ , respectively). (b) and (d) The same STM images as in (a) and (c), respectively, where substrate features have been enhanced by merging the image with its inverse filtered FFT taken considering only substrate contribution. The high-symmetry axes are marked by arrows at the bottom of (a) and are oriented the same for all figures. Diamond features of the substrate (the same as those discussed in Chapter 5) have been marked by black diamonds.

However, not all of the deposited  $C_{60}$  molecules adsorb at these sites, with some appearing at different locations on the surface. Identifying these other adsorption sites with respect to the surface proves difficult. Given the considerations of chemistry and geometry discussed above, other similar potential adsorption sites could be those marked in red on

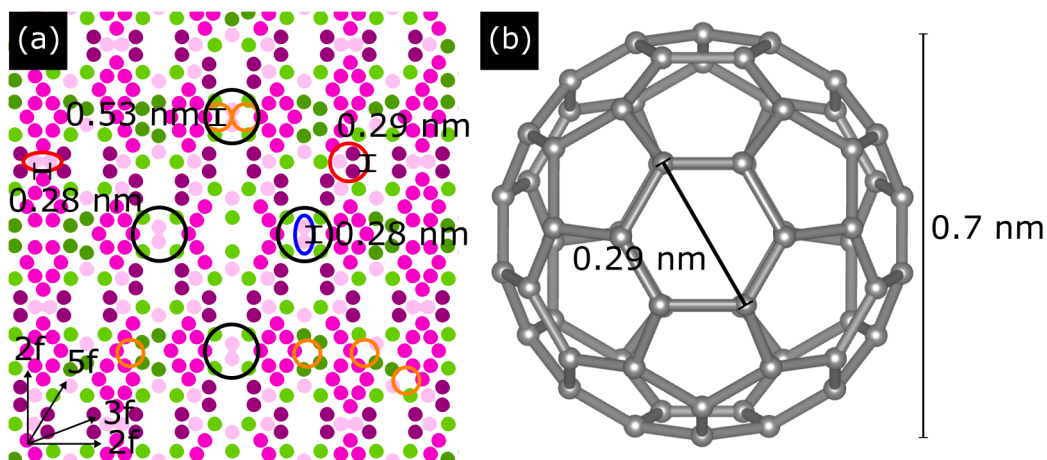


Figure 7.4: (a) Section of the 2f-Ag-In-Yb model atomic structure (purple: 2<sup>nd</sup> shell Ag/In, light green: 3<sup>rd</sup> shell Yb, light pink: 4<sup>th</sup> shell Ag/In, dark pink: 5<sup>th</sup> shell Ag/In and dark green: glue Yb - 1<sup>st</sup> shell has been omitted). The high-symmetry axes of the surface are marked by arrows. Black circles have been overlaid to indicate C<sub>60</sub> adsorption locations. 2<sup>nd</sup> and 4<sup>th</sup> shell Ag/In dimers with separations similar to the C-C separation marked on the C<sub>60</sub> atomic model in (b) are highlighted in red and blue. Hollow sites with a separation similar to the cage diameter of C<sub>60</sub> (again marked in (b)) are marked by orange circles.

the model in Figure 7.4(a). These include another 4<sup>th</sup> shell Ag/In dimer with the same separation as the dimer marked in blue but with atoms arranged along the perpendicular 2-fold direction. See top-left of Figure 7.4(a) for an example. There is also a triangular arrangement composed of two 2<sup>nd</sup> shell and one 4<sup>th</sup> shell Ag/In atoms. An example is marked at the top-right of Figure 7.4(a). The separation between any two atoms within these triangles is the same as the 0.29 nm C-C separation in C<sub>60</sub>. Both of these motifs repeat throughout the model structure.

Adsorption of C<sub>60</sub> at hollow surface sites can also not be ruled out. Although not exactly at the centre, plausible hollow adsorption sites do reside in the vicinity of the model C<sub>60</sub> adsorption locations marked by black circles in Figure 7.4(a). Examples are marked by orange circles at the top diamond vertex. Other similar hollow sites are common throughout the model, where examples are also marked by orange circles. Each of these sites is formed from five substrate atoms in a pentagonal arrangement - a good symmetrical match for the C<sub>60</sub> molecule. The approximate ‘diameter’ of these hollows is  $\sim 0.53$  nm. This is relatively close to the cage diameter of C<sub>60</sub> ( $\sim 0.7$  nm) meaning a C<sub>60</sub> molecule could

physically adsorb within these hollows. Adsorption at these sites, however, would suggest a mechanism driven by these geometric factors as opposed to any chemical influence. The pentagonal arrangement of atoms surrounding these hollows is composed of a mixture of 3<sup>rd</sup> shell and glue Yb and 4<sup>th</sup> and 5<sup>th</sup> shell Ag/In atoms. The atomic composition also differs between sites with some not containing any 4<sup>th</sup> shell Ag/In atoms (i.e. the atoms thought to dominate occupied electronic states at the surface, alongside those from the 2<sup>nd</sup> shell).

### Intermediate coverage

Figure 7.5(a) and Figure 7.5(c) show STM images taken after depositing C<sub>60</sub> on the 2f-Ag-In-Yb surface for 25 minutes and 65 minutes, respectively. The estimated coverages are  $\sim 0.25$  ML and  $\sim 0.72$  ML, respectively. By eye, the overlayers appear relatively disordered. However, FFTs taken considering contribution from C<sub>60</sub> only do exhibit diffraction maxima, indicating some form of order in the overlayer structure in both cases. In Figure 7.5(b), the FFT taken from the C<sub>60</sub> overlayer in Figure 7.5(a), two sets of spots aligned along both 2-fold axes are visible, as highlighted in blue. In fact, the separations between these spots matches those observed in the clean surface data, where an FFT taken from the clean surface at positive bias is shown inset for comparison. This is consistent with the adsorption of C<sub>60</sub> in a row-like structure. This backs up the suggestion of adsorption at the 4<sup>th</sup> shell Ag/In sites at the diamond vertices discussed previously, where these sites form row features on the clean surface (see Chapter 5 for a more in-depth discussion of these rows).

The FFT of the C<sub>60</sub> overlayer at slightly higher sub-ML coverage (i.e. Figure 7.5(c)) is shown in Figure 7.5(d). It exhibits extra sets of spots oriented at an angle of 45° with respect to the horizontal, as highlighted in yellow. Spots of the same arrangement and separation are also visible in the clean surface data, but only at positive bias where Yb contribution dominates STM contrast (see inset in Figure 7.5(b) and discussion in Chapter 5). These features still, however, could result from adsorption at the 4<sup>th</sup> shell Ag/In sites at the diamond vertices. The four Yb atoms surrounding these sites (see the locations marked by black circles in Figure 7.4(a) for reference) form the distribution of large protrusions which dominate STM data at positive bias on the clean 2f-Ag-In-Yb surface. Therefore, it follows that adsorption of C<sub>60</sub> molecules at the suggested 4<sup>th</sup> shell Ag/In sites would produce similar FFT features, where these sites reside at the centre of the four Yb atoms.

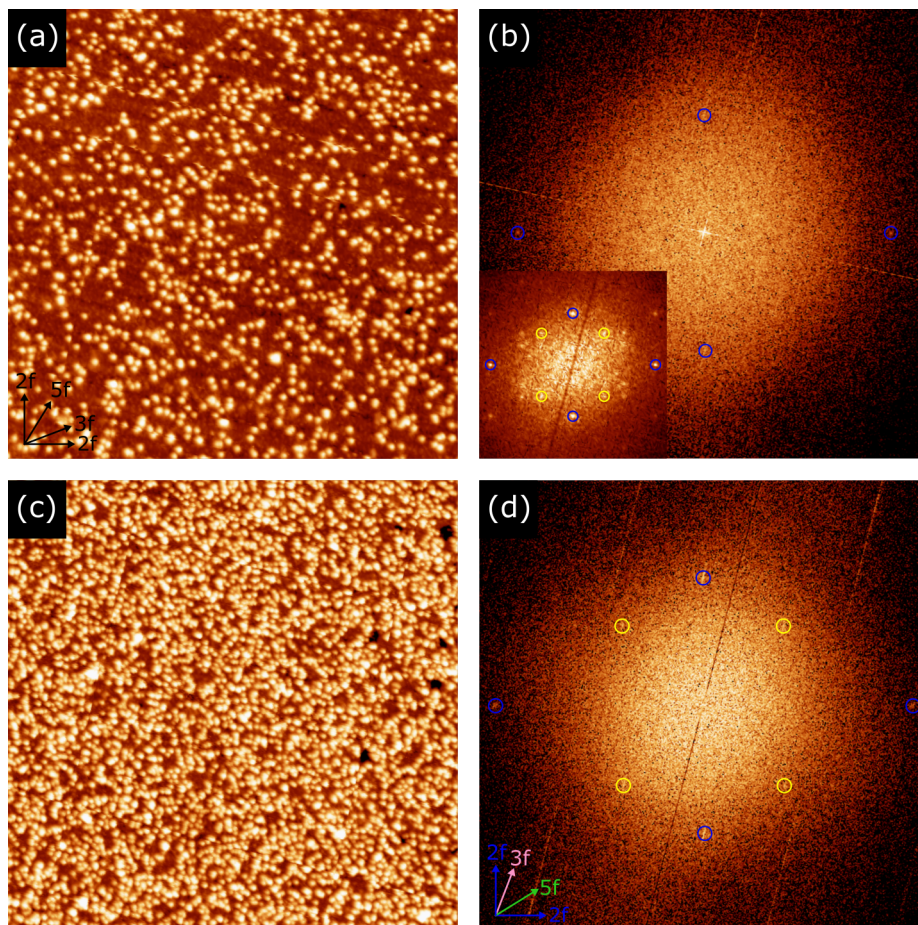


Figure 7.5: (a) STM image ( $148 \text{ nm} \times 148 \text{ nm}$ ) of  $\sim 0.25 \text{ ML}$  of  $\text{C}_{60}$  deposited on the 2f-Ag-In-Yb surface ( $V_b = -2.0 \text{ V}$ ,  $I_t = 0.2 \text{ nA}$ ). (c) STM image ( $198 \text{ nm} \times 198 \text{ nm}$ ) of  $\sim 0.72 \text{ ML}$  of  $\text{C}_{60}$  deposited on the 2f-Ag-In-Yb surface ( $V_b = -1.5 \text{ V}$ ,  $I_t = 0.2 \text{ nA}$ ). The high-symmetry axes are marked by arrows at the bottom of (a) and are oriented the same for (c). (b) and (d) FFTs from (a) and (c), respectively, taken considering only  $\text{C}_{60}$  contribution. Inset in (b) is the FFT taken from the clean 2f-Ag-In-Yb surface at positive bias for comparison. The high-symmetry axes are marked by arrows at the bottom of (b) and are oriented the same for (d). Coloured circles mark maxima which are discussed in the text.

Again however, these adsorption sites are clearly not the only sites  $\text{C}_{60}$  adopts on the surface at these intermediate coverages. There seems to be a range of other sites which contribute to the formation of the somewhat disordered overlayers observed. Again, it is

difficult to pick out any specific features or motifs which would indicate the location of these adsorption sites with respect to the substrate surface. There are also no obvious examples of fully formed ‘diamonds’ of adsorbed C<sub>60</sub> at these intermediate coverages, as would be the case if adsorption occurred at only these 4<sup>th</sup> shell Ag/In sites. As mentioned, the 2f-Ag-In-Yb surface contains atoms from all shells of the Tsai-type clusters from which it is formed. The result is a dense, chemically complex surface plane. It is likely that there are a range of closely-spaced competing adsorption sites with similar adsorption potential. This, alongside the large relative size of the C<sub>60</sub> molecules, could induce the observed disorder in the overlayers. Preferential adsorption of C<sub>60</sub> molecules at some 4<sup>th</sup> shell Ag/In sites could become less energetically favourable due to electronic repulsion effects from C<sub>60</sub> molecules adsorbed at other sites in the close vicinity. In this case, adsorption would occur at the next most stable site. An element of quasicrystallinity may be apparent in the overlayer at larger length-scales due to this aspect of ‘partial’ preferential adsorption. However, adsorption at other sites incorporates some disorder into the overlayer.

As mentioned in the introduction, a disordered layer has been reported previously for C<sub>60</sub> deposition on the 5f-Ag-In-Yb surface [72]. Adsorption of C<sub>60</sub> on the high-symmetry surfaces of the *i*-Ag-In-Yb substrate appears different to that observed on the 2f-Al-Pd-Mn surface. On 2f-Al-Pd-Mn, a clear chemical affinity for Mn substrate atoms was apparent and a quasiperiodic overlayer was formed. The sparsity of Mn as the minority constituent at the 2f-Al-Pd-Mn surface was reported to be a key factor in the formation of a quasiperiodic C<sub>60</sub> overlayer on this surface [19]. At the 5f-Ag-In-Yb surface, 4<sup>th</sup> shell Ag/In atoms make up 47% of the surface atomic composition. The rest is Yb. At the 2f-Ag-In-Yb surface, Ag/In atoms make up 76% of the surface atomic composition (15% 1<sup>st</sup> shell, 14% 2<sup>nd</sup> shell, 15% 4<sup>th</sup> shell and 32% 5<sup>th</sup> shell), with the rest being Yb. In both cases, there is a relatively homogeneous distribution of different elements at the surface in a stoichiometric sense. Yb is the minority constituent at the 2f-Ag-In-Yb surface. However, as mentioned, Yb dominates the unoccupied states at the 2f-Ag-In-Yb surface and so is considered chemically unlikely as an adsorption site for C<sub>60</sub> (an electron acceptor). Further to this, the nearest neighbour distance between the suggested 2<sup>nd</sup> and 4<sup>th</sup> shell Ag/In adsorption sites (i.e. those marked in blue and red in Figure 7.4(a)) is much smaller than that for Mn on the 2f-Al-Pd-Mn surface ( $\sim 0.4$  nm smaller). The same is true for the 4<sup>th</sup> shell Ag/In atom nearest neighbour distance on the 5f-Ag-In-Yb surface. The proximity of nearest Mn neighbours was reported previously to induce spatial perturbations in the C<sub>60</sub> overlayer on 2f-Al-Pd-Mn as a result of the increased molecule-molecule interaction [19]. These notions

may explain the disordered nature of  $C_{60}$  overlayers on the 2f-Ag-In-Yb and 5f-Ag-In-Yb surfaces, where both lack a viable (chemically and geometrically) minority constituent for continued quasiperiodic growth. The element of order on the 2f-Ag-In-Yb surface could then still be explained by adsorption at the subset of 4<sup>th</sup> shell dimer sites (i.e. those marked in blue in Figure 7.4(a)), where the nearest neighbour distance between these sites is much larger and their density much lower.

### High-coverage

Figure 7.6(a) shows an STM image taken after depositing  $C_{60}$  on the surface for 160 minutes - the maximum dose time attempted in this investigation. Saturation of the first-layer is apparent, alongside the early beginnings of a second-layer (see areas marked by black circles). The estimated coverage is  $\sim 1.05$  ML. A higher coverage would be expected here assuming a continuation of the linear dose-coverage relationship which is observed during completion of the first-layer. This suggests a decrease in sticking coefficient once the first-layer is complete. However, further experiments involving higher dose times would be required to confirm this. The FFT of the overlayer in Figure 7.6(a) is shown in Figure 7.6(b). The same spots arranged along the 2-fold direction are still apparent but appear less pronounced. The spots arranged at  $45^\circ$  to the horizontal have disappeared. This would suggest that, after the sites of ordered preferential adsorption have been filled, adsorption continues in a somewhat disordered fashion filling the other remaining sites in between.

## 7.4 Summary

In this chapter, the results from a  $C_{60}$  adsorption investigation on the 2f-Ag-In-Yb surface were presented. At low coverage, preferential adsorption close to specific sites dominated Yb and 4<sup>th</sup> shell Ag/In substrate atoms was observed. This was inferred by comparing the locations of  $C_{60}$  molecules with the underlying substrate structure, where both were resolved by STM at low coverage. Adsorbed molecules were observed to be coincident with locations where, if no molecule was adsorbed, large substrate protrusions would be evident by STM at positive bias. These large substrate protrusions are known to reside at locations dominated by Yb and 4<sup>th</sup> shell Ag/In atoms (see Chapter 5). Considering that 4<sup>th</sup> shell Ag/In sites contribute to the occupied electronic states at the 2f-Ag-In-Yb surface (see again Chapter 5), it is suggested that the chemical affinity between these sites

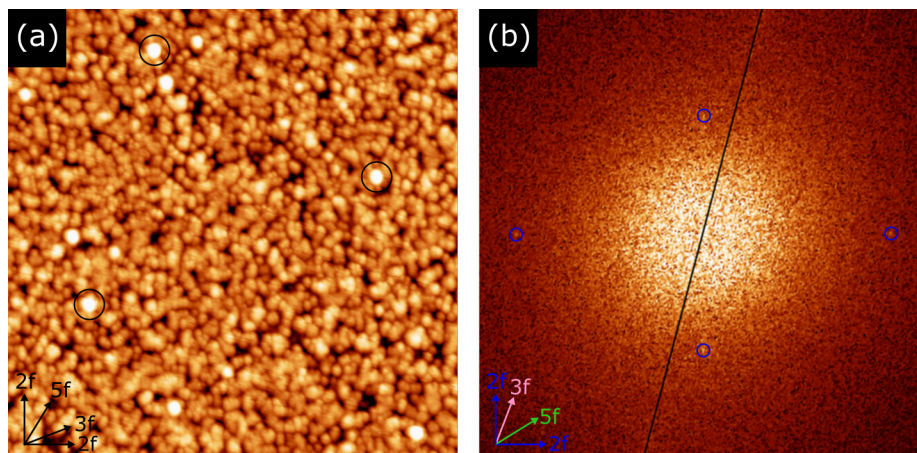


Figure 7.6: (a) STM image ( $110 \text{ nm} \times 110 \text{ nm}$ ) of  $\sim 1.05 \text{ ML}$  of C<sub>60</sub> deposited on the 2f-Ag-In-Yb surface ( $V_b = -1.5 \text{ V}$ ,  $I_t = 0.2 \text{ nA}$ ). The high-symmetry axes are marked by arrows at the bottom of (a). (b) FFT from (a) taken considering only C<sub>60</sub> contribution. The high-symmetry axes are marked by arrows at the bottom of (b). Coloured circles mark maxima which are discussed in the text.

and C<sub>60</sub>, an electron acceptor, results in the preferential adsorption observed. Similarly, the separation between 4<sup>th</sup> shell Ag/In atoms at these sites matches well with specific C-C separations in the C<sub>60</sub> molecule. Examples of adsorption at other locations was also apparent. However, determination of the exact location of these other adsorption sites was hampered by the proximity of substrate atoms and the large relative size of the C<sub>60</sub> molecules. Other potential adsorption sites based on chemical and geometric factors were suggested.

At intermediate coverages, similar conclusions were drawn. C<sub>60</sub> overlayers appeared relatively disordered by eye, but FFTs taken considering only C<sub>60</sub> contribution indicated maxima coinciding with those observed in FFTs taken from clean surface data at positive bias. This again suggested preferential adsorption at the Yb and 4<sup>th</sup> shell Ag/In based sites which are resolved at positive bias on the clean surface. Concurrent adsorption of C<sub>60</sub> at a range of other locations resulted in an element of disorder in the overlayers and this was amplified as the coverage was further increased. This element of disorder was assigned to chemical and geometric effects where there is a lack of adequately spaced, chemically viable adsorption sites at the surface for quasiperiodic growth. LEED experiments would be useful in these intermediate to higher coverage regimes to confirm any long-range order

in the overlayer structure.

This investigation highlights the importance of substrate/adsorbate selection in these kinds of investigations. Although  $C_{60}$  has formed quasicrystalline overlayers on other 2-fold QC surfaces and 2f-Ag-In-Yb has been used as a template for quasicrystalline growth of other adsorbate molecules, combining the two does not simply result in the formation of a quasicrystalline overlayer. Further investigations involving different experimental conditions (i.e. substrate temperature, deposition flux etc.) could reveal a different growth mode and overlayer structure. Attempting a much higher coverage of  $C_{60}$  would also be interesting to assess the existence of any form of rotational epitaxy.

## Chapter 8

# Summary and outlook

The work undertaken here aimed to further our understanding of the surfaces of QCs and related overlayer structures. This was accomplished by investigating the clean high-symmetry surfaces of the *i*-Ag-In-Yb QC, as well as these surfaces after deposition of different elemental and molecular adsorbates.

In terms of clean surface investigations discussed in Chapter 5, new information was provided through further explorations of the 2f-Ag-In-Yb and 5f-Ag-In-Yb surfaces. On the 2-fold surface, a previously unobserved bias-dependency of STM contrast was found, providing fresh insights into the surface structure. At negative bias, atoms of the 2<sup>nd</sup> and 4<sup>th</sup> Ag/In shells of the Tsai-type building blocks were predominantly observed. At positive bias, resolution was dominated by Yb contrast. This is consistent with previous theoretical density of states calculations for related 1/1 approximant structures where Yb was observed to dominate unoccupied states. The inhomogeneous nature of the STM data from this surface was attributed to chemical disorder at the Ag/In sites. A re-investigation of the clean 5f-Ag-In-Yb surface by STM revealed an unusual motion of atoms on the surface. The sites where movement occurred were consistent with the 5-fold symmetry of the surface. Three potential mechanisms for the motion, involving ‘simple’ surface diffusion and phason-assisted movement, were proposed and discussed.

In Chapter 6, metal adsorption on the 5f-Ag-In-Yb surface was investigated. Firstly, data from previous adsorption experiments on this surface were re-assessed, indicating the motion of adsorbate species between successive STM scans. With particular focus on the Pb/5f-Ag-In-Yb system, it was found that Pb adatoms move across their previously determined first- and second-layer adsorption sites. The movement was assigned to the changing

potential energy landscape created by the moving atoms in the underlying clean substrate. Secondly, the results from a Ag adsorption investigation on the surface were presented. Motion of Ag was observed at the theoretically predicted first-layer adsorption sites at low coverages where pentagonal arrangements of adsorbed Ag were apparent. Clustered 3D growth of Ag at CC locations was also evident with clusters exhibiting a range of sizes and  $\tau$ -scaled pentagonal arrangements being common. As coverage was increased, continued growth and coalescence of these clusters occurred, eventually making way for a disordered 3D overlayer at high coverages.

After this,  $C_{60}$  adsorption on the 2f-Ag-In-Yb surface was investigated in Chapter 7. An element of preferential adsorption was observed at particular 4<sup>th</sup> shell Ag/In sites. This was assigned to the chemical affinity between  $C_{60}$  and these sites and the geometry of the sites. Adsorption at a range of other undetermined sites was also apparent, adding an element of disorder to the overlayer structure which was accentuated as the coverage was increased. This was assigned to the large relative size of  $C_{60}$  molecules and the high atomic density at the substrate surface where a lack of sufficiently spaced, chemically feasible adsorption sites were available.

Further studies which would complement the results presented in this thesis are discussed at the end of each results chapter. In a more general sense, these investigations highlight some areas which would be interesting for future exploration. First of all, the new datasets and interpretations presented here highlight the importance of the continued investigation of systems which have already been previously studied. New and interesting phenomena can still be discovered, like the movement of atoms observed on the clean 5f-Ag-In-Yb surface. Further investigations of this motion will be important in order to ascertain the driving mechanism. If the motion is phason-related, further data taken under altered experimental conditions (i.e. differing substrate temperatures) could provide direct information on phasonic behaviour, where this has typically been inferred from indirect observations in the past. Such studies would also help advance our understanding of the mechanisms behind QC growth. Re-visiting other QC surfaces to assess any similar forms of movement would be helpful to build our knowledge in this relatively unstudied area.

Further to this, although adsorption on QC surfaces is one of the more well-studied areas in the field, there still remains many interesting unexplored systems. This is highlighted by the variation in growth modes of different metal adsorbates on the 5f-Ag-In-Yb surface. Take, for example, Ag and In which are both substrate constituents. A clear QC ML structure was observed after In deposition, but this is not the case for Ag adsorption,

---

as presented in Chapter 6. Co-depositing Ag and In could help explain these differences and perhaps reveal the nature of the chemical disorder Ag/In sites in the substrate. Co-depositing a stoichiometric mix of Ag, In and Yb could then provide insights into the growth of QCs on the atomic scale. More generally, building on the library of systems studied so far by investigating as many QC substrate/adsorbate combinations as possible will continue to provide new information on QC properties and will likely result in many more novel discoveries.

# List of Figures

2.1	(a-f) The five 2D Bravais lattices (oblique, rectangular, centred rectangular, square and hexagonal, respectively), with lattice vectors marked by arrows and axes of rotational symmetry indicated according to the key in each (the number in brackets specifies the angle of rotation). (f) A simple demonstration of the incompatibility of a periodic pentagonal lattice in terms of rotational symmetry and the ability to fill all space. . . . .	6
2.2	(a) Specification of (a) the coordinate system and (b) crystal planes in a cubic unit cell. . . . .	7
2.3	(a) A patch of the P1 PT. (b) Inflation/deflation of the tiling using substitution. (c) The proto-tiles and their corresponding matching rules. Tiles are colours coded according to these matching rules in all figures. . . . .	9
2.4	(a-c) Observed and (e-f) calculated diffraction patterns from the 5-fold, 3-fold and 2-fold orientations of the <i>i</i> -Al-Mn phase from left to right, respectively. The 5-fold patterns have been indexed using the icosahedral reciprocal basis vectors (see Figure 2.5), where vector $\mathbf{a}_1$ is perpendicular to the page. Reproduced from [5] and [28]. . . . .	10
2.5	(a) The six reciprocal basis vectors of an iQC. (b) Projection of these vectors along a 5-fold direction, where vector $\mathbf{a}_1$ is perpendicular to the page. . . .	11
2.6	Generation of a 1D Fibonacci chain from a 2D hypercubic lattice using (a) the section method and (b) the strip-projection method. . . . .	13

- 2.7 Demonstration of (a) a phason flip and (b) (2/1) and (3/2) approximant creation in the 1D Fibonacci chain. Both techniques involve a modification of the generation of a 1D Fibonacci chain from a 2D hypercubic lattice using the section method (Figure 2.6(a)). These modifications are discussed in the text. . . . . 18
- 2.8 (a-c) HRTEM images (8 nm × 21 nm) from *d*-Al-Cu-Co at 1123 K showing structural rearrangements of atomic clusters and the corresponding redistribution of the Penrose tiles as a function of time (0, 8 and 115 s respectively). (d) The positions of the tile vertices marked A and B in (a-c) in perp-space alongside a circular window displaying the size of an OD which generates a Penrose tiling with the same vertex density as that observed experimentally. Reproduced and modified from [44]. . . . . 19
- 2.9 (a) The first five of a set of infinite coordination polyhedra that can describe the atomic structure around any Al atom in face-centre Al. Their radii have a ratio from left to right of  $1:\sqrt{2}:\sqrt{3}:\sqrt{4}:\sqrt{5}$ , with the smallest radius being 2.863 Å. Reproduced from [48]. (b) Model atomic structure of a C<sub>60</sub> molecule. 22
- 2.10 The concentric shells of the Tsai-type clusters. From left to right (1<sup>st</sup> shell to 5<sup>th</sup> shell): a disordered 4 Cd atom tetrahedron, a 20 Cd atom dodecahedron ( $r = 0.46$  nm), a 12 Yb atom icosahedron ( $r = 0.56$  nm), a 30 Cd atom icosidodecahedron ( $r = 0.65$  nm) and a 92 Cd atom RTH unit ( $r = 0.78$  nm), where the radii given are those for the Cd-Yb structure. Reproduced and modified from [52]. . . . . 23
- 3.1 A schematic of a step-terrace surface structure in the TSK model. Surface atomic sites and defects are labelled. These are discussed further in the text. Reproduced from [1]. . . . . 29
- 3.2 (a-c) STM images of the step-terrace morphology (250 nm × 250 nm, 300 nm × 300 nm and 400 nm × 400 nm, respectively) and (d-f) corresponding LEED patterns from the 5-fold [71], 3-fold [73] and 2-fold [74] surfaces of *i*-Ag-In-Yb, respectively. Reproduced from [62]. . . . . 30

- 3.3 (a) 5-fold plane from the *i*-Ag-In-Yb model, where green circles correspond to 3<sup>rd</sup> shell Yb sites, red circles to 4<sup>th</sup> shell Ag/In sites and gold circles to CC positions. Inset is a Tsai-type cluster truncated through its centre perpendicular to its 5-fold axis. (b) STM image of the 5f-Ag-In-Yb surface taken at negative sample bias voltage (30 nm × 30 nm). (c-e) Comparison of pentagonal features in the model, at negative sample bias voltage and at positive sample bias voltage, respectively. 4<sup>th</sup> shell Ag/In sites are resolved in (d), whilst 3<sup>rd</sup> shell Yb sites are resolved in (e). (a,c) Reproduced and modified from [77], (b) from [78], (d) from [71] and (e) from [72]. . . . . 32
- 3.4 The three thin film growth modes, with coverage (displayed to the right) increasing in the downwards direction. (a) Layer-by-layer (Frank-van der Merve), (b) layer plus island (Stranski-Krastanov) and (c) island (Volmer-Weber) growth. Reproduced and modified from [1]. . . . . 33
- 3.5 (a) STM image (150 nm × 150 nm) and (b) LEED pattern (150 eV) from ~ 10 ML of Ag deposited on the 5f-Al-Pd-Mn surface. Angles between island edges and diffraction maxima of 12° or some multiple have been highlighted in (a) and (b), respectively. Inset in (a) is an atomically resolved STM image (9.4 nm × 9.4 nm) from on top of an Ag island at ~ 100 ML coverage. It indicates hexagonal symmetry. This is due to the formation Ag(111) nanocrystals, rotationally aligned with respect to the substrate. The spots corresponding to one specific hexagonal domain are highlighted by black circles in (b). Reproduced and modified from [89] and [88]. . . . . 35
- 3.6 (a) STM image (70 nm × 70 nm) from ~ 5 ML of Cu deposited on the 5f-Al-Pd-Mn surface. Five domains of row structure are evident with orientation along the high-symmetry directions of the substrate. Separations between rows follow a Fibonacci sequence, with one marked in white. (b) LEED pattern (177 eV) from the Cu film at a substrate temperature of 85 K. Periodic separations between high-intensity streaks are marked in white. Aperiodically spaced maxima within streaks are highlighted in red and blue. (c) Structural model comprising of a vicinal surface formed via a 13.28° miscut from the (100) direction in a body-centred tetragonal structure. The step-terrace structure is indicated at the top and *L* and *S* separations are marked at the bottom. Reproduced and modified from [91]. . . . . 37

- 3.7 (a) STM image ( $45 \text{ nm} \times 45 \text{ nm}$ ) from  $\sim 0.04 \text{ ML}$  of Al deposited on the 5f-Al-Cu-Fe surface. Red contrast corresponds to substrate and blue is deposited Al. Two enlarged ‘starfish’ features are shown to the right. (b) Model of the growth mechanism of Al starfish features. Solid circles represent substrate atoms and hatched circles correspond to deposited Al. Reproduced and modified from [93]. . . . . 38
- 3.8 (a) Atomic density distribution along the 5-fold direction in the *i*-Ag-In-Yb model. The surface plane and planes which describe Pb layers in the overlayer structure are marked. The corresponding shell in the RTH cluster is given in parentheses. (b-d) Corresponding in-plane atomic structure for the first, second and intermediate, and third layer respectively. STM images of each layer are shown inset. (b) Surface In and Yb sites represented by red and green circles, respectively. In sites corresponding to first layer Pb adsorption positions are shown in grey. (c) Blue and magenta circles correspond to Yb and In sites and second and intermediate Pb adsorption positions, respectively. (d) Purple circles represent Yb sites corresponding to third layer Pb adsorption positions. Reproduced and modified from [78]. 40
- 3.9 (a) STM image ( $50 \text{ nm} \times 50 \text{ nm}$ ) from a quasicrystalline  $\text{C}_{60}$  layer on the 5f-Al-Cu-Fe surface. Bright (B) and dark (D) contrast molecules are indicated. The apparent height difference between a pair of B and D molecules is indicated in the form of a line scan. (b) Extracted positions of B molecules (top) and corresponding autocorrelation pattern (bottom). Reproduced and modified from [101]. . . . . 42
- 3.10 (a) STM image ( $75 \text{ nm} \times 75 \text{ nm}$ ) from a quasicrystalline Pn layer on the 5f-Ag-In-Yb surface. (b) Extracted positions of Pn molecules (top) with (left) and without (right) orientation included and corresponding autocorrelation (bottom). Reproduced and modified from [101]. . . . . 43
- 4.1 The UHV surface analytical system used for acquisition of the majority of data presented in the results sections of this thesis. Major components have been labelled. . . . . 47
- 4.2 Operation of (a) a rotary pump, (b) a turbomolecular pump and (c) an ion pump. Reproduced and modified from [1]. . . . . 49

4.3	Operation of (a) a Pirani gauge and (b) an ion gauge. Reproduced and modified from [1]. . . . .	50
4.4	Setup used for (a) the Czochralski and (b) the Bridgman crystal growth methods. Reproduced and modified from [113]. . . . .	53
4.5	(a) Ion sputtering and (b) annealing as surface cleaning techniques. The resulting surface composition after each process is displayed to the right. Atoms of the sample are coloured grey, foreign species within the sample bulk are coloured dark grey, surface contaminants are coloured black and impinging ions are coloured white. Reproduced and modified from [1]. . . . .	54
4.6	(a) Projected 2D Ewald construction for diffraction from a 2D surface lattice. (b) Schematic of a standard LEED experimental setup. Reproduced and modified from [1]. . . . .	57
4.7	(a) Energy diagram showing the quantum mechanical tunnelling of electrons from an STM tip to a sample surface held a positive bias. $E_{F1}$ and $E_{F2}$ are the Fermi levels of the surface and tip, respectively. $\phi_1$ and $\phi_2$ are the work functions of the surface and tip, respectively. $\phi_B$ is the effective barrier height, $d$ is effective tunnelling gap and $V$ is the bias voltage. (b) Schematic of an STM setup. Reproduced and modified from [1]. . . . .	60
5.1	(a) STM image (75 nm $\times$ 35 nm, $V_b = +1.1$ V) from the clean 2f-Ag-In-Yb surface displaying a zigzag row structure. (b) The section of the image marked by a square in (a), rotated and enlarged. Rows are highlighted in red, their zigzag nature in blue and $\tau$ -scaled ‘linking’ protrusions in pink. (c) Model $i$ -Ag-In-Yb plane (10 nm $\times$ 10 nm) intersecting CCs. Clusters centres are blue, 1 <sup>st</sup> shell Ag/In atoms are pink, 2 <sup>nd</sup> and 4 <sup>th</sup> shell Ag/In atoms are light pink, 3 <sup>rd</sup> shell Yb atoms are light green, 5 <sup>th</sup> shell Ag/In atoms are red and glue Yb atoms are dark green. This model plane describes the features observed by STM, which are again marked on the image with the same colour coding as in (b). Reproduced and modified from [74]. . . . .	66

- 5.2 (a) High resolution STM image ( $65 \text{ nm} \times 65 \text{ nm}$ ,  $V_b = +0.8 \text{ V}$ ) from the clean 2f-Ag-In-Yb surface. Row structures and corresponding separations along both 2-fold axes are marked. The separation between horizontal rows is placed at an average of the two observed row separations ( $2.06 \pm 0.07 \text{ nm}$  and  $2.4 \pm 0.1 \text{ nm}$ ). (b) 4<sup>th</sup> shell of the model *i*-Ag-In-Yb plane used to describe the 2f-Ag-In-Yb surface. Row structures are again marked, formed by 4<sup>th</sup> shell dimers. Reproduced and modified from [124]. . . . . 67
- 5.3 (a-d) Successive STM scans ( $5 \text{ nm} \times 5.5 \text{ nm}$ ) showing the diffusion of a single atomic vacancy on the Ge(111)*c*( $2 \times 8$ ) surface at room temperature. The time between scans varies from 37-67 s. The arrow in (a) shows where an atomic vacancy was created via atomic manipulation with the STM tip. Reproduced and modified from [131]. (e-g) Successive STM scans ( $14 \text{ nm} \times 7 \text{ nm}$ ) showing the diffusion on In atoms (bright protrusions) embedded in a Cu(001) surface layer at room temperature. The time between scans is indicated. Reproduced and modified from [132]. . . . . 69
- 5.4 (a) and (b) STM images ( $50 \text{ nm} \times 50 \text{ nm}$ ,  $I_t = 0.186 \text{ nA}$ ) from the same area of the 2f-Ag-In-Yb surface taken at  $V_b = +2.5 \text{ V}$  and  $-0.8 \text{ V}$ , respectively. Magnified views ( $12 \text{ nm} \times 12 \text{ nm}$ ) of the sections marked by a black square in (a) and (b) are shown inset. (c) and (d) FFTs of (a) and (b), respectively. High-symmetry axes are marked at the bottom of (c) and are oriented the same for (d). Spots are marked by different coloured circles depending on their orientation. Spots oriented along high-symmetry axes are colour coded the same as the arrows in (c). The basis vectors marked in white can be used to index all spots. (e) and (f) A zoomed in section ( $17 \text{ nm} \times 17 \text{ nm}$ ) of the inverse of the filtered FFTs from all maxima in (c) and (d), respectively. The high-symmetry axes marked by arrows at the bottom of (e) and are oriented the same for (a), (b) and (f). Diamond features referred to in the text have been marked in (a), (b), (e) and (f). . . . . 72

- 5.5 (a) Model *i*-Ag-In-Yb plane describing the 2f-Ag-In-Yb surface structure (20 nm × 20 nm). Different coloured circles represent different shells in the Tsai-type cluster (blue: 1<sup>st</sup> shell Ag/In, purple: 2<sup>nd</sup> shell Ag/In, light green: 3<sup>rd</sup> shell Yb, light pink: 4<sup>th</sup> shell Ag/In, dark pink: 5<sup>th</sup> shell Ag/In and dark green: glue Yb). Diamond tiles describing the arrangement of bright protrusions in STM data have been marked. The high-symmetry axes are marked at the bottom and are oriented the same for all figures. (b) and (d) Diamond features observed at +2.5 V and -0.8 V, respectively (12 nm × 12 nm, same as inset in Figure 5.4(a) and (b), respectively). (c) and (e) Model features corresponding to those in (b) and (e), respectively (7 nm × 7 nm). . . . . 74
- 5.6 (a) and (b) Model 2f-Ag-In-Yb planes (20 nm × 20 nm) considering only Yb sites and 2<sup>nd</sup> and 4<sup>th</sup> shell Ag/In sites, respectively. Colour coding is the same as in Figure 5.5. Four Yb atom squares corresponding to the large bright protrusions observed by STM have been marked in (a). Rows of high atomic density have been marked in both (a) and (b), with the corresponding row separations given. Alignment of model features along different directions have been marked in both (a) and (b). . . . . 76
- 5.7 LEED pattern (15 eV) from the 5f-Ag-In-Yb surface.  $\tau$ -scaled separations between spots have been marked on (a). The projected 5-fold icosahedral reciprocal basis vectors have been marked on (b). . . . . 79

- 5.8 (a-e) Successive STM scans ( $12 \text{ nm} \times 12 \text{ nm}$ ,  $V_b = -0.8 \text{ V}$ ,  $I_t = 0.08 \text{ nA}$ ) taken from the same area of the 5f-Ag-In-Yb surface (marked by a square in Supporting Figure 5.1). The time between scans is  $\sim 130 \text{ s}$ . Different circles mark areas where movement is observed: solid white circles indicate a protrusion which disappears in the subsequent frame, dashed white circles show the empty site in this subsequent frame, dashed black circles highlight empty sites which are filled in the subsequent frame and solid black circles mark the filled site. Semi-circles indicate areas where a protrusion appears/disappears at the same site between multiple consecutive frames. (f) A map ( $46 \text{ nm} \times 46 \text{ nm}$ ) of all sites where movement is observed between the seven successive scans in Supporting Figure 5.1. (g) Autocorrelation ( $23 \text{ nm} \times 46 \text{ nm}$ ) of the map in (f). (h) Autocorrelation ( $23 \text{ nm} \times 46 \text{ nm}$ ) of the STM image in the first frame of Supporting Figure 5.1.  $\sim 2.5 \text{ nm}$  edge-length pentagons,  $\tau$ -deflated versions and  $\tau^2$ -deflated versions have been marked in (f-h). . . . . 81
- 5.9 (a) STM image ( $8 \text{ nm} \times 8 \text{ nm}$ ,  $V_b = -0.8 \text{ V}$ ,  $I_t = 0.08 \text{ nA}$ ) taken from the 5f-Ag-In-Yb surface (magnified section of Figure 5.8(c)). Sites where movement is observed across the seven successive scans in Supporting Figure 5.1 are marked and numbered. Sites 1, 5 and 6 are filled in this image. (b) and (c) A section of atomic sites from the 5f-Ag-In-Yb surface model corresponding to the area of the surface in (a) (gold: CCs, light green: 3<sup>rd</sup> shell Yb, light pink: 4<sup>th</sup> shell Ag/In and dark green: glue Yb). The scale is the same as in (a). Atomic sites and interstitial sites with geometry similar to the movement sites marked in (a) have been marked in (b) and (c), respectively, and numbered accordingly. Small-scale separations and angles between sites are summarised in Table 5.1.  $2.5 \text{ nm}$  edge-length pentagons have been overlaid on all figures. . . . . 85

- 5.10 STM image ( $46 \text{ nm} \times 46 \text{ nm}$ ,  $V_b = -0.8 \text{ V}$ ,  $I_t = 0.08 \text{ nA}$ ) taken from the 5f-Ag-In-Yb surface (same as frame 1 in Supporting Figure 5.1). A set of large, stationary protrusions corresponding to an experimental CC distribution have been marked by black crosses. (b) The model 5-fold *i*-Ag-In-Yb CC plane ( $60 \text{ nm} \times 60 \text{ nm}$ ) with the best match to the experimentally extracted CC distribution from (a). (c) Same as (a) with a section of the matching model plane in (b) overlaid. Inset bottom left and right are the reverse FFT and autocorrelation of the STM image, respectively. (d) Model phason-related CC distribution ( $60 \text{ nm} \times 60 \text{ nm}$ ) associated with the CC distribution in (b). Additional phason-related sites are shown as red circles. A patch of the Penrose P1 tiling has been overlaid and enlarged inset. Dashed tiles indicate a possible tile flip considering phason-related positions. 2.5 nm edge-length pentagons,  $\tau$ -deflated versions and  $\tau^2$ -deflated versions are overlaid on all figures. . . . . 89
- 5.11 Enlarged version ( $35 \text{ nm} \times 35 \text{ nm}$ ) of the model phason-related plane in Figure 5.10(d). Experimental movement positions (black circles) are overlaid. (b) Perp-space profile of the matching experimental movement sites and phason-related model sites. The large circle indicates the size of the original OD used to generate CC model sites only. . . . . 91
- 5.12 STM image ( $8 \text{ nm} \times 8 \text{ nm}$ ,  $V_b = -0.8 \text{ V}$ ,  $I_t = 0.08 \text{ nA}$ ) taken from the 5f-Ag-In-Yb surface (same as Figure 5.9(a)). (b) A section of the phason-related model CC distribution (gold: original CC sites and red: phason-related sites). The scale is the same as in (a). A set of sites with geometry similar to (a) have been marked in (b) and numbered accordingly. Two potential model sites are marked for 3. Small-scale separations and angles between sites are summarised in Table 5.2. A 2.5 nm edge-length pentagon has been overlaid in both figures. . . . . 92
- 6.1 (a-c) STM images ( $10 \text{ nm} \times 10 \text{ nm}$ ) of Ag deposited on the 5f-Al-Pd-Mn surface at 0.2, 0.5 and 1.7 ML, respectively. (d-e) STM images ( $10 \text{ nm} \times 10 \text{ nm}$ ) of Ag deposited on the p-10f surface of the  $\xi'$ -Al-Pd-Mn approximant phase at 0.2, 0.4 and 5 ML, respectively. The height histograms for each image are shown inset. Reproduced and modified from [145]. . . . . 98

- 6.2 (a) and (b) Calculated adsorption energies for first-layer and second-layer Ag adsorption at heights  $z = 1.2 \text{ \AA}$  and  $1.4 \text{ \AA}$ , respectively. The calculated adsorption energies (in eV) and corresponding colour-coding are shown on the right hand side of both figures, where a more negative energy relates to a more stable adsorption site. Red and black pentagons have been overlaid corresponding to the expected first- and second-layer adsorption sites. Substrate Yb and In atoms are shown in green and red, respectively. Reproduced and modified from [146]. (c) A section of atomic sites from the 5f-Ag-In-Yb surface model with sites from the vacant model planes representing first-layer Bi/theoretical first-layer Ag and first-layer Pb/theoretical second-layer Ag adsorption overlaid (gold: CCs, light green: 3<sup>rd</sup> shell Yb, light pink: 4<sup>th</sup> shell Ag/In, dark green: glue Yb, grey: first-layer Bi/theoretical first-layer Ag and blue: first-layer Pb/theoretical second-layer Ag). (d) Atomic density distribution of the *i*-Ag-In-Yb QC along the 5-fold direction. Arrows indicate the vacant model planes corresponding to first-layer Bi/theoretical first-layer Ag and first-layer Pb/theoretical second-layer Ag adsorption. Reproduced and modified from [77]. . . . . 101
- 6.3 (a) and (b) STM images ( $26 \text{ nm} \times 26 \text{ nm}$ ,  $V_b = -0.9 \text{ V}$ ,  $I_t = 0.5 \text{ nA}$ ) taken from the first-layer and second-layer of Pb deposited on the 5f-Ag-In-Yb surface. Examples of first-layer pentagonal arrangements and second-layer decagonal arrangements have been marked in (a) and (b), respectively. (c) A section of atomic sites from the 5f-Ag-In-Yb surface model (gold: CCs, light green: 3<sup>rd</sup> shell Yb, light pink: 4<sup>th</sup> shell Ag/In and dark green: glue Yb). A 2.5 nm edge-length pentagon has been overlaid on the pentagonal arrangement of CCs. The model first-layer and second-layer adsorption sites determined by Sharma et al. [78] are shown in grey and blue, respectively. A 0.97 nm edge-length pentagon has been overlaid on first-layer sites, with  $\tau$ -inflated pentagons (rotated by  $36^\circ$  with respect to each other) overlaid on the second-layer sites. . . . . 104

- 6.4 (a-d) and (i-k) Successive STM scans ( $5 \text{ nm} \times 5 \text{ nm}$ ,  $V_b = -0.9 \text{ V}$ ,  $I_t = 0.5 \text{ nA}$ ) taken from the same area of the first- and second-layer of Pb deposited on the 5f-Ag-In-Yb surface, respectively. The corresponding motifs are marked by a dashed circle in Supporting Figure 6.1/Figure 6.3(a) and Supporting Figure 6.2/Figure 6.3(b), respectively. (e-h) and (l-m) Sections of the atomic sites from the 5f-Ag-In-Yb surface model (gold: CCs, light green: 3<sup>rd</sup> shell Yb, light pink: 4<sup>th</sup> shell Ag/In and dark green: glue Yb). The scale is the same as in (a-d) and (i-k). Occupied adsorption sites in (a-d) and (i-k) are shown by filled grey circles in (e-h) and blue circles in (l-m), respectively. Empty circles represent unoccupied sites. . . . . 105
- 6.5 (a) and (c) STM images ( $60 \text{ nm} \times 60 \text{ nm}$ ) of  $\sim 0.05 \text{ ML}$  of Ag deposited on the 5f-Ag-In-Yb surface ( $V_b = -0.8 \text{ V}$ ,  $I_t = 0.1 \text{ nA}$  and  $V_b = 0.4 \text{ V}$ ,  $I_t = 0.1 \text{ nA}$ , respectively). (b) and (d) The same STM images as in (a) and (c), respectively, where substrate features have been enhanced by merging the image with its inverse filtered FFT taken considering only substrate contribution. Patches of a 2.5 nm edge-length Penrose P1 tiling have been overlaid with vertices residing at large protrusions corresponding to 4<sup>th</sup> Ag/In atoms surrounding CCs in (b) and ring features corresponding to 3<sup>rd</sup> Yb atoms surrounding CCs in (d). The features marked in different colours in all figures are discussed in the text. . . . . 108
- 6.6 (a-e) Successive STM scans ( $10 \text{ nm} \times 10 \text{ nm}$ ,  $V_b = -0.8 \text{ V}$ ,  $I_t = 0.1 \text{ nA}$ ) taken from the same area of  $\sim 0.05 \text{ ML}$  of Ag deposited on the 5f-Ag-In-Yb surface (same as area marked by black square in Supporting Figure 6.6). Solid circles mark sites occupied by an Ag adatom. Dashed circles mark sites occupied by an Ag adatom in a previous or subsequent scan. (f-j) Sections of atomic sites from the 5f-Ag-In-Yb surface model corresponding to the area of the surface in (a-e), respectively (gold: CCs, light green: 3<sup>rd</sup> shell Yb, light pink: 4<sup>th</sup> shell Ag/In and dark green: glue Yb). Theoretically predicted first- and second-layer Ag adsorption sites [146] are shown in grey and blue, respectively. A set of first-layer sites with geometry similar to sites in (a-e) are marked and numbered accordingly. Filled grey circles represent positions which are occupied in the corresponding STM image and empty grey circles represent those which are not. 2.5 nm edge-length pentagons have been overlaid on all figures. . . . . 112

- 6.7 (a-e) Successive STM scans ( $10 \text{ nm} \times 10 \text{ nm}$ ,  $V_b = -0.8 \text{ V}$ ,  $I_t = 0.1 \text{ nA}$ ) taken from the same area of  $\sim 0.05 \text{ ML}$  of Ag deposited on the 5f-Ag-In-Yb surface. Same area as motif marked by a half red/half blue circle in Supporting Figure 6.6. In the third scan (c), the size of the central protrusion increases. It stays at this larger size in (d) and (e). A black line has been overlaid on the same area in each figure to highlight this size increase. . . . . 114
- 6.8 (a) and (c) STM images of  $\sim 0.3 \text{ ML}$  of Ag deposited on the 5f-Ag-In-Yb surface ( $81 \text{ nm} \times 81 \text{ nm}$ ,  $V_b = -0.8 \text{ V}$ ,  $I_t = 0.1 \text{ nA}$  and  $60 \text{ nm} \times 60 \text{ nm}$ ,  $V_b = 1.5 \text{ V}$ ,  $I_t = 0.1 \text{ nA}$ , respectively). Inset in (a) is the height profile taken along the black line in the figure. (b) and (d) Same STM images as in (a) and (c), respectively, where substrate features have been enhanced by merging the image with its inverse filtered FFT taken considering only substrate contribution. Patches of a  $2.5 \text{ nm}$  edge-length Penrose P1 tiling have been overlaid with vertices describing the arrangement of substrate features. The features marked in different colours in all figures are discussed in the text. . . . . 115
- 6.9 (a) and (b) Height histograms taken from an STM image of the clean 5f-Ag-In-Yb surface and of  $\sim 0.3 \text{ ML}$  of Ag deposited on the surface (Figure 6.8(a)), respectively. . . . . 117
- 6.10 (a-d) Sections of the STM scan of  $\sim 0.3 \text{ ML}$  of Ag deposited on the 5f-Ag-In-Yb surface in Figure 6.8(d) ( $9 \text{ nm} \times 9 \text{ nm}$ ,  $V_b = 1.5 \text{ V}$ ,  $I_t = 0.1 \text{ nA}$ ). The dashed yellow pentagons in (a) and the numbered pentagons in (b-c) are the same as the features marked this way in Figure 6.8(c) and (d). Sets of small Ag protrusions have been numbered in (a-d). (e) A section of atomic sites from the 5f-Ag-In-Yb surface model (gold: CCs, light green: 3<sup>rd</sup> shell Yb, light pink: 4<sup>th</sup> shell Ag/In and dark green: glue Yb). Theoretically predicted first- and second-layer Ag adsorption sites [146] are shown in grey and blue, respectively. Features have been marked on the model which correspond to features observed in the STM data. These are discussed in the text.  $2.5 \text{ nm}$  edge-length pentagons have been overlaid in black on all figures. . . . . 119

- 6.11 (a) STM image of  $\sim 0.8$  ML of Ag deposited on the 5f-Ag-In-Yb surface ( $54 \text{ nm} \times 54 \text{ nm}$ ,  $V_b = 1.8 \text{ V}$ ,  $I_t = 0.1 \text{ nA}$ ). Inset is a height histogram taken from the image. (b) Same as (a), where features discussed in the text have been marked. Inset is a the height profile taken along the black line in the figure. (c) STM image of  $\sim 1.4$  ML of Ag deposited on the 5f-Ag-In-Yb surface ( $64 \text{ nm} \times 64 \text{ nm}$ ,  $V_b = -1.1 \text{ V}$ ,  $I_t = 0.1 \text{ nA}$ ). (d) STM image of  $\sim 2.4$  ML of Ag deposited on the 5f-Ag-In-Yb surface ( $98 \text{ nm} \times 98 \text{ nm}$ ,  $V_b = 1.0 \text{ V}$ ,  $I_t = 0.1 \text{ nA}$ ). Inset in (c) and (d) are height histograms taken from the image. . . . . 124
- 7.1 (a) STM image of  $\text{C}_{60}$  on the 2f-Al-Pd-Mn surface. A black Fibonacci square grid has been overlaid ( $S = 1.26 \text{ nm}$ ,  $L = 2.04 \text{ nm}$ ) where the majority of  $\text{C}_{60}$  molecules reside at the vertices. A white  $\tau$ -deflated Fibonacci square grid ( $S' = S/\tau$ ,  $L' = L/\tau$ ) has also been overlaid explaining the remaining minority of  $\text{C}_{60}$  molecules. (b) and (c) Comparison of  $\text{C}_{60}$  features observed by STM and the model 2f-Al-Pd-Mn structure.  $S$  and  $L$  and  $\tau$ -deflated distances are marked. Reproduced and modified from [19]. . . . . 131
- 7.2 (a) STM image of  $\sim 0.37$  ML of Pn deposited on the 2f-Ag-In-Yb surface ( $76 \text{ nm} \times 76 \text{ nm}$ ). The high-symmetry directions of the substrate are shown in black. (b) FFT of (a) taken considering only Pn contribution. Spots aligned along the 2-fold axes are circled white.  $\tau$ -scaled spots aligned along the 5-fold direction are circled green. (c) STM image of  $\sim 0.8$  ML of Pn deposited on the 3f-Ag-In-Yb surface ( $17 \text{ nm} \times 50 \text{ nm}$ ). High-symmetry directions of the substrate are shown in white. Common Pn motifs are marked in blue. (d) and (e) FFT and autocorrelation, respectively, of (c) considering Pn contribution only. (a) and (b) Reproduced and modified from [103]. (c-e) Reproduced and modified from [104]. . . . . 132

- 7.3 (a) and (c) STM images ( $122 \text{ nm} \times 122 \text{ nm}$ ) of  $\sim 0.05 \text{ ML}$  of  $\text{C}_{60}$  deposited on the 2f-Ag-In-Yb surface ( $V_b = +2.0 \text{ V}$ ,  $I_t = 0.2 \text{ nA}$  and  $V_b = -1.5 \text{ V}$ ,  $I_t = 0.1 \text{ nA}$ , respectively). (b) and (d) The same STM images as in (a) and (c), respectively, where substrate features have been enhanced by merging the image with its inverse filtered FFT taken considering only substrate contribution. The high-symmetry axes are marked by arrows at the bottom of (a) and are oriented the same for all figures. Diamond features of the substrate (the same as those discussed in Chapter 5) have been marked by black diamonds. . . . . 135
- 7.4 (a) Section of the 2f-Ag-In-Yb model atomic structure (purple: 2<sup>nd</sup> shell Ag/In, light green: 3<sup>rd</sup> shell Yb, light pink: 4<sup>th</sup> shell Ag/In, dark pink: 5<sup>th</sup> shell Ag/In and dark green: glue Yb - 1<sup>st</sup> shell has been omitted). The high-symmetry axes of the surface are marked by arrows. Black circles have been overlaid to indicate  $\text{C}_{60}$  adsorption locations. 2<sup>nd</sup> and 4<sup>th</sup> shell Ag/In dimers with separations similar to the C-C separation marked on the  $\text{C}_{60}$  atomic model in (b) are highlighted in red and blue. Hollow sites with a separation similar to the cage diameter of  $\text{C}_{60}$  (again marked in (b)) are marked by orange circles. . . . . 136
- 7.5 (a) STM image ( $148 \text{ nm} \times 148 \text{ nm}$ ) of  $\sim 0.25 \text{ ML}$  of  $\text{C}_{60}$  deposited on the 2f-Ag-In-Yb surface ( $V_b = -2.0 \text{ V}$ ,  $I_t = 0.2 \text{ nA}$ ). (c) STM image ( $198 \text{ nm} \times 198 \text{ nm}$ ) of  $\sim 0.72 \text{ ML}$  of  $\text{C}_{60}$  deposited on the 2f-Ag-In-Yb surface ( $V_b = -1.5 \text{ V}$ ,  $I_t = 0.2 \text{ nA}$ ). The high-symmetry axes are marked by arrows at the bottom of (a) and are oriented the same for (c). (b) and (d) FFTs from (a) and (c), respectively, taken considering only  $\text{C}_{60}$  contribution. Inset in (b) is the FFT taken from the clean 2f-Ag-In-Yb surface at positive bias for comparison. The high-symmetry axes are marked by arrows at the bottom of (b) and are oriented the same for (d). Coloured circles mark maxima which are discussed in the text. . . . . 138
- 7.6 (a) STM image ( $110 \text{ nm} \times 110 \text{ nm}$ ) of  $\sim 1.05 \text{ ML}$  of  $\text{C}_{60}$  deposited on the 2f-Ag-In-Yb surface ( $V_b = -1.5 \text{ V}$ ,  $I_t = 0.2 \text{ nA}$ ). The high-symmetry axes are marked by arrows at the bottom of (a). (b) FFT from (a) taken considering only  $\text{C}_{60}$  contribution. The high-symmetry axes are marked by arrows at the bottom of (b). Coloured circles mark maxima which are discussed in the text. . . . . 141

# List of Tables

2.1	The Fibonacci chain and corresponding Fibonacci numbers generated using $L$ and $S$ segments. . . . .	8
4.1	Theoretical calculations of the time per ML coverage of a surface and mean free path for different pressures as calculated for $O_2$ molecules at room temperature. . . . .	46
5.1	Distances and angles between numbered sites in Figure 5.9(a), (b) and (c). Angles are measured as the smallest angle from the horizontal direction. . .	86
5.2	Distances and angles between numbered sites in Figure 5.12(a) and (b). Angles are measured as the smallest angle from the horizontal. . . . .	91
6.1	Distances and angles between numbered sites in Figure 6.6(a-j). Angles are measured as the smallest angle from the horizontal. . . . .	113
6.2	Distances and angles between numbered sites in Figure 6.10(b-e). Angles are measured as the smallest angle from the horizontal. . . . .	121
6.3	Comparative properties of different metal adsorbates deposited on the 5f-Ag-In-Yb surface. . . . .	126

# Bibliography

- [1] K. Oura, V. G. Lifshits, A. A. Saranin, A. V. Zotov, and M. Katayama. *Surface science: an introduction*. Springer Science & Business Media, 2013.
- [2] G. Binnig and H. Rohrer. Scanning tunneling microscopy. *Surface Science*, 126(1-3):236–244, 1983.
- [3] L. Pauling. The stochastic method and the structure of proteins. *Am. Sci.*, 43:285, 1955.
- [4] E. Belin-Ferr. *Basics of thermodynamics and phase transitions in complex intermetallics*. World Scientific, 2008.
- [5] D. Shechtman, I. Blech, D. Gratias, and J. W. Cahn. Metallic phase with long-range orientational order and no translational symmetry. *Phys. Rev. Lett.*, 53(20):1951–1953, 1984.
- [6] L. Pauling. Apparent icosahedral symmetry is due to directed multiple twinning of cubic crystals. *Nature*, 317(6037):512–514, 1985.
- [7] X. Zeng, G. Ungar, Y. Liu, V. Percec, A. E. Dulcey, and J. K. Hobbs. Supramolecular dendritic liquid quasicrystals. *Nature*, 428(6979):157–160, 2004.
- [8] S. Fischer, A. Exner, K. Zielske, J. Perlich, S. Deloudi, W. Steurer, P. Lindner, and S. Förster. Colloidal quasicrystals with 12-fold and 18-fold diffraction symmetry. *Proceedings of the National Academy of Sciences*, 108(5):1810–1814, 2011.
- [9] K. Hayashida, T. Dotera, A. Takano, and Y. Matsushita. Polymeric quasicrystal: Mesoscopic quasicrystalline tiling in ABC star polymers. *Phys. Rev. Lett.*, 98(19):195502, 2007.

- [10] A. P. Tsai, J. Q. Guo, E. Abe, H. Takakura, and T. J. Sato. Alloys: A stable binary quasicrystal. *Nature*, 408(6812):537–538, 2000.
- [11] J. Q. Guo, E. Abe, and A. P. Tsai. Stable icosahedral quasicrystals in binary Cd-Ca and Cd-Yb systems. *Phys. Rev. B*, 62(22):R14605–R14608, 2000.
- [12] A. P. Tsai, A. Inoue, and T. Masumoto. A stable quasicrystal in Al-Cu-Fe system. *Japanese Journal of Applied Physics*, 26(9):L1505–L1507, 1987.
- [13] A. P. Tsai, Y. Yokoyama, A. Inoue, and T. Masumoto. Formation, microstructure, chemical long-range order, and stability of quasicrystals in Al-Pd-Mn alloys. *Journal of Materials Research*, 6(12):2646–2652, 1991.
- [14] C. Dong and J. M. Dubois. Quasicrystals and crystalline phases in  $\text{Al}_{65}\text{Cu}_{20}\text{Fe}_{10}\text{Cr}_5$  alloy. *Journal of Materials Science*, 26(6):1647–1654, 1991.
- [15] M. Klyueva, D. Shulyatev, N. Andreev, N. Tabachkova, T. Sviridova, and A. Suslov. New stable icosahedral quasicrystal in the system Al-Cu-Co-Fe. *Journal of Alloys and Compounds*, 801:478–482, 2019.
- [16] J. M. Dubois. *Useful quasicrystals*. World Scientific, 2005.
- [17] V. Fournée, J. Ledieu, M. Shimoda, M. Krajčí, H. R. Sharma, and R. McGrath. Thin film growth on quasicrystalline surfaces. *Israel Journal of Chemistry*, 51(11-12):1314–1325, 2011.
- [18] S. Förster, K. Meinel, R. Hammer, M. Trautmann, and W. Widdra. Quasicrystalline structure formation in a classical crystalline thin-film system. *Nature*, 502(7470):215–218, 2013.
- [19] S. Coates, J. A. Smerdon, R. McGrath, and H. R. Sharma. A molecular overlayer with the fibonacci square grid structure. *Nature Communications*, 9(3435):1–5, 2018.
- [20] M. Paßens and S. Karthäuser. Rotational switches in the two-dimensional fullerene quasicrystal. *Acta Crystallographica Section A*, 75(A75):41–49, 2019.
- [21] C. Kittel. *Introduction to solid state physics*. J. Wiley, 2005.

- [22] J. Bamberg, G. Cairns, and D. Kilminster. The crystallographic restriction, permutations, and Goldbach's conjecture. *The American Mathematical Monthly*, 110(3):202–209, 2003.
- [23] J. Als-Nielsen and D. McMorrow. *Elements of Modern X-ray Physics*. John Wiley & Sons, Ltd, 2011.
- [24] T. Dotera. Toward the discovery of new soft quasicrystals: From a numerical study viewpoint. *Journal of Polymer Science Part B: Polymer Physics*, 50(3):155–167, 2012.
- [25] R. Penrose. The role of aesthetics in pure and applied mathematical research. *Bull. Inst. Math. Appl.*, 10:266–271, 1974.
- [26] R. Penrose. Pentaplexity: a class of non-periodic tilings of the plane. *The mathematical intelligencer*, 2(1):32–37, 1979.
- [27] N. G. de Bruijn. Algebraic theory of Penrose's non-periodic tilings of the plane. *Kon. Nederl. Akad. Wetensch. Proc. Ser. A*, 43(84):1–7, 1981.
- [28] A. Yamamoto and K. Hiraga. Structure of an icosahedral Al-Mn quasicrystal. *Phys. Rev. B*, 37:6207–6214, 1988.
- [29] J. Ledieu, R. McGrath, R. D. Diehl, T. A. Lograsso, D. W. Delaney, Z. Papadopolos, and G. Kasner. Tiling of the fivefold surface of  $\text{Al}_{70}\text{Pd}_{21}\text{Mn}_9$ . *Surface Science*, 492(3):L729–L734, 2001.
- [30] P. Kramer and R. Neri. On periodic and non-periodic space fillings of  $\mathbb{E}^m$  obtained by projection. *Acta Crystallographica Section A*, 40(5):580–587, 1984.
- [31] W. Steurer and S. Deloudi. *Crystallography of quasicrystals: concepts, methods and structures*. Springer, 2009.
- [32] H. R. Sharma, M. Shimoda, and A. P. Tsai. Quasicrystal surfaces: structure and growth of atomic overlayers. *Advances in Physics*, 56(3):403–464, 2007.
- [33] W. Steurer and J. Dshemuchadse. *Intermetallics: structures, properties, and statistics*, volume 26. Oxford University Press, 2016.

- [34] C. Janot. Quasicrystals: A primer. *Monographs on the Physics and Chemistry of Materials*, Oxford University Press, Oxford, 1992.
- [35] H. R. Sharma. *Structure, morphology, and dynamics of quasicrystal surfaces*. PhD thesis, Freie Universität Berlin, Universitätsbibliothek, 2002.
- [36] W. Steurer and S. Deloudi. *Cluster Packing from a Higher Dimensional Perspective*, pages 165–170. Springer, 2015.
- [37] P. Guyot, P. Kramer, and M. de Boissieu. Quasicrystals. *Reports on Progress in Physics*, 54(11):1373, 1991.
- [38] S. Coates and R. Tamura. High dimensional approach to antiferromagnetic aperiodic spin systems. *Materials Transactions*, 62(3):307–311, 2021.
- [39] A. P. Tsai. Discovery of stable icosahedral quasicrystals: progress in understanding structure and properties. *Chemical Society Reviews*, 42:5352–5365, 2013.
- [40] M. de Boissieu, H. Takakura, C. P. Gómez, A. Yamamoto, and A. P. Tsai. Structure determination of quasicrystals. *Philosophical Magazine*, 87(18-21):2613–2633, 2007.
- [41] M. de Boissieu. Phason modes in quasicrystals. *Philosophical Magazine*, 88(13-15):2295–2309, 2008.
- [42] J. Dolinšek, T. Apih, M. Simsič, and J. M. Dubois. Self-Diffusion in Icosahedral  $\text{Al}_{72.4}\text{Pd}_{20.5}\text{Mn}_{7.1}$  and Phason Percolation at Low Temperatures Studied by  $^{27}\text{Al}$  NMR. *Phys. Rev. Lett.*, 82:572–575, 1999.
- [43] T. Janssen, G. Chapuis, and M. de Boissieu. *Aperiodic crystals: from modulated phases to quasicrystals*. Oxford University Press, 2007.
- [44] K. Edagawa, K. Suzuki, and S. Takeuchi. High Resolution Transmission Electron Microscopy Observation of Thermally Fluctuating Phasons in Decagonal Al-Cu-Co. *Phys. Rev. Lett.*, 85:1674–1677, Aug 2000.
- [45] E. Abe, S. J. Pennycook, and A. P. Tsai. Direct observation of a local thermal vibration anomaly in a quasicrystal. *Nature*, 421(6921):347 – 350, 2003.
- [46] A. I. Goldman and R. F. Kelton. Quasicrystals and crystalline approximants. *Reviews of Modern Physics*, 65(1):213, 1993.

- [47] A. P. Tsai. Icosahedral clusters, icosahedral order and stability of quasicrystals a view of metallurgy. *Science and Technology of Advanced Materials*, 9(1):013008, 2008.
- [48] W. Steurer. Stable clusters in quasicrystals: fact or fiction? *Philosophical Magazine*, 86(6-8):1105–1113, 2006.
- [49] C. P. Gómez and S. Lidin. Comparative structural study of the disordered  $\text{MCd}_6$  quasicrystal approximants. *Phys. Rev. B*, 68(2):024203, 2003.
- [50] C. P. Gómez and S. Lidin. Structure of  $\text{Ca}_{13}\text{Cd}_{76}$ : A Novel Approximant to the  $\text{MCd}_{5.7}$  Quasicrystals (M=Ca, Yb). *Angewandte Chemie International Edition*, 40(21):4037–4039, 2001.
- [51] C. P. Gómez. *Order and disorder in the RE-Cd and related systems*. PhD thesis, Stockholm University, 2003.
- [52] H. Takakura, C. P. Gómez, A. Yamamoto, M. de Boissieu, and A. P. Tsai. Atomic structure of the binary icosahedral Yb–Cd quasicrystal. *Nature Materials*, 6(1):58, 2007.
- [53] A. L. Mackay. A dense non-crystallographic packing of equal spheres. *Acta Crystallographica*, 15(9):916–918, 1962.
- [54] G. Bergman, J. L. T. Waugh, and L. Pauling. The crystal structure of the metallic phase  $\text{Mg}_{32}(\text{Al}, \text{Zn})_{49}$ . *Acta Crystallographica*, 10(4):254–259, 1957.
- [55] E. Abe, Y. Yan, and S. J. Pennycook. Quasicrystals as cluster aggregates. *Nature Materials*, 3(11):759, 2004.
- [56] C. L. Henley, M. de Boissieu, and W. Steurer. Discussion on clusters, phasons and quasicrystal stabilisation. *Philosophical Magazine*, 86(6-8):1131–1151, 2006.
- [57] W. Steurer. Quasicrystals: What do we know? What do we want to know? What can we know? *Acta Crystallographica Section A*, 74(1):1–11, 2017.
- [58] Dieter J., S. Ritsch, and C. Beeli. Distinguishing quasiperiodic from random order in high-resolution tem images. *Phys. Rev. B*, 55:8175–8183, 1997.
- [59] A. P. Tsai. “Back to the Future”—An Account Discovery of Stable Quasicrystals. *Accounts of Chemical Research*, 36(1):31–38, 2003.

- [60] U. Mizutani, M. Inukai, H. Sato, and E. S. Zijlstra. Hume-Rothery stabilization mechanism and  $e/a$  determination for RT- and MI-type 1/1-1/1-1/1 approximants studied by FLAPW-Fourier analyses. *Chem. Soc. Rev.*, 41:6799–6820, 2012.
- [61] S. S. Hars, H. R. Sharma, J. A. Smerdon, T. P. Yadav, A. Al-Mahboob, J. Ledieu, V. Fournée, R. Tamura, and R. McGrath. Surface structure of the Ag-In-(rare earth) complex intermetallics. *Phys. Rev. B*, 93:205428, 2016.
- [62] C. Cui, M. Shimoda, and A. P. Tsai. Studies on icosahedral Ag–In–Yb: a prototype for Tsai-type quasicrystals. *RSC Advances*, 4(87):46907–46921, 2014.
- [63] A. P. Tsai and M. Yoshimura. Highly active quasicrystalline Al-Cu-Fe catalyst for steam reforming of methanol. *Applied Catalysis A: General*, 214(2):237–241, 2001.
- [64] J. M. Dubois, S. S. Kang, and J. Von Stebut. Quasicrystalline low-friction coatings. *Journal of Materials Science Letters*, 10(9):537–541, 1991.
- [65] S. Takeuchi, H. Iwanaga, and T. Shibuya. Hardness of quasicrystals. *Japanese Journal of Applied Physics*, 30(3R):561, 1991.
- [66] W. Kossel. Extending the law of Bravais. *Nach. Ges. Wiss. Göttingen*, 143:25, 1927.
- [67] I. N. Stranski. Zur theorie des kristallwachstums. *Zeitschrift für Physikalische Chemie*, 136(1):259–278, 1928.
- [68] J.Q. Guo and A.P. Tsai. Stable icosahedral quasicrystals in the Ag-In-Ca, Ag-In-Yb, Ag-In-Ca-Mg and Ag-In-Yb-Mg systems. *Philosophical Magazine Letters*, 82(6):349–352, 2002.
- [69] S. Ohhashi, J. Hasegawa, S. Takeuchi, and A. P. Tsai. Crystal growth of quasicrystal and partial phase diagram involving quasicrystal in the Ag-In-Yb system. *Philosophical Magazine*, 87(18-21):3089–3094, 2007.
- [70] H. R. Sharma, M. Shimoda, S. Ohhashi, and A. P. Tsai. First UHV surface studies of single-grain icosahedral Ag–In–Yb quasicrystal. *Philosophical Magazine*, 87(18-21):2989–2994, 2007.
- [71] H. R. Sharma, M. Shimoda, K. Sagisaka, H. Takakura, J. A. Smerdon, P. J. Nugent, R. McGrath, D. Fujita, S. Ohhashi, and A. P. Tsai. Structure of the fivefold surface of the Ag-In-Yb icosahedral quasicrystal. *Phys. Rev. B*, 80(12):121401, 2009.

- [72] P. J. Nugent, J. A. Smerdon, R. McGrath, M. Shimoda, C. Cui, A. P. Tsai, and H. R. Sharma. Step-terrace morphology and reactivity to  $C_{60}$  of the five-fold icosahedral Ag–In–Yb quasicrystal. *Philosophical Magazine*, 91(19-21):2862–2869, 2011.
- [73] C. Cui, P. J. Nugent, M. Shimoda, J. Ledieu, V. Fourne, A. P. Tsai, R. McGrath, and H. R. Sharma. The atomic structure of the threefold surface of the icosahedral Ag–In–Yb quasicrystal. *Journal of Physics: Condensed Matter*, 24(44):445011, 2012.
- [74] C. Cui, P. J. Nugent, M. Shimoda, J. Ledieu, V. Fournée, A. P. Tsai, R. McGrath, and H. R. Sharma. Structure of the twofold surface of the icosahedral Ag–In–Yb quasicrystal. *Journal of Physics: Condensed Matter*, 26(1):015001, 2013.
- [75] Y. Ishii and T. Fujiwara. Hybridization mechanism for cohesion of Cd-based quasicrystals. *Phys. Rev. Lett.*, 87(20):206408, 2001.
- [76] H. R. Sharma, G. Simutis, V. R. Dhanak, P. J. Nugent, C. Cui, M. Shimoda, R. McGrath, A. P. Tsai, and Y. Ishii. Valence band structure of the icosahedral Ag–In–Yb quasicrystal. *Physical Review B*, 81(10):104205, 2010.
- [77] S. S. Hars, H. R. Sharma, J. A. Smerdon, S. Coates, K. Nozawa, A. P. Tsai, and R. McGrath. Growth of a bismuth thin film on the five-fold surface of the icosahedral Ag–In–Yb quasicrystal. *Surface Science*, 2018.
- [78] H. R. Sharma, K. Nozawa, J. A. Smerdon, P. J. , I. McLeod, V. R. Dhanak, M. Shimoda, Y. Ishii, A. P. Tsai, and R. McGrath. Templated three-dimensional growth of quasicrystalline lead. *Nature Communications*, 4:2715, 2013.
- [79] F. C. Frank and J. H. van der Merwe. One-dimensional dislocations. I. Static theory. *Proc. R. of Soc. Lond. A*, 198(1053):205–216, 1949.
- [80] F. Frank and J. H. Van der Merwe. One-dimensional dislocations. II. Misfitting monolayers and oriented overgrowth. *Proc. R. of Soc. Lond. A*, 198(1053):216–225, 1949.
- [81] I. N. Stranski and L. Krastanow. Zur theorie der orientierten ausscheidung von ionenkristallen aufeinander. *Monatshefte für Chemie und verwandte Teile anderer Wissenschaften*, 71(1):351–364, 1937.

- [82] M. Volmer and A. Weber. Keimbildung in übersättigten gebilden. *Zeitschrift für physikalische Chemie*, 119(1):277–301, 1926.
- [83] R. McGrath, J. A. Smerdon, H. R. Sharma, W. Theis, and J. Ledieu. The surface science of quasicrystals. *Journal of Physics: Condensed Matter*, 22(8):084022, 2010.
- [84] M. Shimoda. Thin metal films on quasicrystalline surfaces. *Progress in Surface Science*, 75(3):87–108, 2004.
- [85] M. Shimoda, T. J. Sato, A. P. Tsai, and J. Q. Guo. Epitaxial film growth on quasiperiodic surfaces. *Journal of Alloys and Compounds*, 342(1):441–444, 2002.
- [86] M. Shimoda, T. J. Sato, A. P. Tsai, and J. Q. Guo. Epitaxial crystalline film with psuedo-tenfold symmetry formed by Au-deposition on a decagonal  $\text{Al}_{72}\text{Ni}_{12}\text{Co}_{16}$  quasicrystal. *Phys. Rev. B*, 62(17):11288, 2000.
- [87] M. Shimoda, J. Q. Guo, T. J. Sato, and A. P. Tsai. Surfactant-mediated growth of  $\text{AuAl}_2$  film on a decagonal  $\text{Al}_{72}\text{Ni}_{12}\text{Co}_{16}$  quasicrystal. *Surface Science*, 482-485:784–788, 2001.
- [88] V. Fournée, A.R. Ross, T.A. Lograsso, J.W. Evans, and P.A. Thiel. Growth of Ag thin films on complex surfaces of quasicrystals and approximant phases. *Surface Science*, 537(1):5–26, 2003.
- [89] V. Fournée, T. C. , A. R. Ross, T. A. Lograsso, J. W. Evans, and P. A. Thiel. Nucleation and growth of ag films on a quasicrystalline Al-Pd-Mn surface. *Phys. Rev. B*, 67:033406, Jan 2003.
- [90] J. Ledieu, J. T. Hoefl, D. E. Reid, J. A. Smerdon, R. D. Diehl, T. A. Lograsso, A. R. Ross, and R. McGrath. Pseudomorphic growth of a single element quasiperiodic ultrathin film on a quasicrystal substrate. *Phys. Rev. Lett.*, 92(13):135507, 2004.
- [91] K. Pussi, M. Gierer, and R. D. Diehl. The uniaxially aperiodic structure of a thin Cu film on fivefold i-Al-Pd-Mn. *Journal of Physics: Condensed Matter*, 21(47):474213, 2009.
- [92] J. Ledieu, J. T. Hoefl, D. E. Reid, J. A. Smerdon, R. D. Diehl, N. Ferralis, T. A. Lograsso, A. R. Ross, and R McGrath. Copper adsorption on the fivefold  $\text{Al}_{70}\text{Pd}_{21}\text{Mn}_9$  quasicrystal surface. *Phys. Rev. B*, 72(3):035420, 2005.

- [93] T. Cai, J. Ledieu, R. McGrath, V. Fournée, T. Lograsso, A. Ross, and P. Thiel. Pseudomorphic starfish: nucleation of extrinsic metal atoms on a quasicrystalline substrate. *Surface Science*, 526(1-2):115–120, 2003.
- [94] T. Cai, V. Fournée, T. Lograsso, A. Ross, and P. A. Thiel. STM study of the atomic structure of the icosahedral Al-Cu-Fe fivefold surface. *Phys. Rev. B*, 65:140202, 2002.
- [95] K. J. Franke, H. R. Sharma, W. Theis, P. Gille, Ph. Ebert, and K. H. Rieder. Quasicrystalline epitaxial single element monolayers on icosahedral Al-Pd-Mn and decagonal Al-Ni-Co quasicrystal surfaces. *Phys. Rev. Lett.*, 89(15):156104, 2002.
- [96] J. A. Smerdon, J. K. Parle, L. H. Wearing, T. A. Lograsso, A. R. Ross, and R. McGrath. Nucleation and growth of a quasicrystalline monolayer: Bi adsorption on the fivefold surface of i-Al<sub>70</sub>Pd<sub>21</sub>Mn<sub>9</sub>. *Phys. Rev. B*, 78(7):075407, 2008.
- [97] J. Ledieu, L. Leung, L. H. Wearing, R. McGrath, T. A. Lograsso, D. Wu, and V. Fournée. Self-assembly, structure, and electronic properties of a quasiperiodic lead monolayer. *Phys. Rev. B*, 77(7):073409, 2008.
- [98] S. Coates, S. Thorn, R. McGrath, H. R. Sharma, and A. P. Tsai. Unique growth mode observed in a Pb thin film on the threefold surface of an i-Ag-In-Yb quasicrystal. *Phys. Rev. Materials*, 4:026003, 2020.
- [99] J. Ledieu, C. A. Muryn, G. Thornton, R. D. Diehl, T. A. Lograsso, D. W. Delaney, and R. McGrath. C<sub>60</sub> adsorption on the quasicrystalline surface of Al<sub>70</sub>Pd<sub>21</sub>Mn<sub>9</sub>. *Surface Science*, 472(1):89–96, 2001.
- [100] V. Fournée, É. Gaudry, J. Ledieu, M-C. De Weerd, D. Wu, and T. Lograsso. Self-organized molecular films with long-range quasiperiodic order. *ACS Nano*, 8(4):3646–3653, 2014.
- [101] J. A. Smerdon, K. M. Young, M. Lowe, S. S. Hars, T. P. Yadav, D. Hesp, V. R. Dhanak, A. P. Tsai, H. R. Sharma, and R. McGrath. Templated quasicrystalline molecular ordering. *Nano Letters*, 14(3):1184–1189, 2014.
- [102] N. Kalashnyk, J. Ledieu, É. Gaudry, C. Cui, A. P. Tsai, and V. Fournée. Building 2D quasicrystals from 5-fold symmetric corannulene molecules. *Nano Research*, 11(4):2129–2138, 2018.

- [103] A. Alofi, D. Burnie, S. Coates, R. McGrath, and H. R. Sharma. Adsorption of Pentacene on the 2-Fold Surface of the Icosahedral Ag-In-Yb Quasicrystal. *Materials Transactions*, 62(3):312–316, 2021.
- [104] H. R. Sharma, S. Coates, A. Alofi, and R. McGrath. Growth of pentacene molecules on tsai-type quasicrystals and related crystal surfaces. *Journal of Vacuum Science & Technology A*, 40(1):013211, 2022.
- [105] D. Ēcija, J. I. Urgel, A. C. Papageorgiou, S. Joshi, W. Auwärter, A. P. Seitsonen, S. Klyatskaya, M. Ruben, S. Fischer, S. Vijayaraghavan, J. Reichert, and J. V. Barth. Five-vertex Archimedean surface tessellation by lanthanide-directed molecular self-assembly. *Proceedings of the National Academy of Sciences*, 110(17):6678–6681, 2013.
- [106] J. I. Urgel, D. Ēcija, W. Auwrter, A. C. Papageorgiou, A. P. Seitsonen, S. Vijayaraghavan, S. Joshi, S. Fischer, J. Reichert, and J. V. Barth. Five-Vertex Lanthanide Coordination on Surfaces: A Route to Sophisticated Nanoarchitectures and Tessellations. *The Journal of Physical Chemistry C*, 118(24):12908–12915, 2014.
- [107] J. I. Urgel, D. Ēcija, and G. Lyu. Quasicrystallinity expressed in two-dimensional coordination networks. *Nature Chemistry*, 8:657–662, 2016.
- [108] N. A. Wasio, R. C. Quardokus, R. P. Forrest, C. S. Lent, S. A. Corcelli, J. A. Christie, K. W. Henderson, and S. A. Kandel. Self-assembly of hydrogen-bonded two-dimensional quasicrystals. *Nature*, 507(7490):86, 2014.
- [109] M. Paßens, V. Caciuc, N. Atodiresei, M. Feuerbacher, M. Moors, R. E. Dunin-Borkowski, S. Blügel, R. Waser, and S. Kärthäuser. Interface-driven formation of a two-dimensional dodecagonal fullerene quasicrystal. *Nature Communications*, 8:15367, 2017.
- [110] P. A. Thiel. Structure and oxidation at quasicrystal surfaces. *Progress in Surface Science*, 75(3-8):191–204, 2004.
- [111] P. J. Nugent, G. Simutis, V. R. Dhanak, R. McGrath, M. Shimoda, C. Cui, A. P. Tsai, and H. R. Sharma. Surface oxidation of the icosahedral Ag-In-Yb quasicrystal. *Phys. Rev. B*, 82(1):014201, 2010.
- [112] W. Boyes. *Instrumentation Reference Book (4th Edition)*. Elsevier, 2010.

- [113] A. P. Tsai and C. Cui. Crystal Growth of Quasicrystals. In *Handbook of Crystal Growth*, pages 1113–1156. Elsevier, 2015.
- [114] C. Cui and A. P. Tsai. Growth of large single-grain quasicrystals in the Ag-In-Yb system by Bridgman method. *Journal of Crystal Growth*, 312(1):131–135, 2009.
- [115] J. Czochralski. Ein neues verfahren zur messung der kristallisationsgeschwindigkeit der metalle. *Zeitschrift für physikalische Chemie*, 92(1):219–221, 1918.
- [116] P. W. Bridgman. Certain physical properties of single crystals of tungsten, antimony, bismuth, tellurium, cadmium, zinc, and tin. *Proceedings of the American Academy of Arts and Sciences*, 60(6):305–383, 1925.
- [117] P.R. Puckett, S.L. Michel, and W.E. Hughes. Ion beam etching. In *Thin Film Processes II*, pages 749–782. Elsevier, 1991.
- [118] B. Bolliger, M. Erbudak, D. D. Vvedensky, M. Zurkirch, and A. R. Kortan. Surface structural transitions on the icosahedral quasicrystal Al<sub>70</sub>Pd<sub>20</sub>Mn<sub>10</sub>. *Phys. Rev. Lett.*, 80(24):5369–5372, 1998.
- [119] Z. Shen, M. J. Kramer, C. J. Jenks, A. I. Goldman, T. Lograsso, D. Delaney, M. Heitzig, W. Raberg, and P. A. Thiel. Crystalline surface structures induced by ion sputtering of Al-rich icosahedral quasicrystals. *Phys. Rev. B*, 58(15):9961–9971, 1998.
- [120] B. Bolliger, M. Erbudak, A. Hensch, and D.D. Vvedensky. Surface structural phase transitions on icosahedral Al-Pd-Mn. *Mat. Sci. Eng.: A*, 294–296:859–862, 2000.
- [121] I. Horcas, Rs. Fernández, J. M. Gomez-Rodriguez, J. W. S. X. Colchero, J. W. S. X. M. Gómez-Herrero, and A. M. Baro. WSXM: a software for scanning probe microscopy and a tool for nanotechnology. *Review of Scientific Instruments*, 78(1):013705, 2007.
- [122] D. Nečas and P. Klapetek. Gwyddion: an open-source software for SPM data analysis. *Open Physics*, 10(1):181–188, 2012.
- [123] D. Burnie, S. Coates, R. McGrath, and H.R. Sharma. Bias-voltage dependent STM images from the 2-fold surface of the icosahedral Ag-In-Yb quasicrystal. *Journal of Physics: Conference Series*, 1458:012017, 2020.

- [124] S. Coates. *Quasicrystal systems with simple symmetries*. PhD thesis, University of Liverpool, 2019.
- [125] F. Besenbacher, E. Lægsgaard, and I. Stensgaard. Fast-scanning STM studies. *Materials Today*, 8(5):26–30, 2005.
- [126] K. Morgenstern. Fast scanning tunnelling microscopy as a tool to understand changes on metal surfaces: from nanostructures to single atoms. *physica status solidi (b)*, 242(4):773–796, 2005.
- [127] P. A. Thiel, M. Shen, D. J. Liu, and J. W. Evans. Coarsening of two-dimensional nanoclusters on metal surfaces. *The Journal of Physical Chemistry C*, 113(13):5047–5067, 2009.
- [128] J. A. Smerdon, L. Leung, J. K. Parle, C. J. Jenks, R. McGrath, V. Fournée, and J. Ledieu. Formation of a quasicrystalline Pb monolayer on the 10-fold surface of the decagonal Al–Ni–Co quasicrystal. *Surface Science*, 602(14):2496–2501, 2008.
- [129] H. R. Sharma, V. Fournée, M. Shimoda, A. R. Ross, T. A. Lograsso, P. Gille, and A. P. Tsai. Growth of Bi thin films on quasicrystal surfaces. *Phys. Rev. B*, 78:155416, Oct 2008.
- [130] J. Ledieu, M. Krajčič, J. Hafner, L. Leung, L. H. Wearing, R. McGrath, T. A. Lograsso, D. Wu, and V. Fournée. Nucleation of Pb starfish clusters on the five-fold Al–Pd–Mn quasicrystal surface. *Phys. Rev. B*, 79:165430, Apr 2009.
- [131] A. J. Mayne, F. Rose, C. Bolis, and G. Dujardin. An scanning tunnelling microscopy study of the diffusion of a single or a pair of atomic vacancies. *Surface Science*, 486(3):226–238, 2001.
- [132] R. van Gastel, E. Somfai, W. van Saarloos, and J. W. M. Frenken. A giant atomic slide-puzzle. *Nature*, 408:665, 2000.
- [133] K. Nishimoto, T. Sato, and R. Tamura. Low-temperature superstructures of a series of Cd<sub>6</sub>–M (M= Ca, Y, Sr, Pr, Nd, Sm, Gd, Tb, Dy, Ho, Er, Tm, Yb and Lu) crystalline approximants. *Journal of Physics: Condensed Matter*, 25(23):235403, 2013.

- [134] K. Nozawa and Y. Ishii. Electronic structures and stability of Ag-In-Ca surfaces. *Journal of Physics: Conference Series*, 226:012030, 2010.
- [135] M. Shimoda and H. R. Sharma. Sputter-induced crystalline layers and epitaxial overlayers on quasicrystal surfaces. *Journal of Physics: Condensed Matter*, 20(31):314008, 2008.
- [136] H. R. Sharma, P. J. Nugent, T. C. Q. Noakes, J. Smerdon, J. Parle, A. P. Tsai, and R. McGrath. Medium energy ion scattering (MEIS) study from the five-fold surface of icosahedral Ag-In-Yb quasicrystal. In *Journal of Physics: Conference Series*, volume 809, page 012017. IOP Publishing, 2017.
- [137] D. Rouxel and P. Pigeat. Surface oxidation and thin film preparation of AlCuFe quasicrystals. *Progress in Surface Science*, 81:488–514, 2006.
- [138] N. Ferralis, K. Pussi, and R. D. Diehl. Debye temperature of the 10-fold d-AlNiCo quasicrystal surface. *Surface Science*, 602(6):1223–1226, 2008.
- [139] A. L. Pope, T. M. Tritt, R. Gagnon, and J. Strom-Olsen. Electronic transport in Cd-Yb and Y-Mg-Zn quasicrystals. *Applied Physics Letters*, 79(15):2345–2347, 2001.
- [140] R. Tamura, Y. Murao, S. Takeuchi, K. Tokiwa, T. Watanabe, T. J. Sato, and A. P. Tsai. Anomalous Transport Behavior of a Binary Cd-Yb Icosahedral Quasicrystal. *Japanese Journal of Applied Physics*, 40(Part 2, No. 9A/B):L912–L914, sep 2001.
- [141] S. Hars. *Surface structure and epitaxy on Ag-In-Rare earth quasicrystals and related approximants*. PhD thesis, University of Liverpool, 2015.
- [142] P. Nugent. *Surfaces of the icosahedral Ag-In-Yb quasicrystal: structure, reactivity and thin film growth*. PhD thesis, University of Liverpool, 2011.
- [143] K. Young. *Epitaxy on quasicrystals: metals, semi-metals and molecules*. PhD thesis, University of Liverpool, 2012.
- [144] M. Krajčí, J. Hafner, J. Ledieu, V. Fournée, and R. McGrath. Quasiperiodic Pb monolayer on the fivefold *i*-Al-Pd-Mn surface: Structure and electronic properties. *Phys. Rev. B*, 82:085417, 2010.

- [145] V. Fournée, A.R. Ross, T.A. Lograsso, J.W. Evans, and P.A. Thiel. Growth of Ag thin films on complex surfaces of quasicrystals and approximant phases. *Surface Science*, 537(13):5 – 26, 2003.
- [146] K. Nozawa and Y. Ishii. First-principles study of adsorption of Ag on Ag-In-Yb quasicrystal surface. *International Scientific Conference on Engineering and Applied Sciences*, pages 197–206, 2018.
- [147] L. Vitos, A.V. Ruban, H.L. Skriver, and J. Kollár. The surface energy of metals. *Surface Science*, 411(1):186–202, 1998.
- [148] J. Ledieu and V. Fournée. Surfaces of quasicrystals. *Comptes Rendus Physique*, 15(1):48–57, 2014.
- [149] J. A. Smerdon, N. Cross, V. R. Dhanak, H. R. Sharma, K. M. Young, T. A. Lograsso, A. R. Ross, and R. McGrath. Structure and reactivity of bi allotropes on the fivefold icosahedral al–pd–mn quasicrystal surface. *Journal of Physics: Condensed Matter*, 22(34):345002, 2010.
- [150] S. Even-Dar Mandel and R. Lifshitz. Electronic energy spectra of square and cubic fibonacci quasicrystals. *Philosophical Magazine*, 88(13-15):2261–2273, 2008.
- [151] R. Ilan, E. Liberty, S. Even-Dar Mandel, and R. Lifshitz. Electrons and phonons on the square fibonacci tiling. *Ferroelectrics*, 305(1):15–19, 2004.
- [152] S. Even-Dar Mandel and R. Lifshitz. Electronic energy spectra and wave functions on the square fibonacci tiling. *Philosophical Magazine*, 86(6-8):759–764, 2006.
- [153] S. Coates, R. McGrath, and H. R. Sharma. Influence of differences in orientational planar density on the growth of Pb on the i-Ag–In–Yb quasicrystal. *Journal of Physics: Condensed Matter*, 32(42):425006, 2020.
- [154] R. C. Haddon, R. E. Palmer, H. W. Kroto, and P. A. Sermon. The fullerenes: Powerful carbon-based electron acceptors [and discussion]. *Philosophical Transactions: Physical Sciences and Engineering*, 343(1667):53–62, 1993.

# Appendix A

## List of publications

### A.1 Project publications

- **D. Burnie**, S. Coates, R. McGrath, and H.R. Sharma. Bias-voltage dependent STM images from the 2-fold surface of the icosahedral Ag-In-Yb quasicrystal. *Journal of Physics: Conference Series*, 1458:012017, 2020.
- S. Coates, **D. Burnie**, H. R. Sharma, R. McGrath, T. Yamada and R. Tamura. Surface diffusion on the 2-fold surface of the icosahedral Ag-In-Yb quasicrystal. *In preparation*.

### A.2 Future publications

- **D. Burnie**, S. Coates, R. McGrath, and H.R. Sharma. C<sub>60</sub> adsorption on the 2-fold surface of the icosahedral Ag-In-Yb quasicrystal. *In preparation*.
- **D. Burnie**, S. Coates, R. McGrath, and H.R. Sharma. Surface diffusion on the 5-fold surface of the icosahedral Ag-In-Yb quasicrystal. *In preparation*.
- **D. Burnie**, R. McGrath, and H.R. Sharma. Ag adsorption and diffusion on the 5-fold surface of the icosahedral Ag-In-Yb quasicrystal. *In preparation*.

# Appendix B

## List of presentations

### B.1 Oral

- *Atomic diffusion on the fivefold surface of the *i*-Ag-In-Yb quasicrystal.* EC-MetAC 2020, 2020.

### B.2 Poster

- *Atomic diffusion on the fivefold surface of the *i*-Ag-In-Yb quasicrystal.* ISSC-23, 2020.
- *Molecular thin films on quasicrystal surfaces.* Surface Science Day 2019, 2019.
- *Bias-dependency and  $C_{60}$  growth on the 2-fold surface of the *i*-Ag-In-Yb quasicrystal.* Molecules at Surfaces: What do we really know?, 2019.
- *Bias-dependency and  $C_{60}$  growth on the 2-fold surface of the *i*-Ag-In-Yb quasicrystal.* ICQ14, 2019.
- *Growth of  $C_{60}$  on the 2-fold Surface of the *i*-Ag-In-Yb Quasicrystal.* Surface Science Day 2018, 2018.
- *Growth of  $C_{60}$  on the 2-fold Surface of the *i*-Ag-In-Yb Quasicrystal.* C-MAC Days, 2018.

- 
- *Growth of C60 on the 2-fold Surface of the i-Ag-In-Yb Quasicrystal.* C-MAC Euroschool, 2018.
  - *Molecular thin films on quasicrystal surfaces.* Surface Science Day 2017, 2017.
  - *The ZnPc/Al<sub>9</sub>Co<sub>2</sub> interface.* C-MAC Days, 2017.

